

**Electrical and Optical
Modeling of Thin-Film
Photovoltaic Modules**

Mario Zinßer

Electrical and Optical Modeling of Thin-Film Photovoltaic Modules

Zur Erlangung des akademischen Grades eines

**DOKTORS DER INGENIEURWISSENSCHAFTEN
(Dr.-Ing.)**

von der KIT-Fakultät für Elektrotechnik und Informationstechnik
des Karlsruher Instituts für Technologie (KIT)
angenommene

DISSERTATION

von

M.Sc. Mario Zinßer

geboren in Kirchheim unter Teck

Tag der mündlichen Prüfung:

Hauptreferent:

Korreferent:

22.12.22

Prof. Dr.-Ing. Michael Powalla

Prof. Dr.-Ing. Thomas Kirchartz

The electronic version of this dissertation is available at:
<https://publikationen.bibliothek.kit.edu>

Composition of the doctoral committee:

Prof. Dr.-Ing. Michael Powalla (first examiner)
Prof. Dr.-Ing. Thomas Kirchartz (second examiner)
Prof. Dr.-Ing. Marc Hiller (chair person)
Prof. Dr. Tabea Arndt
Prof. Dr.-Ing. Christian Koos

This dissertation has been published at the Light Technology Institute (LTI) of the Karlsruhe Institute of Technology (KIT), Germany and at Zentrum für Sonnenenergie- und Wasserstoff-Forschung Baden-Württemberg (ZSW), Germany.

This work was supported Financed by the Ministry of Science, Research and the Arts of Baden-Württemberg as part of the sustainability financing of the projects of the Excellence Initiative II and the German Academic Scholarship Foundation. This thesis is published as part of the Project CIGSTheoMax under the contract number 0324353A of the German Federal Ministry for Economic Affairs and Climate Action.



Gefördert durch:



aufgrund eines Beschlusses
des Deutschen Bundestages

Keywords: solar cells, solar modules, thin-film, modeling, finite element method (FEM), transfer-matrix method, forecasting, performance loss, holistic loss analysis, topology optimization, yield calculation, maximum efficiency, technological limits

Cover image: Spatial voltage distribution of a generic solar cell.

Nutshell image: bluringmedia - stock.adobe.com.

Copyright © 2022 Mario Zinßer

*To my strong mother,
who supports me non-stop in every imaginable issue
and truly always encourages me in each of my dreams.*

Statement of Authorship

Eidesstattliche Versicherung gemäß § 13 Absatz 2 Ziffer 3 der Promotionsordnung des Karlsruher Instituts für Technologie (KIT) für die KIT-Fakultät für Elektrotechnik und Informationstechnik

Bei der eingereichten Dissertation zu dem Thema „Electrical and Optical Modeling of Thin-Film Photovoltaic Modules“ handelt es sich um meine eigenständig erbrachte Leistung.

Ich habe nur die angegebenen Quellen und Hilfsmittel benutzt und mich keiner unzulässigen Hilfe Dritter bedient. Insbesondere habe ich wörtlich oder sinngemäß aus anderen Werken übernommene Inhalte als solche kenntlich gemacht.

Die Arbeit oder Teile davon habe ich bislang nicht an einer Hochschule des In- oder Auslands als Bestandteil einer Prüfungs- oder Qualifikationsleistung vorgelegt.

Die Richtigkeit der vorstehenden Erklärungen bestätige ich.

Die Bedeutung der eidesstattlichen Versicherung und die strafrechtlichen Folgen einer unrichtigen oder unvollständigen eidesstattlichen Versicherung sind mir bekannt.

Ich versichere an Eides statt, dass ich nach bestem Wissen die reine Wahrheit erkläre und nichts verschwiegen habe.

Stuttgart, 27.10.2022

Mario Zinßer

German Abstract – Kurzfassung

Heutzutage ist durch viele wissenschaftliche Studien nachgewiesen, dass die Erde längst dem **Klimawandel** unterworfen ist. Daher muss die gesamte Menschheit vereint handeln, um die schlimmsten Katastrophenszenarien zu verhindern. Ein vielversprechender Ansatz - wenn nicht sogar der vielversprechendste überhaupt - um diese angesprochene, größte Herausforderung in der Geschichte der Menschheit zu bewältigen, ist es, den Energiehunger der Menschheit durch die **Erzeugung erneuerbarer und unerschöpflicher Energie** zu sättigen. Die **Photovoltaik (PV)-Technologie** ist ein vielversprechender Anwärter, die leistungsstärkste erneuerbare Energiequelle zu stellen, und spielt aufgrund ihrer direkten Umwandlung des Sonnenlichtes und ihrer skalierbaren Anwendbarkeit in Form von großflächigen Solarmodulen bereits jetzt eine große Rolle bei der Erzeugung erneuerbarer Energie. Im PV-Sektor sind Solarmodule aus Siliziumwafern die derzeit vorherrschende Technologie. Neu aufkommende PV-Technologien wie die **Dünnschichttechnologie** haben jedoch vorteilhafte Eigenschaften wie einen sehr geringen Kohlenstoffdioxid (CO₂)-Fußabdruck, eine kurze energetische Amortisierungszeit und das Potenzial für eine kostengünstige monolithische Massenproduktion, obwohl diese derzeit noch nicht final ausgereift ist. Um die Dünnschichttechnologie jedoch gezielt in Richtung einer breiten Marktreife zu entwickeln, sind **numerische Simulationen** eine wichtige Säule für das wissenschaftliche Verständnis und die technologische Optimierung. Während sich traditionelle Simulationsliteratur häufig mit materialspezifischen Herausforderungen befasst, konzentriert sich diese Arbeit auf **industriearientierte Herausforderungen auf Modulebene**, ohne die zugrundeliegenden Materialparameter zu verändern.

Um ein **allumfassendes, digitales Modell** eines Solarmoduls zu erstellen, werden in dieser Arbeit **mehrere Simulationsansätze** aus verschiedenen physikalischen Bereichen kombiniert. Zur Abbildung elektrischer Effekte, einschließlich der räumlichen Spannungsvariation innerhalb des Moduls, wird eine **Finite Elemente Methode (FEM) zur Lösung der räumlich quantisierten Poisson-Gleichung** verwendet. Um optische Effekte zu berücksichtigen, wird eine **generalisierte Transfermatrix-Methode (TMM)** verwendet. Alle Simulationsmethoden sind in dieser Arbeit von Grund auf neu programmiert worden, um eine Verknüpfung aller Simulationsebenen mit dem höchstmöglichen Grad an Anpassung und Verknüpfung zu ermöglichen. Die Simulation und die Korrektheit der Parameter wird durch externe Quanteneffizienz (EQE)-Messungen, experimentelle Reflexionsdaten und gemessene Strom-Spannungs (I-U)-Kennlinien verifiziert. Der Kernpunkt der Vorgehensweise dieser Arbeit ist eine **ganzheitliche Simulationsmethodik** auf Modulebene. Dies ermöglicht es, die Lücke zwischen der Simulation auf Materialebene über die Berechnung von

Laborwirkungsgraden bis hin zur Bestimmung der von zahlreichen Umweltfaktoren beeinflusste Leistung der Module im Freifeld zu überbrücken. Durch diese Verknüpfung von Zellsimulation und Systemdesign ist es lediglich aus Laboreigenschaften möglich, das **Freifeldverhalten von Solarmodulen zu prognostizieren**. Sogar das **Zurückrechnen von experimentellen Messungen zu Materialparameter** ist mittels des in dieser Arbeit entwickelten Verfahrens des **Reverse Engineering Fittings (REF)** möglich.

Das in dieser Arbeit entwickelte numerische Verfahren kann für mehrere Anwendungen genutzt werden. Zunächst können durch die Kombination von elektrischen und optischen Simulationen **ganzheitliche Top-Down-Verlustanalysen** durchgeführt werden. Dies ermöglicht eine wissenschaftliche Einordnung und einen quantitativen Vergleich aller Verlustleistungsmechanismen auf einen Blick, was die **zukünftige Forschung und Entwicklung in Richtung von technologischen Schwachstellen von Solarmodulen lenkt**. Darüber hinaus ermöglicht die Kombination von Elektrik und Optik die Detektion von Verlusten, die auf dem nichtlinearen Zusammenspiel dieser beiden Ebenen beruhen und auf eine räumliche Spannungsverteilung im Solarmodul zurückzuführen sind.

Diese Arbeit verwendet die entwickelten **numerischen Modelle ebenfalls für Optimierungsprobleme**, die an digitalen Modellen realer Solarmodule durchgeführt werden. Häufig auftretende Fragestellungen bei der Entwicklung von Solarmodulen sind beispielsweise die Schichtdicke des vorderen optisch transparenten, elektrisch leitfähigen Oxids (TCO) oder die Breite von monolithisch verschalteten Zellen. Die Bestimmung des Optimums dieser mehrdimensionalen Abwägungen zwischen optischer Transparenz, elektrischer Leitfähigkeit und geometrisch inaktiver Fläche zwischen den einzelnen Zellen ist ein Hauptmerkmal der Methodik dieser Arbeit. Mittels des FEM-Ansatzes dieser Arbeit ist es möglich, alle **gegenseitigen Wechselwirkungen** über verschiedene physikalische Ebenen hinweg zu berücksichtigen und ein **ganzheitlich optimiertes Moduldesign** zu finden. Auch topologisch komplexere Probleme, wie das Finden eines **geeigneten Designs für das Metallisierungsgitter**, können auf Grundlage der Simulation mittels der Methode der **Topologie-Optimierung (TO)** gelöst werden. In dieser Arbeit wurde das TO-Verfahren zum ersten Mal für monolithisch integrierte Zellen eingesetzt. Darüber hinaus wurde gezeigt, dass sowohl einfache Optimierungen der TCO-Schichtdicken als auch Topologie-Optimierungen stark **von den vorherrschenden Beleuchtungsverhältnissen abhängen**. Daher ist eine **Optimierung auf den Jahresertrag** anstelle des Laborwirkungsgrades für industriennahe Anwendungen wesentlich sinnvoller, da die mittleren Jahreseinstrahlungen deutlich von den Laborbedingungen abweichen. Mit Hilfe dieser Ertragsoptimierung wurde in dieser Arbeit für die Kupfer-Indium-Gallium-Diselenid $\text{CuIn}_{1-x}\text{Ga}_x\text{Se}_2$ (CIGS)-Technologie ein Leistungsgewinn von über 1 % im Ertrag für einige geografische Standorte und gleichzeitig eine Materialeinsparung für die Metallisierungs- und TCO-Schicht von bis zu 50 % errechnet.

Mit Hilfe der numerischen Simulationen dieser Arbeit können alle denkbaren technologischen Verbesserungen auf Modulebene in das Modell eingebracht werden. Auf diese Weise wurde das **aktuelle technologische Limit für CIGS-Dünnschicht-Solarmodule** berechnet. Unter Verwendung der Randbedingungen der derzeit verfügbaren Materialien, Technologie- und Fertigungstoleranzen und des derzeit besten in der Literatur veröffentlichten CIGS-Materials ergibt sich ein

theoretisches Wirkungsgradmaximum von 24 % auf Modulebene. Das derzeit beste veröffentlichte Modul mit den gegebenen Restriktionen weist einen Wirkungsgrad von 19,2 % auf ^[1]. Verbessert sich der CIGS-Absorber vergleichbar mit jenem von Galliumarsenid (GaAs) im Hinblick auf dessen Rekombinationsrate, ergibt sich ein erhöhtes Wirkungsgradlimit von etwa 28 %. Im Falle eines idealen CIGS-Absorbers ohne intrinsische Rekombinationsverluste wird in dieser Arbeit eine maximale Effizienzobergrenze von 29 % berechnet.



Kurz zusammengefasst lässt sich sagen, dass die in dieser Arbeit entwickelte Simulationsmethodik die beiden physikalischen Ebenen der Optik und der Elektrik in Dünnschicht-Solarmodulen in einem digitalen Modell kombiniert. Dies ermöglicht die Vorhersage von I-U-Kennlinien, die Zuordnung und Quantifizierung von Verlustmechanismen, die Optimierung von Modulgeometrien und die Bestimmung der aktuellen technologischen Grenzen der Dünnschicht-Solarmodultechnologie. Auf diese Weise verleiht diese Arbeit numerischen Dünnschicht-PV-Simulationen einen ganzheitlichen Charakter und treibt zukünftige Solarmodulforschung und -entwicklung und für allumfassende PV-Software voran.

Abstract

Nowadays, it is proven by many scientific studies that earth is subject to **climate change**. Therefore, all of humanity must take united action to prevent the most catastrophic scenarios. To solve this greatest challenge in the history of mankind, a promising approach, if not the most promising one, is to quench mankind's thirst for energy by **using renewable and inexhaustible energy sources**. **Photovoltaic (PV) technology** is a promising candidate for the most relevant renewable energy source and is already a big player in renewable energy production, due to its direct conversion of the sun's radiation and its scalable applicability in the form of large-scale solar modules. Within the PV sector, the currently most prevalent technology are silicon-wafer-based solar modules. Nevertheless, new emerging PV technologies like **thin-film PV** have superior features such as a very low carbon footprint, short energy payback times, and a potential for cheap monolithic large-scale production, although their development is currently less mature. In order to purposefully improve thin-film technology towards market maturity, **numerical simulations** are a strong tool for scientific understanding and technological optimization. While traditional simulation literature often deals with material-specific challenges, this work is focused on **industry-oriented issues at device level** without addressing the actual material parameters.

To create a **comprehensive digital model** of a solar device, **multiple simulation approaches** from different physical fields are combined in this work. When considering electrical effects including the intra-device voltage distribution, a **finite element method (FEM) is used for solving the spatially quantized Poisson's equation**. To account for optical effects, a **generalized transfer-matrix method (TMM)** is implemented. All simulation methods are programmed from scratch to allow a linkage of all simulation levels with the highest possible degree of adaptation and interconnection. The simulation methodology is verified by external quantum efficiency (EQE) measurements, experimental reflection data, and measured current-voltage characteristics (I-V characteristics). The key point of this work's methodology is an **all-in-one, holistic simulation methodology** on the device level. This allows bridging the gap between simulating at material level, calculating laboratory efficiencies, and determining actual device performances in the field, which are influenced by multiple environmental factors. Due to this connection of cell simulation and system design, it is possible to **predict the outdoor behavior** of solar devices by only knowing the laboratory characteristics, and even calculate backwards **from actual experimental measurements to material parameters**. The latter procedure is developed within this work and is called **reverse engineering fitting (REF)**.

The numerical procedure developed in this work can be used for multiple applications. Foremost, **all-in-one top-down loss analyses** can be executed due to the combination of electrical and optical simulations. This allows for a scientific classification and quantitative comparison of all power loss mechanisms at the same time, which **guides future research and development** towards the

technological bottlenecks of solar modules. Moreover, the combination of electrics and optics enables users to detect losses that are based on the non-linear interplay of those two levels, a result of the spatial voltage distribution across the solar device.

This work uses the developed **numerical models for optimization problems** carried out on digital models of real-world solar devices. Frequently posed problems in solar module development are, for instance, the thickness of the front transparent conducting oxide (TCO) layer or the width of monolithically interconnected cells. A key feature of this work's methodology is determining the optimum of these multi-dimensional trade-offs between optical transmittance, electrical conductivity, and geometrical inactive area between the individual cells. The FEM approach of this work is able to **consider all mutual interactions** throughout different physical levels and **finds a globally optimized module design**. Even topologically more complex problems, such as finding a **suitable pattern for the metallization grid** can be accomplished, using the method of **topology optimization (TO)**. In this work, the procedure of TO has been used for the first time for monolithically integrated cells. Moreover, it has been shown that straightforward optimizations of TCO layer thicknesses as well as topology optimizations strongly **depend on the prevailing irradiation conditions**. Therefore, an **optimization for annual yield** instead of power conversion efficiency (PCE) at standard test conditions, meaning 1000 W/m² irradiance, 25°C module temperature, and AM1.5G spectral distribution (STC) much more reasonable for industry-oriented applications, since annual mean irradiances significantly differ from STC in the laboratory. By using this yield optimization, a gain of over 1 % in yield for some geographic locations and at the same time material consumption savings for the grid and TCO layer of up to 50 % are calculated for the copper indium gallium diselenide CuIn_{1-x}Ga_xSe₂ (CIGS) technology.

Using this work's numerical simulations, all conceivable technological improvements on the module level can be introduced into the model. This way, the **current technological limit for thin-film CIGS solar modules** is calculated. Within the boundary conditions of currently available materials, technologies, and production tolerances and the currently best CIGS material published in literature, a **theoretical efficiency maximum of 24 % on module level** is found, while the currently best published module with the given restrictions has a PCE of 19.2% [1]. If the CIGS absorber improves comparably to the one of gallium arsenide (GaAs) in terms of recombination rates, an advanced limit of around 28 % is determined. In case of an ideal CIGS absorber without any intrinsic recombination losses, a maximum upper PCE limit of 29 % is calculated in this work.



In a nutshell, the simulation methodology developed in this work combines the two different physical levels of optics and electrics in thin-film solar devices in one digital model. This allows for the prediction of I-V characteristics, the allocation and quantification of loss mechanisms, the optimization of device geometries, and the exploration of the limits of thin-film solar module technology. By doing so, this work adds a holistic character to numerical thin-film PV simulations and supports future solar module research and all-in-one PV software development.

Contents

German Abstract – Kurzfassung	vii
Abstract	xi
Acronyms and Symbols	xxi
1 Introduction and Motivation	1
2 Fundamentals of Photovoltaic Devices	5
This Chapter’s Guiding Scientific Question	5
2.1 Electronical Description of Semiconductors	6
2.2 Electronical Behavior of P-n Junctions	7
2.2.1 Electronical Status in Electrochemical Equilibrium	8
2.2.2 Applying Voltage in Forward Direction to the P-n Junction	9
2.2.3 Applying Illumination to the P-n Junction	9
2.2.4 J–V Characteristics and Distinctive Quantities	10
2.3 Physical Structure of Thin-film Solar Cells	12
2.3.1 Characteristics of Transparent Conductive Oxides	12
2.3.2 Electrical Transport Support of Metallization Grid Structures	13
2.3.3 Load Resistance of a Solar Cell	13
2.3.4 Spatially Resolved Cell Properties	14
2.4 Electrical Modeling of Solar Cells	15
2.4.1 Single-Diode Equivalent-Circuit Model	15
2.4.2 Resulting Characteristic Solar Cell Parameters	16
2.4.3 Implications of Parasitic Influences on Diode Parameters and Solar Cell Parameters	17
2.4.4 Diode Network Model	18
2.5 Connecting Multiple Cells with a Module Interconnect	19
2.6 Theoretical Efficiency Limit of Solar Devices	20
Answering this Chapter’s Guiding Scientific Question	21
3 Current Literature Status and Objective of this Thesis	23
3.1 Current Status of Spatially Resolved Simulations on Thin-film Photovoltaic Cells and Modules	24
3.2 Objective of this Thesis	26

4	Modeling Solar Devices – Optical and Electrical Simulation Methods	29
	This Chapter’s Guiding Scientific Question	29
4.1	Spatial Quantization via Meshing Algorithm	31
4.1.1	Triangulation Algorithm for Generating a Valid Mesh	32
4.1.2	Detailed Modeling of Contour Patterns	32
4.2	Optical Model	35
4.2.1	Lambert-Beer Method	36
4.2.2	Transfer-Matrix Method	37
4.3	Electrical Model	41
4.3.1	Electrical Problem Definition	42
4.3.2	Physics within Finite Elements	43
4.3.2.1	Net Generated Current within Finite Elements	43
4.3.2.2	Transport Resistances to Neighbor Elements	45
4.3.3	Equation System	47
4.3.3.1	Physical Motivation and Deduction	47
4.3.3.2	Matrix Formulation of FEM Problem	48
4.3.4	Simulating the Module Interconnect	49
4.3.5	Solving the Non-linear Equation System	51
4.4	Resulting Characteristics of the Digital Model	53
4.4.1	Spatially Resolved Potential and Current Distributions	53
4.4.2	Opto-electronic Properties of the Solar Device	55
4.4.2.1	Total Current and Power of the Solar Device	55
4.4.2.2	I–V Characteristic of the Solar Device	56
4.4.2.3	MPP Tracking and Power Conversion Efficiency of the Device	56
4.5	Fitting Experimental Data	57
4.6	Simulating Day Yield for a Solar Device	59
4.6.1	Calculating the Solar Position	59
4.6.2	Daily Power Integration of the Solar Device	60
4.6.3	Yearly Power Integration of the Solar Device	61
	Answering this Chapter’s Guiding Scientific Question	61
5	Checking for Validity – Verification of the Digital Device Model	63
	This Chapter’s Guiding Scientific Question	63
5.1	Finding the Input Parameters – Gathering Data for Simulation Model	64
5.1.1	Geometrical Data	64
5.1.2	Electrical Data	65
5.1.3	Optical Data	66
5.1.4	I–V Characteristic of Internal Semiconductor Material	68
5.2	Calculating Backwards – From Module Level to Material Level via Reverse Engineering Fitting	69
5.2.1	Procedure of the REF Approach	70
5.2.2	Application of the REF Approach to Real-world Solar Devices	71
5.3	Forecast I–V Curves for Different Solar Devices	73
5.4	Scientific Relevance of Spatially Resolved FEM	75
	Answering this Chapter’s Guiding Scientific Question	77

6 Finding the Bottleneck – Holistic Top-Down Loss Analysis	79
This Chapter’s Guiding Scientific Question	79
6.1 Overview of All Loss Mechanisms	81
6.2 Mathematical Calculation of All Loss Mechanisms	81
6.2.1 Edge Area	82
6.2.2 External Shading	82
6.2.3 Module Interconnect Area Loss	83
6.2.4 Grid Shading	84
6.2.5 Tilted Effective Area	84
6.2.6 Reflection, Parasitic Absorption, and Incomplete Absorption	84
6.2.7 Local MPP Mismatch	85
6.2.8 Reverse Current under Grid	85
6.2.9 Ohmic Losses in Contact Layers	85
6.2.10 Ohmic Losses in Module Interconnect	86
6.2.11 P2 Contact Resistance	86
6.2.12 P1 and P3 Shunts	86
6.2.13 External Contact Resistance	87
6.3 Applied Loss Analysis on Solar Cells	87
6.3.1 Verification by Reflection Measurements	87
6.3.2 Comparing Measured Data to Simulated Loss Analysis	88
6.3.3 Finding the Ideal TCO Thickness	89
6.3.4 Different TCO Thicknesses Suitable for Different Irradiation Intensities	91
6.4 Applied Loss Analysis on Solar Modules	93
6.4.1 Evolving the Digital Model and its Parameters under Standard Testing Conditions	93
6.4.2 Holistic Loss Analysis from Shockley-Queisser Limit to Module Level	95
Answering this Chapter’s Guiding Scientific Question	95
7 Predicting Power in the Field – Time-resolved Yield Forecast for Modules Exposed to Natural Environmental Conditions	99
This Chapter’s Guiding Scientific Question	99
7.1 Variation of Illumination Intensities	100
7.2 Variation of Temperature	100
7.2.1 Comparison with Theoretical Predictions	101
7.2.2 Comparison with Literature	102
7.3 Applying Real-world Meteorological Data to the Digital Model	103
7.4 From Shockley-Queisser to Module Power – Time-resolved Holistic Loss Analysis for Solar Modules	106
7.5 Possible Improvements on Module Level	109
Answering this Chapter’s Guiding Scientific Question	109
8 Pushing the Performance – Optimizing Power Conversion Efficiency and Annual Yield	113
This Chapter’s Guiding Scientific Question	113
8.1 Optimization of Device Parameters	114
8.2 The Ideal Metallization Grid – Topology Optimization of Metallization Patterns	115

8.2.1	Mathematical Basics – The Problem Formulation	115
8.2.2	Topology Optimization as Improvement Idea	116
8.2.3	Improved Optimization – Calculation of the Gradient	119
8.2.4	Different Optimizing Algorithms	121
8.2.5	Further Refinements for the Optimization Strategy	122
8.2.5.1	Density Filter	122
8.2.5.2	Gaussian Blur	123
8.2.5.3	Batch Optimization	123
8.3	Real-world Applications – From PCE Optimization to Yield Optimization	124
8.3.1	New Grid Designs for Yield Optimization	125
8.3.2	Superior Low-light Behavior Explained by Loss Analysis	128
	Answering this Chapter’s Guiding Scientific Question	129
9	Exploring the Limits – Current Technological Efficiency Limit of CIGS Thin-film Solar Modules	131
	This Chapter’s Guiding Scientific Question	131
9.1	Boundary Conditions for Best Possible Module	132
9.2	Calculating the I–V Curve of the Best CIGS Material in Literature	133
9.3	Simulate Currently Best Possible Module	136
9.3.1	Optimizing Module Geometry Parameters	136
9.3.2	Loss Analysis for Currently Best Possible Module	138
9.4	Outlook in the Future of CIGS Module Limits	139
	Answering this Chapter’s Guiding Scientific Question	140
10	Summary and Outlook	143
A	Demonstration of the Developed Simulation Platform	147
	This Chapter’s Guiding Scientific Question	147
A.1	Overview of the Program	148
A.2	Graphical User Interface of the Simulation Platform	149
A.2.1	Device Simulations within the Simulation Platform	150
	Answering this Chapter’s Guiding Scientific Question	152
B	Calculation of FEM Resistances	155
	This Chapter’s Guiding Scientific Question	155
B.1	Empirical Proof for Correct Calculation of FEM Resistances	156
B.2	Mesh Independence of FEM Resistances	158
B.2.1	Resistance of Single Wire	158
B.2.2	Resistance between Two Finite Elements	158
	Answering this Chapter’s Guiding Scientific Question	161
	List of Figures	163
	List of Tables	167
	List of own Publications	169
	Journal articles	169

Conference contributions 170

Bibliography 171

Acknowledgements 193

Acronyms and Symbols

Acronyms

ADAM	adaptive moment estimation
Ag	silver
AM1.5G	reference global tilted solar spectrum
ARPES	angle-resolved photoemission spectroscopy
ARC	anti-reflective coating
AZO	aluminum-doped zinc oxide
BCP	bathocuproine
BFGS	Broyden–Fletcher–Goldfarb–Shanno
BZO	boron-doped zinc oxide
CIGS	copper indium gallium diselenide $\text{CuIn}_{1-x}\text{Ga}_x\text{Se}_2$
CdS	cadmium sulfide
CdTe	cadmium telluride
CO₂	carbon dioxide
CsFAPbI₃	mixed ionic perovskite $\text{Cs}_x\text{FA}_{1-x}\text{Pb}(\text{I}_y\text{Br}_{1-y})_3$
DC	direct current
DFT	density functional theory
DOS	density of states
EQE	external quantum efficiency
FEM	finite element method
FF	fill factor
GaAs	gallium arsenide
GGI	ratio of gallium to gallium and indium $\text{Ga}/(\text{Ga}+\text{In})$ concentrations
GUI	graphical user interface
HNEI	Hawai'i Natural Energy Institute

IOH	hydrogenated indium oxide
IR	infrared
IQE	internal quantum efficiency
I–V curve	current–voltage curve
I–V characteristic	current–voltage characteristic
i-ZnO	intrinsic zinc oxide
IZO	indium zinc oxide
J–V curve	current–density–voltage curve
J–V characteristic	current–density–voltage characteristic
KIT	Karlsruher Institute for Technology
LTI	Light Technology Institute
MeO-2PACz	[2-(3,6-Dimethoxy-9H-carbazol-9-yl)ethyl]phosphonic acid
MPP	maximum power point
Mo	molybdenum
MoSe₂	molybdenum diselenide
PCBM	[6,6]-Phenyl C ₆₁ butyric acid methyl ester
PEC	photoelectrochemical
PCE	power conversion efficiency
P1	first trench in module interconnect
P2	second trench in module interconnect
P3	third trench in module interconnect
REF	reverse engineering fitting
PV	photovoltaic
SEM	scanning electron microscope
SIMP	solid isotropic material with penalization
SiO₂	silicon dioxide
SRH	Shockley-Read-Hall
STC	standard test conditions, meaning 1000 W/m ² irradiance, 25°C module temperature, and AM1.5G spectral distribution
TCO	transparent conducting oxide
TLM	transfer length measurement
TMM	transfer-matrix method

TMY	typical meteorological year
TO	topology optimization
UH	University of Hawai'i
UV	ultraviolet
ZMO	magnesium-doped zinc oxide $\text{Zn}_x\text{Mg}_{1-x}\text{O}$
ZnOS	zinc oxysulfide $\text{ZnO}_x\text{S}_{1-x}$
ZSW	Zentrum für Sonnenenergie- und Wasserstoff-Forschung Baden-Württemberg

Constants

h	Planck constant: $6.62607015 \cdot 10^{-34}$ Js
\hbar	Reduced Planck constant: $h/(2\pi)$
c	Speed of light: 299792458 m/s
ε_0	Vacuum permittivity: $8.8541878128 \cdot 10^{-12}$ C/(Vm)
k_B	Boltzmann constant: $1.380649 \cdot 10^{-23}$ J/K
π	Circle constant: 3.14159265358979...
q_e	Elementary charge: $1.602176634 \cdot 10^{-19}$ C

Latin Symbols and Variables

This directory only lists repeating and recurring symbols. Symbols that are only used once are defined on site in the main text.

A_{edge}	edge area of a solar module
A_{tot}	total area of a solar module
C	set of all elements within the active area of the meshing domain
D_c	conduction band densities of states in J
D_v	valence band densities of states in J
E	energy in J
E_c	conduction band edge
E_F	fermi level
$E_{F,e}$	quasi-Fermi level of electrons
$E_{F,h}$	quasi-Fermi level of holes
$E_{F,i}$	intrinsic quasi-Fermi level

E_{gap}	band gap of a semiconductor
E_{v}	valence band edge
$f(E)$	Fermi–Dirac distribution
$f_{\text{SIMP}}^{\text{con}}(x_k)$	weighting factor for the conductivity SIMP function
$f_{\text{SIMP}}^{\text{gen}}(x_k)$	weighting factor for the generation SIMP function
f_{optics}	prefactor for optical calculations
FF	fill factor in %
\mathcal{G}	set of all finite elements with grid
\mathbf{G}	stiffness matrix for the coupled equation system
I	current in A
I_{sc}	short-circuit current
I_{net}^k	effectively generated current in the k -th element
j	current density in $\frac{\text{A}}{\text{m}^2}$
j_0	reverse saturation current density
j_{MPP}	current density at the maximum power point
j_{sc}	short-circuit current density
j_{ph}	photocurrent density
k	wavenumber in $\frac{1}{\text{m}}$
\mathcal{K}	set of all elements within the meshing domain
N_{c}	effective conduction band densities of states in $\frac{1}{\text{m}^3}$
N_{D}^+	density of singly ionized donor atoms in $\frac{1}{\text{m}^3}$
N_{A}^-	density of singly ionized acceptor atoms in $\frac{1}{\text{m}^3}$
N_{v}	effective valence band densities of states in $\frac{1}{\text{m}^3}$
n	electron density in $\frac{1}{\text{m}^3}$
n_{i}	intrinsic electron density
n_{d}	diode ideality factor
$\mathcal{N}(k)$	set of neighboring elements of the k -th finite element
m_{e}^*	effective electron mass in kg
m_{h}^*	effective hole mass in kg
p	hole density in $\frac{1}{\text{m}^3}$
p_{i}	intrinsic hole density
P	power in W

P_{MPP}	power at the maximum power point
\mathcal{P}_1	set of all elements within the P1 area of the meshing domain
\mathcal{P}_2	set of all elements within the P2 area of the meshing domain
\mathcal{P}_3	set of all elements within the P3 area of the meshing domain
P_p	nominal power of solar device at STC in W_p
Q_e^{lum}	external luminescence quantum efficiency
r	area-normalized resistance in Ωm^2
r_s	area-normalized series resistance
r_{sh}	area-normalized shunt resistance
R	resistance in Ω
R_L	load resistance
R_s	series resistance
R_{sh}	shunt resistance
$R_{\text{back}}^{k,n}$	resistor within the FEM on the back side from the k -th to the n -th element
$R_{\text{front}}^{k,n}$	resistor within the FEM on the front side from the k -th to the n -th element
R_{\square}	sheet resistance in Ω_{\square}
\mathbb{R}	domain of all real numbers
\mathbb{R}^+	domain of all positive real numbers
\mathcal{S}_{12}	set of all elements between the P1 and P2 area of the meshing domain
\mathcal{S}_{23}	set of all elements between the P2 and P3 area of the meshing domain
T	temperature in K
V	voltage in V
V_{diff}	diffusion voltage
V_k	voltage drop in the k -th finite element
V_{MPP}	voltage at the maximum power point
V_{oc}	open-circuit voltage
V_{op}	operating voltage of a solar cell
$\mathcal{W}(x)$	Lambert W function
x_k	grid density of the k -th element

Greek Symbols and Variables

This directory only lists repeating and recurring symbols. Symbols that are only used once are defined on site in the main text.

Δ	Laplace operator (second spatial derivative) in $\frac{1}{\text{m}^2}$
∇	nabla operator (first spatial derivative) in $\frac{1}{\text{m}}$
ϵ_r	relative permittivity
λ	wavelength in m
λ_{gap}	corresponding wavelength to the band gap energy
μ_e	chemical energy potential of electrons in J
μ_h	chemical energy potential of holes in J
ρ	resistivity in Ωm
σ	conductivity in $\frac{\text{S}}{\text{m}}$
Φ	electrical potential in V
Φ_{back}	electrical potential at the back contact
Φ_{front}	electrical potential at the front contact
χ	chemical potential of a semiconductor
ω	angular frequency in Hz

1

Introduction and Motivation

"We have long known, on the basis of a massive scientific record, that the urgency of acting to mitigate climate change is real and cannot be ignored."

– Barack Obama

This quote from former United States president Barack Obama ^[2] clearly emphasizes the need for immediate action on climatic issues. To act as quickly as possible is an inevitable next step for all of humanity. In fact, already a rising number of environmental disasters can already be observed in the last decades ^[3]. The observed upward trend is prominently seen in weather-based disasters and not in geophysically caused events. This prompts the assumption that this progress arises from anthropogenic changes in the atmosphere and most likely is, most likely, the result of global warming. Even more specific about the physical problems is a quote by technology entrepreneur Elon Musk.

"We are running the most dangerous experiment in history right now, which is to see how much carbon dioxide the atmosphere can handle before there is an environmental catastrophe."

– Elon Musk

He directly addresses carbon dioxide (CO₂) emissions as the main contribution to climatic change. Indeed, the increased CO₂ emissions are indeed correlated with the world's primary energy consumption ^[4, 5] and climate change ^[6]. Humanity probably faces its largest single challenge in meeting the global energy demand while reducing harmful greenhouse gases in the atmosphere. Accomplishing this challenge requires scientific research, industrial production, and, finally, a very large installation volume of environmentally friendly electricity generation technologies ^[7].

The world's current energy generation is mainly based on burning fossil fuels, which releases large quantities of emission into the atmosphere, most of all CO₂. Therefore, humankind as a whole, regardless of individual political beliefs, religious views, or places of origin, faces the task to transform into a carbon-neutral species by reducing its carbon footprint. Ultimately, the existence of fossil fuels is limited either way. Thus, the question is not whether we should use renewables, but when do we start utilizing them on a large scale?

Furthermore, mankind will consume more and more energy for the sake of increasing prosperity and technological advancement. The overall consumed energy in 2021 of 155 PWh^[8] is equal to an average power generation of 17.7 TW. This is roughly four orders of magnitude lower than the 174000 TW of power arriving from the sun to the earth via radiation^[9] and results in an interpolated value of 0.725 on the interpolated Kardashev scale^[10, 11]. Therefore, large-scale renewable energy generation also pushes mankind further towards evolving into a highly technologized and interplanetary species.

This urgent need for global action on climate stabilization has also been recognized in politics. In 1997 the Kyoto protocol set binding limits under international law for the emissions of greenhouse gases in industrialized countries^[12]. The subsequent Paris agreement in 2015 stipulated a limitation of man-made global warming to well below 2 K compared to pre-industrial levels^[13]. However, studies have shown that even the 2 K target may not be sufficient to safely prevent irreversible damages to the earth's fragile environmental system^[14].

Fortunately, there is an unstoppable trend for renewable energy generation^[2], which seems to be the solution to many problems, far beyond energy supply and global climate change^[15]. In 2021, renewables generated 13.8 PWh, which corresponds to a share of 8.9 %_{abs} within global energy production^[8]. This ratio splits up into 6.8 %_{abs} generated by hydropower, 1.0 %_{abs} by wind, 0.6 %_{abs} by solar, and 0.5 %_{abs} by other renewable energy sources. These figures show that there is huge potential for global improvement and, due to the rising energy demand^[4], a rising market that is also economically viable^[16].

Since the largest source of energy in the solar system is by far the sun, it is most reasonable to directly convert sunlight to a technically useful energy form like electricity. In fact, nature has developed exactly this idea of converting solar energy into chemical binding energy within biomass on a large scale, namely by evolving the Calvin cycle^[17] within the process of photosynthesis. Its performance of light-to-biomass efficiency is limited at 4.6 % for C3 photosynthesis (pure Calvin cycle) and 6 % for C4 photosynthesis (pre-incorporation of four-carbon molecules)^[18]. While there have been ideas for using photosynthesis to meet humanity's growing thirst for energy^[19, 20], the first direct photovoltaic (PV) cell was developed in 1954. PV systems provide higher efficiencies and are a more scalable technology. This device was made from a silicon p-n junction and had an efficiency of solar radiation to electrical power of 6 %^[21].

As the PV technology is extensively scalable, it is very suitable to generate clean electrical energy. Moreover, the natural peaks in power consumption during daytime match perfectly with the maximum point in daily solar irradiance. PV technology was said to be very expensive for a long time, which is not true any more nowadays. As a matter of fact, installing PV modules is even economically profitable^[22]. In regions with high irradiation intensities, PV is the cheapest power-generating technology of all time^[23].

The wafer-based silicon technology is the currently prevalent PV technology, with a global annual production of 137 GW_p, corresponding to 95 % of all PV production in 2020^[24]. While crystalline silicon PV modules and wind turbines are the workhorses of the initial push towards a worldwide

renewable energy generation on the TW scale, new emerging PV technologies like the thin-film technology are evolving [25]. These new systems are technologically less mature, but have clear advantages in terms of carbon footprint. Whereas crystalline silicon modules entail around 50 to 60 grams of CO₂ equivalent emission per kilowatt hour, thin-film modules only exhibit around 12 to 20 g/kWh [26]. These values are far ahead of the 1100 g/kWh for coal-based power generation, 450 g/kWh for power from natural gas, or 50 g/kWh for nuclear power generation [27]. Additionally, thin-film modules combine high cell efficiencies [28, 29, 30], rapid energy payback due to a low consumption of energy and active material [31, 32], and the potential for cheap monolithic and large-scale manufacturing at moderate temperatures [33, 34, 35]. Thin-film technology offers a wide range of applications: the integration into efficient tandem applications [36, 37, 38, 39], their possibility for ink-based fabrication techniques [40], their application in photoelectrochemical (PEC) hydrogen production [37, 41, 42, 43], and the feasibility for flexible substrates [36, 44, 45, 46], which even leads to wearable PV modules [47].

In order to stay within Swanson's law [48] and to be able to compete with the current market-dominating wafer-based silicon technology [49, 50], thin-film modules need to offer comparably high cell and module efficiencies. For gallium arsenide (GaAs), the current record cell efficiency in laboratory environments is given by 29.1 % [28], for perovskites by 25.5 % [51], for copper indium gallium diselenide $\text{CuIn}_{1-x}\text{Ga}_x\text{Se}_2$ (CIGS) by 23.4 % [52], and for cadmium telluride (CdTe) by 22.1 % [53]. On the module level, however, record efficiencies are much lower [54, 55, 56]. Since large-scale power generation is based on large-area modules, targeted research on this level is of crucial necessity [57]. One of the best goal-driven ways to systematically analyze internal device physics is automated computer-aided modeling [58]. It is, therefore, not surprising that thin-film solar devices are under frequent investigation by simulation approaches from different aspects such as drift-diffusion modelling [59], optical simulations [60], as well as electrical approaches [61, 62]. Even more than stand-alone laboratory experiments, simulations offer the possibility to understand physical processes and help to minimize loss paths in the current state-of-the-art technology. A qualitative allocation and quantitative characterization of all relevant loss mechanisms is hence of utmost importance in order to minimize parasitic power losses. Since the correlations within solar devices are too complex for a sufficiently precise algebraic calculation, numerical simulation models are necessary. The most common way to do so are finite element method (FEM) models [61, 62, 63, 64, 65, 66, 67, 68]. Using this powerful technique, individual loss mechanisms can be detected, allocated and quantified. Individual mechanisms have been investigated a lot, especially electrical shunts [61, 62], ohmic resistances in the TCO and the grid [69], contact resistances [70, 71], spatial distributions of local MPP mismatches [64, 72], and shaded p-n junction area [73]. However, in literature, there is a lack of a single comprehensive thin-film analysis that contains all losses, from the physical limit down to the actual module power. FEM models allow to match all relevant losses to their physical mechanisms and bring them into proportion to each other. As electrical, electronical, and optical effects interfere with each other, a coupling of several physical models will be needed for developing a digital model of a solar device. Such a holistic simulation methodology is valuable to guide further development efforts towards increased module performance.

Since outdoor solar modules are almost never operated under standard test conditions, meaning 1000 W/m² irradiance, 25°C module temperature, and AM1.5G spectral distribution (STC), but are exposed to real-world conditions, meteorological effects need to be considered [74]. With an industry-oriented approach, goals in development not only need to be set towards increased efficiencies of single cells in the laboratory, but also towards higher net energy yields of entire modules in the field. Such real-world loss analyses and optimizations constitute the point where the benefit of this work comes in.

This work starts with explaining the fundamentals of thin-film PV cells and modules, in order to understand the necessary basics. Afterwards, a short overview of the published literature on the topic is given, followed by a methodology chapter. All algorithms in this part are self-implemented within this work without the use of commercial third-party software. The subsequent result chapters are, one by one, about holistic loss analyses, real-world yield prediction, module optimization, and technological efficiency limits.

Each chapter starts with a guiding scientific question to clearly focus the reader's perspective on a defined goal within this chapter. At the end of each chapter, this question will be answered in a few simple words, presenting the core issue in a nutshell. Thereby, this work gradually introduces jargon-specific buzzwords and tries to avoid unnecessarily smart-sounding and long expressions in order to make the results of this work available to a huge spectrum of people ^[75].

2

Fundamentals of Photovoltaic Devices

This chapter gives a brief introduction to solar cells and modules in order to create a basic understanding and define all necessary quantities. The starting point will be the electro-chemical description of a semiconductor. For a solar cell, the current flow must be directed, which can be achieved by a p-n junction of two differently doped semiconductors. Although this work is not about semiconductor physics, p-n junctions are the essential part for most solar cells and its current–voltage characteristic (I–V characteristic) is a fundamental knowledge for this thesis. Hence, its basic setup and electrical modeling will be explained. Since for real applications solar modules instead of single cells are needed, the interconnection of the cells will be explained afterwards. Finally, upper theoretical efficiency limits of solar devices are outlined and discussed.

This Chapter's Guiding Scientific Question

How do solar devices convert photon energy into electric energy and how is this effect used in large-scale applications?

2.1 Electronical Description of Semiconductors

Within a periodic crystal lattice the energetic positions of electrons are no longer determined by molecular orbitals. However, their dispersion relation is significantly affected by the influence of the lattice. The energetic position of electrons in solids form continuous bands in the reciprocal space, which is called band structure. In modern physics there are several methods to calculate this structure. The most common ones are the tight binding model [76] and the density functional theory (DFT) [77, 78]. Experimental measurements are often done via angle-resolved photoemission spectroscopy (ARPES) [79, 80, 81]. The most crucial bands of a semiconductor are the two bands at the edge of electron occupation. The highest occupied band at zero temperature is called the valence band with its highest possible energy E_v . At non-vanishing temperature electrons can also be excited into the band with the next higher energy. This band is called conduction band and consists of a lowest possible energy E_c . The intermediate regime with no allowed states between those two bands is called band gap E_{gap} . A significant outcome of band structures are the effective electron and hole masses m_e^* and m_h^* . In principle these values are tensors due to the possibility of different crystal axis. However, for isotropic materials they can be determined via the reciprocal curvature of the energetic bands [82] using the wavenumber k and the reduced Planck constant \hbar .

$$m_e^* = \hbar^2 \left(\frac{d^2 E_c}{dk^2} \right)^{-1} \quad (2.1a)$$

$$m_h^* = \hbar^2 \left(\frac{d^2 E_v}{dk^2} \right)^{-1} \quad (2.1b)$$

Furthermore, the quasi Fermi levels of electrons and holes are called $E_{F,e}$ and $E_{F,h}$. They mark the highest occupied state under unexcited conditions [83]. At a given temperature T the charge carrier densities of electrons and holes within the Boltzmann statistic [84] for decent doping densities are given by [85]

$$n(E_{F,e}) = \underbrace{2 \left(\frac{m_e^* k_B T}{2\pi \hbar^2} \right)^{\frac{3}{2}}}_{=N_c} \exp \left(\frac{E_{F,e} - E_c}{k_B T} \right) \quad (2.2a)$$

$$p(E_{F,h}) = \underbrace{2 \left(\frac{m_h^* k_B T}{2\pi \hbar^2} \right)^{\frac{3}{2}}}_{=N_v} \exp \left(\frac{E_v - E_{F,h}}{k_B T} \right), \quad (2.2b)$$

where k_B is the Boltzmann constant. In electrochemical equilibrium charge carrier densities are denoted with the subscript i . In this statistic, there are equally many electrons as holes $n_i = p_i$. The resulting intrinsic Fermi level $E_{F,i}$ is then given via

$$\begin{aligned} E_{F,i} &= \frac{E_c - E_v}{2} + \frac{k_B T}{2} \log \left(\frac{N_v}{N_c} \right) \\ &= \frac{E_c - E_v}{2} + \frac{3k_B T}{4} \log \left(\frac{m_h^*}{m_e^*} \right). \end{aligned} \quad (2.3)$$

The second line in Equation (2.3) can be concluded by using Equations (2.2a) and (2.2b). For $T = 0$ or the same band curvature of conduction and valence band the intrinsic Fermi level is exactly in the middle of the band gap. By introducing impurity atoms into an intrinsic semiconductor

lattice (doping) the Fermi level can be shifted towards the conduction band (n-doping) or towards the valence band (p-doping). Applying an external voltage or exposing the semiconductor to illumination leads to the creation of electron-hole pairs. However, this leads to a conflict since many free electrons tend to push the Fermi level upwards and many free holes tend to push it downwards. The solution is to define two separate quasi Fermi levels for both charge carriers.

$$E_{F,e} = E_{F,i} + k_B T \log\left(\frac{n}{n_i}\right) \quad (2.4a)$$

$$E_{F,h} = E_{F,i} - k_B T \log\left(\frac{p}{p_i}\right) \quad (2.4b)$$

As mentioned for the electrochemical equilibrium is $n = n_i$ and $p = p_i$. Therefore, both second terms in the Equations (2.4a) and (2.4b) vanish, resulting in a single Fermi level for both charge carrier types. All mentioned energetic positions are shown in Figure 2.1. Furthermore, the

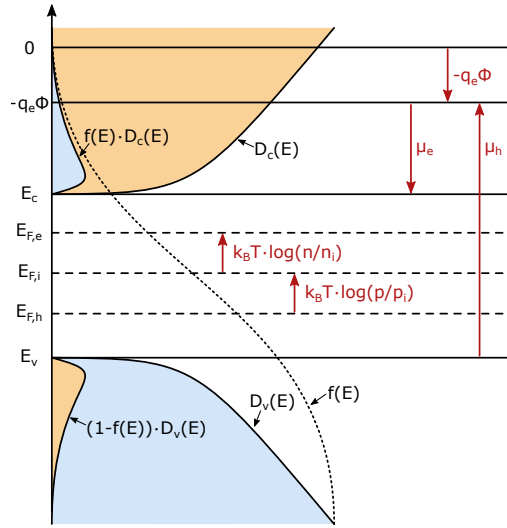


Figure 2.1: Energetic levels within a semiconductor. Starting from the vacuum level the electrical and chemical potentials define the valence and conduction band edges. Within the band gap the intrinsic Fermi level and both electron and hole quasi Fermi levels are located. Additionally the Fermi-Dirac distribution for a finite temperature is shown. Based on its shape the conduction band is filled with electrons (blue areas) or holes (orange areas).

electrical potential Φ and two chemical potential energies μ_e and μ_h for electrons and holes are visually illustrated. Each band consists of an electronical density of states D_v and D_c . Blue areas mark the fraction of states occupied with electrons, whereas orange regions represent holes. The distribution obeys the Fermi-Dirac distribution $f(E)$ [83, 86].

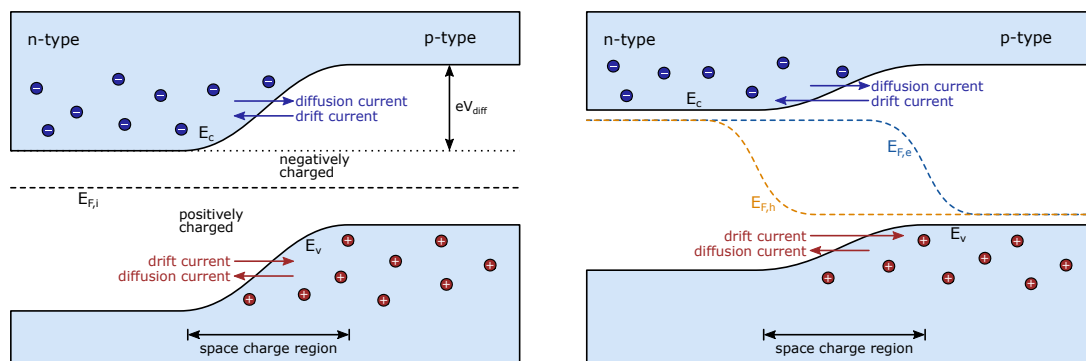
2.2 Electronical Behavior of P-n Junctions

This work focuses on electrical and optical simulations mostly without electronical semiconductor effects. However, for electrical simulations, a material level current–density–voltage curve (J–V curve) is needed as input. Hence, in this paragraph, the current voltage characteristic for a p-n junction will be derived from basic semiconductor properties.

To gain power from solar cells, a directed current flux is needed within the device. This entails a charge carrier separation in the absorber material after electron-hole pairs are generated. One possible way to accomplish this requirement is a p-n junction. Its electrical characteristics are described in the following.

2.2.1 Electrical Status in Electrochemical Equilibrium

Using donor and acceptor atoms, free charge carriers can be introduced into the material without touching the electrical neutrality. An n-type semiconductor contains free electrons as majority charge carriers, whereas in a p-type semiconductor holes are mainly responsible for charge transport, as seen in Figure 2.2a. Bringing together two differently doped semiconductors creates a concentration gradient across the interface. Therefore, both majority charge carriers diffuse into the other region, where they act as minority charge carriers and directly recombine with the prevalent majority carriers. Due to the recombination near the interface, free charge carriers are rare. A carrier depletion region evolves. Since the doped atomic cores contain an electrical charge, a region with a positive charge density on the n-type side and a negative region forms on the p-type side. This entire area is called the space charge region. A spatial distribution of the charge density $\rho(x)$ always implies an electric field according to Maxwell's equations [87] and an electrical potential according to Poisson's equation [88]. Within the Schottky model the charge densities are approximated as Heaviside step functions implying a linear electric field and a hyperbolic electrical potential. Due to the created electric field the remaining free carriers experience a restoring force. An imaginary establishing drift current increases until it compensates the diffusion current. Due to the mutual cancellation of the two imagined currents, there is no net current flow. Figure 2.2a shows the band diagram in equilibrium state. The Fermi levels of both half spaces have matched at the interface leading to curvatures of the conduction and valence band. Therefore, a built-in voltage V_{diff} evolves.



(a) After the electrochemical equilibrium has evolved the valence and conduction band have bent to match the intrinsic Fermi level. Electrons and holes have diffused into the other layer as minority charge carriers leading to a space charge region at the interface. The emerged built-in voltage V_{diff} acts as an energetic barrier for an electrical current.

(b) Applying a voltage in forward bias bends the bands again and the quasi Fermi levels split within the space charge region. Under illumination electron-hole pairs are created. The established electric field guide the charge carriers in a collective direction leading to an increased drift current, which can be used as generated power.

Figure 2.2: Band structure of a p-n junction in electrochemical equilibrium and under illumination.

To calculate the band diagram mathematically, the van Roosbroeck equation system^[89, 90] needs to be solved. It contains Poisson's equation^[88] and the continuity equations for both electrons and holes.

$$-\varepsilon_0\varepsilon_r\Delta\Phi(r) = q_e \cdot (p(E_{F,h}(r)) - N(E_{F,e}(r)) + N_D^+(r) - N_A^-(r)) \quad (2.5a)$$

$$\nabla \cdot \underline{j}_e(r) = q_e \cdot (R(E_{F,e}(r), E_{F,h}(r)) - G(r)) \quad (2.5b)$$

$$\nabla \cdot \underline{j}_h(r) = q_e \cdot (G(r) - R(E_{F,e}(r), E_{F,h}(r))) \quad (2.5c)$$

Here, ε_0 is the vacuum permittivity, ε_r the relative permittivity, r the three-dimensional space coordinate, q_e the elementary charge, N_D^+ and N_A^- the densities of ionized built-in donor and acceptor dopants, \underline{j}_e and \underline{j}_h the electron and hole current densities and $R(E_{F,e}, E_{F,h})$ and G the recombination and generation rates. This system can be numerically efficiently solved by using Scharfetter-Gummel currents^[91] in drift-diffusion models^[59, 92]. It yields the electrical potential Φ and the quasi Fermi levels $E_{F,e}$ and $E_{F,h}$ as a function of space.

2.2.2 Applying Voltage in Forward Direction to the P-n Junction

To overcome the energy barrier $q_e V_{\text{diff}}$ an external applied voltage V can be used. Connecting the p-type semiconductor with the negative contact leads to a reverse bias. The electric field is amplified, which creates a larger drift current. A new equilibrium is formed with a larger space charge region. Therefore, the voltage barrier has increased to $V_{\text{diff}} + V$. Only the minority charge carriers can be used for a negligibly low reverse saturation current.

Under forward bias (positive contact on p-type side) the external field counteracts the built-in potential. This reduces the barrier height to $V_{\text{diff}} - V$. As a result the space charge region shrinks and the drift current decreases. Under the applied voltage both electrons and holes are generated. Since more electrons lead to an increase of the Fermi level and more holes lead to a decrease, the intrinsic Fermi level is no longer an adequate description of the p-n junction. The solution are two quasi Fermi levels, as they are defined in Equations (2.4a) and (2.4b). Since both charge carrier densities n and p are larger than the intrinsic concentrations n_i and p_i , both quasi Fermi levels split within the space charge region. From Equations (2.2a) and (2.2b) it can be seen that the shifted quasi Fermi levels lead to exponentially more free majority charge carriers. Therefore, the current across the junction increases exponentially with the external voltage V . Mathematically this is formulated in the Shockley equation^[93] with the reverse saturation current density j_0 ^[94].

$$j(V) = j_0 \left(\exp\left(\frac{q_e V}{k_B T}\right) - 1 \right) \quad (2.6)$$

2.2.3 Applying Illumination to the P-n Junction

In order to make use of the photoelectric effect^[95], a p-n junction under illumination with forward bias needs to be considered. Absorbed photons create electron-hole pairs within the absorbing layers of the solar cell. The electrical field causes a charge separation of the free charge carriers. Hence, a macroscopically directed photocurrent is established leading to an increased drift current as seen in Figure 2.2b. Since the electrical field follows the direction of the applied voltage the generated photocurrent is opposed to the voltage. The electrons can be extracted as a direct current (DC) at the n-type side of the p-n junction and guided across a load resistance. After their

energy was used at the load resistance, the electrons are feed back into the p-side, where they recombine with the majority holes. The photocurrent is therefore a voltage-independent current. However, to maximize the electrical power density output $p(V) = -j(V) \cdot V$, the voltage needs to be as large as possible. Yet, for too high voltages the diffusion current increases exponentially, as it can be seen in Equation (2.6). To gain the maximum possible power, a consideration must be made between these two effects. From the band bending in Figure 2.2b it can be seen that the maximum voltage is given as the difference between both quasi Fermi levels^[85]. Using Equations (2.4a) and (2.4b) it can be concluded

$$\begin{aligned}
 q_e V_{\text{diff}} &= E_{F,e} - E_{F,h} \\
 &= E_{F,i} + k_B T \log\left(\frac{n}{n_i}\right) - E_{F,i} + k_B T \log\left(\frac{p}{p_i}\right) \\
 &= k_B T \log\left(\frac{n \cdot p}{n_i \cdot p_i}\right) \\
 &= E_{\text{gap}} - k_B T \log\left(\frac{N_c \cdot N_v}{n \cdot p}\right)
 \end{aligned} \tag{2.7}$$

Hence, the maximum possible voltage is E_{gap} either for $T = 0$ or if all states within the valence and conduction band are occupied. The electrical goal therefore is to push the quasi Fermi levels as near as possible towards the band edges, which is according to Equations (2.2a) and (2.2b) possible with a huge doping.

2.2.4 J–V Characteristics and Distinctive Quantities

The above dependency of the current density $j(V)$ as a function of the applied voltage V is visualized as a current–density–voltage characteristic (J–V characteristic) in Figure 2.3. Shown are both current densities with and without illumination. Within the bottom right quadrant, power is produced by irradiation, whereas in the top right quadrant external power is consumed. In a first order approximation these curves are separated by a constant value. At the y-intercept the short current density j_{sc} can be identified, whereas at the x-intercept the open-circuit voltage V_{oc} is defined.

Another important quantity is the power density p . It can be calculated as the product of current density and voltage.

$$p(V) = j(V) \cdot V \tag{2.8}$$

Both the power density and the current density can be expressed as the absolute quantities power P and current I by the multiplication with the active solar cells area A .

$$P(V) = p(V) \cdot A \tag{2.9a}$$

$$I(V) = j(V) \cdot A \tag{2.9b}$$

The maximum power point (MPP) of a solar cell is defined as the optimum of the power curve as a function of voltage. The corresponding quantities are named with the corresponding subscript p_{MPP} , j_{MPP} , and V_{MPP} . Hence, the derivative vanishes at V_{MPP} .

$$\frac{dP(V)}{dV} = 0 \tag{2.10}$$

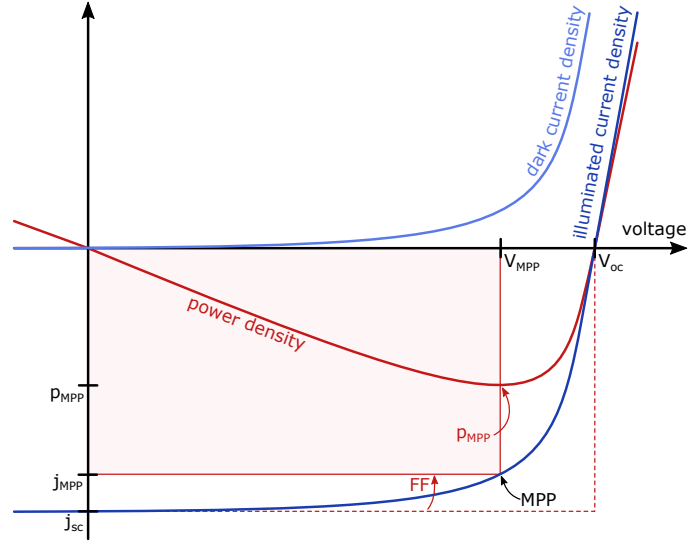


Figure 2.3: I–V characteristic of a dark and illuminated solar cell. If the circuit is shorted the current density j_{sc} flows. However, for open clamps the voltage V_{oc} is present. Multiplying the current density with the voltage yields the power density. Its extremum denotes the maximum power point (MPP).

Another important quantity is the electrical fill factor (FF). It determines how efficiently the maximum voltage V_{op} and current density j_{sc} are utilized at the MPP and is calculated via

$$FF = \frac{j_{MPP} V_{MPP}}{j_{sc} V_{oc}}. \quad (2.11)$$

Finally, the power conversion efficiency (PCE) of an current–voltage curve (I–V curve) is defined as the fraction of electrical output power P_{out} at the MPP with respect to the irradiation input power P_{in} .

$$PCE = \frac{P_{out}^{MPP}}{P_{in}} = \frac{V_{MPP} \cdot I_{MPP}}{P_{in}} = \frac{FF \cdot V_{oc} \cdot I_{sc}}{P_{in}} \quad (2.12)$$

Further characterizing quantities are the external quantum efficiency (EQE) and the internal quantum efficiency (IQE). With these wavelength-dependent quantities the opto-electronical properties of the solar cell can be examined. The EQE is defined as

$$EQE(\lambda) = \frac{\text{collected electrons}(\lambda)}{\text{incident photons}(\lambda)}, \quad (2.13)$$

while the IQE is given by

$$IQE(\lambda) = \frac{\text{collected electrons}(\lambda)}{\text{absorbed photons}(\lambda)}. \quad (2.14)$$

Reflection and a comparably low diffusion length typically damp the EQE and IQE for all wavelengths. Most window layers typically absorb at short wavelengths, which is why parasitic absorption and front surface recombination has strong impacts within the blue part of the EQE and IQE spectrum. Long wavelengths are dominantly influenced by rear surface recombination and a non-sufficient absorption of the absorber material.

2.3 Physical Structure of Thin-film Solar Cells

As described in the previous section, most solar cells have p-n junction with a space charge region and an electric field as seen in Figure 2.4 in order to achieve a properly directed current. This current however is directed out of plane and needs to be extracted across the cell. Hence, electrically conductive layers are introduced at the front and back side of the cell. The goal of these layers is to collect the generated current across the cell and guide it towards an external cell contact. Since materials with good conductivities are needed, metals would be the first approach. For the back side of a (regular) cell, metals do not pose a problem and are often used as back contact ^[31]. However, for the front side (or in case of tandem or bifacial applications for both sides), light needs to pass through the conducting layer. Since metals do not transmit electromagnetic waves in the visible range, where the sun spectrum has its maximum irradiation power density (will later be shown in Figure 2.10), other materials need to be considered as light passing contacts. Requirements for these materials are a preferably high optical transmittance at the visible range of the solar spectrum and simultaneously a high electrical conductivity σ .

2.3.1 Characteristics of Transparent Conductive Oxides

One class of materials that combines these two requirements is the class of transparent conducting oxides (TCOs) ^[38] and are therefore suitable for an electrode application. TCOs are semiconductors with a comparably high doping. Therefore, their conductivity

$$\sigma = q_e \mu n \quad (2.15)$$

is rather high because of the large charge carrier density n due to the high doping level. Here, μ is the mobility of the charge carriers and is given by

$$\mu = \frac{q_e \tau}{m^*}, \quad (2.16)$$

where m^* is the effective charge carrier mass and τ the scattering time of the charge carriers. In a solid state material, there exist multiple mechanisms of scattering, exemplarily the scattering at grain boundaries in polycrystalline materials, phonon scattering, or impurity scattering. The total scattering time τ_{tot} can be calculated via Matthiessen's rule ^[96] by the summation of all reciprocal times.

$$\frac{1}{\tau_{\text{tot}}} = \sum_i \frac{1}{\tau_i} \quad (2.17)$$

According to Equation (2.15), a higher doping of these materials leads to a high charge carrier density and therefore improves the conductivity of TCOs. By using degenerated semiconductors, their conductivity levels can even be comparably high as in metals ^[97]. However, the increased free charge carrier density and plasma edge ^[98, 99]

$$\omega_p = \sqrt{\frac{n q_e^2}{\epsilon_0 m_e^*}} \quad (2.18)$$

reduces their optical transmittance. Therefore, advanced techniques, such as enhancing the charge carrier mobility ^[100] instead of the charge carrier density, need to be applied.

For each solar device configuration, this trade-off between optical transparency and electrical conductivity needs to be re-evaluated and individually optimized.

2.3.2 Electrical Transport Support of Metallization Grid Structures

At some point, the method of improving a TCO layer reaches its technological limits, giving rise to the idea of supporting metal structures. These metallization grid patterns are put on top of the transparent front contact layer as seen in Figure 2.4. Grids are typically made out of metal and hence cast shadows on the active solar cell. However, due to their high conductivity the grid lines act as low-resistive highways for generated charge carriers. Using an appropriate design of the grid structure, the decreased illuminated area due to shadowing is offset by a better conductivity.

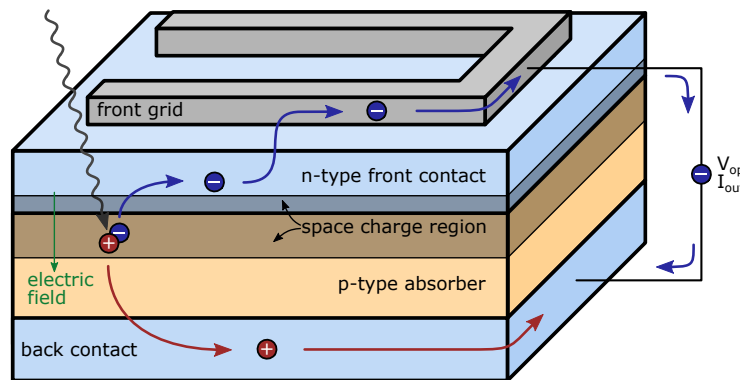


Figure 2.4: Generic schematic of a solar cell. A space charge region is formed between a n-type and a p-type layer. While on the back side a separate contact layer is introduced, the n-type semiconductor has the double functionality to serve simultaneously as part of the p-n junction and as front contact layer. To improve the front conductivity often metallic grid structures are used.

In conclusion, the front contact layers are always a trade-off between a good conductivity and a high transmittance. An optimum of these two dependencies is not trivial at all but rather of great interest within the solar community ^[101, 102, 103].

2.3.3 Load Resistance of a Solar Cell

At the external cell contact the operating voltage V_{op} is applied. Simultaneously the totally extracted current I_{out} can be measured leading to the I-V characteristic in Figure 2.3. By using Ohm's law, the corresponding load resistance R_L can be calculated via

$$R_L = \frac{V_{op}}{I_{out}} \quad (2.19)$$

to operate the cell at V_{op} . Since the solar cell is a non-linear component its differential resistance need to be defined as

$$R_{cell} = \frac{dV_{op}}{dI_{out}} = \left(\frac{dI_{out}}{dV_{op}} \right)^{-1}. \quad (2.20)$$

Using the definition of the MPP it can be shown that

$$\begin{aligned} 0 &\stackrel{(2.10)}{=} \frac{dP(V_{op})}{dV_{op}} \\ &= \frac{d(I_{out}V_{op})}{dV_{op}} \\ &= \frac{dI_{out}}{dV_{op}}V_{op} + I_{out} \underbrace{\frac{dV_{op}}{dV_{op}}}_{=1} \\ \Leftrightarrow -\frac{I_{out}}{V_{op}} &= \frac{dI_{out}}{dV_{op}} \\ \Leftrightarrow -R_L &= R_{cell}. \end{aligned}$$

With the definitions in Equations (2.19) and (2.20) it can be seen the maximum power is extracted if the attached load resistance is exactly the same size as the differential internal resistance of the solar cell. The opposite sign results from the fact that at one resistor energy is produced and at the other one energy is consumed.

2.3.4 Spatially Resolved Cell Properties

At each point of the solar cell, the correlation of the local voltage drop $V_{local} = \Phi_{front} - \Phi_{back}$ and the locally generated net current density $j(V_{local})$ in the direction out of the plane is given by the current voltage relation in Figure 2.3. This I–V curve will be called the internal semiconductor I–V characteristic on the material level. At the external contacts, where the current is extracted, V_{local} will be exactly V_{op} for negligible external contact resistances. However, due to the finite conductivities of both front and back contacts the front and back potentials Φ_{front} and Φ_{back} and therefore the local voltage drop V_{local} are not constant but rather spatially distributed as illustrated in Figure 2.5. Such intra-device potential distributions have already been measured experimentally [104, 105]. For a power-producing solar cell V_{local} is given by V_{op} at the contact point and increases with rising distance. However, it will never be larger than V_{oc} at any point of the cell since in regions with $V_{local} = V_{oc}$ there are no lateral currents, which could further increase the voltage drop. The slope of the potential distribution is primarily affected by the local contact resistances, which can two-dimensionally vary across the cell [69]. In Figure 2.5 a constant resistivity in only one dimension is shown for reasons of simplicity and improved intelligibility. Large resistances lead to low conductivities and hence to a steep potential distribution.

On top of the large ohmic losses due to a high resistivity, the local voltage drop can have massive influences on the local current generation. Due to a different local voltage drop each point of the cell operates at a different voltage within the internal semiconductor I–V curve. Thus, the current generation is also a function of space. In the most extreme case, parts of the cell with $V_{local} = V_{oc}$ do not produce current at all. The external operating voltage V_{op} of the entire cell should therefore not set to the MPP of the internal semiconductor I–V curve but rather be adapted so that most

areas of the cell are operated near the MPP. Hence, V_{op} should be slightly below the MPP of the internal semiconductor I–V curve. This mechanism of losing current generation is called a local MPP mismatch [72, 64] and will be discussed in detail in Section 6.2.7. Thus, treating a solar cell as a single component is always an approximation even for defect-free cells because of this intrinsic electrical spatial inhomogeneity. The justification of this approximation crucially depends on the sheet resistance of the contact layers and is no longer valid in the case of cells with comparably high sheet resistances (e.g. thin layers or high specific resistances) or a large lateral current flow (e.g. concentrator cells) [106, 107]. At the cell's external contact point the operating voltage V_{op} and the totally generated current I_{out} is measured. This relation results in a new I–V characteristic of the entire cell, which mainly differs in the series resistance and generated current from the internal I–V curve. Therefore, a distinction must always be made between the internal semiconductor I–V curve and the external cell I–V curve. One goal of this work will be the transition from one curve to the other in both directions.

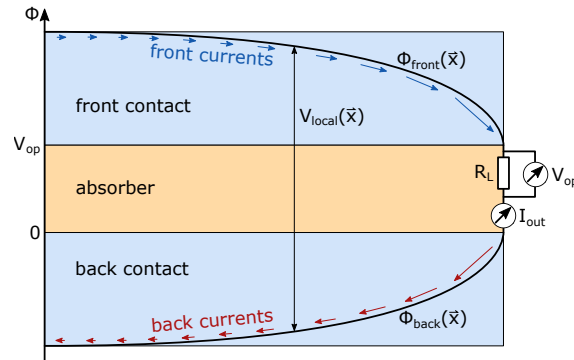


Figure 2.5: Spatially resolved potential distribution of a solar cell. At the cell's external contact point the load resistances R_L is applied. This yields a voltage drop of V_{op} at this position. This one-dimensional schematic illustrates how back and front potential drift towards a larger local voltage drop for finite conductivities of the contact layers.

2.4 Electrical Modeling of Solar Cells

The electrical behavior of solar cells needs to be implemented into an equivalent-circuit diagram. Equation (2.6) models the I–V curve for a simple p–n junction. The exponential term in this equation represents the recombination of the free charge carriers. In real solar cells, different mechanisms of recombination [108] can occur. To model the different effects with high accuracy, an I–V characteristic can be calculated by adding up multiple exponential terms. This approach is called multi-diode equivalent-circuit model. However, for most cells a single diode is of sufficient accuracy, which is why this thesis will only cover single-diode equivalent circuits. An empirical diode ideality factor n_d [109] is introduced to account for this lumping.

2.4.1 Single-Diode Equivalent-Circuit Model

In order to model not only a dark p–n junction but an illuminated solar cell, an additional current generation term j_{ph} needs to be introduced. Moreover, for non-ideal cells an additional series resistance r_s is implemented. As can be seen from Figure 2.6, the voltage across the diode is

reduced since r_s acts as voltage divider. The voltage $V = \Phi_{\text{front}} - \Phi_{\text{back}}$ therefore is reduced by the voltage across the series resistance $j(V)r_s$. Using this expression immediately reveals a numerical challenge to this equation: The expression is dependent on itself, which is called an implicit equation. A solution to this issue is the Lambert W function ^[110], which is explained in detail in Section 4.3.2.1. Finally, to model realistic solar cells, a shunting path across a shunt resistance r_{sh} needs to be implemented as well. The final equation for a single-diode equivalent-circuit model under illumination is given by

$$j(V) = -j_{\text{ph}} + \underbrace{j_0 \left(\exp \left(\frac{q_e(V - j(V)r_s)}{n_d k_B T} \right) - 1 \right)}_{=j_d} + \underbrace{\frac{V - j(V)r_s}{r_{\text{sh}}}}_{=j_{\text{sh}}}. \quad (2.21)$$

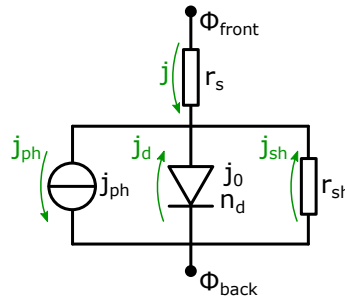


Figure 2.6: single-diode equivalent-circuit model of a solar cell. A realistic solar cell is represented by an ideal cell with a diode and a current source and the two parasitic series and shunt resistances.

2.4.2 Resulting Characteristic Solar Cell Parameters

As it will be seen later in Section 4.5, diode parameters are not a decent way to compare the performance of solar cells unless they are fitted with highest accuracy. The solar cell parameters V_{oc} , j_{sc} , and FF are more representative and can be received from three prominent points on the I–V characteristic: the short-circuit point, the open circuit voltage point, and the MPP. All these points are characterized by a mathematical restriction, which enables to calculate all quantities from Equation (2.21).

The short-circuit current density j_{sc} is defined as the negative current density at zero voltage.

$$j_{\text{sc}} = -j(0) = j_{\text{ph}} - j_0 \left(\exp \left(\frac{-q_e j_{\text{sc}} r_s}{n_d k_B T} \right) - 1 \right) + \frac{j_{\text{sc}} r_s}{r_{\text{sh}}} \quad (2.22)$$

This formula is a implicit equation, meaning j_{sc} depends on itself within this formulation. By using the Lambert W function ^[110] it can be brought into an explicit formulation, which has been done in ^[111, 112]. The Lambert W function is a mathematical function that represents the converse relation of the expression $f(x) = x \cdot e^x$. For a sufficiently small series resistance, j_{sc} is in good approximation given by

$$\lim_{r_s \rightarrow 0} j_{\text{sc}} = j_{\text{ph}}. \quad (2.23)$$

The open-circuit voltage is determined by a vanishing current density $j(V_{oc}) = 0$. Since the resulting expression is an implicit equation, it is not trivially solvable for the voltage. Again, by using the Lambert W function ^[110] it can be achieved by the expression

$$V_{oc} = \left(r_{sh}(j_{ph} + j_0) - \frac{n_d k_B T}{q_e} \cdot \mathcal{W} \left(\frac{q_e j_0 r_{sh}}{n_d k_B T} \cdot \exp \left(\frac{q_e r_{sh}(j_{ph} + j_0)}{n_d k_B T} \right) \right) \right). \quad (2.24)$$

The MPP is defined as the extremum of the produced power in Equation (2.8). Inserting Equation (2.21) for the current density, the constraint in Equation (2.10) needs to be solved for the voltage. The resulting transcendental equation need to be solved numerically. In this work a Newton-Raphson method ^[113] with V_{oc} as initial guess will be used. The current density j_{MPP} can be calculated from the voltage V_{MPP} via Equation (2.21).

$$j_{MPP} = j(V_{MPP}) \quad (2.25)$$

2.4.3 Implications of Parasitic Influences on Diode Parameters and Solar Cell Parameters

In its last consequence, every loss effect leads to a decreased solar cell efficiency. However, to interpret the corresponding solar cell parameters, Figure 2.7 shows the most important correlations. Especially for the reversed direction the flow chart can be used. It shows which solar cell parameter is dominantly influenced by which loss mechanism and diode parameter. Solid lines indicate a strong impact, whereas dashed lines represent a weak correlation.

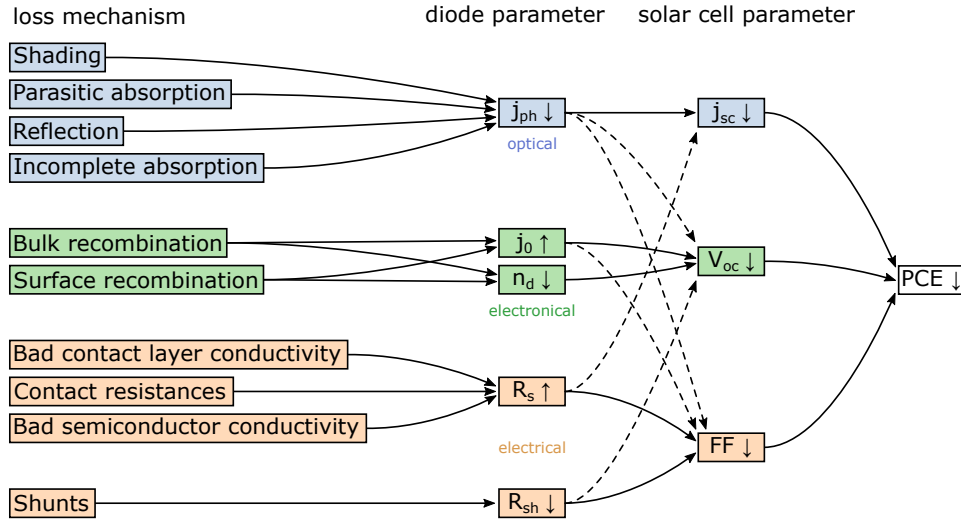


Figure 2.7: Influence of loss mechanisms, diode parameters, and solar cell parameters. Solid lines denote a strong influence, whereas dashed lines indicate weak impact.

It should be noted that the schematic is only valid in the near surrounding of the MPP. In extreme cases each diode parameter can influence almost every solar cell parameter. All optical loss mechanisms have a direct influence on the generated photocurrent and thus on the short-circuit current. Marginally V_{oc} and the FF are also affected due to the shift of the I-V curve. All recombination mechanisms effect j_0 and n_d , which are mainly related to the open-circuit voltage.

Finally, the FF is determined by the shunt and series resistance, which are mainly influenced by ohmic resistances, contact resistances, and electrical leakage currents. Very high recombination rates also affect the FF.

2.4.4 Diode Network Model

As described in section 2.3.4 the electrical properties across the cell are a function of space since the voltage drop is intrinsically a space-dependent distribution. The simplest approach of a single-diode equivalent-circuit model ignores these spatial differences and uses averaged mean values, where all properties are lumped into a single component^[114]. However, this approximation is not sufficient for several solar cells and predicts incorrect I–V curves^[107, 115]. In order to account for a spatial sheet resistance distribution, diode network models have been introduced^[116]. Figure 2.8 shows a schematic of such a diode network model. Basically the solar cell is divided into small domains, which are assumed to be electrically equivalent within their restricted expansion. These domains are extremely small and do not represent polycrystalline grains, despite the close resemblance. Within every domain a single-diode equivalent-circuit model is installed from the front contact point to the back contact point. Using several distributed single-diode equivalent circuits, a spatial voltage distribution and thus a spatial current generation distribution can be taken into account^[117]. Even cells with spatially inhomogeneous properties can be modeled with this approach^[118, 119, 62]. On the front and back sides, the contact points of all domains are connected within a resistor network. This enables the locally generated current to be collected and guided towards a global cell contact. The value of these resistors reflects the spatially varying sheet resistances across the solar cell. Although the resulting potential distribution is quantized, with sufficiently fine domains it yields a good approximation to reality. The open-source circuit simulation tool SPICE^[120] is a possible way of implementing such such networks^[121, 122].

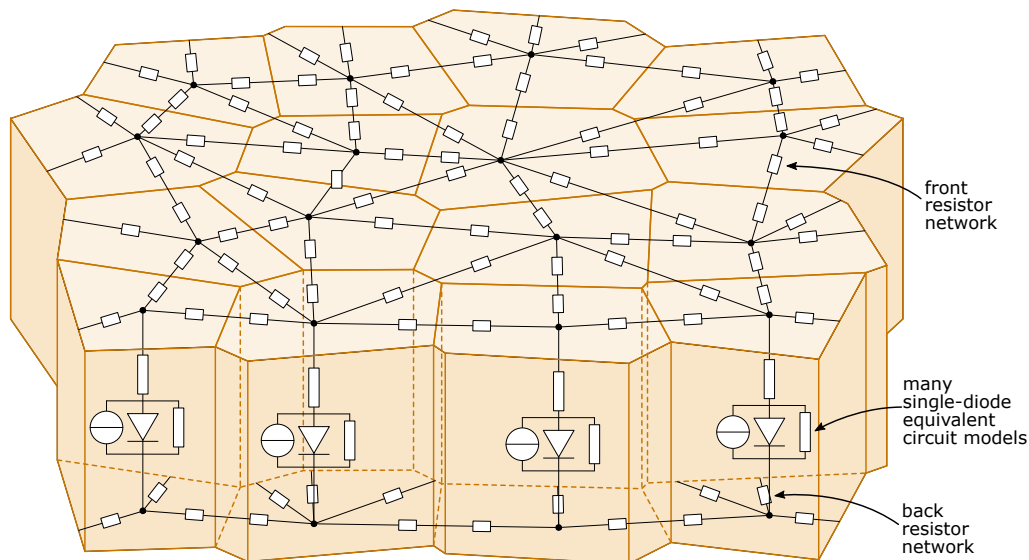


Figure 2.8: In a multi-diode network model, multiple subdomains contain a single-diode equivalent circuit. Every subdomain is connected to its neighbors at the front and back via a resistor network. This allows a spatially resolved representation of a solar cell.

At this point, the difference between a multi-diode network model and a multi-diode equivalent-circuit model should be clearly emphasized. While the first was described above, the latter was briefly broached in the introduction of Section 2.4. The purpose of multi-diode equivalent-circuit models is to physically appropriately represent different recombination mechanisms. However, the effects of a spatially extended solar cell are not taken into account. Within the multi-diode network model consisting of several individual single-diode equivalent circuits, all recombination effects are lumped all into each single diode, but a spatial dependence of the potential distribution and inhomogeneities are part of the simulation concept. In principle, the combination of both models is also conceivable.

2.5 Connecting Multiple Cells with a Module Interconnect

To bring solar devices into large-scale application, single cells are not an appropriate option. Typical devices should be of the order of several square meters for large-area power production. However, cells with the extension over several meters would suffer from an extremely high series resistance, as well as a high total current at a low voltage. According to Figure 2.7, a decreased FF would significantly lower the total PCE. As the ohmic losses increase quadratically with the amount of flowing current ^[123], a method for lowering the current while maintaining the total power is needed. The method of choice for this requirement is to serially connect multiple cells to one module. It is necessary to produce all cells with the same size resulting in roughly the same amount of generated current. This equally distributed current flux is needed for a serial interconnection. If effects like pollution, particle contamination ^[124], or partial shading ^[125, 126] break this symmetry, dark cells act as a resistive dissipative component leading to issues like hot spots ^[127, 128] or other operation complications, which can be anticipated by introducing bypass diodes ^[129, 130]. Moreover, a single cell produces an output voltage on the same order of magnitude as the electronic band gap of its absorber material. Since solar radiation in the visible spectrum is to be absorbed, this is less than 1 V, which is a too low voltage to feed the generated power into the electrical grid. Within a series circuit the voltages of all individual cells add up to a larger voltage, which is easier to handle. Solar modules also consist of an encapsulating layer for the protection of potentially damaging environmental influences.

Basically, two fundamental technologies for solar modules exist ^[131]. The wafer-based method is mainly employed by bulk crystalline silicon solar cells, which are electrically wired by interconnect ribbons ^[132]. The ribbons guide current from the front contact of one cell to the back contact of the next one. With this method a serial connection after the production and sorting of the individual cells is possible ^[133].

The competing technology to the ribbon-based serial interconnection is the monolithic integration ^[134]. This in-situ method allows for an interconnection of multiple cells directly during the manufacturing process. During the deposition of the front and back contact and absorber layers, the films are electrically interrupted by needle scribing or laser scribing ^[135]. Using three trenches P1, P2, and P3, it is possible to guide the current from the front contact of the first cell to the back contact of the second cell within second trench in module interconnect (P2) as indicated by the green arrows in Figure 2.9. The interruptions at the first trench in module interconnect (P1) and the third trench in module interconnect (P3) prevent the current from flowing backwards. However, badly insulating materials can lead to significant shunt currents (red arrows), which is particularly

the case for the current across P1 [136, 137]. Between the trenches P1 and P2 and between P2 and P3 gaps are left to compensate for technological inaccuracies. However, since no photocurrent can be generated within the interconnect area, it is also called dead area. Therefore, the method of interconnecting cells within a module comes with the cost of taking active area of the photovoltaic device. It is therefore of great importance to keep the module interconnect as small as possible while still maintaining the conductivity across P2 and the insulating behavior across P1 and P3.

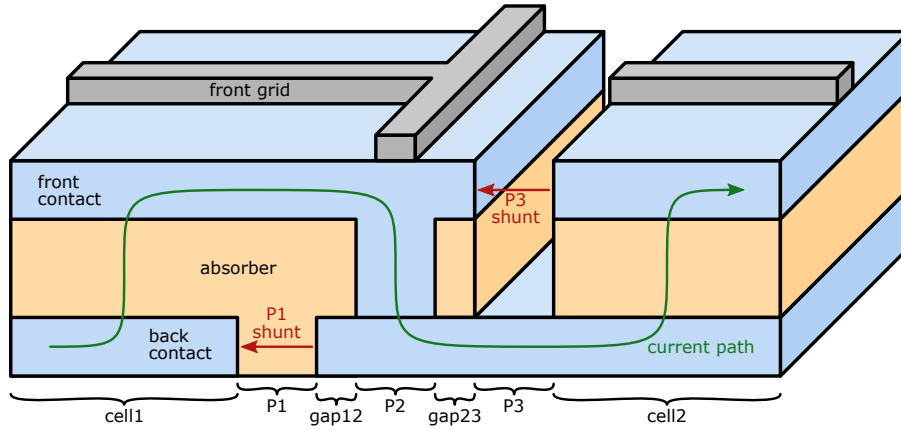


Figure 2.9: Monolithic module interconnect between two thin-film solar cells. Across the filled trench P2 current can flow from the front contact of the first cell to the back contact of the second cell. The trenches P1 and P3 prevent the current from flowing backwards and shunting the module.

2.6 Theoretical Efficiency Limit of Solar Devices

Solar devices suffer from multiple loss mechanisms. On the one hand, there are losses that can be prevented like ohmic losses, contact resistances, shunts, reflection, or parasitic absorption. However, there are a few fundamental losses, which cannot be physically overcome. The red line in Figure 2.10 shows the spectral irradiance $s(\lambda)$ of the reference global tilted solar spectrum (AM1.5G) [138]. It combines the direct sunlight and the scattered fraction from the atmosphere. The jagged appearance mainly rises from passing through earth's atmosphere and the associated absorption e.g. by water vapor. For defining the PCE, light with this spectral distribution hits the solar device. Photons with a lower energy than the band gap of the absorber material cannot excite electrons and thus are transmitted and do not contribute to the generated power. From this point of view, the aim is therefore to keep the band gap as low as possible. Photons with a higher energy than the band gap E_{gap} , can be absorbed and create electron-hole pairs as described in Section 2.2.3. An excited electron receives the full amount of the photon energy. However, its thermal relaxation towards the band gap is on a much shorter time scale than its extraction out of the p-n junction [139]. Thus, the remaining energy is converted into heat and lost for power generation. The resulting maximum photocurrent $j_{\text{ph}}^{\text{SQ}}$ with respect to these thermalisation and transmission losses can be calculated via [140]

$$j_{\text{ph}}^{\text{SQ}} = \frac{q_e}{hc} \int_0^{\lambda_{\text{gap}}} \lambda s(\lambda) d\lambda, \quad (2.26)$$

where h is the Planck constant and c the speed of light. The combination of these loss mechanisms marks the ultimate efficiency limit for solar devices ^[141, 142]. By using two or more stacked p-n junctions in tandem devices, the spectral losses can be reduced ^[143]. However, this work focuses only on single junction solar cells.

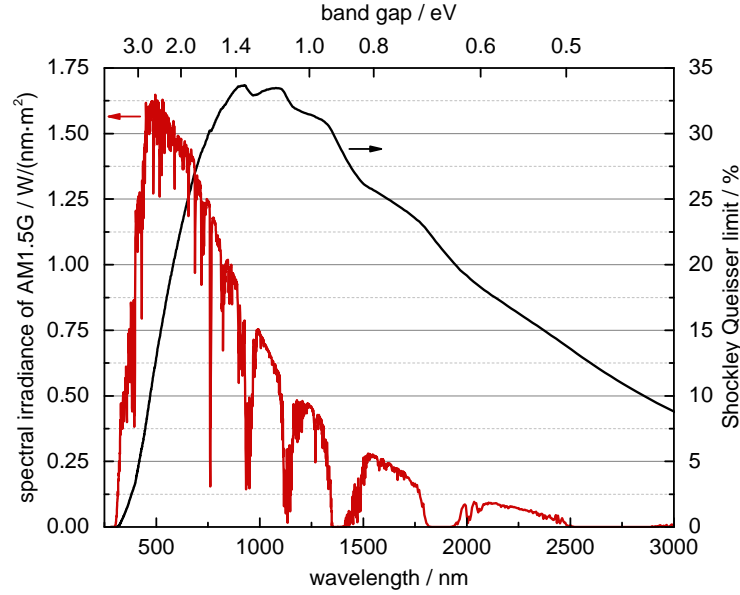


Figure 2.10: The red line shows the spectral irradiance of AM1.5G. This means that the sun's generated spectrum passed 1.5 atmospheric length scales and thus exhibits absorption dips. In black the Shockley-Queisser limit is shown, which marks the upper theoretical limit of solar devices.

Since the solar device is operated at a finite temperature $T > 0$ above absolute zero, it acts itself as a black body and emits radiation. These recombination losses follow Planck's law for idealized black bodies ^[144] up to the band gap E_{gap} of the absorber material ^[145, 146]. The corresponding voltage-dependent current is given by ^[147]

$$j_0^{\text{SQ}} = \frac{2\pi q_e}{h^3 c^2} \int_{E_{\text{gap}}}^{\infty} \frac{E^2}{e^{\frac{E}{k_B T}} - 1} dE \quad (2.27)$$

with the photon energy E . As for an assumed ideal solar device the effects of r_s and r_{sh} vanish and n_d is exactly 1, Equation (2.21) is a trivial exponential correlation.

$$j(V) = -j_{\text{ph}} + j_0 \left(e^{\frac{q_e V}{k_B T}} - 1 \right) \quad (2.28)$$

Since this is an explicit expression it can be solved for V . By inserting Equations (2.26) and (2.27) and assuming a temperature of 300 K the voltage at the MPP V_{MPP} can be analytically calculated via the definition $d/dV (j(V) \cdot V) = 0$. Knowing V_{MPP} and thus the corresponding current density j_{MPP} , it is a trivial task to calculate the PCE via Equation (2.12). Thus, the maximum efficiency only depends on the band gap E_{gap} of the absorber material. This dependence is shown as a black line in Figure 2.10 and is called the Shockley-Queisser limit ^[148]. The maximum efficiency of around 33% is at a band gap of 1.34 eV and is by far smaller than a comparable Carnot efficiency ^[149] for a classic thermodynamic engine of $1 - T_{\text{earth}}/T_{\text{sun}}$ of 94.8% with the Earth's temperature T_{earth} of around 300 K under operating conditions and the sun's temperature T_{sun} of 5778 K. The difference in both numbers is mainly due to thermodynamic entropy.



Answering this Chapter's Guiding Scientific Question

How do solar devices convert photon energy into electric energy and how is this effect used in large-scale applications?

Incident photons that are not reflected, transmitted, or parasitically absorbed create electron-hole pairs within the absorber layer due to the photoelectric effect. They are spatially separated and bidirectionally guided towards the front and back sides of the solar absorber. The adjacent contact layers further guide the charge carriers towards a central contact point. This results in ohmic losses and therefore builds a spatial gradient in the voltage distribution. To keep this effect as small as possible, multiple cells are serially connected with a monolithic module interconnect for large-scale applications.

3

Current Literature Status and Objective of this Thesis

***T**his chapter gives a short introduction into published literature on the topic of this thesis. It starts with the simulation of photovoltaic devices in general and subsequently specifically addresses spatially resolved solar device simulations. Afterwards, clearly formulated goals of this work are outlined. These objectives are intentionally kept very short to give the reader a clear motivation for the presence and necessity of this thesis.*

3.1 Current Status of Spatially Resolved Simulations on Thin-film Photovoltaic Cells and Modules

With the increasing computing power of integrated circuits ^[150], computer simulations get more and more popular in supporting scientific research and guiding its progress. Most of the simulation programs and scripts written for solar cell physics are drift-diffusion models ^[59, 92, 151, 152, 153, 154, 155, 156, 157, 158, 159]. Within this kind of simulation, material parameters like the doping level or band gap are considered and by using an externally calculated generation rate, a spatially resolved band diagram can be calculated. From this distribution, physical quantities like the charge density distribution, internal currents, or I–V curves of the internal semiconductor p–n junction can be concluded. Such simulations are mostly one-dimensional since there is often no necessity for more dimensions due to the thin-film nature without much lateral transport effects except for the electrical current through the contact layers. However, for the investigation of inhomogeneities, multi-dimensional simulation approaches in at least two or sometimes three dimensions need to be considered ^[160].

Drift-diffusion models do not take into account lateral electric transport effects at the contacts. However, this is necessary to simulate an I–V curve exactly how it is measured in the laboratory. The easiest method to do so is to introduce a series and shunting resistance, where all transport losses and shunting effects are lumped into one single resistor, respectively ^[161, 162, 163]. Even early approaches of optimizing grid patterns have been performed with these analytic models ^[164, 165, 166]. Such approaches are called single-diode equivalent-circuit models and have already been introduced in this thesis in Section 2.4.1. Still today, this is a widely spread concept and is a fast and easy way to obtain solar cell parameters and therefore compare multiple solar devices with each other. In Section 4.5, a methodology to fit experimental data with the single-diode equivalent-circuit model is introduced.

However, the assumed concept of a transport effect lumped into single resistors and therefore the assumption of a uniform p–n junction across the entire solar device is no longer valid for cells with high currents (e.g. concentrator cells ^[167]) or large sheet resistances (e.g. thin layers ^[69, 65], high specific resistances ^[67] or large area ^[106]). Moreover, using this concept, much information is lost about where and how electrical losses occur. Therefore, spatially resolved simulations are necessary to overcome these issues. They effectively represent a diode network model, which is an entire network of multiple single-diode equivalent circuits. Such diode network models have been introduced in Section 2.4.4 and include a spatial distribution of sheet resistances ^[115, 116]. A commonly used program to simulate diode network models is the open-source circuit simulation tool SPICE ^[120]. This general-purpose program was often used in literature to calculate such networks ^[121, 122, 168].

Due to the non-negligible resistivity of contact layers, a spatial gradient within the voltage distribution of the electrical contacts evolves. In fact, the locally existing voltage steps between front to back contacts tend to become strongly spatially dependent with decreasing conductivity of the contacts or increasing area of the solar device. Therefore, the local operating voltages shift away from the externally measured MPP of the entire device. For the silicon-wafer technology, this problem has been tackled by using half-cut cells. Due to this local voltage-shifting effect, the generated current densities become spatially dependent as well, even for perfectly homogeneous solar devices ^[117, 169], but even more for cells with local inhomogeneities ^[118, 170, 171, 172]. Assumptions like doubling the cell area will double the measured current are not valid in general, as it will be

shown in section 5.4. Scaling up the area of solar devices is a necessary step towards applied PV. However, this changes the electrics of the entire cell and the calculation of its consequences is a non-trivial task. Moreover, to properly simulate solar modules instead of single solar cells, module interconnects need to be included in the model. For its physically correct modeling, a locally variable voltage distribution is a necessary feature. In order to come up with this spatially dependent voltage distribution, FEM simulations become irreplaceable [65, 67, 66, 68]. Some models consider only one single contact layer that has ohmic losses and keep an optional second contact layer (additional metallization grid or metallic back contact) entirely on the same potential for reasons of runtime efficiency [173, 61]. This is a good approximation for sufficiently conductive grid patterns, but not valid in general. Other simulation tools assume all contacting layers to be ohmically lossy layers [174, 63], which yields more precise results and more detailed loss analyses, but requires per simulated layer quadratically more computational power.

Spatially resolved FEM simulations have a huge variety of additional possible applications and further advantages. A short overview of them is given in the following listing.

- FEM modeling yields a visualization of the internal spatial distribution of electrical potentials or other physical quantities. This furthers a deeper understanding of the ongoing physical effects, which leads to a more targeted improvement of solar devices.
- Even experimentally inaccessible or hard-to-acquire data, such as the direction of current flow or the charge carrier density, become accessible due to spatially resolved simulations.
- Simulations with a spatially distributed resistor arrangement offer the additional advantage to study local impurities and inhomogeneities. Its origins, physical causes, and implications can be examined in detail by multi-dimensional analyses, which cannot be achieved by models with a lumped series resistance [62].
- Numerical simulations enable to shorten laboratory times by forecasting I–V curves and PCEs for multiple sets of parameters (different layer thicknesses, changed sheet resistances, modified illumination conditions, etc.). This enables rapid changes within computer-aided models instead of resource-intensive experiments in the laboratory.
- Another benefit of computational simulations is the possibility for automated design optimization, as well as finding suitable parameters for physical quantities or geometries or even in topologically more challenging problems such as the optimization of the metallization grid pattern. The latter aspect will be discussed at the end of this section.
- Probably the biggest advantage of numerical simulations with a spatially distributed resistor network is the possibility to break down different loss mechanisms. Individual mechanisms have been examined frequently, especially recombination losses [175], electrical shunts [62, 61], ohmic resistances in the TCO and the grid [69], the spatial distribution of local MPP mismatches [64], shaded p-n junction area [73], contact resistances [71, 70], and optical losses [176, 177]. However, multi-level FEM models are able to quantitatively separate all those loss mechanisms and bring them into proportion with each other. The simultaneous simulation of all the loss mechanisms is the only way of keeping track of their mutual influence. This approach has already been published for silicon solar cells [178, 179]. However, for the thin-film technology, only the physical principles have been outlined [180] and a first approach for a semi-holistic simulation has been published [72] with the open-source software PVMOS [181].

The next consequent step after knowing all the loss mechanisms is the optimization of solar devices. For simple, isolated problems, straight forward solutions with analytical calculations are possible, as it is the case for the optimum width of a monolithically integrated cell within an module ^[182]. However, FEMs can be used for a huge variety of questions, like the optimization of the contact layer thickness within an arbitrarily shaped cell ^[183]. For some problems, not only a single variable needs to be optimized, but a high level of complexity and a large number of spatial degrees of freedom is required. This is exemplarily the case for the one-dimensional ratio of gallium to gallium and indium Ga/(Ga+In) concentrations (GGI) profile within the absorber of a CIGS device or the two-dimensional grid-pattern design. For this kind of problem, more advanced strategies than a simple optimizer are necessary. The most common approach to do so is the method of topology optimization (TO). Similarly, TO can be applied to Poisson problems within a FEM model ^[184]. By using the methods of moving asymptotes ^[185], the design of two-dimensional grid patterns can be optimized ^[186]. Such methodology has been applied to solar cells ^[187] and to solar pin-up modules ^[188, 189], but not yet to monolithically integrated cells.

3.2 Objective of this Thesis

In a nutshell, the goal of this work is to develop and test a software to precisely simulate, holistically analyze and globally optimize thin-film solar devices under laboratory and field conditions and predict maximum efficiency potentials on the module level.

In detail, this includes multiple smaller tasks and aims. The first one is to develop a numerical model, which is capable of simulating the electrical and optical behavior of solar cells and modules. This computer-aided designing requires an adaptive and flexible meshing algorithm, the development and linkage of multiple physical models, and fast matrix solvers adapted to the problem formulation. The optical and electrical models on the device level must realistically reproduce the physical processes inside the device.

A major goal of this thesis is the all-in-one loss analysis starting from the internal absorber material level down to the produced module power. This requires not only the correct physical calculation, but also the possibility to allocate all relevant losses to their corresponding loss mechanisms and extract their magnitude. Furthermore, to allow a holistic top-down loss analysis from the physical efficiency limit down to the actual module power, the developed methodology needs to have an interface to a drift-diffusion model. Since several quantities on the material level are difficult to measure experimentally, an advantage of the holistic approach is that it enables to calculate in the backwards direction and draw conclusions for these parameters from measured data, in order not to have to rely on estimated values in the literature. The aspiration of this work is to apply this approach not only under laboratory conditions but also under real-world conditions in the field including temperature variations, illumination fluctuations and realistic module geometries. All calculated simulation results need to be verified with independent, experimental real-world measurements on physical devices. This is the only way to verify and prove a correct numerical simulation procedure.

Moreover, this work aspires to not only calculate the performance and give a categorization of all relevant losses, but also to develop new strategies of device optimization on the basis of physical reasons. These procedures are supposed to be real-world oriented and work for yield computations of monolithically interconnected cells instead of only performance improvements of single cells under laboratory conditions.

Finally, the last aim of this work is to use the evolved simulation methodology to calculate the current technological efficiency limit of thin-film copper indium gallium diselenide $\text{CuIn}_{1-x}\text{Ga}_x\text{Se}_2$ (CIGS) modules. For this purpose, only materials, technologies, and production tolerances that are currently available are used.

4

Modeling Solar Devices – Optical and Electrical Simulation Methods

In order to fulfill the objective of this thesis, a simulation methodology for thin-film solar devices needs to be established. The goal of this chapter is to describe the developed simulation procedure that is used in this work. A digital model is developed to simulate the behaviour of solar cells and modules based on experimentally measured input data. Since this work aims for a holistic but also flexible and connected approach of solar device simulation, no commercially available programs have been used. Every algorithm and procedure described in this section was programmed from scratch, which gives the operator a large degree of adaptability. Only this in-house programming allows the holistic nature of this work's solar simulation, as this enables the complete interlinking of all used simulation methods. All developed simulation methods are implemented into a simulation platform that is briefly introduced in Appendix A.

This Chapter's Guiding Scientific Question

How can characteristic parameters of solar devices be optically and electrically modeled by numerical simulations?

The digital model developed in this work is divided into multiple modules representing the physical processes. These modules are interconnected to provide a full representation of the solar device behaviour. A special consideration of the method developed here is the separation of the semiconductor model, the optical model, and the electrical model. The semiconductor model is a drift-diffusion model programmed elsewhere as described above to provide the I–V characteristic for the given generation profile. The optical model provides the charge carrier generation profile in the absorber material of the solar device. The electrical model describes how the local current generated by the device is transported to the contacts where the power can be consumed. Since at least one side of a solar cell employs a transparent contact with material properties that affect both the optical and the electrical conditions, it is important to link these two models. The following sections describe the techniques and physical models employed.

The electrical model is built up from five different layers as seen in Fig. 4.1. The central layer is the absorber material (orange), representing the function of the solar cell where the photocurrent is generated. In order to simulate their physical behavior, drift-diffusion models are used [59, 92]. Within this work however, the characteristic of the absorber layer is an input for the digital model. In the simplest case, the entire electronic behavior is described by an I–V curve reaching at least from 0 V to the open-circuit voltage. On both sides of the absorber layer, an electrically conducting contact layer (blue) is placed over the entire surface. Its function is to guide the generated photocurrent towards an external contact point, where the total current I_{out} is measured across an external load resistance at the operating voltage V_{op} . Afterwards, it is guided back into the rear conducting layer to complete the circuit. Optionally, structured opaque metallic grid layers (gray) can be placed on top of the contact layers. Although they cast shadows on the absorber layer and hence prohibit a photocurrent generation underneath them, they can cause a substantial improvement. Due to their comparably high electrical conductivity, the purpose of the grid structures is to reduce the electrical collection losses.

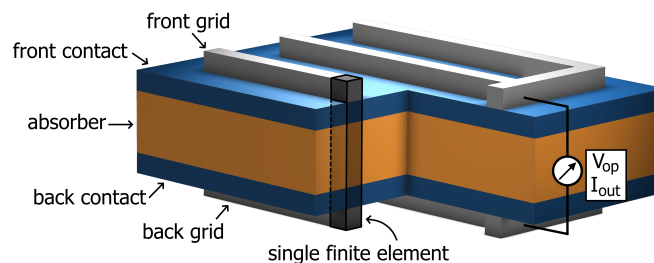


Figure 4.1: Setup of a generic thin-film solar cell [107]. Within the absorber layer (orange) a certain photocurrent is generated across the entire cell. Electrically conducting contacts (blue) and optional grid layers (gray) guide the current towards the cell’s external contacts on the front and back side. These two contacts are connected via a load resistance, where the total generated current I_{out} at the operating voltage V_{op} is measured.

Since optical and electrical effects are present within solar cells, both need to be considered within the simulation. Optical effects can be described by a Lambert-Beer approach [190, 191]. Its input data is the attenuation coefficient for each layer and their thickness. If the complex refractive data of each layer within the stack is known, a more sophisticated approach can be accomplished via a transfer-matrix method (TMM) [192, 60, 193, 194, 195]. In principle, the method of ray tracing can be used for rather complex structures or high degrees of roughness, but it is often not worth the runtime, since a TMM approach provides sufficiently accurate results. For the electrical simulation, Poisson’s differential equation for electrostatics [88] needs to be solved. In the case of complex

geometries, a segmentation into multiple finite elements is needed [62, 65, 181]. Such a FEM reveals a system of coupled equations, which needs to be solved. A single finite element containing all layers is shown in Figure 4.1.

This chapter is structured as follows. In the beginning, the method of meshing is presented and technical terms are defined. Subsequently, the optical simulation methods are presented. Their results will play a role in the electrical model afterwards. Finally, the determination of the external measurable characteristics from the simulations is presented.

4.1 Spatial Quantization via Meshing Algorithm

Discretizing the partial differential equations into a numerically solvable problem requires a division of the entire simulation domain into smaller subdomains. These subdomains will be called finite elements. Each finite element consists of a central node, which is also named mesh point. Furthermore, a borderline separates two neighboring finite elements. All borderlines surrounding a finite element represent the enclosing shell of this element. The set of all finite elements is called mesh.

In this work, a two-dimensional mesh is used. However, in order to sufficiently represent the physical reality within thin-film solar cells, a second two-dimensional mesh with the same element distribution is placed on top of the first one. This procedure generates a quasi-three-dimensional meshing character. The goal of the used mesh is to represent a given input shape with its contours in a precise way with as few finite elements as possible.

There are multiple ways to construct different types of meshes, e.g. a quadtree mesh [196]. However, within this work, a Delaunay mesh [197] is used. It connects the finite elements to a network of triangles, in a way that no other mesh point is contained within the circumcircle of any triangle. The connected finite elements are subsequently next neighbors. For the borderlines between two elements, the perpendicular bisector of the two connected next neighbors is used. The resulting dual graph is called Voronoi diagram [198, 199]. The created polygonal shapes are called Voronoi cells and are assigned as the surrounding border of the finite elements. Voronoi diagrams have the property that each position in the plane is within the euclidean nearest Voronoi cell.

One key feature of the Delaunay-Voronoi meshing method is that the connection and hence the direction of a current between two finite elements is perpendicular to the borderline. This enables a determination of the current without the use of trigonometric functions, angles or displacement currents. While this property is also true for e.g. equidistant square meshes, in the Delaunay-Voronoi method all elements can be placed arbitrarily within the meshing domain. This adaptability allows to reduce the amount of necessary points to exactly reproduce the shape of any arbitrary contour with the Voronoi cells. An exact reproducing is the coincidence of the borderlines of the finite elements with the edge of a given contour. Consequently, a finite element is completely on only one side of the contour but never reaches across a contour line. This is necessary to ensure that the material properties are uniform within each element.

4.1.1 Triangulation Algorithm for Generating a Valid Mesh

As described in the previous section, a Delaunay-Voronoi mesh is used within this work. Firstly, a Delaunay triangulation is accomplished and afterwards, the Voronoi diagram is generated as the dual graph. To achieve the Delaunay triangulation, the Bowyer-Watson algorithm ^[200, 201] is used to insert a new meshpoint into the meshing domain. However, this procedure requires a valid starting triangulation. For this purpose, four additional surrounding meshpoints serve as the starting domain. They form a rectangle and are Delaunay-triangulated via two congruent triangles called supertriangles ^[202]. After all regular meshpoints are inserted, these starting points and the supertriangles are removed.

In order to insert a new meshpoint into the existing meshing domain, a modified version of the Bowyer-Watson algorithm is used. In Figure 4.2a a Delaunay triangulation is shown, where all meshpoints are represented as intersections. The cross marks a position for a new meshpoint, which needs to be inserted. The rules for meshpoint insertion are discussed in Section 4.1.2. For the Bowyer-Watson algorithm all triangles whose circumcircle includes the position need to be found. These triangles will be called \mathcal{N}_0 triangles. The following procedure describes an efficient way of finding all \mathcal{N}_0 triangles without having to check all present triangles. In the first step, the triangle containing the new position inside its area is searched for since if the triangle itself contains the position, its circumcircle contains the position as well. Examining whether a position is within or outside a triangle is a rather time-efficient task in barycentric coordinates ^[203]. This process is even accelerated by dividing the domain into multiple subdomains, in order to look up only triangles in the vicinity of the position. Moreover, this allows to parallelize the procedure. Having found the surrounding triangle, its circumcircle automatically includes the new position since the whole triangle area lies within its circumcircle. Therefore, the first \mathcal{N}_0 triangle is found and marked in red in Figure 4.2b. All triangles having two or one common corner points with the \mathcal{N}_0 triangle are marked as \mathcal{N}_1 (orange) and \mathcal{N}_2 (yellow) triangles, respectively. Subsequently, all \mathcal{N}_1 triangles are checked to see if their circumcircles involve the new position (Figure 4.2c). If they do, then these triangles are reassigned to the \mathcal{N}_0 set. This process of adding triangles to the \mathcal{N}_0 and \mathcal{N}_1 sets and checking all \mathcal{N}_1 triangles repeats until no \mathcal{N}_1 contains the new position within its circumcircle, as in Figure 4.2d. The \mathcal{N}_2 triangles don't need to be checked since their circumcircle cannot extend further into the red area than the ones of the orange \mathcal{N}_1 triangles (see Figure 4.2e). Afterwards, all \mathcal{N}_0 triangles are deleted from the meshing domain leaving behind a polygonal hole around the new meshing position. Finally, all edges of this polygon are connected with the new meshpoint resulting in an new valid Delaunay mesh as it is shown in Figure 4.2f.

After inserting all meshpoints to the meshing domain, a Voronoi diagram is created from the Delaunay mesh. While there are multiple algorithms for directly creating the Voronoi diagram from scratch ^[204, 205], the procedure of this work uses the perpendicular bisectors of the Delaunay triangulation to generate the Voronoi cells.

4.1.2 Detailed Modeling of Contour Patterns

As discussed in the introduction of this section, the Delaunay-Voronoi meshing combines the advantages of having current flows perpendicular across the borderlines of the finite elements and the possibility of placing new meshpoints at arbitrary positions. The latter property will be used in this section to exactly reproduce a given input shape containing multiple contour segments. Geometries are typically defined with specific points (contour junctions) that are connected by

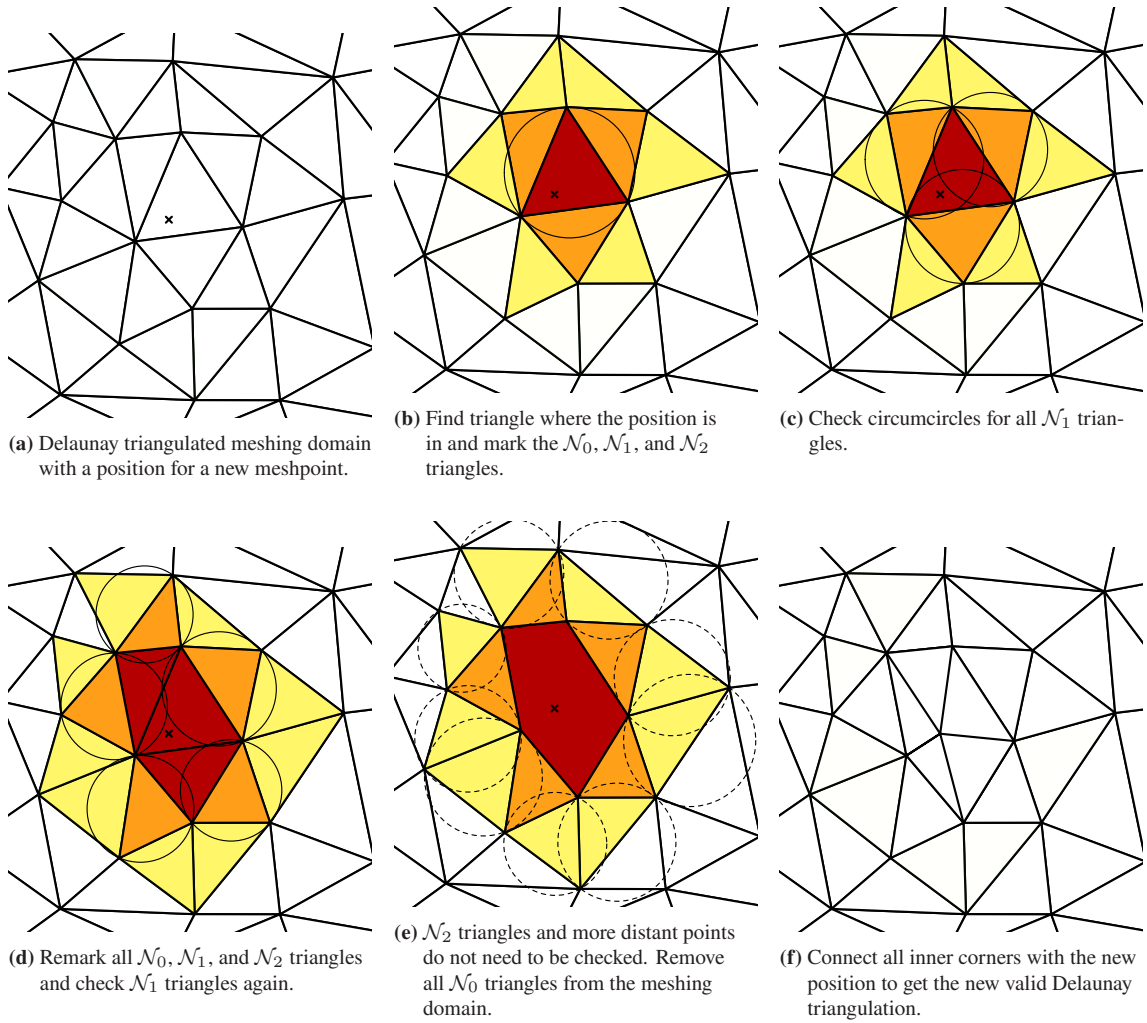


Figure 4.2: Modified Bowyer-Watson algorithm. Starting from a valid Delaunay triangulation of multiple meshpoints, the Bowyer-Watson algorithm enables to insert a new meshpoint and locally adapt the triangulation. In the first step, all triangles with their circumcircle containing the new position need to be found. Using this modification, not all triangles have to be checked, which reduces the runtime of the procedure.

lines (contour segments) as seen in Figure 4.3. A closed set of lines forms a polygonal region, which can be defined as an area with specific properties, such as having a grid or not. Since the border between two Voronoi cells lies directly in the middle of both meshpoints, implementing pairs of two cohesive mirror points along contour segments with the distance d_{seg} to the segment ensures two pure single mesh points. This method was developed independently within this work. These paired points are shown as solid black points in Figure 4.3. The meshpoint pairs are placed with a distance d_{point} to the next pair. This ensures that both adjacent finite elements are exactly separated by the contour segment of the input shape. This behavior is shown in Figure 4.4, where the border between orange and gray marks a contour segment. If two or more contour segments intersect with each other, a contour junction is created. These junctions are separately meshed with two meshpoints for each segment on a circle with the radius d_{junc} around the junction, as it is shown in the inset of Figure 4.4. These two meshing procedures ensure an exact representation of the input geometry with finite elements. Afterwards, the remaining area is meshed with regular meshpoints that do not belong to a mirror meshpoint pair. These meshpoints are represented as gray points with a black border in in Figure 4.3.

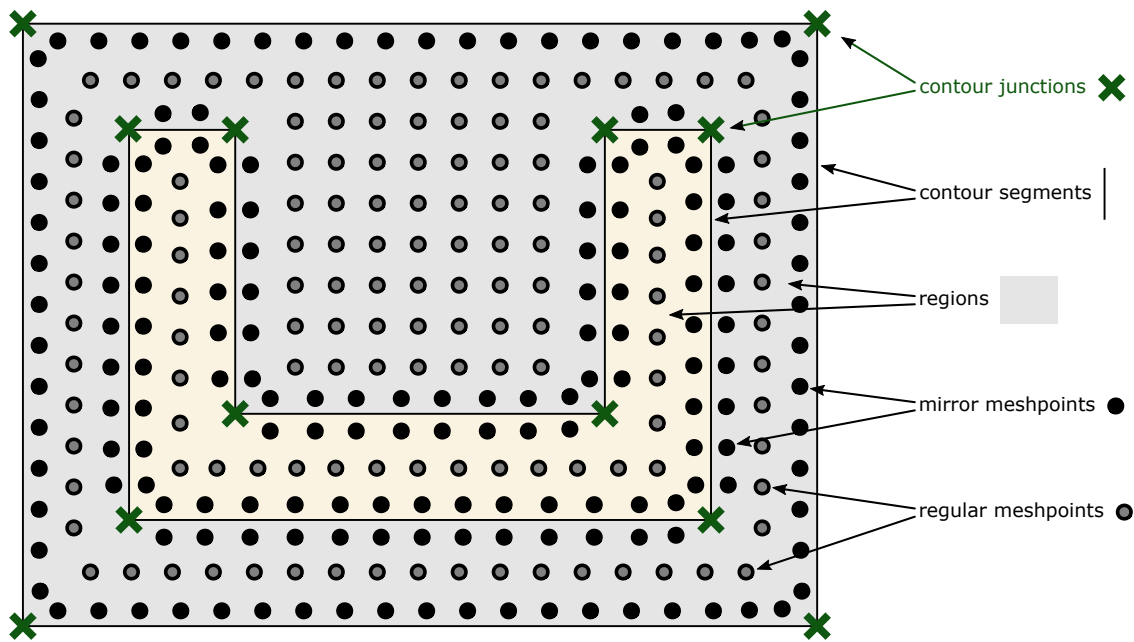


Figure 4.3: Definitions within the contour meshing procedure. All green crosses form the contour junctions, which are connected by contour segments. The areas enclosed by segments are called regions. Each contour segment is meshed by special mirror points. Afterwards, the remaining area is filled up with regular meshing points.

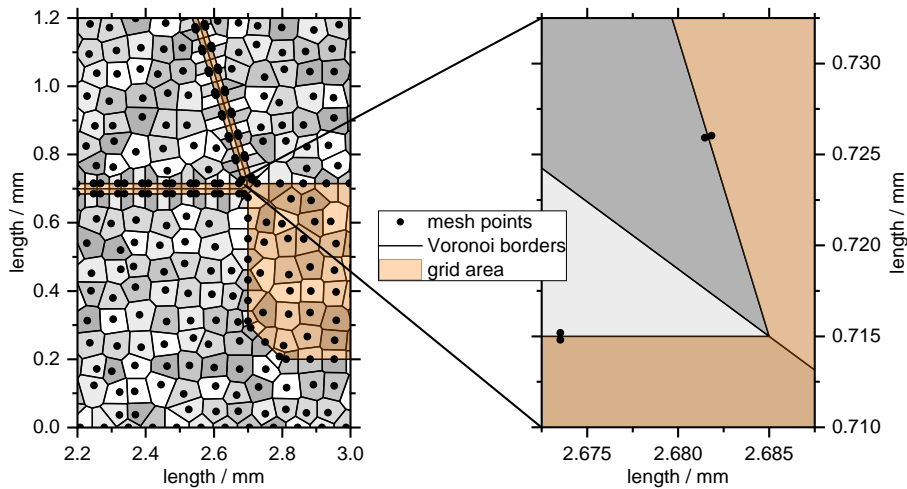


Figure 4.4: The orange-colored area represents one geometric region, whereas all gray scale elements form another region. The method of mirror points guarantees an overlap-free mapping of both regions and their shared border. This algorithm is designed to work for border segments and border edges.

At the outer edge of the geometry, the second mirror point outside the input geometry is not inserted into the meshing domain, resulting in an enclosed area. Hence, arbitrary geometries can be meshed with finite elements. Furthermore, regions in the interior of the domain can also be kept clear of meshpoints. Using this feature in the simulation, holes within a meshing domain can be produced. After meshing the contour segments, interior meshpoints are inserted into the meshing domain. Usually they are equidistantly placed and slightly randomly moved for numerical stability reasons. However, there are forbidden areas, where no interior meshpoint is allowed to be placed in order to not destroy any contour meshing of the segments or the junctions. These areas can be geometrically

determined and are circles with the radius d_{junc} around contour junctions and parallel corridors along contour segments with the diameter $(d_{\text{point}}^2 + 4d_{\text{seg}}^2)^{\frac{1}{2}}$. An example mesh of the Lake Superior, which is often used as a meshing benchmark [206], can be seen in Figure 4.5.

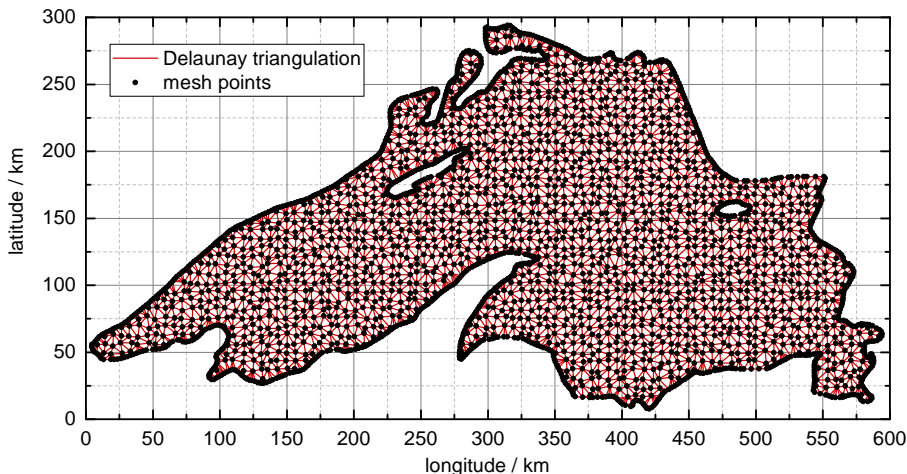


Figure 4.5: Due to its multifarious shape with spiky corners and interior islands, Lake Superior is a challenging two-dimensional standard geometry to mesh. The shown meshing domain is generated with the presented meshing technique of mirror points. The black points represent the meshing points and the red connection lines show their corresponding Delaunay triangulation accomplished with the Bower-Watson algorithm.

4.2 Optical Model

Optical effects play an essential role for solar cell performance, especially in the form of reflection, parasitic absorption and transmission. Therefore, the impact of all layers within the solar cells needs to be modeled. The easiest approach to include reflection and absorption is an augmented model of exponentially decaying light intensity [190, 191]. However, to include intra-device interferences, a more sophisticated model is needed. One appropriate one-dimensional algorithm is the transfer-matrix method (TMM) [192, 193, 194, 195, 207], which was implemented in this work and will be described in detail in Section 4.2.2. Due to its one-dimensionality, only a layer stack with smooth interfaces can be modeled exactly. There are several methods to approximate rough surfaces with a scalar scattering theory [208, 209, 194, 210]. Because of distinct interference maxima due to standing waves, non-linear heating effects might occur [211, 212], but are not considered in this work because of its subordinate role in this case. In order to exactly model three-dimensional geometries, numerically expensive ray tracing methods must be used [213]. However, this method is not used in this work since a one-dimensional model provides sufficiently accurate results.

In detail, the most accurate results are achieved by applying the optical model directly within a drift-diffusion model. By doing so, effects of an increased space-charge region, diffusion, and enhanced interface currents can be considered physically correctly. However, within this work a linear impact of the light intensity damping on the consequently generated photocurrent is assumed as it will be shown in Equation (4.18). As it will be proven in Section 5.3, this approximation is by far sufficient enough for standard solar cells. Therefore, the following two sections are dedicated to deriving an optical damping factor f_{optics} using the simple Lambert-Beer method and the more complex TMM method as implemented in this work.

4.2.1 Lambert-Beer Method

The most trivial approach to include optical effects within a digital model of a solar cell is an exponential damping [190, 191]. Depending on the wavelength λ , each material has a linear attenuation coefficient $\alpha(\lambda)$. This leads to an exponentially decaying light intensity $I(z)$ along the propagation direction z starting from an initial intensity I_0 .

$$I(z) = I_0 \cdot e^{-\alpha(\lambda) \cdot z} \quad (4.1)$$

The attenuation coefficient can be determined from the complex refractive index $\hat{n} = n + ik$ via

$$\alpha(\lambda) = \frac{4\pi k}{\lambda}. \quad (4.2)$$

For multiple layers, the damping effect of each layer is determined successively. This can be observed by the several slopes of the black line in Figure 4.6. The example represents a layer stack with two thin, partially transparent layers covering an absorber material with $k = 1$. This situation is present in thin-film solar cells with parasitic absorption occurring in window and buffer layers. The transmitted light power calculated here is available for the solar cell to convert into electrical power.

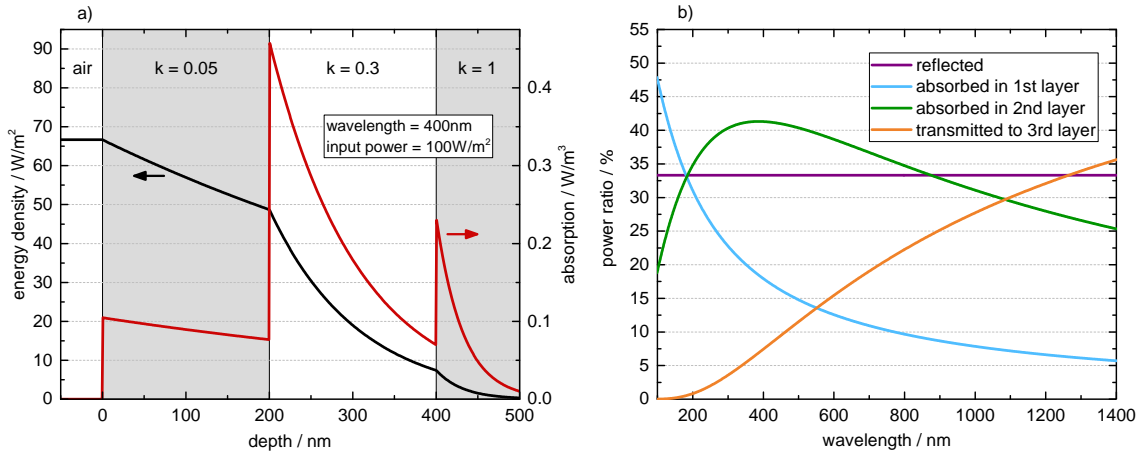


Figure 4.6: Optics with Lambert-Beer approach. Plot a) shows the energy density and the spatially resolved local absorption at each point of the one-dimensional layer stack for a single wavelength of 400 nm. An empirical value for reflection of 33% is used. In plot b) the wavelength is varied and the light intensity is split up into a reflected, transmitted, and absorbed power ratio.

In order to include reflection effects within this model of exponential damping, an additional reflection term is inserted into the model. This value cannot be calculated trivially within this approach and hence needs to be an input. In Figure 4.6 an empirical reflection of 33% is used for all wavelengths.

To gain a spatially resolved absorption profile $A(z)$, the spatial derivative of Equation (4.1) is needed.

$$A(z) = -\frac{\partial I(z)}{\partial z} = \alpha(\lambda) \cdot I_0 \cdot e^{-\alpha(\lambda) \cdot z} \quad (4.3)$$

The total absorption of a single layer A_{layer} is calculated via the integral of the absorption over the entire layer thickness d_{layer} .

$$A_{\text{layer}} = \int_0^{d_{\text{layer}}} A(z) dz \quad (4.4)$$

The light intensity passing the last layer is referred to as transmitted light. Additionally to the reflection and transmission, the absorbing factors of both layers are shown as a function of wavelength in Figure 4.6 b). Since the reflection is assumed to be wavelength-independent in the shown example, it is constant over the entire range. In the current example, photons with smaller wavelengths are directly absorbed in the first layer due to the large attenuation coefficient with an inverse dependency of the wavelength. Large wavelengths, however, mainly pass the first layer and are absorbed in the second one due to its larger attenuation coefficient. Wavelengths surpassing 1000 nm primarily do not get absorbed in the first layer and are significantly transmitted through the layer stack.

Finally, the optical factor f_{optical} is determined as the absorbed power in the absorber layer divided by the entire incident irradiation. This model correctly calculates a larger absorption for thicker layers, giving insight into a first principle for optimizing the optics for thin-film solar cells.

4.2.2 Transfer-Matrix Method

The content of this section has been developed and implemented in collaboration with Tim Helder.

As it can be seen in Figure 4.6, intra-device interferences due to standing waves are not encountered within a simple model of exponentially decaying light intensity. Moreover, the reflection ratio needs to be an empirical input for the model. However, if the complex refractive index \hat{n}_i is known for each layer, the approach of TMM is capable of describing both features. The TMM basically combines the polarization-dependent refraction between two optical materials and the propagation within a single material. In the following, all complex values are denoted with a hat on top of the symbol.

To describe the refraction at any interface, Snell's law is used to determine the angle of refraction $\hat{\vartheta}_i$ from the given complex refraction indexes \hat{n}_i and \hat{n}_{i+1} .

$$\frac{\sin(\hat{\vartheta}_i)}{\sin(\hat{\vartheta}_{i+1})} = \frac{\hat{n}_{i+1}}{\hat{n}_i} \quad (4.5)$$

All angles are measured towards a perpendicular line of the interface, as it can be seen in Figure 4.7. Even for a multi-layer stack, all angles can be pre-calculated. Since the refractive indexes are in general complex numbers, the angles need to be complex as well. Even with only real refractive indexes, complex angles occur in the case of total reflection. In this case the real part of $\hat{\vartheta}_i$ is given by $\frac{\pi}{2}$.

Knowing the angle of incidence and the refractive index of two layers, the refraction between two optically different materials can be determined by Fresnel's equations ^[214]. The amount of reflected and transmitted power depends on the polarization of the incident electromagnetic wave. In the following, all materials are assumed to have the same magnetic permeability μ . For the transverse

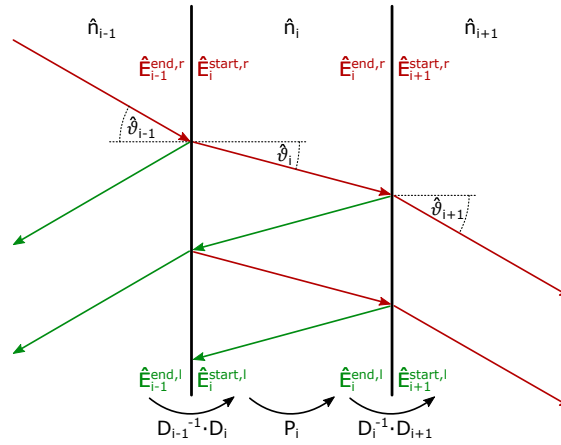


Figure 4.7: Ray paths in TMM. All angles can be calculated via Snell's law of refraction. The refraction from a layer with a complex refractive index \hat{n}_i to two surrounding layers $i - 1$ and $i + 1$ is determined by Fresnel's equations. Finally, the exponential decay during the propagation within a layer is described by the propagation matrix. The TMM combines all features as described in the main text.

electric mode (electric field perpendicular to the interface), the reflected and transmitted ratios of electric fields are given by

$$\frac{\hat{E}_i^{s,end,l}}{\hat{E}_i^{s,end,r}} = r_s = \frac{\hat{n}_i \cos(\hat{\vartheta}_i) - \hat{n}_{i+1} \cos(\hat{\vartheta}_{i+1})}{\hat{n}_i \cos(\hat{\vartheta}_i) + \hat{n}_{i+1} \cos(\hat{\vartheta}_{i+1})} \quad (4.6a)$$

$$\frac{\hat{E}_{i+1}^{s,start,r}}{\hat{E}_i^{s,end,r}} = t_s = \frac{2 \hat{n}_i \cos(\hat{\vartheta}_i)}{\hat{n}_i \cos(\hat{\vartheta}_i) + \hat{n}_{i+1} \cos(\hat{\vartheta}_{i+1})}. \quad (4.6b)$$

In the case of transverse magnetic modes (electric field parallel to the interface), the analog ratios are determined via

$$\frac{\hat{E}_i^{p,end,l}}{\hat{E}_i^{p,end,r}} = r_p = \frac{\hat{n}_{i+1} \cos(\hat{\vartheta}_i) - \hat{n}_i \cos(\hat{\vartheta}_{i+1})}{\hat{n}_{i+1} \cos(\hat{\vartheta}_i) + \hat{n}_i \cos(\hat{\vartheta}_{i+1})} \quad (4.7a)$$

$$\frac{\hat{E}_{i+1}^{p,start,r}}{\hat{E}_i^{p,end,r}} = t_p = \frac{2 \hat{n}_i \cos(\hat{\vartheta}_i)}{\hat{n}_{i+1} \cos(\hat{\vartheta}_i) + \hat{n}_i \cos(\hat{\vartheta}_{i+1})}. \quad (4.7b)$$

For a single-interface refraction, the electric fields can be named by more intuitively understandable names: $\hat{E}_i^{end,r}$ is the incoming electric field \hat{E}_{in} , whereas $\hat{E}_i^{end,r}$ and $\hat{E}_{i+1}^{start,r}$ refer to the reflected and transmitted field \hat{E}_{refl} and \hat{E}_{trans} , respectively. $\hat{E}_{i+1}^{start,r}$, however, is the incoming field from the back side of the layer \hat{E}_{back} and is always zero for the last layer in case of a single light ray from the front side.

Multi-layer solar devices typically do not consist of perfectly smooth interfaces. To consider the resulting partially incoherent light due to scattering effects at rough interfaces [215, 216], modified Fresnel coefficients r'_s , t'_s , r'_p , and t'_p are used within this work. [217] They can be derived from the conventional coefficients r_s , t_s , r_p , and t_p as described in [209]. Therefore, typical internal reflections within thin films and coherent interferences of multi-layer solar cells [218] can be considered simultaneously with incoherent and scattered light within certain limits of validity.

It should be said at this point that \hat{n}_i is also a function of the wavelength. In a matrix form, the perpendicular field equations (4.6a) and (4.6b) can be rewritten as

$$\begin{pmatrix} \hat{E}_i^{\text{s,end,r}} \\ \hat{E}_i^{\text{s,end,l}} \end{pmatrix} = \frac{1}{2} \underbrace{\begin{pmatrix} 1 & \frac{1}{\cos(\hat{\vartheta}_i)\hat{n}_i} \\ 1 & -\frac{1}{\cos(\hat{\vartheta}_i)\hat{n}_i} \end{pmatrix}}_{=(\mathbf{D}_i^{\text{s}})^{-1}} \cdot \underbrace{\begin{pmatrix} 1 & 1 \\ \cos(\hat{\vartheta}_{i+1})\hat{n}_{i+1} & -\cos(\hat{\vartheta}_{i+1})\hat{n}_{i+1} \end{pmatrix}}_{=\mathbf{D}_{i+1}^{\text{s}}} \cdot \begin{pmatrix} \hat{E}_{i+1}^{\text{s,start,r}} \\ \hat{E}_{i+1}^{\text{s,start,l}} \end{pmatrix} \quad (4.8)$$

and the parallel fields (4.7a) and (4.7b) as

$$\begin{pmatrix} \hat{E}_i^{\text{p,end,r}} \\ \hat{E}_i^{\text{p,end,l}} \end{pmatrix} = \frac{1}{2} \underbrace{\begin{pmatrix} \frac{1}{\cos(\hat{\vartheta}_i)} & \frac{1}{\hat{n}_i} \\ \frac{1}{\cos(\hat{\vartheta}_i)} & -\frac{1}{\hat{n}_i} \end{pmatrix}}_{=(\mathbf{D}_i^{\text{p}})^{-1}} \cdot \underbrace{\begin{pmatrix} \cos(\hat{\vartheta}_{i+1}) & \cos(\hat{\vartheta}_{i+1}) \\ \hat{n}_{i+1} & -\hat{n}_{i+1} \end{pmatrix}}_{=\mathbf{D}_{i+1}^{\text{p}}} \cdot \begin{pmatrix} \hat{E}_{i+1}^{\text{p,start,r}} \\ \hat{E}_{i+1}^{\text{p,start,l}} \end{pmatrix}. \quad (4.9)$$

Within these equations the refraction matrices \mathbf{D}_i and their inverse $(\mathbf{D}_i)^{-1}$ occur. The exponentially decaying light intensity of Equation 4.1 can also be expressed in a matrix formulation

$$\begin{pmatrix} \hat{E}_i^{\text{start,r}} \\ \hat{E}_i^{\text{start,l}} \end{pmatrix} = \underbrace{\begin{pmatrix} \exp\left(-i\frac{2\pi\hat{n}_i}{\lambda}\cos(\hat{\vartheta}_i)\cdot z\right) & 0 \\ 0 & \exp\left(i\frac{2\pi\hat{n}_i}{\lambda}\cos(\hat{\vartheta}_i)\cdot z\right) \end{pmatrix}}_{=\mathbf{P}_i} \cdot \begin{pmatrix} \hat{E}_i^{\text{end,r}} \\ \hat{E}_i^{\text{end,l}} \end{pmatrix} \quad (4.10)$$

with the propagation matrix \mathbf{P}_i . The key point of the TMM is to combine all back and forth propagating fields into one single complex value, each corresponding to one row of the matrix notation.

The main task is to calculate the reflected and transmitted light intensity throughout the entire layer stack. Therefore, all matrices according to Figure 4.7 for all N layers are multiplied with each other in order to get a total transfer-matrix \mathbf{M} .

$$\begin{pmatrix} \hat{E}_0^{\text{end,r}} \\ \hat{E}_0^{\text{end,l}} \end{pmatrix} = \underbrace{\mathbf{D}_0^{-1} \cdot \left[\prod_{i=0}^N \mathbf{D}_i \cdot \mathbf{P}_i \cdot \mathbf{D}_i^{-1} \right]}_{=\mathbf{M}} \cdot \mathbf{D}_{N+1} \cdot \begin{pmatrix} \hat{E}_N^{\text{start,r}} \\ \hat{E}_N^{\text{start,l}} \end{pmatrix} \quad (4.11)$$

Knowing the incident light intensity $\hat{E}_{\text{in}} = \hat{E}_0^{\text{end,r}}$ and assuming no incoming light from the back $\hat{E}_{\text{back}} = \hat{E}_N^{\text{start,l}} = 0$, the reflected and transmitted electric fields can be determined. Afterwards, the back and forth propagating fields at the beginning of each layer are iteratively calculated. Knowing the electric field strength at the beginning of a layer i , their value can be easily determined with a length-modified propagation matrix \mathbf{P}'_i at any point within the layer. Finally, to conclude the energy density at any arbitrary point within or outside the layer stack, the Poynting vector $\underline{S}(z)$ [219] is calculated from the electric fields [192] for perpendicular modes

$$\underline{S}^{\text{s}}(z) \cdot \underline{e}_z = \frac{\Re\left(\hat{n}(z) \cdot \cos(\hat{\vartheta}(z)) \cdot \left(\hat{E}^{\text{s,r}}(z) + \hat{E}^{\text{s,l}}(z)\right)^* \cdot \left(\hat{E}^{\text{s,r}}(z) - \hat{E}^{\text{s,l}}(z)\right)\right)}{2\mu_0 c \cdot \Re\left(\cos(\hat{\vartheta}_0)\right)} \quad (4.12)$$

and parallel modes

$$\underline{S}^p(z) \cdot \underline{e}_z = \frac{\Re \left(\hat{n}(z) \cdot \cos(\hat{\vartheta}^*(z)) \cdot \left(\hat{E}^{p,r}(z) + \hat{E}^{p,l}(z) \right) \cdot \left(\hat{E}^{p,r}(z) - \hat{E}^{p,l}(z) \right)^* \right)}{2\mu_0 c \cdot \Re \left(\cos(\hat{\vartheta}_0^*) \right)}. \quad (4.13)$$

A star * in this case denotes a complex conjugate. The above-derived equations can be used to visualize the propagation of a diagonally polarized light ray through a layer stack in the following example. A wavelength of 400 nm, an angle of incidence of 17° , and an irradiance of $100 \frac{\text{W}}{\text{m}^2}$ is assumed. In a first step, the diagonal polarization is split up into perpendicular and parallel fractions by using trigonometrical functions. Then the method of TMM is applied to both polarizations for electric fields (plot c) in Figure 4.8) and energy density (plot a)). Compared to Figure 4.6, the same

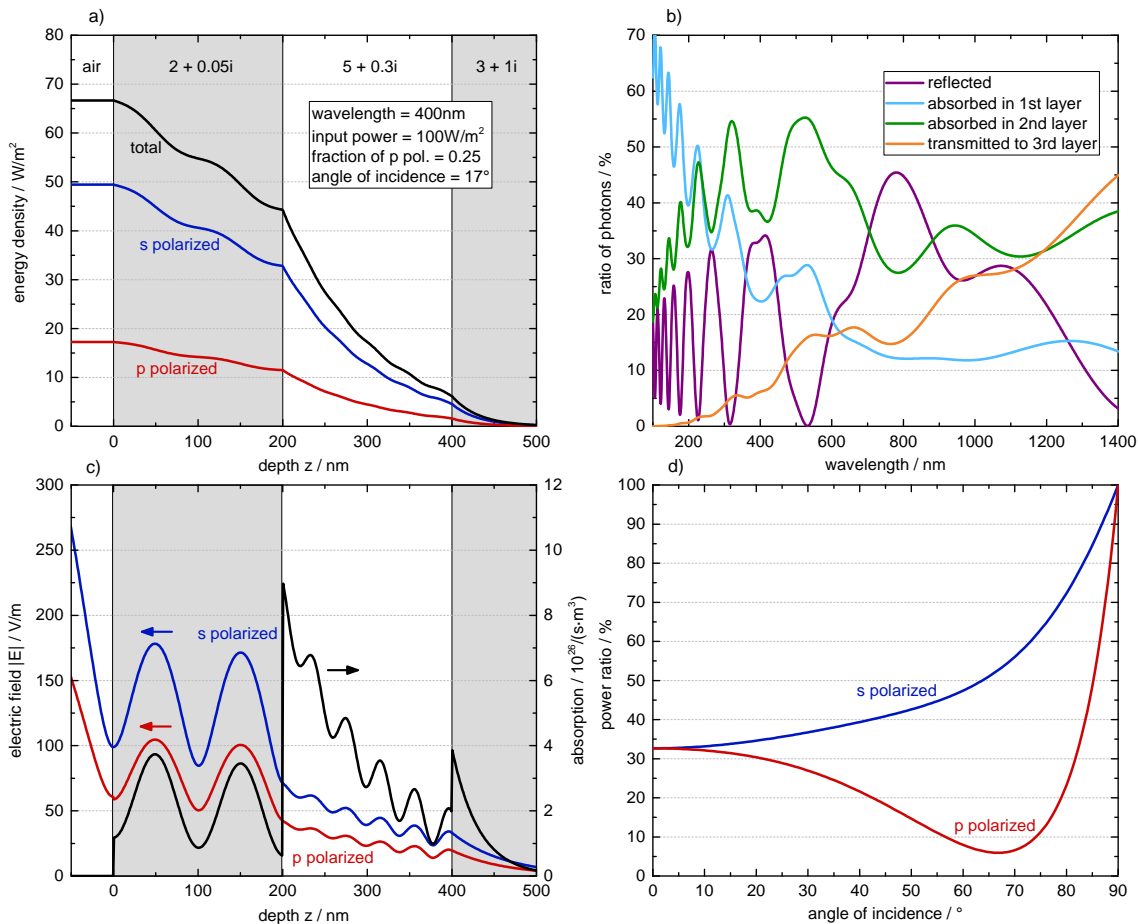


Figure 4.8: Optics with TMM. Plots a) and c) show the energy densities, electric fields, and amount of absorbed photons for a $100 \frac{\text{W}}{\text{m}^2}$ light ray with 400 nm wavelength under an angle of incidence of 17° . In b) the total counts of photons in each layer are plotted as a function of the incident wavelength analog to Figure 4.6 b). Both wavelength-dependent plots show the same basic behavior. However, TMM is also able to determine the reflection without any additional inputs and correctly models thin-film interferences. In plot d) the angle of incidence is varied, resulting in a typical shape for perpendicular and parallel reflection ratios.

exponential decay is visible. However, in the TMM a harmonic modulation due to standing waves inside each layer is observed.

Using the wavelength-dependent photon energy $E_{\text{ph}} = \frac{hc}{\lambda}$, the energy flow can be converted into a flux of photons. This transformation is especially useful in the case of solar cells, where a single photon with sufficiently high energy usually can only generate one single exciton, no matter its total amount of energy, although there are attempts to force photons to generate multiple electron-hole pairs [220]. The amount of locally absorbed photons is given by the sum of the spatial derivations of Equations 4.12 and 4.13. Its oscillating behavior can be seen as the black line in Figure 4.8 c).

To gain the total total amount of absorbed photons within one layer, the integral in Equation (4.4) can be used. Variation in the wavelength in Figure 4.8 b) is based on the same behavior as for the Lambert-Beer approach in Figure 4.6. However, strongly pronounced thin-film interferences can be observed as a function of wavelength. This represents the previously announced combination of exponential decay and interference patterns. In Figure 4.8 d) the reflected ratio of perpendicular and parallel polarized power is plotted over the initial angle of incidence. The perpendicular polarized reflection is progressively increasing with a larger angle of incidence. However, the parallel reflection consists of a distinct dip. The minimum of it is close to Brewster's angle [221] of the first two layers $\Re(\arctan(\frac{\hat{n}_0}{\hat{n}_1})) = \Re(\arctan(\frac{1}{2+0.05i})) \approx 63.4^\circ$. Due to the presence of the underlying layers with different refractive indexes, it is not exactly at this angle and the parallel reflection does not completely vanish.

As for the Lambert-Beer model, the final aim of the TMM is to determine an optical damping factor f_{optics} as necessary to simulate the optical effects in the solar device. In this model it is defined as the proportion of absorbed photons in the absorber layer $n_{\text{ph}}^{\text{abs}}$ with respect to all incoming photons $n_{\text{ph}}^{\text{inc}}$ within the AM1.5G spectrum down to the absorber band gap energy E_{gap} . For each discrete step in the spectrum, a wavelength-dependent TMM calculation is performed in the optical model of this work. All absorbed photons within the absorber layer are summed up and divided by the total amount of incoming photons. Therefore, the optical factor is determined as the ratio $f_{\text{optics}} = n_{\text{ph}}^{\text{abs}}/n_{\text{ph}}^{\text{inc}}$ and is specific to the employed materials and layer thicknesses. The reduction of the spectral information to a simple factor significantly reduces the runtime for subsequent simulations with the same material stack and spectral distribution of the illumination.

4.3 Electrical Model

The final goal of this section is to establish a sufficiently accurate electrical model of thin-film solar cells. Hence, spatial variations of potential distributions, ohmic effects, shunts, and non-linear current generation need to be taken into account. These effects play a crucial role in solar cell modeling, especially for large currents or big resistivities, as has been experimentally measured and outlined elsewhere [104, 105, 115, 222].

4.3.1 Electrical Problem Definition

The main quantities of interest are the lateral voltage and current distributions within the conductive layers of solar cells. A theoretical starting point for deriving an electrical model are Maxwell's equations ^[87] in the differential form in SI convention.

$$\nabla \cdot \underline{D} = \rho \quad (4.14a)$$

$$\nabla \cdot \underline{B} = 0 \quad (4.14b)$$

$$\nabla \times \underline{E} = \frac{\partial \underline{B}}{\partial t} \quad (4.14c)$$

$$\nabla \times \underline{H} = \frac{\partial \underline{D}}{\partial t} + \underline{j} \quad (4.14d)$$

Here, \underline{E} is the electric field, \underline{B} the magnetic flux density, \underline{D} the displacement field, \underline{H} the magnetic field intensity, ρ the charge density, and \underline{j} the current density. Due to the symmetry of second derivatives ^[223], the divergence of the curl of any vector field vanishes. Both inhomogeneous Maxwell's equations can be put into this identity.

$$\begin{aligned} 0 &= \text{div}(\text{rot}(\underline{H})) \\ &= \nabla \cdot (\nabla \times \underline{H}) \\ &\stackrel{(4.14d)}{=} \nabla \cdot \left(\frac{\partial \underline{D}}{\partial t} + \underline{j} \right) \\ &= \frac{\partial}{\partial t} \nabla \cdot \underline{D} + \nabla \cdot \underline{j} \\ \stackrel{(4.14c)}{\Leftrightarrow} 0 &= \frac{\partial \rho}{\partial t} + \nabla \cdot \underline{j} \end{aligned} \quad (4.15)$$

Equation (4.15) is also referred as the continuity equation of electrodynamics. To further proceed, $\frac{\partial \rho}{\partial t} = j_z$ is used as definition for the current density perpendicular to the conductive layers, which is the locally generated photocurrent density generated by the solar cell. Using the local conductivity σ and its integrated inverse resistance R , an equation for the lateral surface current density j_{xy} and electrical potential Φ can be derived.

$$\begin{aligned} 0 &= j_z + \nabla \cdot \underline{j}_{xy} \\ 0 &= \int_V j_z \, dV + \int_V \nabla \cdot \underline{j}_{xy} \, dV \\ 0 &= I_z + \int_{\partial V} \nabla \cdot \underline{j}_{xy} \, d\Omega \\ 0 &= I_z - \int_{\partial V} \sigma \Delta \Phi \, d\Omega \\ 0 &= I_z - \frac{1}{R} \Delta \Phi \\ \Leftrightarrow \Delta \Phi &= RI_z \end{aligned} \quad (4.16)$$

In the first step an integration over a control volume V with its rim area $\partial V = \Omega$ was executed, in the second step Gauss's theorem was used, and in the third step Ohm's law $\underline{j} = \sigma \cdot \underline{E}$ and the relation $\underline{E} = -\nabla \cdot \Phi$ was used. The first summand in Equation (4.16) contains the locally generated photocurrent, whereas the second summand represents the lateral current within the

conductive layers (contacts). The final Equation (4.17) is Poisson's equation for the electrical potential distribution [88]. The main goal for this section is to solve this equation at any given point within the solar cell.

4.3.2 Physics within Finite Elements

Within this subsection, the two summands in Equation (4.16) will be determined. The spatially resolved solution to this equation lays the foundation for the electrical simulation. In order to fulfill the equation at any point of the solar cell, a two-dimensional discretization is used. The used meshing algorithm is described in Section 4.1. In Figure 4.9 a visual representation of the electrical model is given. For better visualization only quadratic finite elements are shown. However, the base area of the elements can have any convex polygonal shape. The current paths within one finite element can be divided into two different sections. One is the current generation (green arrows) and the other ones are the current transport paths on the front (blue arrows) and back side (red arrows). These current paths directly correspond to the two summands in Equation (4.16) and are examined in more detail in the following two paragraphs.

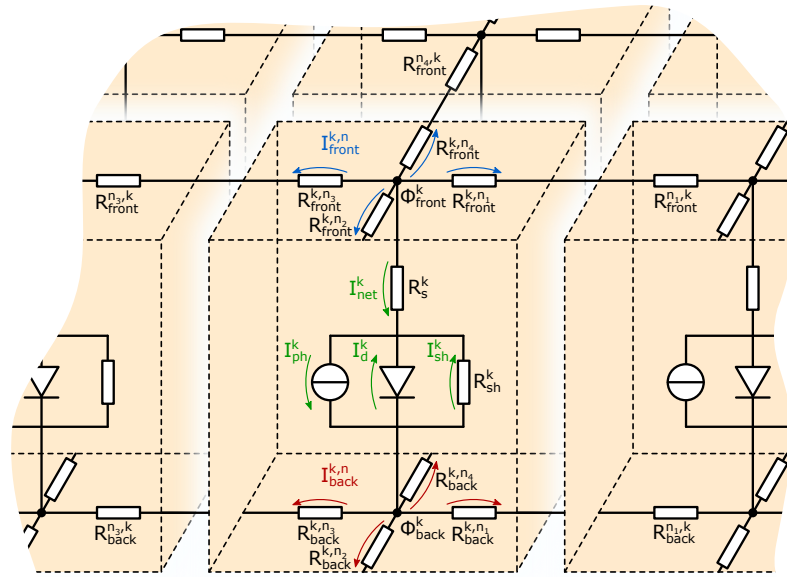


Figure 4.9: The electrical part of the finite element model consists of a single-diode equivalent-circuit model (green arrows) and current paths along resistors on the front (blue arrows) and back side (red arrows) [107]. For clarity reasons only quadratic finite elements are shown.

4.3.2.1 Net Generated Current within Finite Elements

Each finite element k is at a constant temperature T and consists of an electrical front and back potential Φ_{front}^k and Φ_{back}^k . Between those two potentials, a single-diode equivalent circuit is placed, which generates the net current I_{net}^k . Besides a voltage-independent generated photocurrent I_{ph} , it contains two interior resistances for series R_s and shunt R_{sh} , and a diode with a reverse saturation current I_0 and a diode factor n_d^{mat} .

The optical factor f_{optics} defined in Section 4.2 is used in order to reduce the perfectly generated photocurrent I_{ph}' to the actually generated photocurrent $I_{\text{ph}} = f_{\text{optics}} \cdot I_{\text{ph}}'$ by accounting for the optical behavior. With this linear dependence of I_{ph} , a light-dependency of semiconductor properties is neglected. However, a direct device level impact of the overlying optics on the totally generated current is achieved. The total net generated current I_{net}^k across the k -th element is given by the sum of the photocurrent I_{ph}^k and both voltage-dependent diode current I_{d}^k and shunt current I_{sh}^k . Besides the damping of the optical effects on the reduced photocurrent, a strong dependency on the voltage drop $V_k = \Phi_{\text{front}}^k - \Phi_{\text{back}}^k$ can be observed. In general I_{net}^k can be either positive or negative and is determined from Equation (2.21) via the implicit form of the single-diode equivalent-circuit model.

$$\begin{aligned} I_{\text{net}}^k &= -f_{\text{optics}} \cdot I_{\text{ph}} \\ &+ I_0 \cdot \left(\exp \left(\frac{q_e \cdot (\Phi_{\text{front}}^k - \Phi_{\text{back}}^k - I_{\text{net}}^k R_s)}{n_{\text{d}}^{\text{mat}} k_{\text{B}} T} \right) - 1 \right) \\ &+ \frac{\Phi_{\text{front}}^k - \Phi_{\text{back}}^k - I_{\text{net}}^k R_s}{R_{\text{sh}}}, \end{aligned} \quad (4.18)$$

Here k_{B} is the Boltzmann constant and q_e the elementary charge. In order to express the implicit Equation (4.18) as an explicit formulation [112, 224] the Lambert W function [110] is used.

$$\begin{aligned} I_{\text{net}}^k \left(\Phi_{\text{front}}^k, \Phi_{\text{back}}^k \right) &= \frac{n_{\text{d}}^{\text{mat}} k_{\text{B}} T}{q_e R_s} \cdot \mathcal{W}(f_{\text{Lam}}) \\ &+ \frac{1}{R_s + R_{\text{sh}}} \cdot \left(\Phi_{\text{front}}^k - \Phi_{\text{back}}^k - R_{\text{sh}} \cdot (f_{\text{optics}} \cdot I_{\text{ph}} + I_0) \right), \end{aligned} \quad (4.19)$$

where $\mathcal{W}(x)$ is the Lambert W function and

$$\begin{aligned} f_{\text{Lam}} &= \frac{q_e I_0 R_s R_{\text{sh}}}{n_{\text{d}}^{\text{mat}} k_{\text{B}} T \cdot (R_s + R_{\text{sh}})} \\ &\cdot \exp \left(\frac{q_e R_{\text{sh}} \cdot \left(R_s \cdot (f_{\text{optics}} \cdot I_{\text{ph}} + I_0) + \Phi_{\text{front}}^k - \Phi_{\text{back}}^k \right)}{n_{\text{d}}^{\text{mat}} k_{\text{B}} T \cdot (R_s + R_{\text{sh}})} \right). \end{aligned} \quad (4.20)$$

The Lambert W function $\mathcal{W}(x)$ is defined for arguments $x > -\frac{1}{e}$. Finally, it remains to be clarified how the function value \mathcal{L} of the Lambert W function is calculated numerically efficiently. This work uses Halley's method [225] to iteratively approximate its value. As an initial guess the approximation

$$\mathcal{L}_0 = \frac{3}{4} \log(x + 1) \quad (4.21)$$

is used. With the help of the first and second derivatives, the iteration rule

$$\mathcal{L}_{i+1} = \mathcal{L}_i - \frac{\mathcal{L}_i e^{\mathcal{L}_i} - \mathcal{L}_i}{e^{\mathcal{L}_i} (\mathcal{L}_i + 1) - (\mathcal{L}_i + 2) \frac{\mathcal{L}_i e^{\mathcal{L}_i} - \mathcal{L}_i}{2\mathcal{L}_i + 2}} \quad (4.22)$$

can be derived. It is iteratively executed $\lceil \frac{1}{3} \log_{10}(x) \rceil$ times with a minimum of four iterations. This ensures a sufficiently precise accuracy for double precision with a 52 bit long mantissa [111, 226].

An implementation of the calculation of the Lambert W function in C# is shown in the following code block. It computes the first branch of the Lambert W function from real input values.

```

1 double LambertWfunction(double x)
2 {
3     // Lambert W is not defined for values < -exp(-1)
4     if (x < -Math.Exp(-1))
5         throw new Exception("Lambert W function is not defined for " + x);
6
7     // determine number of iterations (empirically found)
8     int maxIterations = Math.Max(4, (int)Math.Ceiling(Math.Log10(x) / 3));
9
10    // set a rough initial guess
11    double w = 3 * Math.Log(x + 1) / 4;
12
13    // Iteratively use Halley's method via Equation (5.9) in R. M. Corless
14    // et al., Advances in Computational Mathematics 5, 329-359 (1996)
15    for (int i = 0; i < maxIterations; i++)
16    {
17        double exp = Math.Exp(w);
18        w = w - (w*exp-x) / (exp * (w+1) - (w+2) * (w*exp-x) / (2*w+2));
19    }
20    return w;
21 }

```

It was written to work efficiently and fast and takes about 132 ns on average for numbers between 0 and 10^8 on a Microsoft Windows 10 machine (Version 10.0.17763 Build 17763) with an Intel i9-9900K processor with 8 physical cores running on 3.60 GHz and a physical RAM of 32 GB.

4.3.2.2 Transport Resistances to Neighbor Elements

As shown in Figure 4.9, every finite element k is electrically connected at the front and back side to each of its neighbors n out of its set of neighbors $\mathcal{N}(k)$. The connecting resistances are split into two separate resistors $R^{k,n}$ and $R^{n,k}$, where the first one belongs to the k -th finite element and the second one to the n -th element. Across these resistances at the front and back side, the currents $I_{\text{front}}^{k,n}$ and $I_{\text{back}}^{k,n}$ can flow from one finite element to a neighboring element. The splitting of the connection resistance into two separate resistors allows to easily implement transitions from non-grid elements to grid elements, as seen in Figure 4.10. Most elements in a meshing domain of a thin-film solar cell are non-grid elements. Hence, only a TCO layer contributes to the conductivity to neighboring elements. However, for grid elements, charge carriers can be guided via the TCO layer or alternatively via a typically much better conducting grid layer. In this work, a parallel circuit of the TCO resistance $R_{\text{TCO}}^{k,n}$ and grid resistance $R_{\text{grid}}^{k,n}$ is assumed.

$$R^{k,n} = \begin{cases} R_{\text{TCO}}^{k,n} & k \text{ is non-grid element} \\ \frac{R_{\text{TCO}}^{k,n} \cdot R_{\text{grid}}^{k,n}}{R_{\text{TCO}}^{k,n} + R_{\text{grid}}^{k,n}} & k \text{ is grid element} \end{cases} \quad (4.23)$$

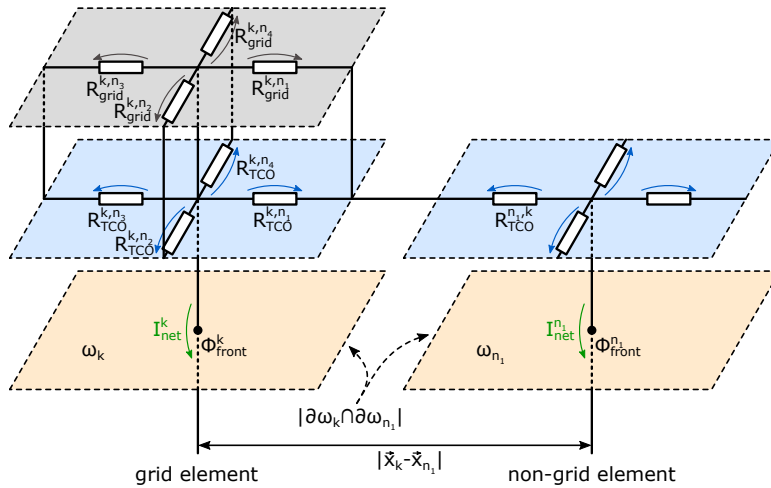


Figure 4.10: For non-grid elements (right hand side) there is only a single TCO resistor connecting the k -th element with the n -th. However, for grid elements (left hand side) the TCO resistor and the grid resistor are put into a parallel circuit. This method assumes no contact resistance between the TCO and grid layers.

This way, no contact resistance between both layers is taken into account. If one wants to take this effect into account, an additional potential is needed on each side of the solar cell, which results in a much longer time to solve the equation system. Although it can be easily implemented [169], it will turn out that it is not needed to model a vast majority of the physically produced cells.

Determination of Finite Element Transport Resistances

The final step to accomplish the determination of the electrical transport resistances is to calculate the single resistors within a finite element of each layer $R_{\text{layer}}^{k,n}$.

Both resistors within the grid and TCO are calculated via

$$R_{\text{layer}}^{k,n} = \rho_{\text{layer}} \cdot \frac{\|\underline{x}_k - \underline{x}_n\|}{2A_{\text{layer}}} \quad (4.24)$$

with the specific resistance ρ_{layer} of the corresponding layer, the cross-section area A_{layer} , and the distance $\|\underline{x}_k - \underline{x}_n\|$ between the k -th and the n -th element. This is geometrically visualized as the orange volume in Figure 4.11. $R^{k,n}$ only reaches to the border of the Voronoi cell. Since this border line is exactly in the middle of the two elements due to the Voronoi construction, the factor $\frac{1}{2}$ is introduced in Equation (4.24). The cross-section area A_{layer} is calculated via the shared border length $|\partial\omega_k \cap \partial\omega_n|$ of the Voronoi boundaries of the k -th and the n -th elements' base areas ω_k and ω_n and the corresponding layer thickness d_{layer} .

$$A_{\text{layer}} = d_{\text{layer}} \cdot |\partial\omega_k \cap \partial\omega_n| \quad (4.25)$$

In Appendix B, it will be demonstrated that this way of calculating the transport resistances is the proper way and represents the correct physical behavior.

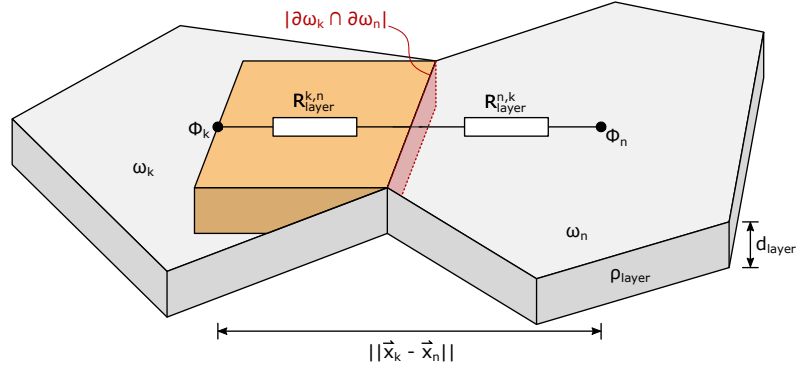


Figure 4.11: The two finite elements k and n share the common border $|\partial\omega_k \cap \partial\omega_n|$. This length together with the layer thickness d_{layer} and the distance between both central mesh points $|\underline{x}_k - \underline{x}_n|$ is used to determine the transport resistance $R_{\text{layer}}^{k,n}$.

4.3.3 Equation System

Once all required principles within a finite element are known, it is at the time to assemble the deduced findings. The aim is to derive a single equation for each electrical potential within a finite element. Therefore, two equations for each element will be determined, one at the front potential Φ_{front}^k and one at the back potential Φ_{back}^k . Since each equation will be linked to the neighboring potential via the current flux, a coupled equation system will be the result.

4.3.3.1 Physical Motivation and Deduction

The process of solving Poisson's Equation (4.17) for each finite element is the basic idea of the electrical simulation. The equation can also be derived via Kirchhoff's current law [227], which states that summing up all currents $\sum_i I_i$ at any node in the circuit equals zero. This law is applied at Φ_{front}^k and Φ_{back}^k in Figure 4.9.

$$0 = \sum_{n \in \mathcal{N}(k)} I_{\text{front}}^{k,n} (\Phi_{\text{front}}^k, \Phi_{\text{front}}^n) + I_{\text{net}}^k (\Phi_{\text{front}}^k, \Phi_{\text{back}}^k) \quad (4.26a)$$

$$0 = \sum_{n \in \mathcal{N}(k)} I_{\text{back}}^{k,n} (\Phi_{\text{back}}^k, \Phi_{\text{back}}^n) - I_{\text{net}}^k (\Phi_{\text{front}}^k, \Phi_{\text{back}}^k) \quad (4.26b)$$

Therefore, all finite elements simultaneously act as current source due to I_{net}^k and as a discretized computation point for the meshing domain. Using Ohm's law and the above derived expressions for the transport currents and generated currents, the final coupled equations for the FEM can be obtained.

$$0 = \sum_{n \in \mathcal{N}(k)} \frac{\Phi_{\text{front}}^k - \Phi_{\text{front}}^n}{R_{\text{front}}^{k,n} + R_{\text{front}}^{n,k}} + I_{\text{net}}^k (\Phi_{\text{front}}^k, \Phi_{\text{back}}^k) \quad (4.27a)$$

$$0 = \sum_{n \in \mathcal{N}(k)} \frac{\Phi_{\text{back}}^k - \Phi_{\text{back}}^n}{R_{\text{back}}^{k,n} + R_{\text{back}}^{n,k}} - I_{\text{net}}^k (\Phi_{\text{front}}^k, \Phi_{\text{back}}^k) \quad (4.27b)$$

As for every equation system, boundary conditions for some elements are needed. Figure 4.1 shows that the cell is operated at the voltage V_{op} . This voltage is applied to one or multiple external cell contacts, both at the front and back side of the solar cell. All finite elements that are connected to the external contact belong to the set $\mathcal{E}_{\text{front}}$ or $\mathcal{E}_{\text{back}}$ and receive the following corresponding boundary conditions.

$$\Phi_{\text{front}}^k = V_{\text{op}} \quad (4.28a)$$

$$\Phi_{\text{back}}^k = 0 \quad (4.28b)$$

However, if a contact resistance $R^{\text{cont},k}$ at the k -th element between the external cell contact and the virtually attached cable is assumed the boundary conditions transform to

$$0 = R_{\text{front}}^{\text{cont},k} \cdot \left(\sum_{n \in \mathcal{N}(k)} \frac{\Phi_{\text{front}}^k - \Phi_{\text{front}}^n}{R_{\text{front}}^{k,n} + R_{\text{front}}^{n,k}} + I_{\text{net}}^k \left(\Phi_{\text{front}}^k, \Phi_{\text{back}}^k \right) \right) + \Phi_{\text{front}}^k - V_{\text{op}} \quad (4.29a)$$

$$0 = R_{\text{back}}^{\text{cont},k} \cdot \left(\sum_{n \in \mathcal{N}(k)} \frac{\Phi_{\text{back}}^k - \Phi_{\text{back}}^n}{R_{\text{back}}^{k,n} + R_{\text{back}}^{n,k}} - I_{\text{net}}^k \left(\Phi_{\text{front}}^k, \Phi_{\text{back}}^k \right) \right) + \Phi_{\text{back}}^k. \quad (4.29b)$$

In this general formulation the case of no contact resistance is included as well.

4.3.3.2 Matrix Formulation of FEM Problem

For several aspects a closed matrix formulation has certain advantages although it seems to be not very transparent at first glance. With the help of the vector of all potentials $\underline{\Phi}$, the vector of all generated currents $\underline{I}_{\text{net}}(\underline{\Phi})$, and the conductivity stiffness matrix \mathbf{G} , Equations (4.26a) and (4.26b) can be rewritten into a single equation.

$$0 = \mathbf{G} \cdot \underline{\Phi} + \underline{I}_{\text{net}}(\underline{\Phi}) \quad (4.30)$$

Since for a meshing domain with N elements, $2N$ electrical potentials have to be considered, the definitions $i' = \lfloor \frac{i}{2} \rfloor$ and $j' = \lfloor \frac{j}{2} \rfloor$ will be used in the following. The vector of all front and back potentials is then given by

$$\underline{\Phi} = \begin{pmatrix} \Phi_{\text{front}}^0 \\ \Phi_{\text{back}}^0 \\ \vdots \\ \Phi_{\text{front}}^N \\ \Phi_{\text{back}}^N \end{pmatrix} \quad (4.31)$$

or equivalently

$$(\underline{\Phi})_i = \begin{cases} \Phi_{\text{front}}^{i'} & i \text{ is even} \\ \Phi_{\text{back}}^{i'} & i \text{ is odd.} \end{cases} \quad (4.32)$$

Further, the vector of generated currents $\underline{I}_{\text{net}}(\Phi)$ within each finite element is defined as

$$(\underline{I}_{\text{net}}(\Phi))_i = \begin{cases} V_{\text{op}} & i \text{ is even} \wedge i' \in \mathcal{E}_{\text{front}} \\ 0 & i \text{ is odd} \wedge i' \in \mathcal{E}_{\text{back}} \\ (-1)^i \cdot I_{\text{net}}^{i'} & \text{else.} \end{cases} \quad (4.33)$$

Here the simplified boundary conditions (4.28a) and (4.28b) have been implemented and the term $(-1)^i$ accounts for the sign in equations (4.26a) and (4.26b). Finally, the conductivity stiffness matrix \mathbf{G} results in

$$(\mathbf{G})_{ij} = \begin{cases} -1 & i \text{ is even} \wedge i' \in \mathcal{E}_{\text{front}} \wedge i = j \\ -\frac{1}{R_{\text{front}}^{i',j'} + R_{\text{front}}^{j',i'}} & i \text{ is even} \wedge i' \notin \mathcal{E}_{\text{front}} \wedge j' \in \mathcal{N}(i') \\ \sum_{j' \in \mathcal{N}(i')} \frac{1}{R_{\text{front}}^{i',j'} + R_{\text{front}}^{j',i'}} & i \text{ is even} \wedge i' \notin \mathcal{E}_{\text{front}} \wedge i = j \\ 0 & i \text{ is odd} \wedge i' \in \mathcal{E}_{\text{back}} \wedge i = j \\ -\frac{1}{R_{\text{back}}^{i',j'} + R_{\text{back}}^{j',i'}} & i \text{ is odd} \wedge i' \notin \mathcal{E}_{\text{back}} \wedge j' \in \mathcal{N}(i') \\ \sum_{j' \in \mathcal{N}(i')} \frac{1}{R_{\text{back}}^{i',j'} + R_{\text{back}}^{j',i'}} & i \text{ is odd} \wedge i' \notin \mathcal{E}_{\text{back}} \wedge i = j \\ 0 & \text{else.} \end{cases} \quad (4.34)$$

Multiplying out Equation (4.30) with the definitions (4.32), (4.33), and (4.34), Equations (4.27a) and (4.27b) can be received, which shows the equality of both formulations.

4.3.4 Simulating the Module Interconnect

As described in Section 2.5, for thin-film solar cells a monolithic module interconnect is often used. To simulate this electrical behavior three new finite elements with different equivalent electrical circuits are introduced. They are shown in Figure 4.12 in green (P1), blue (P2), and pink (P3).

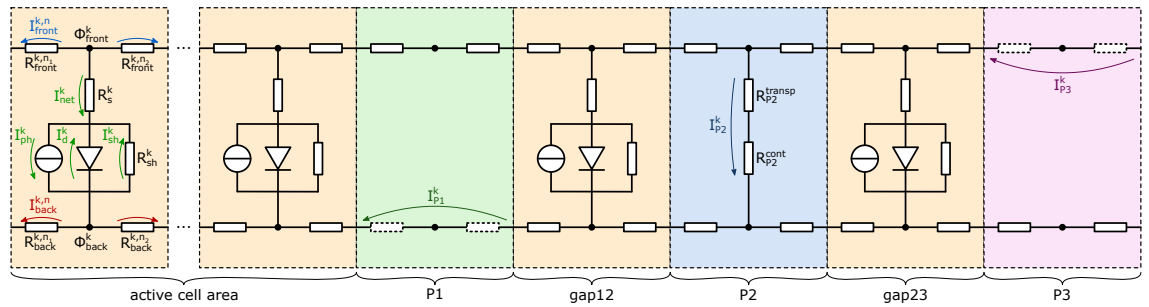


Figure 4.12: One-dimensional model for a monolithic module interconnect as shown in Figure 2.9 [228]. The current I_{P2}^k connects the front of the first cell with the back of the next cell. I_{P1}^k and I_{P3}^k model shunt currents across the trenches.

The equivalent circuitry is described in the following. Finite elements in the regular cell area or within the gaps contain the standard setup as described in Section 4.3.2. However, elements within the P1 and P3 areas lack the current generation term I_{net}^k since there is no operative p-n junction present. Moreover, the back resistances of P1 elements and the front resistances of P3 elements are determined by the conductivity of the absorber layer and the conductivity of air and potential defects like particles, respectively. They therefore have a low conductivity. For the P1 resistances, this is mostly due to the expanded space charge region into the P1 gap^[137]. For elements within a P2 region the horizontally flowing current typically flows from the front to the back side via the TCO-filled P2 gap. This transfer current in the k -th element is named I_{P2}^k and is dominantly dependent on the horizontal transport resistance of the TCO $r_{\text{P2}}^{\text{transp}}$ within the thickness of the absorber layer d_{absorber} and the contact resistance $r_{\text{P2}}^{\text{cont}}$ between the TCO and the back contact layer.

$$I_{\text{P2}}^k \left(\Phi_{\text{front}}^k, \Phi_{\text{back}}^k \right) = \frac{V_k}{R_{\text{P2}}^{\text{transp}} + R_{\text{P2}}^{\text{cont}}} = \frac{\Phi_{\text{front}}^k - \Phi_{\text{back}}^k}{\rho_{\text{P2}}^{\text{transp}} d_{\text{absorber}} \omega_k^{-1} + r_{\text{P2}}^{\text{cont}} \omega_k^{-1}} \quad (4.35)$$

The described arrangement enables to correctly simulate all relevant currents within a monolithic module interconnect, which is mainly given by I_{P2}^k . Moreover, shunt currents across the absorber layer in P1 I_{P1}^k and across the gap in P3 (typically air) I_{P3}^k can be simulated as a loss current. Combined with the Equations (4.27a) and (4.27b), the current I_{P2}^k yield the following coupled equation system.

$$0 = \sum_{n \in \mathcal{N}(k)} \underbrace{\frac{\Phi_{\text{front}}^k - \Phi_{\text{front}}^n}{R_{\text{front}}^{k,n} + R_{\text{front}}^{n,k}}}_{\text{front currents } I_{\text{front}}^{k,n}} + \begin{cases} I_{\text{net}}^k \left(\Phi_{\text{front}}^k, \Phi_{\text{back}}^k \right) & k\text{-th FE is in cell region} \\ 0 & k\text{-th FE is in P1 or P3 region} \\ I_{\text{P2}}^k \left(\Phi_{\text{front}}^k, \Phi_{\text{back}}^k \right) & k\text{-th FE is in P2 region} \end{cases} \quad (4.36)$$

$$0 = \sum_{n \in \mathcal{N}(k)} \underbrace{\frac{\Phi_{\text{back}}^k - \Phi_{\text{back}}^n}{R_{\text{back}}^{k,n} + R_{\text{back}}^{n,k}}}_{\text{back currents } I_{\text{back}}^{k,n}} - \begin{cases} I_{\text{net}}^k \left(\Phi_{\text{front}}^k, \Phi_{\text{back}}^k \right) & k\text{-th FE is in cell region} \\ 0 & k\text{-th FE is in P1 or P3 region} \\ I_{\text{P2}}^k \left(\Phi_{\text{front}}^k, \Phi_{\text{back}}^k \right) & k\text{-th FE is in P2 region} \end{cases} \quad (4.37)$$

Since modules typically span across a large area, techniques of minimizing the required amount of finite elements have to be used. Under the assumption of a sufficiently good homogeneity, periodic boundary conditions can be set in order to decrease the effectively simulated area. Both directions, perpendicular and parallel to the interconnect trenches, will be discussed in the following. Shrinking the simulation area by a reducing factor perpendicular to the module interconnect is a comparably trivial task. The smallest periodic structure needs to be determined, which is mainly given by the grid pattern. The simulation can then be limited to this area. Afterwards, the generated current must be multiplied with the reducing factor. Without any grid, the simulation could even be accomplished by a one-dimensional simulation along the current flow and afterwards extruded into the missing direction.

Decreasing the simulation area in the parallel direction, however, requires a more sophisticated approach. Basically periodic boundary conditions need to be implemented. Using this procedure, only one cell as shown in Figure 4.12 needs to be electrically simulated starting from the regular cell area until the P3 trench. Each finite element at the right edge of a P3 region is allocated to a

corresponding element bordering the cell area on the left side to satisfy periodicity requirements. Within these elements the equations to be solved are given by

$$0 = \Phi_{\text{front}}^{\text{P3}} - \Phi_{\text{front}}^{\text{cell}} - V_{\text{op}} \quad (4.38a)$$

$$0 = \Phi_{\text{back}}^{\text{P3}} - \Phi_{\text{back}}^{\text{cell}} - V_{\text{op}}. \quad (4.38b)$$

This ensures an equally large voltage drop from front to back side, which is needed to set multiple cells together to one module. Simultaneously the transition from a high potential at P3 to a low potential within the cell region is accomplished.

4.3.5 Solving the Non-linear Equation System

All necessary equations that construct the equation system have been physically motivated and deduced in the previous sections. In short, Equations (4.27a) and (4.27b) are used for finite elements within the regular cell area or the interconnect gap areas gap12 and gap23. For modules the current I_{net}^k is replaced with Equation (4.35) within P2 elements and vanishes for P1 and P3 elements. As boundary conditions Equations (4.29a) and (4.29b) are used. Especially due to the diode equation in (4.19) these equations lead to a highly non-linear equation system of N finite elements.

$$\begin{aligned} 0 &= \begin{pmatrix} F_0^{\text{front}}(\Phi_{\text{front}}^0, \Phi_{\text{back}}^0, \{\Phi_{\text{front}}^n | n \in \mathcal{N}(0)\}) \\ F_0^{\text{back}}(\Phi_{\text{front}}^0, \Phi_{\text{back}}^0, \{\Phi_{\text{back}}^n | n \in \mathcal{N}(0)\}) \\ \vdots \\ F_N^{\text{front}}(\Phi_{\text{front}}^N, \Phi_{\text{back}}^N, \{\Phi_{\text{front}}^n | n \in \mathcal{N}(N)\}) \\ F_N^{\text{back}}(\Phi_{\text{front}}^N, \Phi_{\text{back}}^N, \{\Phi_{\text{back}}^n | n \in \mathcal{N}(N)\}) \end{pmatrix} \\ &= \underline{F}(\Phi_{\text{front}}^0, \Phi_{\text{back}}^0, \dots, \Phi_{\text{front}}^N, \Phi_{\text{back}}^N) \\ &= \underline{F}(\Phi) \end{aligned} \quad (4.39)$$

Here $\underline{F}(\Phi)$ is the residual function. The method for solving the equation system is to find the root of $\underline{F}(\Phi)$. Because of the non-linearity, iterative numerical solvers are needed to efficiently solve the system. Within this work the Newton-Raphson method^[113, 229] is used. This root-finding algorithm requires the first derivative of the given residual function with respect to the variables

$\underline{\Phi}$. Since the residual function is a vector, the derivative results in a matrix, which is called the Jacobian matrix $\mathbf{J}_{\underline{F}}(\underline{\Phi})$ of the residual $\underline{F}(\underline{\Phi})$.

$$\mathbf{J}_{\underline{F}}(\underline{\Phi}) := \text{grad}_{\underline{\Phi}} \underline{F}(\underline{\Phi}) = \begin{pmatrix} \frac{\partial F_0^{\text{front}}}{\partial \Phi_{\text{front}}^0} & \frac{\partial F_0^{\text{front}}}{\partial \Phi_{\text{back}}^0} & \cdots & \frac{\partial F_0^{\text{front}}}{\partial \Phi_{\text{front}}^N} & \frac{\partial F_0^{\text{front}}}{\partial \Phi_{\text{back}}^N} \\ \frac{\partial F_0^{\text{back}}}{\partial \Phi_{\text{front}}^0} & \frac{\partial F_0^{\text{back}}}{\partial \Phi_{\text{back}}^0} & \cdots & \frac{\partial F_0^{\text{back}}}{\partial \Phi_{\text{front}}^N} & \frac{\partial F_0^{\text{back}}}{\partial \Phi_{\text{back}}^N} \\ \vdots & \vdots & \ddots & \vdots & \vdots \\ \frac{\partial F_N^{\text{front}}}{\partial \Phi_{\text{front}}^0} & \frac{\partial F_N^{\text{front}}}{\partial \Phi_{\text{back}}^0} & \cdots & \frac{\partial F_N^{\text{front}}}{\partial \Phi_{\text{front}}^N} & \frac{\partial F_N^{\text{front}}}{\partial \Phi_{\text{back}}^N} \\ \frac{\partial F_N^{\text{back}}}{\partial \Phi_{\text{front}}^0} & \frac{\partial F_N^{\text{back}}}{\partial \Phi_{\text{back}}^0} & \cdots & \frac{\partial F_N^{\text{back}}}{\partial \Phi_{\text{front}}^N} & \frac{\partial F_N^{\text{back}}}{\partial \Phi_{\text{back}}^N} \end{pmatrix} \quad (4.40)$$

Using $\mathbf{J}_{\underline{F}}(\underline{\Phi})$, the residual $\underline{F}(\underline{\Phi})$ can be linearly approximated with a first order Taylor series ^[230] at a given input vector $\underline{\Phi}_i$.

$$\underline{F}(\underline{\Phi}) = \mathbf{J}_{\underline{F}}(\underline{\Phi}_i) \cdot \underline{\Phi} + \underline{F}(\underline{\Phi}_i) - \mathbf{J}_{\underline{F}}(\underline{\Phi}_i) \cdot \underline{\Phi}_i \quad (4.41)$$

Since the root of $\underline{F}(\underline{\Phi})$ is of interest, it is set to zero and the equation can be solved for $\underline{\Phi}$, which is the iteratively next approximation $\underline{\Phi}_{i+1}$ for the actual root.

$$\underline{\Phi}_{i+1} = \underline{\Phi}_i - \mathbf{J}_{\underline{F}}^{-1}(\underline{\Phi}_i) \cdot \underline{F}(\underline{\Phi}_i) \quad (4.42)$$

Using this iteration instruction, the root of $\underline{F}(\underline{\Phi})$ can be approximated. However, since inverses of large matrices are numerically time-consuming, the linear equation system

$$\mathbf{J}_{\underline{F}}(\underline{\Phi}_i) \cdot \Delta \underline{\Phi} = \underline{F}(\underline{\Phi}_i) \quad (4.43)$$

is solved instead, where the difference vector $\Delta \underline{\Phi}$ is given by $\underline{\Phi}_i - \underline{\Phi}_{i+1}$. To efficiently solve this kind of large equation system, biconjugate gradient methods ^[231] with an incomplete lower–upper (LU) decomposition ^[232] as preconditioner are used within this work.

The only issue that remains to be addressed, is the initial guess $\underline{\Phi}_0$. Because of the expected electrical potentials within a monolithically interconnected module, the following initial guesses for front and back potentials are used.

$$\Phi_{\text{front,init}}^k = \begin{cases} V_{\text{op}} & k\text{-th element in cell, P1, gap12, P2, or gap23 region} \\ 2V_{\text{op}} & k\text{-th element in P3 region} \end{cases} \quad (4.44a)$$

$$\Phi_{\text{back,init}}^k = \begin{cases} -\frac{V_{\text{op}}}{10} & k\text{-th element in cell or P1 region} \\ V_{\text{op}} - \frac{V_{\text{op}}}{10} & k\text{-th element in gap12, P2, gap23, or P3 region} \end{cases} \quad (4.44b)$$

The empirical term $-\frac{V_{\text{op}}}{10}$ gives the simulation more numerical stability, because it avoids zeros within $\underline{\Phi}$, which often leads to instabilities. Finally the solution vector $\underline{\Phi}$ and hence, every front and back potential Φ_{front}^k and Φ_{back}^k can be calculated. From this vector any other property of the solar cell can be derived. These applications will be the topic of the next section.

4.4 Resulting Characteristics of the Digital Model

Having calculated the vector $\underline{\Phi}$ of all front and back potentials within the solar device, all other characteristics including potential and current distributions, I–V curves, and PCEs can be deduced. These applications will be the topic of this section.

4.4.1 Spatially Resolved Potential and Current Distributions

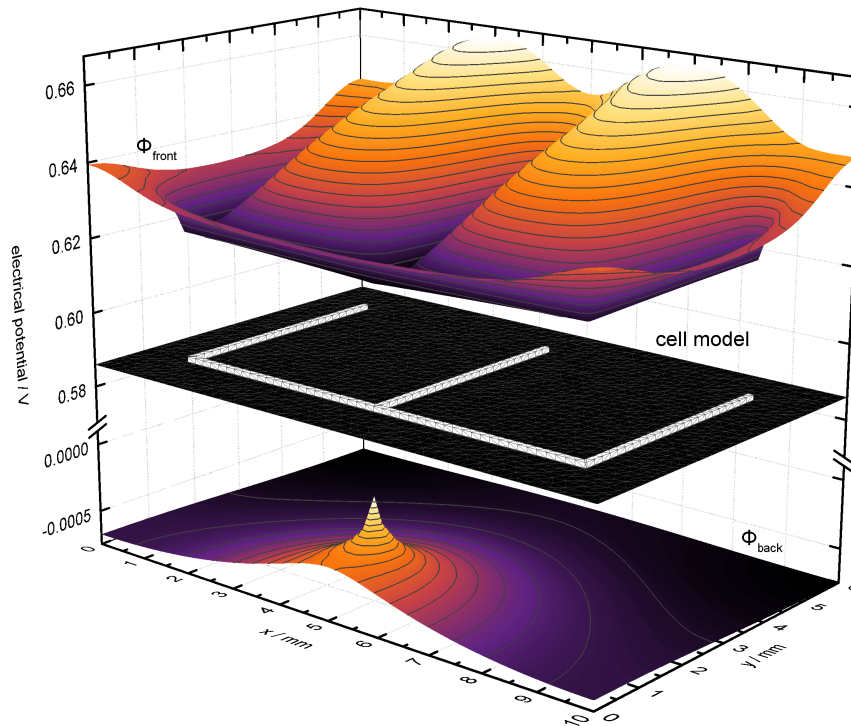


Figure 4.13: Back and front potentials within a solar cell. The external cell contact is located in the bottom center of the white grid stripe. Starting from this point, the back potential decreases. The front potential however is flat along the grid pattern but increases with rising distance to the grid as well.

All front and back potentials can be spatially plotted to receive an electrical potential distribution across the cell for the physical equilibrium state. This has been plotted in Figure 4.13 in combination with a visual model of the cell. Black areas on the model mark active cell regions, whereas the white stripes show a grid pattern on the front side. In this example the back side is covered by a metallic contact layer resulting in a comparably flat parabolic potential distribution. The front potential stays flat along the well conducting grid lines, but increases rapidly with increasing distance to the grid within the TCO area. The operating voltage of the cell is $V_{op} = 0.618$ V. However, the local voltage drop for most finite elements is due to the increasing voltage distribution larger than V_{op} . A histogram of the internal voltage drops of all finite elements is shown in Figure 4.14. A accumulation just above V_{op} can be seen. These are mainly elements located on the grid pattern. Most of the elements experience a larger internal voltage drop up to 0.04 V. This results in an around 10% lower net generated current I_{net}^k within these elements (black line in Figure 4.14). Spatially resolved intra-device voltage distributions have been experimentally measured [104, 105] and their parabolic voltage increase is in accordance with the shown simulated voltage behavior.

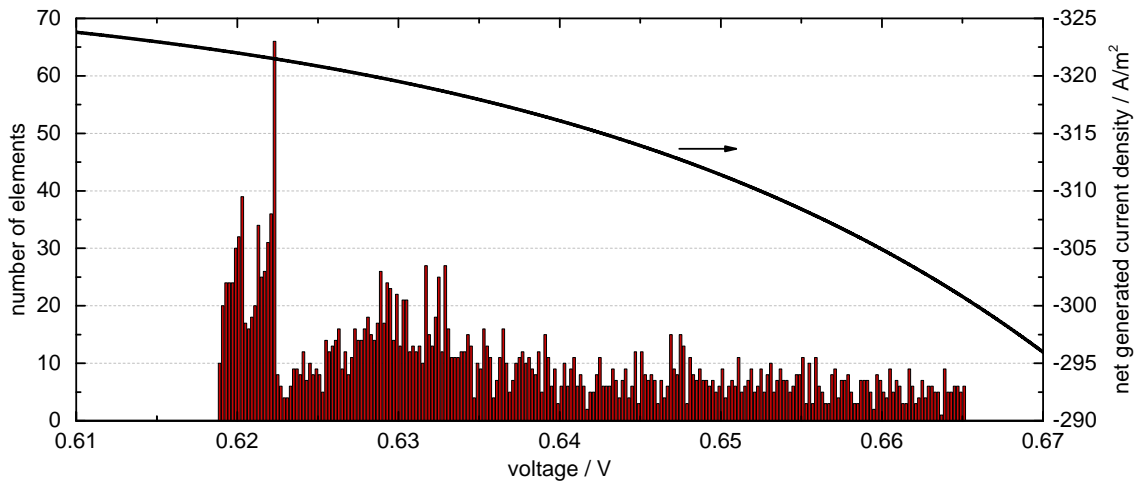


Figure 4.14: Histogram of the internal voltage drop of all finite elements of the cell in Figure 4.13. The lowest occurring voltage drop is at 0.618 V, which is the operating voltage V_{op} . All other elements consist of a higher voltage drop producing a lower amount of current as indicated by the black line.

According to Equations (4.29a) and (4.29b), the transport currents between two finite elements can be calculated with the help of the given potentials and resistances. For a better visualization, all currents of an element are vectorially summed up yielding a single resulting current direction and magnitude for each element. This current flux distribution on the front side is shown in Figure 4.15 as a vector plot in black. It is noticeable that all arrows point perpendicular to the contour lines of the voltage distribution. This feature is in accordance with the principle of the path of least resistance. Therefore, most of the current first flows to the closest metallization grid line. Taking advantage of the lower sheet resistance, the current direction then follows the grid structure until reaching the external cell contact.

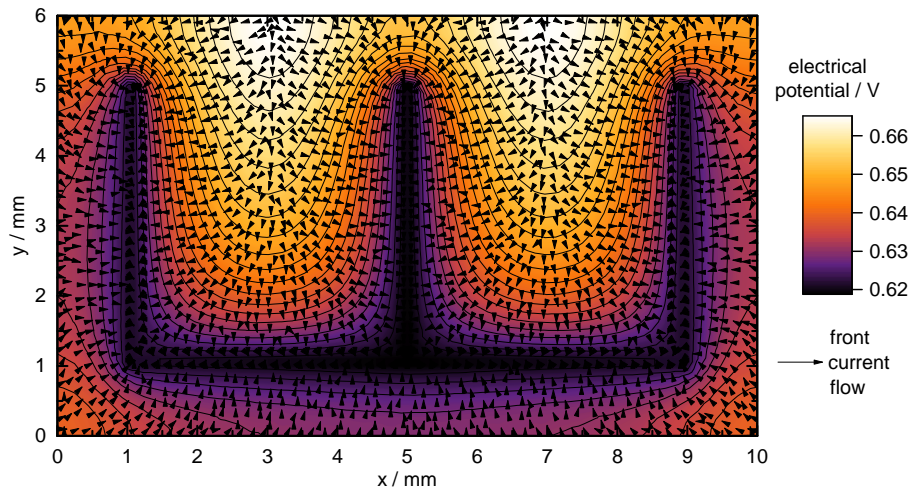


Figure 4.15: Current distribution of the cell in Figure 4.13. The arrows represent the direction of the front current, which is always perpendicular to the electrical potential. As the potential on the grid structure is comparably low, the grid lines act as highways for the electrical current.

So far only electrical quantities within single cells have been investigated. With Figure 4.16, the attention will now be focused on the spatially resolved voltage distribution of a periodic module element. On the bottom side, all defined regions are color-marked to identify the type of each

spatial area. The left hand side is a regular cell region as it was described in the text above. The right hand side includes the module interconnect, which consists of the three trenches P1, P2 and P3 and spacing regions gap12 and gap23 in between. Periodic boundary conditions from Equations (4.38a) and (4.38b) have been applied to this setup. Within the cell area, the same parabolic behavior of the electrical potentials as in a standard cell can be observed. Along the P1 trench however the back contact is interrupted, resulting in a strong increase of the back potential towards the front potential. Within the entire P2 region the front and back sides of the elements are only separated by the transport R_{P2}^{transp} and contact resistance R_{P2}^{cont} according to Equation (4.35). Since these resistances are typically comparably low, both potentials nearly touch each other. Most of the current is delivered from the back to the front side in this region. While the back potential stays on roughly the same value across the P3 trench, the front potential drastically increases due to the potential of the next following cell, as required by the periodic boundary conditions.

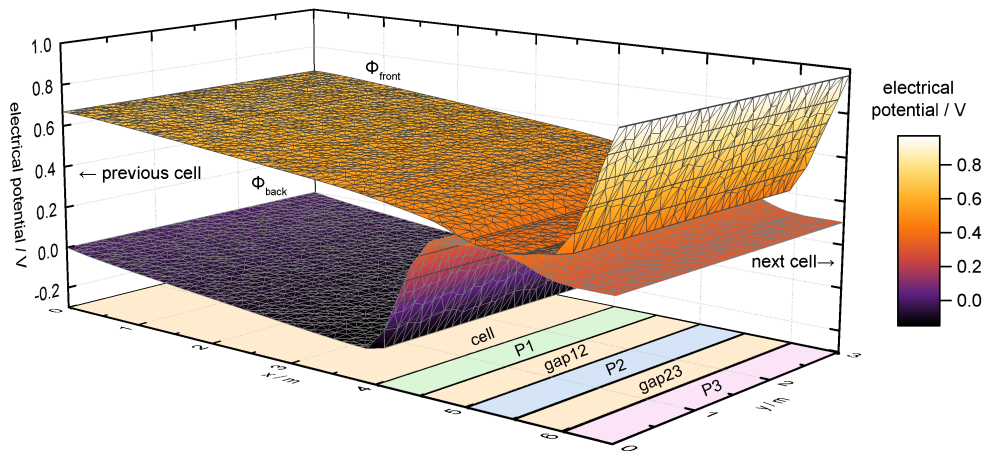


Figure 4.16: Back and front potentials within a periodic element of a solar module. A prominent feature is the presence of nearly touching front and back potentials within the P2 region. Moreover, across P1 and P3 the potentials have a strong slope due to the periodic boundary conditions.

4.4.2 Opto-electronic Properties of the Solar Device

The actual performance of solar cells and modules is determined by the finally produced electrical power. In this section all opto-electronic characteristics will be derived from the potential and current distributions. These might be the external characteristic I–V curve, the voltage-dependent power, or the total PCE.

4.4.2.1 Total Current and Power of the Solar Device

The key elements for all electric analyses are the operating voltage V_{op} and produced current I_{out} at the device. The voltage is already known as it is a key part of the boundary conditions, regardless of whether the cell boundary conditions (4.29a) and (4.29b) or module conditions (4.38a) and (4.38b) are considered. However, the corresponding totally generated current needs to be determined

from the current distribution. For cells it can be easily calculated as the sum over all individually generated currents within all finite elements from the set of all elements \mathcal{K} .

$$I_{\text{out}}(V_{\text{op}}) = \sum_{k \in \mathcal{K}} I_{\text{net}}^k \quad (4.45)$$

For modules however the above equation does not hold since shunt currents across P1 and P3 feed back charge into the cell. This mechanism wastes the produced power because the current is not guided towards the external contact. A more sophisticated approach for the totally generated power within modules is the sum over all incoming currents at all external front contact elements $\mathcal{E}_{\text{front}}$.

$$I_{\text{out}}(V_{\text{op}}) = \sum_{k \in \mathcal{E}_{\text{front}}} \left(I_{\text{net}}^k - \sum_{n \in \mathcal{N}(k)} I_{\text{front}}^{k,n} \right) \quad (4.46)$$

Since the contact element itself can produce current as well, the term $I_{\text{front}}^{k,n}$ is added to the sum. Equation (4.46) is valid for both modules and cells, which is why it will be used throughout this entire work.

4.4.2.2 I–V Characteristic of the Solar Device

As an I–V curve reveals most of a solar device’s characteristic information, a way of obtaining these curves needs to be implemented in the software. Basically the operating voltage V_{op} within the boundary conditions of the simulation is varied and the corresponding generated current $I_{\text{out}}(V_{\text{op}})$ is plotted as a function of V_{op} . This can be seen as black line in Figure 4.17 for the cell introduced in Figure 4.13. For comparison the input I–V characteristic of the internal semiconductor as would be obtained from a drift-diffusion simulation is shown in gray. The calculated cell characteristics indicate the effects of the contacts. A decrease of the short-circuit current due to optical effects and a FF decrease due to ohmic losses can be observed. In summary, the simulation presented in this section generates a real measurable I–V curve from a semiconductor characteristic curve. Both red lines are the product of current and voltage leading to the effectively produced power. Since the produced current has a negative sign, the produced power is negative as well. The voltage at the minimum of the curve is called maximum power voltage $V_{\text{op}}^{\text{MPP}}$. A distinct difference of the $V_{\text{op}}^{\text{MPP}}$ of both curves is clearly visible. This difference is mainly due to electrical cell losses and will be addressed in Section 6.2.7. How to find $V_{\text{op}}^{\text{MPP}}$ will be the topic of the next paragraph.

4.4.2.3 MPP Tracking and Power Conversion Efficiency of the Device

To apply the appropriate voltage $V_{\text{op}}^{\text{MPP}}$ in order to simulate the device at its MPP, a gradient free optimization method is needed. Within this work, a one-dimensional version of the downhill simplex algorithm^[233] is used with the optimization function $I_{\text{out}}(V_{\text{op}})$, the corresponding variable V_{op} , and the empirical initial guess $V_{\text{op}} = \frac{19}{20} V_{\text{oc}}$. The produced power $P_{\text{out}}^{\text{MPP}}$ at the MPP is determined via

$$P_{\text{out}}^{\text{MPP}} = V_{\text{op}}^{\text{MPP}} \cdot I_{\text{out}}^{\text{MPP}}. \quad (4.47)$$

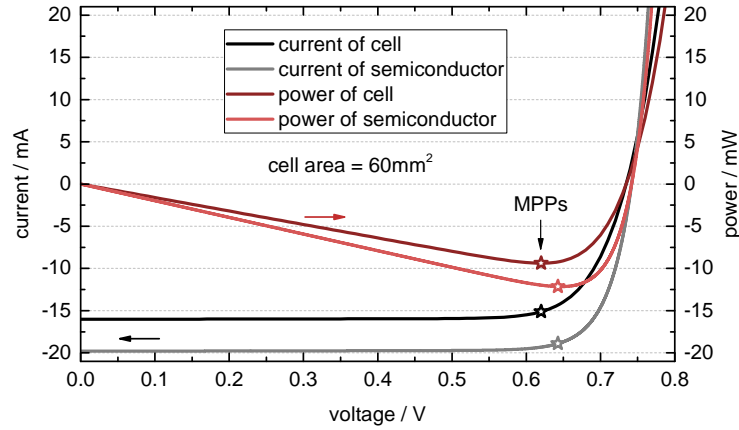


Figure 4.17: Simulated I–V curve of the cell in Figure 4.13. In gray the initial I–V curve of the semiconductor is plotted, which is used as an input for the simulation. I_{sc} and FF losses can be seen in the cell characteristic. The red curves represent the produced power.

To receive a device efficiency, the optical input power P_{in} needs to be determined via the integral over the spectral irradiance $s(\lambda)$ over the entire input spectrum. Finally, the PCE is given as the fraction of both power calculations.

$$\text{PCE} = \frac{P_{out}^{MPP}}{P_{in}} = \frac{V_{op}^{MPP} \cdot I_{out}^{MPP}(V_{op})}{\int_{\mathbb{R}^+} s(\lambda) d\lambda} \quad (4.48)$$

4.5 Fitting Experimental Data

The methodology of this chapter allows to simulate I–V data for a given voltage and therefore at arbitrary, discrete points. As for experimentally created data, simulated data also need to be processed by regression within the single-diode equivalent-circuit model in order to further analyze it. However, a fitting procedure with highly non-linear input data is very sensitive to the fitting parameters. Moreover, fitting characteristic I–V curves of solar devices suffer from mutual influence of the fitting parameters and their non-uniqueness [234]. Therefore, for traditional fitting procedures, a sophisticated initial guess is required [235]. In the past years, fitting oblique asymptotes [236], artificial neural networks [237, 238], generic algorithms [239], or particle swarm approaches [240] have been used for this task, showing the complexity of extracting diode parameters from experimental IV data.

Due to the addressed non-linearity and the fact that the fitting parameters can differ in several orders of magnitude, a numerically robust algorithm needs to be applied [111]. This short procedure explains how data is fitted within this work and is subdivided into two sections. First, an initial guess for the start values of the fitting parameters is calculated and afterwards the actual fitting algorithm is performed. The initial guess for the fitting algorithm is obtained by the following procedure.

1. In order to smooth the data and not be sensitive to outlier data and noise, a cubic Savitsky-Golay filter [241] with a window size of 9 is applied to the experimental data. Moreover, to put the data in the appropriate quadrant, the current values are eventually multiplied by (-1) .

2. A rough estimation for the MPP is given as the discrete data point with the maximum power calculated via $P_i = V_i \cdot I_i$.
3. From the last data point with a negative current and the first data point with a positive current, the open-circuit voltage V_{oc} is estimated by linear interpolation. In case of only negative currents it is calculated via $V_{oc} = 1.2 \cdot V_{MPP}$.
4. The diode ideality factor is calculated via $n_d = 2 \cdot \frac{V_{oc}}{V_{olt}}$.
5. A linear fit with all data points with a voltage below 20% of V_{oc} is performed. Its inverse slope is taken as the shunting resistance R_{sh} and the y-intercept as the photocurrent I_{ph} .
6. The five data points with the largest voltage are fitted linearly. The inverse slope of the regression is taken as the initial guess for the series resistance R_s .
7. As a last step, the reverse saturation current is calculated via the diode equation (4.18) at the voltage $V = V_{oc}$ and hence $I(V_{oc}) = 0$ via the term $I_0 = \frac{I_{ph} - V_{oc}/R_{sh}}{\exp(q_e V_{oc}/(n_d k_B T)) - 1}$.

After calculating start values for all five fitting parameters, a Levenberg–Marquardt algorithm [242, 243] is used in order to perform a regression to all data points. This algorithm requires a gradient and therefore partial derivations with respect to all 5 fitting parameters. They can be calculated via the Lambert W function. The initial guesses for the photocurrent and the shunt resistance are typically rather precise. Therefore, in a first run, only I_0 , n_d , and R_s are fitted. Although the achieved fit usually matches the data points very well after this run, a second Levenberg–Marquardt run is executed with all five fitting parameters. An executable version of this fitting algorithm can be found under https://github.com/Pixel-95/SolarCell_DiodeModel_Fitting.

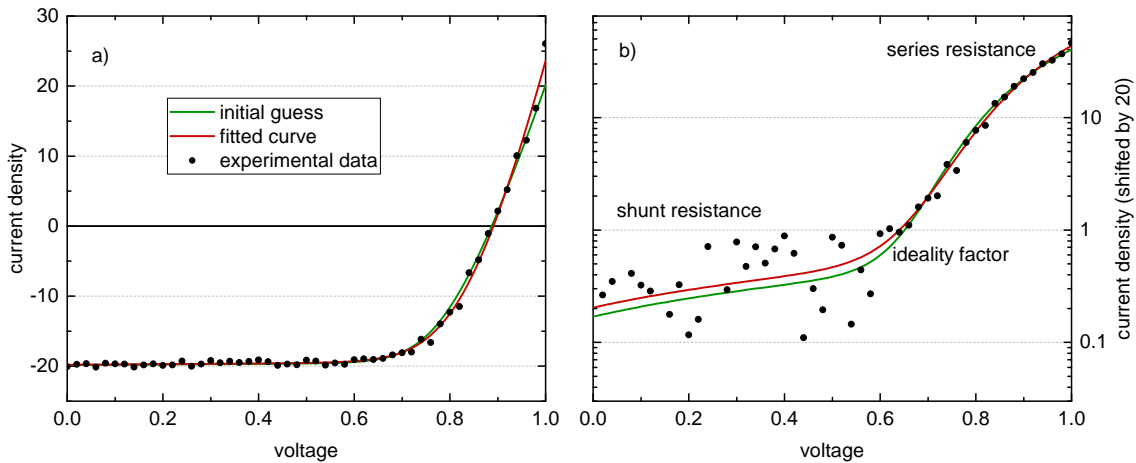


Figure 4.18: Example I–V curves for fitting. Graph a) shows a linear plot, while graph b) has the same data but semi-logarithmic axis. In different regions of the I–V curve, different fitting parameters dominate the behavior of the curve.

An example of this procedure with arbitrary units can be seen in Figure 4.18. Graph a) shows a linear plot, while graph b) shows the same data in a semi-logarithmic plot. The green lines represent the initial guess of the I–V curve, as described above. Afterwards, the Levenberg–Marquardt algorithm is executed, which has the red line as a result. Within the semi-logarithmic plot, three distinct regions can be detected. In each of them, one fitting parameter is dominant and significantly influences the behavior of the curve. In the lower region the shunt resistance is dominant, at the kink the ideality factor is the prevalent parameter and on the top part the series resistance determines the slope of the curve.

Another difficulty in the extraction of single-diode equivalent-circuit model parameters (also known as diode parameters) is their mutual dependency on each other. For example, changes in j_0 or n_d have virtually the same effect on the I–V curve within a certain range. This yields a range of almost equally suitable parameter sets. Figure 4.19 shows the color-coded reciprocal sum of all squared residuals χ^2 with respect to fitted data points. On the dark green diagonal path through the plot, the regression curve fits almost equally well although j_0 varies within several orders of magnitude. Fitted diode parameters should therefore be handled with care, since a mathematical optimum of the regression is not necessarily equivalent to physical reality. The resulting solar cell parameters V_{oc} , j_{sc} , and FF however do not strongly depend on this uncertainty of the fit and therefore, should be used as comparative parameters.

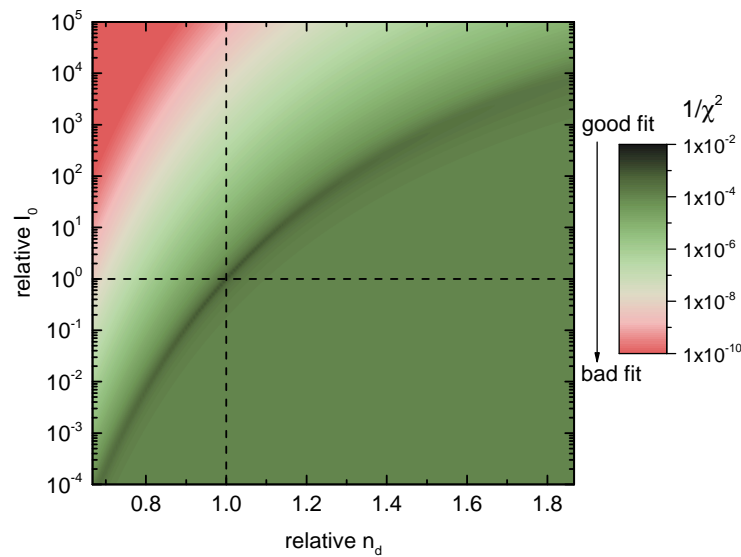


Figure 4.19: Quality of a fit to the single-diode equivalent-circuit model. The color code represents the reciprocal sum of all squared residuals with respect to fitted data points. As indicated by the dark green area, multiple fitting parameter combinations are mathematically suitable. Thus, the optimum of this function is only an approximation to the correct physical equation.

4.6 Simulating Day Yield for a Solar Device

So far, this chapter has explained how power outputs and efficiencies of solar devices can be calculated by simulation. However, in application the value of interest is the daily or yearly yield instead of a laboratory efficiency. This section gives a brief explanation of a method for calculating the daily yield from the PCE of the cell and the meteorological environment data.

4.6.1 Calculating the Solar Position

To be capable of forecast simulations, an algorithm for predicting the solar position in the terrestrial sky is needed. Knowing the azimuth angle α and the elevation angle θ , the two relevant optical features can be implemented. On the one hand, this is the additional atmospheric scattering due to the enlarged path through the atmosphere and on the other hand, the effect of a tilted angle of incidence relative to the mounted angle of the solar module can be given as an input into the

optical model. Only the level of cloud covering during the day needs to be assumed or fed into the simulation. Effects of a changing temperature due to different irradiances mainly affect the module behavior on the semiconductor level and are therefore implemented at the input side for this simulation via a drift-diffusion model.

Many algorithms have been published to determine the solar position of a given location on earth with its latitude ξ and longitude ζ at the local day time t [244, 245, 246, 247]. This work uses a simple yet effective and time-efficient method of calculating the Sun's angular position in the sky [248, 249]. The error of the finally calculated solar angles are smaller than 0.01° within the years 1950 to 2050 [250], which is by far of sufficient accuracy for the yield algorithm in this work. In this algorithm the two main auxiliary variables are the hour angle of given position $\tau(\zeta, t)$ and the Sun's declination angle

$$\delta = \arcsin(\sin(\varepsilon) \sin(\Lambda)), \quad (4.49)$$

where ε is the axial tilt of the earth with respect to the ecliptic plane, also called obliquity of ecliptic and Λ is the ecliptic longitude of the Sun and can be obtained from the equation of the center of the earth around the Sun. Using these two angles and the geographical latitude ξ , the two spherical angles of the Sun's position can be calculated. The azimuth angle α is determined via

$$\alpha = \arctan\left(\frac{\sin(\tau(\zeta, t))}{\cos(\tau(\zeta, t)) \sin(\xi) - \tan(\delta) \cos(\xi)}\right) \quad (4.50)$$

and the actual elevation angle θ_0 is given by

$$\theta_0 = \arcsin(\cos(\delta) \cos(\xi) \cos(\tau(\zeta, t)) + \sin(\delta) \sin(\xi)). \quad (4.51)$$

Due to the effect of refraction within the terrestrial atmosphere, the elevation of the sun is optically seen at a different angle. This effect can be corrected by an approximation, revealing the optically visible elevation angle θ .

$$\theta = \theta_0 + \frac{1.02}{60 \tan\left(\theta_0 + \frac{10.3}{\theta_0 + 5.11}\right)} \quad (4.52)$$

Using the above described algorithm the solar position can be calculated at any given location on earth at any point in time, which can be used to create yearly sun path diagrams. Such a diagram is shown exemplarily in Figure 4.20 for the German city Munich in a Cartesian coordinate system.

4.6.2 Daily Power Integration of the Solar Device

To get the generated power over the course of a day, the momentarily produced power P has to be converted into a daily yield. For this purpose, all daytime hours from sunrise to sunset are split into smaller time steps Δt_i , typically one or five minutes. For each time step, a FEM is executed under the given external conditions like illumination intensity and device temperature, which results in the generated power P_i . Finally, the entirely produced energy E_{day} is calculated as the integral

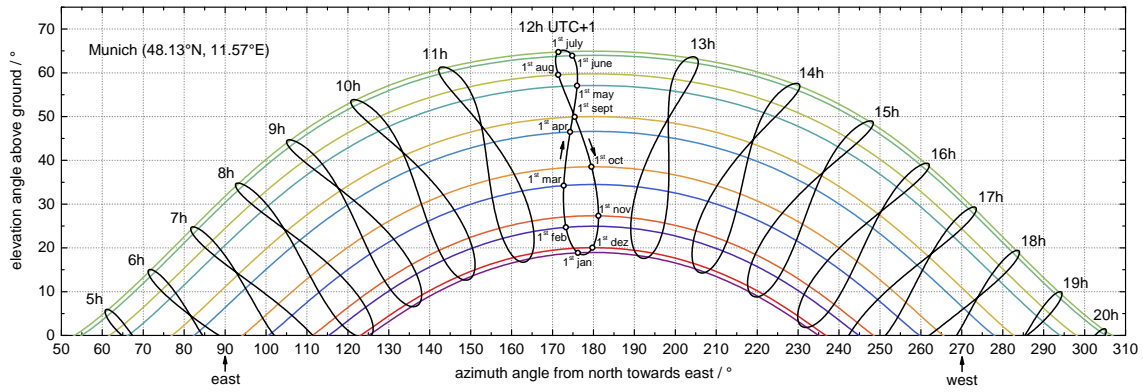


Figure 4.20: Sun path diagram of Munich. Using the geographical latitude ξ and longitude ζ this diagram can be created via varying the local day time within the algorithm described in the main text.

over the momentary power. This integral can be approximated by the finite summation of all time steps i .

$$E_{\text{day}} = \int_{t_{\text{rise}}}^{t_{\text{set}}} P dt \approx \sum_i P_i \cdot \Delta t_i \quad (4.53)$$

4.6.3 Yearly Power Integration of the Solar Device

In principle, for the generated power within the time of one year, the same procedure as in the daily integration could be used. However, due to the long time interval and the therefore many discrete time steps this method would exceed any reasonable runtime to calculate. Therefore, more efficient methods need to be implemented. One way is to process yearly meteorological data upfront. Yearly data within this thesis was gathered from typical meteorological year (TMY) data averaged from 2005 to 2020 from the PVGIS-ERA5 data set^[251] at one hour time steps. This dataset also includes typical atmospheric effects like cloudcover for the given location. The around 140000 individual data points are sorted into bins i according to their illumination intensity P_i^{in} , typically of the size of 10 W/m^2 . For each bin, a FEM simulation is performed and the calculated momentary power is multiplied with the amount of hours h_i under this illumination. Afterwards, each energy within each bin is summed up to receive the entire yearly yield.

$$E_{\text{year}} = \sum_i h_i \cdot P_i^{\text{in}} \quad (4.54)$$

Using this methodology, simulations for equal or similar external conditions can be condensed into one calculation instead of calculating each of them apart from each other.



Answering this Chapter's Guiding Scientific Question

How can characteristic parameters of solar devices be optically and electrically modeled by numerical simulations?

To apply numerical methods on solar devices, a spatial discretization needs to be applied, which divides the entire device into multiple small finite elements. This makes the spatial differential equations inside the semiconductor layer stack solvable for numerical calculations. Due to the complex physics within solar devices, multiple physical models need to be linked in order to receive a holistic model of all physical effects. Incident light rays obey the Fresnel equations and result in typical internal thin-film interferences, which can be modeled by a modified transfer-matrix method. The subsequent generation of electron-hole pairs and their collection is well described by an external drift-diffusion model. Finally, to account for the lateral electrical transport of the charge carriers and their resistive collection losses, a Poisson's equation solver is appropriate to use. Applying discrete voltages to the solar device model, the resulting I-V data can be used to fit solar-module parameters. All of the above mentioned simulation methods are implemented into a simulation platform that is briefly introduced in Appendix A.

5

Checking for Validity – Verification of the Digital Device Model

In the previous chapter, this work's methodology of simulating thin-film solar devices was explained. The focus of this chapter is the implementation and verification of the developed simulation techniques. Electrical and optical experimental data needs to be measured and used as input for the model. Moreover, a procedure called reverse engineering fitting (REF) is introduced, which calculates backwards from the external cell I–V curve to the internal semiconductor I–V curve. Having established a digital twin of the solar device enables to forecast I–V curves and other characteristics. Finally, the relevance of a sophisticated FEM is justified with experiments.

This Chapter's Guiding Scientific Question

Which input parameters are necessary for the digital model and how precise are the numerical results of the simulation models in comparison with experimental verification data?

5.1 Finding the Input Parameters – Gathering Data for Simulation Model

This section deals with the acquisition of experimental input data for the simulation. Predominantly, four basic properties need to be known. Besides the geometry of the device, the electrical resistivity data, the optical refractive data, and the internal semiconductor I–V characteristic on the material level as defined in Section 2.3.4 is needed. All input information is addressed in the following.

5.1.1 Geometrical Data

The spatial data of the solar device in principle is a three dimensional geometry. Since the lateral expanse of solar devices is typically much larger than the thickness (even for wafer-based devices), the geometrical data can be split into two different subgroups. The first one is the lateral geometrical setup containing the physical device dimensions, all regions with grid on top, and for modules the interconnect regions as well. Secondly, for each defined lateral region, a layer stack is defined, as seen exemplarily in Figure 5.1. This determines the optical model due to reflection and parasitic absorption and the electrical behavior via transport properties. Within this work, all layers are considered for the optical model. However, for the electrical model, only the absorber layer, both contact layers and both optional grid layers are taken into account. Considering the buffer layers electronically (green layers in scanning electron microscope (SEM) picture in Figure 5.1), requires the usage of drift-diffusion models.

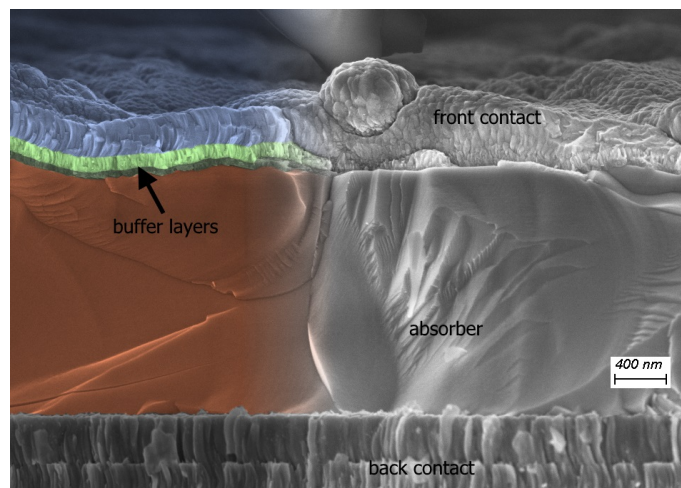


Figure 5.1: SEM cross section of a CIGS thin-film cell. On the left side, the different layers are colored. The back contact is colored in gray, the absorber material in orange, both buffer layers in different shades of green and the front contact in blue.

The exact setup of the device will be explained along with the given experiments within the thesis. Mainly two different thin-film absorber materials are used. One is CIGS and the other is a perovskite absorber.

5.1.2 Electrical Data

Electrical input information is divided into two different categories. The typically minor effects are contact resistances. With the introduced methodology a contact resistance is considered at the front and back external contact. Moreover, for modules a contact resistance is incorporated at P2 areas between the front and back contact layers. However, these effects can often be negligible for real applications due to successful optimization during process development.

The dominant electrical effect of solar devices are specific transport resistivities ρ_l of the l -th conducting layer. Hence, their value needs to be precisely determined. Four-terminal sensing measurements [252] and transfer length measurements (TLMs) [253] offer an experimental access to the sheet resistances R_{\square} . By using the thickness of the measured layer d_l and the relation

$$\rho_l = R_{\square,l} \cdot d_l \quad (5.1)$$

the specific resistivity can be determined. Theoretically, this parameter is material-specific and thus independent of the layer thickness. In Figure 5.2 the specific resistance of aluminum-doped zinc oxide (AZO) ρ_{AZO} is plotted as a function of the thickness of the measured layer. Its strongly non-constant behavior shows that a constant value for ρ_{AZO} does not correctly represent the physical reality. Similar effects have been observed in literature for any kind of material [254, 255, 256, 257] and even theoretical models to explain this behavior exist [258]. Reasons for this effect might be experimental conditions like surface roughness, but also intrinsic thin-film properties like modified charge carrier densities at the surface and even technological issues like time-dependent growing conditions during deposition processes. Therefore, a thickness-dependent specific resistivity

$$\rho_l(d_l) = \rho_l^{\text{bulk}} + (\rho_l^{\text{thin}} - \rho_l^{\text{bulk}}) \cdot e^{-\theta_l \cdot d_l} \quad (5.2)$$

is defined for each material layer l by an exponential decay. In the case of AZO, a bulk resistivity of $\rho_{AZO}^{\text{bulk}} = 8.56 \mu\Omega\text{m}$ and a resistivity of $\rho_{AZO}^{\text{thin}} = 79.8 \mu\Omega\text{m}$ for an infinitesimal thin layer with an exponential decay constant of $\theta_{AZO} = 8.631 \frac{1}{\mu\text{m}}$ are gained from a fit on experimental data in Figure 5.2.

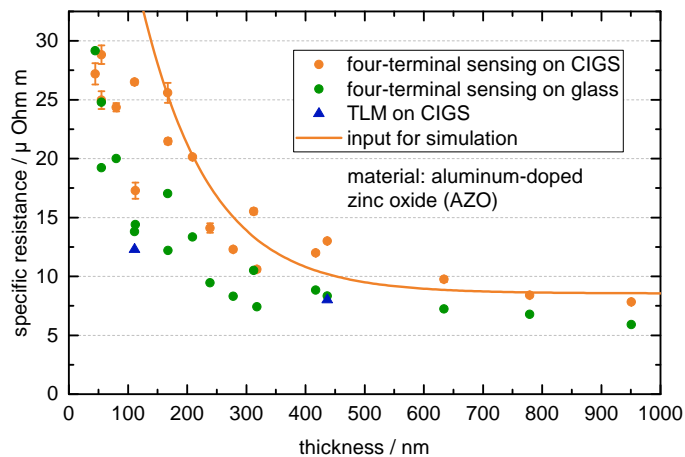


Figure 5.2: Specific resistance as a function of the layer thickness. Theoretically, a constant function is expected. However, due to experimental conditions, intrinsic thin-film properties and technological issues an exponential behavior can be observed. The simulation input is given by the fitted orange line.

As modules in the field are constantly exposed to radiation of the sun, their internal temperature rises. Therefore, temperature-dependent effects of the specific resistance need to be considered as well. In Figure 5.3, the temperature-dependence of an AZO film is shown between 10 °C and 80 °C. Within the measured 70 K-range, it rises only by about 1 %. Similar measurements with similar results have been made for other contact materials and can be found in literature [259, 260, 261, 262]. Due to the only minor changes in resistivity within the given temperature range for multiple different contact materials, the specific resistivity is not considered as a temperature-dependent quantity within this work.

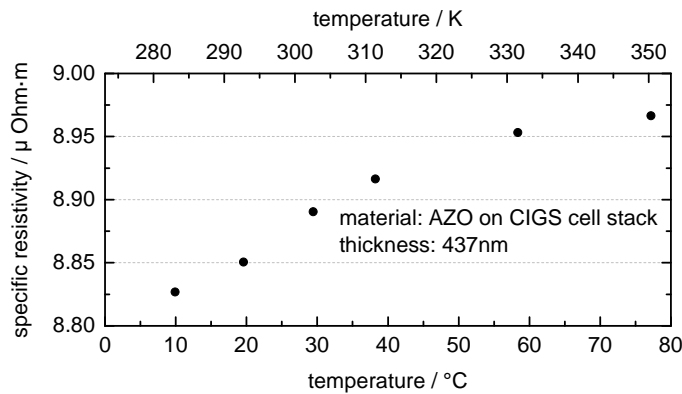


Figure 5.3: Temperature-dependent specific resistivity of a thin AZO film. Within the measured temperature range of 70 K the value varies only by about 1 %.

5.1.3 Optical Data

To calculate Fresnel's equations (4.6a), (4.6b), (4.7a), and (4.7b) and thus the total optical behavior via Equation (4.11), wavelength-dependent complex refractive data must be known. For CIGS, literature data from [263] is used. The optical data is given as a function of the GGI. This work uses data for a GGI of 0.3, which is the average GGI in a typical CIGS solar cell. For all remaining materials, ellipsometry and transmittance measurements are performed and the resulting measurement data is fitted with appropriate optical models. Metallic materials are typically fitted with a Drude-Lorentz model [264, 265], whereas for buffer layers like cadmium sulfide (CdS) or intrinsic zinc oxide (i-ZnO), usually Tauc-Lorentz oscillators are used [266, 267]. For perovskite layers, a combination of eight different Tauc-Lorentz oscillators is commonly used [268, 269]. TCO layers are typically modeled by a combination of a Tauc-Lorentz oscillator for the band gap absorption in the near-ultraviolet range and a Drude model for the partially metallic behavior of the free electron gas in the near-infrared range [270, 271]. Since layer thicknesses for TCOs are often varied within experiments, it is necessary to determine the refractive data for several thicknesses. Such measurements have been performed for AZO for four different layer thicknesses. The resulting complex refractive index $n + ik$ is plotted as a function of wavelength in Figure 5.4. The two regimes of metallic behavior and the band gap absorption can distinctly be observed in the imaginary part k . Both the real and imaginary part of the refractive index show an equivalent wavelength-dependent behavior for all four thicknesses. To check if the small deviations have an impact on the simulations, TMM calculations for a fixed AZO layer thickness have been performed with the four data sets of Figure 5.4. The resulting absorption in the absorber layer differed less than one per mill. Since effects of this minor impact can be neglected, the refractive index is not extended to a thickness-dependent variable within this work's simulation.

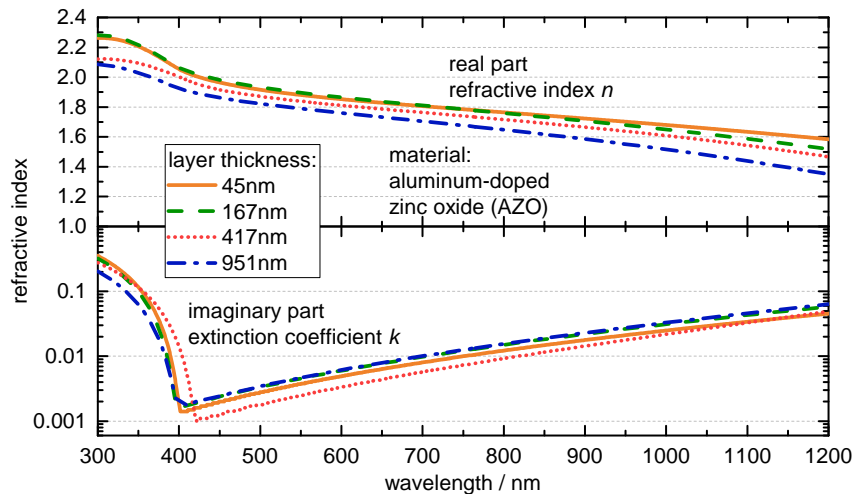
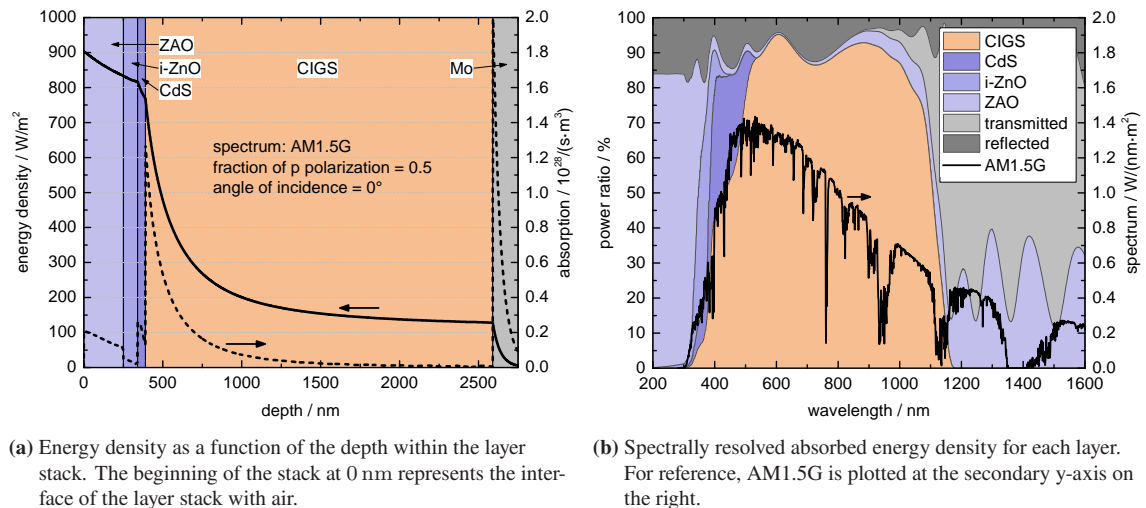


Figure 5.4: Wavelength-dependent complex refractive index of AZO. Four different layer thicknesses have been measured with ellipsometry and transmittance measurements and fitted by a combination of a Tauc-Lorentz oscillator and a Drude model.

The measured optical data can be used to model an entire cell stack. In Figure 5.5a, a typical stack for CIGS cells [31] has been simulated. The energy density at each point is given by the sum of both Poynting vectors from Equations (4.12) and (4.13) and the local absorption by its spatial derivative. All optical losses are visualized within this graph. The initial energy density of around $900 \frac{\text{W}}{\text{m}^2}$ instead of the typical $1000 \frac{\text{W}}{\text{m}^2}$ for AM1.5G is a result of the calculated reflection losses. Parasitic absorption within the window layers appear as further exponential decay of the energy density. The saturation of the energy within the CIGS layer is due to the finite band gap within the CIGS layer. The energy density transmitted through the CIGS layer is therefore also apparent as incomplete absorption.



(a) Energy density as a function of the depth within the layer stack. The beginning of the stack at 0 nm represents the interface of the layer stack with air.

(b) Spectrally resolved absorbed energy density for each layer. For reference, AM1.5G is plotted at the secondary y-axis on the right.

Figure 5.5: Optical behavior of a layer stack for a standard CIGS cell.

Within each layer the absorption can be integrated for each wavelength and plotted spectrally resolved. Such a plot is shown in Figure 5.5b. The absorption onset due to the band gap of the CIGS absorber layer is prominently visible at around 1100 nm. Moreover, the parasitic effect of the window layers in the low-wavelength regime damps the absorption in the CIGS layer. Except

for recombination losses, this graph visualizes an EQE plot [272]. Therefore, a verification of the optical TMM model can be done with a low-recombination cell. In Figure 5.6, both quantities are compared with each other for three different thicknesses of the top AZO layer. The very good agreement for all different AZO thicknesses shows the accuracy of the optical simulation. It can therefore be said with certainty that the described optical model is well suited for modeling all optical processes, which is why the TMM will be used as the standard optical model in this work.

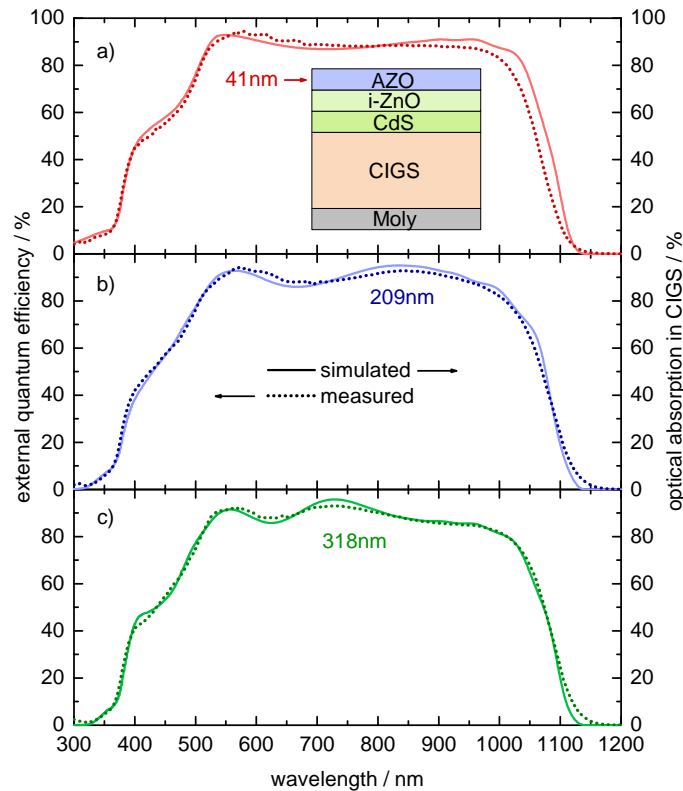


Figure 5.6: Comparison between measured EQE data and simulated absorption in CIGS layer.

For CIGS layer stacks, a molybdenum diselenide (MoSe_2) layer typically forms between the back contact and the absorber layer during the CIGS growth [273]. This around 100 nm thick film is considered within optical simulations, but has only marginal impacts on the optical effects. In this work, it is therefore often left out within the TMM simulations for reasons of simplicity. However, this layer needs to be considered for electrical simulations within drift-diffusion models due to its property to enable a current flow with a lower barrier for charge carriers [274, 275].

5.1.4 I–V Characteristic of Internal Semiconductor Material

The final input for the simulation model of this work is the I–V characteristic of the internal semiconductor. Typically such I–V curves are simulated by drift-diffusion models. However, in this work a new methodology to get this information is developed. This procedure needs a measured I–V curve of a cell or module and all geometrical, optical, and electrical information described above. In a next step, the input I–V curve of the simulation for Equation (4.19) is adapted in a way that the output of the simulation matches the experimentally measured I–V curve. The resulting optimization problem is named REF and explained in detail in the following Section 5.2.

5.2 Calculating Backwards – From Module Level to Material Level via Reverse Engineering Fitting

As introduced in Section 5.1.4, the internal semiconductor I–V curve is needed for Equation (4.19) to be able to perform a FEM simulation. Figure 5.7 describes the internal I–V curve (green) as being located just around the absorber layer since it does not contain any losses due to optics or lateral electric fields. Charge carrier generation is perfect and only electrical recombination losses are included in this I–V curve. The internal I–V curve and the external one for the entire device are compared in Table 5.1. A common option to get the internal I–V curve are drift-diffusion models [59, 92]. They are able to simulate the electrical processes within the semiconductor resulting in an I–V characteristic. The path from the internal towards the external I–V curve can be performed by the combination of optical and electrical simulations as described in Chapter 4. However, this work introduces a method to go the opposite way from the laboratory-measured I–V curve towards the internal curve.

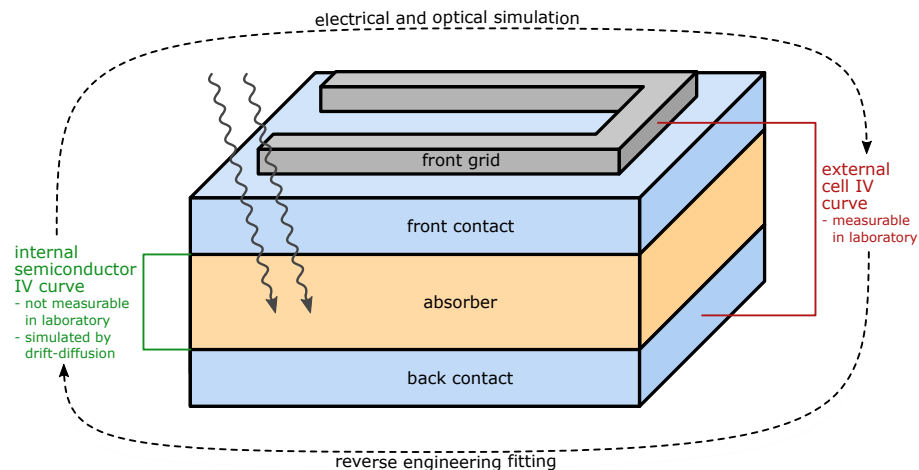


Figure 5.7: Illustration of the internal semiconductor I–V curve vs. the externally measured I–V curve. To go the forward way, standard electrical and optical simulations as described in Chapter 4 are used. However, to get the internal I–V curve from an external measurement, advanced methods are necessary. This work uses the approach of REF.

Table 5.1: Comparison of the internal and the external I–V curves and their typical field of application.

	internal I–V curve	external I–V curve
part of this work’s simulation	input	output
typical device	p-n junction	cell or module
includes optical losses	no	yes
includes electrical losses	no	yes
includes recombination losses	yes	yes
can be measured experimentally	no	yes

The internal I–V characteristic is supplied as a set of all diode parameters, which are given by the generated photocurrent density j_{ph} , the reverse saturation current density j_0 , the diode factor $n_{\text{d}}^{\text{mat}}$, and the two area-normalized semiconductor resistances r_{s} in series and r_{sh} for shunts. In principle, an experimentally measured I–V curve could be straightforwardly fitted by a single-diode equivalent-circuit model. However, the resulting parameters would be significantly influenced by parasitic semiconductor-to-cell losses, especially by optical damping and a non-negligible series resistance^[64], which is also related to cell size. The procedure of REF is a powerful tool to extract the internal semiconductor diode parameters from experimentally measured external I–V curves, where semiconductor-to-cell losses are included in the measurement data. This algorithm subtracts out the optical and electrical losses in order to get the internal I–V curve without the necessity of any drift-diffusion model. All other input data, namely geometrical, electrical, and optical data needs to be known for that process. In Figure 5.7 the REF procedure is represented by the bottom arrow, which points backwards from the external towards the internal I–V curve.

5.2.1 Procedure of the REF Approach

The REF procedure is a process to extract the five diode parameters of the internal I–V curve. In principle, these parameters could have a spatial distribution across the entire solar device, especially for inhomogeneous deposition processes. However this would result in a set of $5n$ parameters for n finite elements. Since this system is massively over-determined, this approach won't result in reasonable parameters. Therefore, the semiconductor material is assumed to have spatially constant parameters resulting in an optimization problem for 5 parameters with the external I–V curve as a low-dimensional input information. Nonetheless, the forward way of simulating materials with local inhomogeneities is a straightforward task for a FEM simulation.

Firstly, an initial parameter set $(j_{\text{ph}}^{\text{mat}}, j_0^{\text{mat}}, n_{\text{d}}^{\text{mat}}, r_{\text{s}}^{\text{mat}}, r_{\text{sh}}^{\text{mat}})$ is needed as an initial guess. It can be obtained from the I-V data, which is given by N experimentally measured voltage-current pairs $(V_i^{\text{exp}}, I_i^{\text{exp}})$. A basic single-diode equivalent-circuit model is fitted via the procedure in Section 4.5 to the experimental I-V data and used as the initial guess. Smaller modifications like adapting the photocurrent density for the amount of grid within the active area, reducing the series resistance by several orders of magnitude or even manual corrections can be done to improve the initial guess.

The resulting diode parameters are passed to each finite element as internal diode parameters. Afterwards, with these parameters an external device I–V curve is simulated, which yields N voltage-current pairs $(V_i^{\text{exp}}, I_{\text{out}}(V_i^{\text{exp}}))$ via Equation (4.46). This simulated I–V curve almost certainly does contain deviations from the measured device I–V curve. The weighted sum of all squared errors χ^2 is defined as

$$\chi^2 = \frac{1}{\sum_{i=0}^{N-1} w_i} \cdot \sum_{i=0}^{N-1} w_i \cdot \left(I_i^{\text{exp}} - I_{\text{out}}(V_i^{\text{exp}}) \right)^2, \quad (5.3)$$

where the weights w_i are given by

$$w_i = \begin{cases} \frac{2(V_{i+1}^{\text{exp}} - V_i^{\text{exp}})}{\log\left(\frac{(I_i^{\text{exp}} - I_{\min})^2}{A^2}\right) + c_0} & \text{for } i = 0 \\ \frac{2(V_i^{\text{exp}} - V_{i+1}^{\text{exp}})}{\log\left(\frac{(I_i^{\text{exp}} - I_{\min})^2}{A^2}\right) + c_0} & \text{for } i = N - 1 \\ \frac{V_{i+1}^{\text{exp}} - V_{i-1}^{\text{exp}}}{\log\left(\frac{(I_i^{\text{exp}} - I_{\min})^2}{A^2}\right) + c_0} & \text{else.} \end{cases} \quad (5.4)$$

Here, I_{\min} is a current that is slightly smaller than the minimum I_i and c_0 is a constant to bring the logarithmized value into a positive regime. The numerator of the weights accounts for non-equidistant voltage steps, whereas the denominator creates a logarithmic dependence on the current, which is a more sophisticated way to treat the exponential behavior of an I–V curve.

Within the iterative process of REF the goal is to find the best possible match of the simulated output I–V curve with the experimentally measured data. Thus, an optimization algorithm needs to be established, which uses the calculated value for χ^2 as residual loss function. Since there is no trivial access to the gradient of this function, only gradient-free algorithms can be used. This work uses a downhill simplex algorithm [233] with the internal diode parameters as fitting parameters. The iterative adjustment converges to the searched diode parameters of the loss-exempt semiconductor material. With the help of the reconstructed internal I–V curve, the raw p-n junction without any optical or electrical losses can be evaluated.

In a nutshell, the REF procedure allows to calculate from a loss-containing external device I–V curve backwards to a loss-exempt internal semiconductor I–V curve and therefore allows the extraction of the loss-free internal semiconductor I–V curve from the experimentally measured external device I–V curve. This enables further performance analysis of the p-n junction, detailed loss analyses, and forecast simulations with the same absorber material but a different arrangement of contact layers.

5.2.2 Application of the REF Approach to Real-world Solar Devices

This section uses a thin-film solar cell with a CIGS absorber and a 278 nm thick AZO layer on top to demonstrate the working principle of the REF procedure. The cells have an active cell area of 50 mm² with a grid area of 1.41 mm² (2.82 %). Their layer stack is given by the following materials: 3 mm soda lime glass / 500 nm molybdenum (Mo) / 2200 nm CIGS / 50 nm CdS / 90 nm i-ZnO / variable thick rf-sputtered AZO / 2500 nm nickel/aluminum/nickel (Ni/Al/Ni) metallization grid [276, 277, 278]. In Figure 5.8, the green triangles show the measured current-voltage pairs $(V_i^{\text{exp}}, I_i^{\text{exp}})$ of a cell with a 278 nm thick AZO layer. The electrical properties as well as the geometrical setup are implemented and the optical factor f_{optics} is calculated via a TMM to 81.6%. The above described REF process is applied to this cell resulting in an external device I–V curve, which is shown as a green line. The internal I–V curve is plotted as black dashed line. From the internal to the external I–V curve, a reduced j_{sc} can be observed, which is caused by the optical losses and taken into account by f_{optics} , as described in Chapter 4.2. Moreover, the resulting logarithmic dependence of V_{oc} on j_{sc} decreases the open-circuit voltage as well. Finally, the electrical losses have a reducing impact on the FF of the cell.

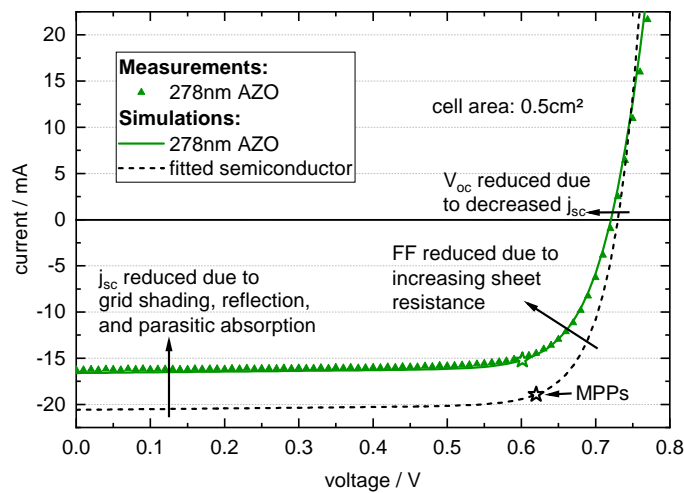


Figure 5.8: I–V characteristics of a REF-fitted CIGS cell. The green triangles mark experimental data, whereas the green solid line stands for the REF-fitted device I–V curve. The black dashed line represents the internal semiconductor’s I–V curve, which can be extracted from the REF process.

Figure 5.9 a) to e) show the diode parameters of the internal semiconductor I–V characteristic during the REF process as a function of the iteration step. Each of them evolves to its designated value before the residuum χ^2 in Figure 5.9 f) according to Equation (5.3) reaches its minimum. The converged diode parameters of the internal I–V characteristic are given by a generated current density of $411.7 \frac{A}{m^2}$, a reverse saturation current density of $2.99 \frac{\mu A}{m^2}$, a diode factor of 1.51, and area-normalized resistivities of $11.3 \text{ p}\Omega \text{ m}^2$ in series and $66.7 \text{ m}\Omega \text{ m}^2$ in parallel.

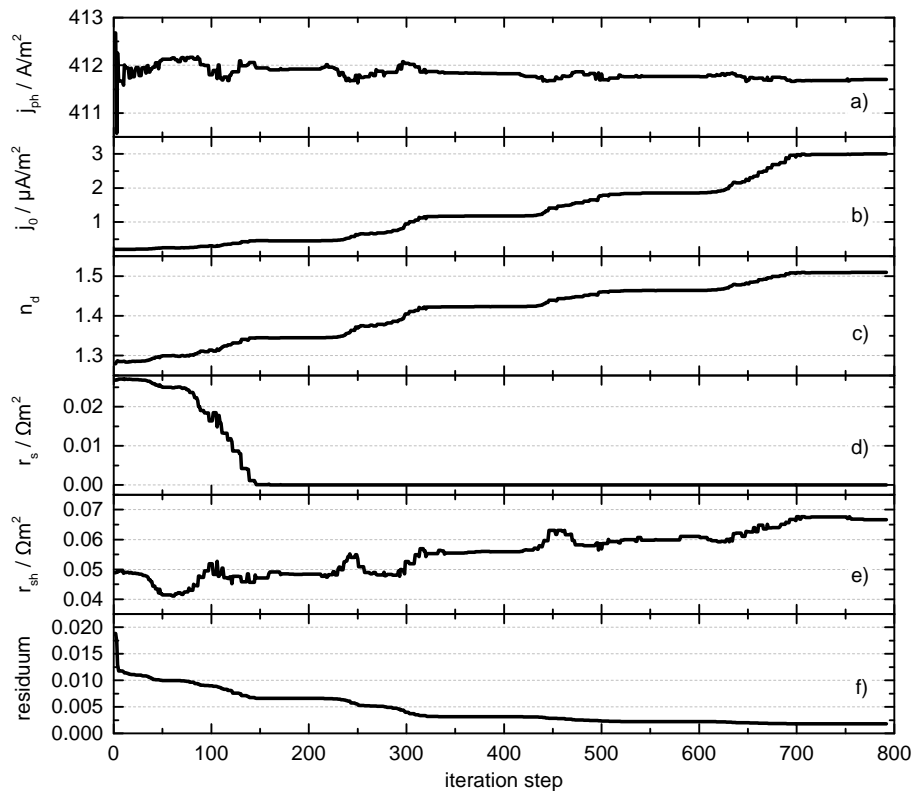


Figure 5.9: Diode parameters of a CIGS cell during the REF process. All parameters are converging towards a global optimum, which is indicated by a minimum in the residuum function χ^2 in graph f).

To verify the REF results, nine further cell configurations have been fabricated, each having a different thickness of the top AZO layer between 41 nm and 1030 nm (See Figure 5.10). This results in different cell I–V curves due to their different optical and electrical losses. However, the internal p-n junction was not changed experimentally. Therefore, the methodology of the REF procedure should be able to identify the same internal I–V curve for each of the cells, despite the fact that their experimentally measured I–V curves differ a lot from each other. The procedure of REF has been applied to each individual cell and the fitted solar cell parameters V_{oc} , FF, and j_{sc} have been extracted. The resulting error range was less than 1% for each parameter and all cells, which is by far a sufficient accuracy. This confirms the assumption of nearly identical semiconductor properties of all cells in this series and it highlights the precision and reliability of the REF algorithm.

5.3 Forecast I–V Curves for Different Solar Devices

After all input information is fed into the model of the solar cell, I–V curves can be digitally calculated. For the following proof of concept, the same thin-film solar cells with a CIGS absorber as in the previous section are used. In Figure 5.10 experimental I–V data is plotted as colored symbols for different thicknesses of the top AZO layer. The data of a cell with a 278 nm thick AZO layer has been used for the REF process as described in the previous section resulting in the REF-fitted internal semiconductor I–V curve (black) and the corresponding FEM-calculated cell I–V curve (green).

Within the digital model of the cell, several parameters can be changed and the resulting I–V characteristic of the varied cell can be forecast. To check both the electrical and the optical simulation for correctness, the thickness of the front TCO layer has been varied. This should have impacts on the optical transmission and thus on j_{sc} and on the lateral sheet resistance and thus on the FF. Both the orange and the blue line in Figure 5.10 represent predicted I–V curves with a different TCO layer thickness. The calculated f_{optics} for the cells with 41 nm and 1030 nm is 82.7% and 74.9%, respectively, and result in a varied j_{sc} , whereas the predicted FFs of 61.0% and 76.5% show a significant change in the cell's electric behavior. The symbols in Figure 5.10 correspond to experimental measurements. The high coefficients of determination¹ of 99.5% (41 nm AZO) and 99.0% (1030 nm AZO) indicate a high precision of forecasting accuracy.

From the I–V curves in Figure 5.10 the solar cell parameters j_{sc} , FF, and V_{oc} can be extracted. These three I–V curves and seven further ones of cells with different AZO thicknesses have been analyzed. The statistical distribution for each solar cell parameter of around 30 cells per thickness configuration is plotted in Figure 5.11 as gray boxes. The height of the box stands for the standard deviation and the whiskers reach to the minimum and maximum values of each thickness group. The dashed black lines represent the AZO thickness-independent semiconductor characteristics, which was REF-fitted in Figure 5.10. The orange lines in all three subplots stand for the predicted values of the simulation.

¹ The coefficient of determination R^2 is a measure of the degree of certainty of two curves. It is defined as one minus the ratio of the sum of all residual squares with respect to the sum of all total squares $R^2 = 1 - \frac{\sum_{i=0}^{N-1} (y_i - p_i)^2}{\sum_{i=0}^{N-1} (y_i - \bar{y})^2}$ with all N measured values y_i , their mean value $\bar{y} = \frac{1}{N} \sum_{i=0}^{N-1} y_i$, and the corresponding predicted value p_i .

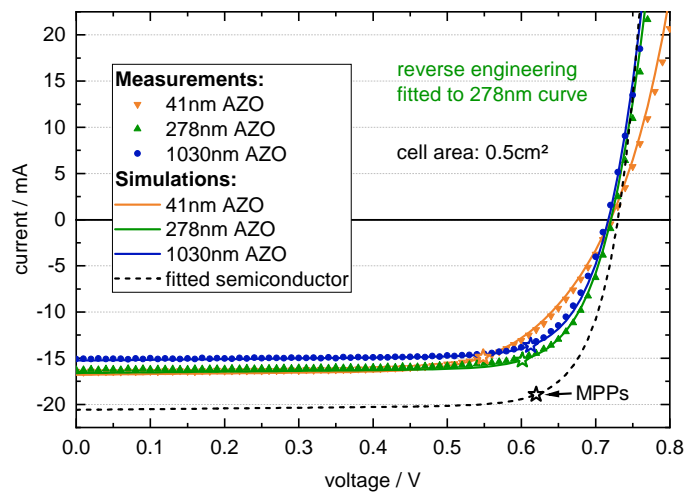


Figure 5.10: I–V characteristics of simulated and measured CIGS cells. The green experimental data is REF-fitted resulting in the green cell fit and the internal semiconductor’s I–V curve in black dashed. Both other cell’s I–V curves for 41 nm and 1030 nm are predicted by the simulation using the black curve as input.

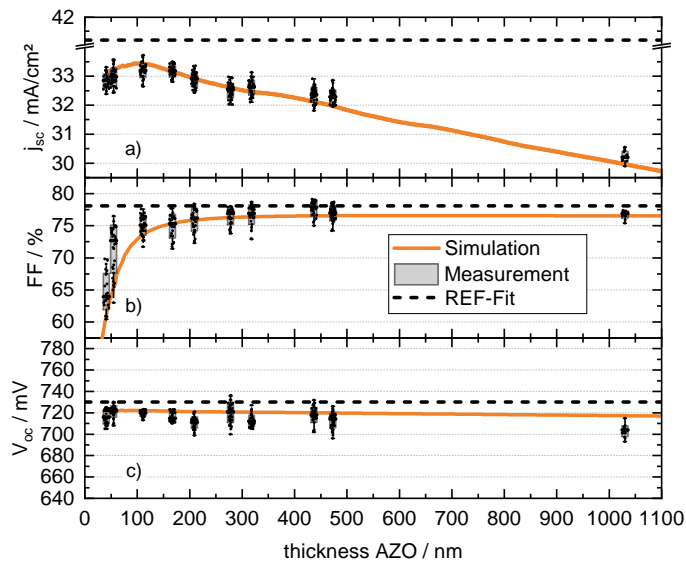


Figure 5.11: Extracted solar cell parameters from Figure 5.10 as a function of the AZO layer thickness. The effects of decreasing j_{sc} , increasing FF, and constant V_{oc} are described in the main text.

Plot 5.11 a) shows the short-circuit current density j_{sc} . The overall downwards trend of the cell’s j_{sc} with rising AZO thickness is due to the increasing parasitic absorption within the AZO layer. Small interference oscillations can be observed as a modulation on top of the downwards trend. Their reason lies in the thin-film interferences within the layer stack of the device. They are theoretically predicted by the TMM and experimentally measured as well. A significant drop of j_{sc} is observed for a AZO layer thickness of around 50 nm. At first this is not very intuitive since thinner AZO layers should result in smaller parasitic absorption and thus in larger short-circuit current densities. The reason for this prominent dip is based on the coexistence of both an optical thin-film interference drop and the increasing local MPP mismatch effect (compare Section 2.3.4) for larger sheet resistances as found for thinner AZO layers. The high accordance of the experimental data with the simulated forecast manifests an accurately interacting model of the optical TMM approach and the electrical FEM simulation.

The FF in plot b) shows a massive drop for low thicknesses and a saturation towards thicker layers on a plateau of 76.6 %. These features are present in the experimental data as well as in the simulated data. The ideal FF of the internal semiconductor curve is independent of the conductivity of all conducting layers including the front AZO layer. Thus, the FF is at a constant level of 78.1 %.

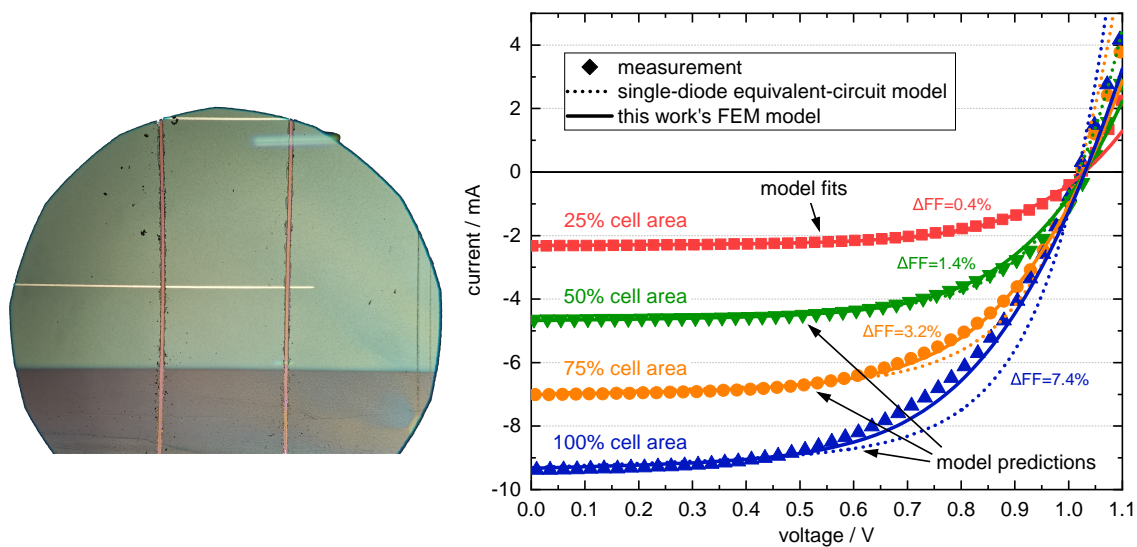
The predicted open-circuit voltage V_{oc} in Figure 5.11 c) lies below the ideal V_{oc} of the semiconductor. This effect is justified by the logarithmic dependence of V_{oc} on j_{sc} . According to Figure 2.7, V_{oc} is mainly affected by intrinsic recombination mechanisms within the internal absorber material. Since these effects are not significantly influenced by the sheet resistances of the front and back contacts, a nearly constant V_{oc} is predicted by the simulation model. This behavior is experimentally verified within its measurement variance. For large thicknesses of the AZO however the open-circuit voltage slightly decreases. This effect is also a present feature for several further analyses which are not shown here. The cause of this drop is attributed to a longer deposition time for the thicker layers. The different thicknesses are achieved by a variation of the belt speed of the inline sputter machine. Therefore, cells with thicker AZO layers are longer exposed to the high temperatures within the sputter process. The resulting temperature of the solar cell and its glass substrate eventually passes a certain critical temperature, at which V_{oc} losses due to high-temperature degradation of the CIGS absorber ^[279, 280] occur. Its reason might be given by interdiffusion processes ^[281] and is still an issue of current research ^[282, 283]. Thus, this minor deviation of the experimental data from the predicted simulation data is not considered as counterexample for the simulation technique but rather as a technological constraint for experimental conditions.

5.4 Scientific Relevance of Spatially Resolved FEM

By using quasi-three-dimensional finite element models, the geometry of a solar cell and the spatially distributed properties and resulting characteristics can be considered. Complex changes in geometry can be easily modeled and implemented. Furthermore, lateral ohmic transport effects can be detected within a FEM model. These effects are not lumped into other resistive effects and can be visualized spatially. Finally, the voltage drop from front to back contact is given as a spatial distribution within an FEM instead of a spatially constant value. The resulting current generation distribution can be rather inhomogeneous due to the non-linearity of Equation (4.19) and thus the entirely generated amount of current can be affected significantly. This is especially the case for large-area devices with high sheet resistances.

However, the simulation process for a finite element model is rather complex and time-consuming in comparison with a simple single-diode equivalent-circuit model. Thus, the question arises whether the FEM model is really necessary or whether the same questions can be answered with a much simpler model. One possible approach to check the relevance of FEM models is to measure small cells and try to extrapolate the I–V curve to larger cells. For this purpose, a perovskite cell with a 48 nm thin grid and 50 nm thin TCO layer is fabricated. The cell has an active cell area of 50 mm² with a grid area of 0.42 mm² (0.84 %). The layer stack is given by the following materials: 1.1 mm Schott D 263[®] T eco glass / 230 nm hydrogenated indium oxide (IOH) / [2-(3,6-Dimethoxy-9H-carbazol-9-yl)ethyl]phosphonic acid (MeO-2PACz) / silicon dioxide (SiO₂) nano particles / mixed ionic perovskite Cs_xFA_{1-x}Pb(I_yBr_{1-y})₃ (CsFAPbIBr) / [6,6]-Phenyl C₆₁ butyric acid methyl ester (PCBM) / bathocuproine (BCP) / indium zinc oxide (IZO) / silver (Ag) metallization grid. ^[38, 284, 285] Its cell size can be experimentally varied by iteratively changing the cell's length perpendicular to its grid fingers. P3 structuring lines are used to define the length as it

is seen in Figure 5.12a. Within each step of cutting the cell, the I–V curve of the remaining cell has been measured and plotted as colored symbols in Figure 5.12b. For the I–V curve of the smallest cell, a single-diode equivalent-circuit model has been fitted (dotted red line) and a FEM model is established by a REF procedure (solid red line). Both models are used to predict the I–V curves for larger cells. The predictions of the single-diode equivalent-circuit model are accomplished by adapting the current by the factor of the relative cell size and thus work by scaling. For the FEM model however, all cropped geometries are implemented and simulated. Both models predict the increasing j_{sc} and constant V_{oc} correctly. Within the single-diode equivalent-circuit model, the FF is a constant parameter for any cell size. This assumption overestimates the FF for larger cells significantly, since the increased transport paths are not considered within this model. The forecast of the FEM model however predicts a decreasing FF (61.1 %, 60.1 %, 58.3 %, 55.8 %) from the smallest to the largest cell. The increased local currents for larger cells cause a steeper increase of the voltage distribution causing more resistive losses. This behavior is correctly modeled within the FEM model resulting in a high coherence of the predicted I–V curves.



(a) Microscope image of a fraction of the perovskite cell. The greenish area is the active cell area, with the white grid structures on top. The orthogonal reddish lines mark the P3 lines, which were used to iteratively decrease the cell size.

(b) The experimental I–V curve of the smallest cell (red squares) is fitted both by a REF procedure (solid red line) and by a single-diode equivalent-circuit model (dotted red line). The predictions for larger cells of both models are compared to experimental data. Whereas V_{oc} does not change and j_{sc} is predicted correctly by both models, the decreasing FF is correctly forecast only by the FEM model.

Figure 5.12: Comparison of a FEM model and a single-diode equivalent-circuit model and experimental validation by cutting perovskite solar cells.

The coefficients of determination for all measured cell sizes and both models are summarized in Table 5.2. For the finite element model constant high coefficients are observed, whereas for the single-diode equivalent-circuit model the coefficients decrease rapidly with an increasing cell size due to the above mentioned lack of spatially distributed electrical information. In summary, it can be said that for a correct FF and thus for an accurate I–V curve and PCE prediction, finite element models are a major improvement in forecasting solar cells parameters with respect to simpler models as the single-diode equivalent-circuit model.

Table 5.2: Coefficients of determination R^2 for the I–V curves in Figure 5.12b comparing single-diode equivalent-circuit model (SDM) and the FEM.

Cell area	R_{SDM}^2	R_{FEM}^2
50 % of initial cell	88.5 %	94.6 %
75 % of initial cell	76.6 %	95.3 %
100 % of initial cell	57.6 %	95.7 %

This spatially resolved effects occur more prominent for cells and modules with bad conducting contact layers. Nevertheless, the present conductivity of current window layers does not allow for neglecting this effect, as it was showed within this section. Thus, for an exact analysis, FEM simulations are essential for accurate scientific investigation.



Answering this Chapter's Guiding Scientific Question

Which input parameters are necessary for the digital model and how precise are the numerical results of the simulation models in comparison with experimental verification data?

The geometric dimensions of the solar device act as basic information, which is used for determining the active area. For the optical model, wavelength-dependent complex refractive data is necessary, while for the electrical model, the specific resistivity of all conducting layers needs to be known. Furthermore, the internal p-n junction requires a temperature-dependent I-V characteristic, which can be obtained via an external drift-diffusion model. For a given temperature, the latter can also be fitted retrospectively due to the holistic approach of this work. To verify the optical model solely, the simulated optical absorption within the absorber layer has been proven to match experimentally measured EQE data and correctly reproduce characteristic interferences of rough thin-film layer stacks. The correct interplay of optical and electrical simulation methods is demonstrated via the high coefficients of determination within the forecast of device I-V curves, especially for different contact layer thicknesses (better than 99%) and different cell sizes (around 95%). From the I-V data, solar-module parameters are shown to be predictable for an arbitrary device geometry with a high precision.

6

Finding the Bottleneck – Holistic Top-Down Loss Analysis

In order to guide research and development efforts towards increasing efficiencies and higher net energy yields, losses within solar modules need to be identified, allocated to their corresponding loss mechanisms, and quantitatively determined. The best way for such systematical analyzes are automated computer-aided modeling approaches as the procedure in this work. To be able to compare all loss mechanisms with each other, it is important to put all identified losses in proportion within a single holistic top-down loss analysis. Therefore, a holistic simulation method including all loss mechanisms is necessary. This work uses the developed linkage of the two simulation levels of optical modified TMM and electrical Poisson's equation solver. Such comprehensive simulation approaches additionally offer the benefit that possible future research improvements can be checked for their contribution on the overall module performance. In fact, within the coupled simulation of this work, effects of technological improvements can be quantitatively evaluated and therefore, priorities can be proposed in the progress of research and development.

This Chapter's Guiding Scientific Question

How can all relevant losses on the device level be allocated and quantified and which loss is the bottleneck for thin-film solar devices?

For the thin-film photovoltaic industry, the physical principles of loss mechanisms have been described in detail ^[180]. Even first simulations have been performed in order to guide industry-oriented development ^[72]. This chapter uses the developed simulation techniques from Chapter 4 to accomplish more detailed and more accurate loss analyses than previously published in literature. Especially the advanced optical model of a modified TMM, which also accounts for partially incoherent interference due to rough interfaces ^[194], and the interplay of optics and electrics are major advantages of this work's procedure.

To give absolute numbers for all involved loss mechanisms, their order of determination is of utmost importance. Therefore, all loss plots within this work will follow the path of the incident photons and after their conversion follow the path of the generated electron hole pairs. Hence, optical losses will always be taken into account before electrical losses. Furthermore, shading of the grid is always listed before parasitic absorption as an example, since grid shading appears chronologically first within the photon path. To get a better visual impression of the loss mechanisms, all loss graphs will be plotted with a logarithmic y-axis. This way, losses that appear later in the loss chain are not artificially compressed.

To finally quantitatively calculate the power loss within each loss mechanism, some definitions need to be introduced. Some of them are already used within the previous chapters, but once more summarized here for better understanding. The set of all elements within the meshing domain is called \mathcal{K} . Each element k has set of neighbors $\mathcal{N}(k) = \{n | n \text{ is neighbor of } k\}$. Furthermore, every element must be part of one of the following subsets as defined in Section 4.3.4:

- Elements within the active cell area are within the subset $\mathcal{C} = \{k | k \text{ is of type cell}\} \in \mathcal{K}$ (orange in Figure 4.12).
- All elements located in the trenches of the module interconnect are within $\mathcal{P}_1 = \{k | k \text{ is of type P1}\} \in \mathcal{K}$ (green in Figure 4.12), or $\mathcal{P}_2 = \{k | k \text{ is of type P2}\} \in \mathcal{K}$ (blue in Figure 4.12), or $\mathcal{P}_3 = \{k | k \text{ is of type P3}\} \in \mathcal{K}$ (pink in Figure 4.12).
- Finally, finite elements between the three trench regions are either in $\mathcal{S}_{12} = \{k | k \text{ is of type gap between P1 and P2}\} \in \mathcal{K}$ or in $\mathcal{S}_{23} = \{k | k \text{ is of type gap between P2 and P3}\} \in \mathcal{K}$ (both orange in Figure 4.12).

For cells instead of modules, all finite elements are within the active cell area \mathcal{C} . Additionally, each element optionally can be part of the following subsets independent of its location within the cell or module.

- The subset of all grid elements is named $\mathcal{G} = \{k | k \text{ is grid element}\}$.
- All elements that are connected to an external front or back contact are within $\mathcal{E}_{\text{front}}$ or $\mathcal{E}_{\text{back}}$, as defined in Section 4.3.3.1.

For the optical loss analysis, a detailed version of the optical loss factor f_{optics}^k in the k -th element needs to be considered. It can be determined with both optical models introduced in Section 4.2 and is still used the same way in Equation (4.18). However, it will now be split up into the different loss factors.

$$f_{\text{optics}}^k = (1 - f_{\text{shade}}^k) \cdot (1 - f_{\text{grid}}^k) \cdot (1 - f_{\text{tilt}}^k) \cdot \left(1 - f_{\text{refl}}^k - \sum_{\substack{l \in \text{paras.} \\ \text{layers}}} f_{\text{abs}}^{k,l} - f_{\text{trans}}^k \right) \quad (6.1)$$

While f_{shade}^k and f_{grid}^k represent the relative external shading and grid shading of the k -th element, f_{tilt}^k is the relative loss in effective area, and f_{refl}^k , $f_{\text{abs}}^{k,l}$, and f_{trans}^k are the relative loss ratios due to reflection, parasitic absorption within the l -th layer of the stack, and incomplete absorption, respectively. The multiplication of the additive inverses of those factors results in the final optical factor, which has linear impacts on the locally generated current according to Equation (4.18).

Finally, all loss analyses will start at the level of the internal p-n junction, and hence at the semiconductor material level. The theoretically produced power of the semiconductors at the MPP at the total module area $A_{\text{tot}} = \sum_{k \in \mathcal{K}} \omega_k$ will be referenced as P_{SC} . As introduced in Section 4.3.2.2, ω_k is the two-dimensional size of k -th finite element.

6.1 Overview of All Loss Mechanisms

In Figure 6.1, a sketch of a generic module section is shown with all possible loss mechanisms. While all optical losses are plotted on top in blue, all geometrical area losses are referenced on the bottom in green. Electrical losses are indicated within the middle of the module in orange. Table 6.1 gives a list of all mechanisms that occur in Figure 6.1 with their detailed name, category, and the section, in which it is described in detail.

6.2 Mathematical Calculation of All Loss Mechanisms

In this section, all loss mechanisms from Table 6.1 are listed individually. Each of them is briefly explained and an exact formula is given, how it is calculated within the finite element model from Chapter 4.

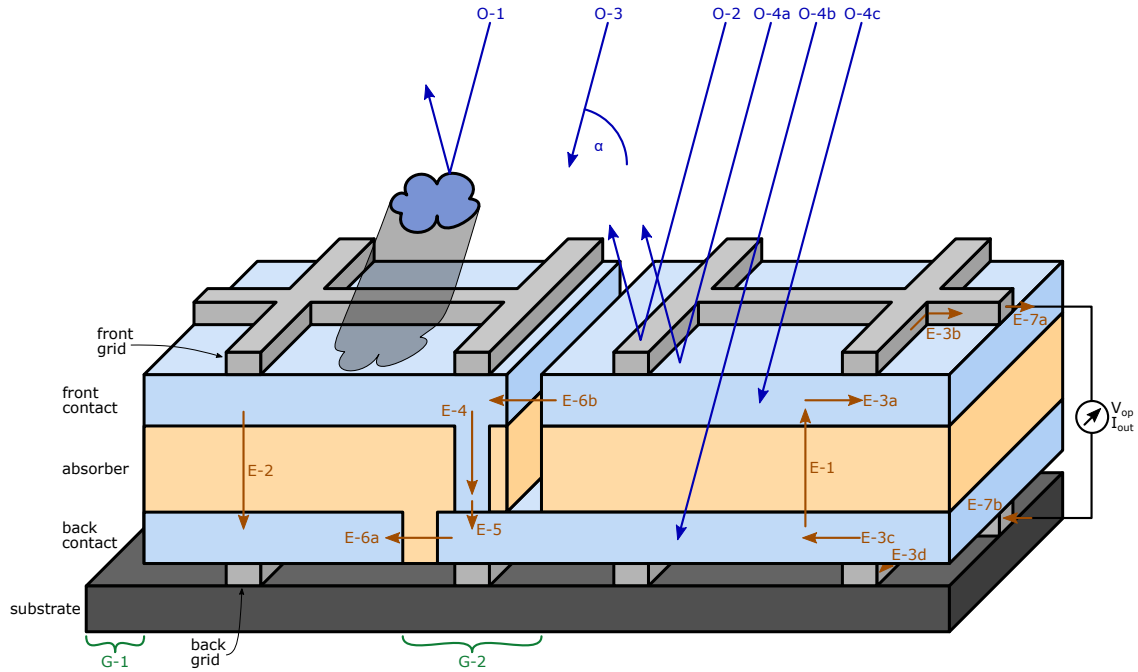


Figure 6.1: Visualization of all loss mechanisms that are calculated within this work. All optical losses are marked in blue, all electrical losses in orange and all geometrical loss mechanisms are painted in green. All the losses can be found in Table 6.1 as well.

6.2.1 Edge Area

Each solar module suffers from a geometrical loss at its edges. Space is required to attach an encapsulant and the mounting frame. Ideally this area vanishes and the bigger the module, the smaller in comparison to its total area A_{tot} is its edge area A_{edge} . Starting from the semiconductor power, this loss can be calculated by comparison of the two areas.

$$P_{loss}^{edge} = P_{SC} \cdot \frac{A_{edge}}{A_{tot}} \quad (6.2)$$

The edge area is not included in simulation domain and therefore needs to be calculated before the actual simulation procedure.

6.2.2 External Shading

Every finite element k is allocated to a given shading factor f_{shade}^k . A factor of 0 means no shading at all, while $f_{shade}^k = 1$ stands for a complete shading of the k -th element. All values in between are possible. In the field, shading can be caused by clouds or trees in the light path. Even in the laboratory, shading can occur due to defining the solar cell's active area by deliberate shading. The entire loss is calculated by the power density $\frac{P_{SC}}{A_{tot}}$ multiplied with the area-weighted shading of all elements \mathcal{K} .

$$P_{loss}^{shade} = \frac{P_{SC}}{A_{tot}} \cdot \sum_{k \in \mathcal{K}} \omega_k \cdot f_{shade}^k \quad (6.3)$$

Table 6.1: List of all loss mechanisms that are calculated within this work.

Abbreviation	Loss mechanism	Type	Section
G-1	Edge area	Geometrical	6.2.1
O-1	External shading	Optical	6.2.2
G-2	Module interconnect area loss	Geometrical	6.2.3
O-2	Grid shading	Optical	6.2.4
O-3	Tilted effective area	Optical	6.2.5
O-4a	Reflection	Optical	6.2.6
O-4b	Incomplete absorption	Optical	6.2.6
O-4c	Parasitic absorption	Optical	6.2.6
E-1	MPP mismatch	Electrical	6.2.7
E-2	Reverse current under grid	Electrical	6.2.8
E-3a	Ohmic losses in front contact	Electrical	6.2.9
E-3b	Ohmic losses in front grid	Electrical	6.2.9
E-3c	Ohmic losses in back contact	Electrical	6.2.9
E-3d	Ohmic losses in back grid	Electrical	6.2.9
E-4	Ohmic losses in module interconnect	Electrical	6.2.10
E-5	P2 contact resistance	Electrical	6.2.11
E-6a	P1 shunts	Electrical	6.2.12
E-6b	P3 shunts	Electrical	6.2.12
E-7a	External front contact resistance	Electrical	6.2.13
E-7b	External back contact resistance	Electrical	6.2.13

Shaded elements are still electrically connected to the cell or module. Therefore, generated current in other elements can flow backwards through these elements, which is directly annihilated for power generation. This additional loss effect is included in the loss of local MPP mismatch in Section 6.2.7.

6.2.3 Module Interconnect Area Loss

All finite elements within the P1, P2, and P3 areas do not generate any photocurrent since they are only used for connecting two monolithically interconnected cells and there is no operative p-n junction present. Therefore, the resulting optical losses can be determined by calculating all non-cell elements $k \in \mathcal{K} \setminus \mathcal{C}$ out from the entire area.

$$P_{\text{loss}}^{\text{inter}} = \frac{P_{\text{SC}}}{A_{\text{tot}}} \cdot \sum_{k \in \mathcal{K} \setminus \mathcal{C}} \omega_k \cdot (1 - f_{\text{shade}}^k) \quad (6.4)$$

By modifying the cell width, the tradeoff between the geometrical fill factor ^[286, 287] and too much current flow can be adapted. The latter results in large resistive ohmic losses ^[288] since the lost power quadratically depends on the generated current per cell. However, this tradeoff is strongly depending on illumination conditions ^[289].

6.2.4 Grid Shading

Within the actual module layer stack, the grid pattern is the first structure that is hit by incident light. For the vast majority of grid designs, the assumption of entirely opaque grid fingers is valid, which leads to $f_{\text{grid}}^k = 1$. However, this work's simulation allows to use semitransparent grid structures as well resulting in the following loss power.

$$P_{\text{loss}}^{\text{grid}} = \frac{P_{\text{SC}}}{A_{\text{tot}}} \cdot \sum_{k \in \mathcal{C}} \omega_k \cdot (1 - f_{\text{shade}}^k) \cdot f_{\text{grid}}^k \quad (6.5)$$

6.2.5 Tilted Effective Area

Modules in the field that are not directly faced towards the sun suffer from the loss of effective area within the sun light. The loss factor f_{tilt} can be trigonometrically calculated when the angle of incidence ϑ_0 is given by

$$f_{\text{tilt}} = \frac{1}{\cos(\vartheta_0)}. \quad (6.6)$$

This factor straight-forwardly goes into the area-weighted summation of all elements.

$$P_{\text{loss}}^{\text{tilt}} = \frac{P_{\text{SC}}}{A_{\text{tot}}} \cdot \sum_{k \in \mathcal{C}} \omega_k \cdot (1 - f_{\text{shade}}^k) \cdot (1 - f_{\text{grid}}^k) \cdot f_{\text{tilt}}^k \quad (6.7)$$

The angle ϑ_0 can be calculated from basic mathematics and does depend on the mounting angle as well as on the time-dependent angle as the Earth rotates.

6.2.6 Reflection, Parasitic Absorption, and Incomplete Absorption

Finally, all light that hits the actual layer stack of each element is known and in most cases given spectrally resolved. Cells that are exposed to this light are modeled by an optical approach like the Lambert-Beer method or the TMM procedure as described in Sections 4.2.1 and 4.2.2. For each element k , a spectrally weighted reflection factor f_{refl}^k , parasitic absorption factor f_{abs}^k , and incomplete absorption factor f_{trans}^k are calculated, respectively. These coefficients also depend on the angle of incidence ϑ_0 as mentioned in Section 4.2.2. Therefore, the effect of a tilted incoming solar ray is considered in the effective area (last section) as well as in the modified reflection (this section). The absolute loss in reflection can be calculated by

$$P_{\text{loss}}^{\text{refl}} = \frac{P_{\text{SC}}}{A_{\text{tot}}} \cdot \sum_{k \in \mathcal{C}} \omega_k \cdot (1 - f_{\text{shade}}^k) \cdot (1 - f_{\text{grid}}^k) \cdot (1 - f_{\text{tilt}}^k) \cdot f_{\text{refl}}^k. \quad (6.8)$$

In practice, the total parasitic absorption of each element is split into each of the different parasitic materials l . Therefore, for the k -th finite element the parasitic absorption in the l -th layer is expressed by the relative factor $f_{\text{abs}}^{k,l}$. The entire absolute parasitic absorption loss is given by

$$P_{\text{loss}}^{\text{abs}} = \frac{P_{\text{SC}}}{A_{\text{tot}}} \cdot \sum_{k \in \mathcal{C}} \omega_k \cdot (1 - f_{\text{shade}}^k) \cdot (1 - f_{\text{grid}}^k) \cdot (1 - f_{\text{tilt}}^k) \cdot \sum_{\substack{l \in \text{paras.} \\ \text{layers}}} f_{\text{abs}}^{k,l}. \quad (6.9)$$

Finally, the relative light transmission f_{trans}^k of the k -th element is called incomplete absorption loss. As for the other two losses, the incomplete absorption is an area-weighted sum over all finite elements within the active cell area \mathcal{C} .

$$P_{\text{loss}}^{\text{trans}} = \frac{P_{\text{SC}}}{A_{\text{tot}}} \cdot \sum_{k \in \mathcal{C}} \omega_k \cdot (1 - f_{\text{shade}}^k) \cdot (1 - f_{\text{grid}}^k) \cdot (1 - f_{\text{tilt}}^k) \cdot f_{\text{trans}}^k \quad (6.10)$$

6.2.7 Local MPP Mismatch

Due to resistive losses within the contact layer, the spatial voltage distribution across a cell is not homogeneous, not even for homogeneous cell materials. In fact, with increasing distance from the external cell contacts, the voltage drop from the front to the back side potential in the k -th element $\Phi_{\text{back}}^k - \Phi_{\text{front}}^k$ increases. This voltage drop will be called the local operating voltage V_k . Since it is non-negligibly higher than the MPP voltage of the internal semiconductor I–V curve for most elements, the net generated current I_{net}^k within these elements according to the Equation (4.18) is lower as well. Hence, the locally decreased net generated current densities add up to a total loss in the generated current I_{out} . To finally calculate a total loss power from this lack of current, the actually generated power of each finite element within the non-grid area $\mathcal{C} \setminus \mathcal{G}$ is summed up and subtracted from the power that every element could produce if it were at its MPP.

$$P_{\text{loss}}^{\text{MPP}} = \frac{P_{\text{SC}}}{A_{\text{tot}}} \cdot \sum_{k \in \mathcal{C}} \omega_k \cdot f_{\text{optics}}^k - \sum_{k \in \mathcal{C} \setminus \mathcal{G}} \omega_k \cdot I_{\text{net}}^k \cdot (\Phi_{\text{back}}^k - \Phi_{\text{front}}^k) \quad (6.11)$$

6.2.8 Reverse Current under Grid

Losses due to the shading of the grid have already been considered optically in Section 6.2.4. Since they are connected electrically to other current generating finite elements, electrical losses can happen as well due to their non-perfect shunting properties. Current can flow backwards and be annihilated for actual power generation, which results in a positive I_{net}^k in Equation (4.18). The final power loss is calculated as the sum of all shunt currents I_{sh}^k within all finite elements with grid on top multiplied with their corresponding local voltage drop.

$$P_{\text{loss}}^{\text{rev}} = \sum_{k \in \mathcal{C} \cap \mathcal{G}} I_{\text{net}}^k \cdot (\Phi_{\text{front}}^k - \Phi_{\text{back}}^k) \quad (6.12)$$

6.2.9 Ohmic Losses in Contact Layers

Locally generated currents need to be guided towards an external cell contact by conducting layers. Due to their finite conductivity, resistive losses occur within the resistor from every element k to its neighbors $n \in \mathcal{N}(k)$. To determine the entire power loss in the l -th conducting layer, a summation over all elements and all of its neighbors is required.

$$P_{\text{loss}}^{\text{ohm},l} = \sum_{k \in \mathcal{C}} \sum_{n \in \mathcal{N}(k)} R_l^{k,n} \cdot (I_l^{k,n})^2 \quad (6.13)$$

Here, l can be the top or bottom TCO layer, but also the top or bottom grid layer. In practice, each of those four losses are calculated separately.

6.2.10 Ohmic Losses in Module Interconnect

Resistive losses also occur within the interconnect. According to Figure 2.9, they can be split into three different regions: The transport losses within the front contact of the P1 and P2 region including the gap between those two, the ohmic path losses within the interconnecting P2 region, and the transport losses within the back contact of the P2 and P3 region including the gap between those two. Each of them can be determined by Ohm's law. While the two lateral losses depend on the lumped resistance $R_{\text{front}}^{k,n}$ and $R_{\text{back}}^{k,n}$, the horizontal loss within the P2 region only depends on the resistivity ρ_{TCO}^k within the front TCO according to Equation (4.35).

$$\begin{aligned}
P_{\text{loss}}^{\text{P2 ohm}} &= \sum_{\substack{k \in \mathcal{P}_1 \\ \cup \mathcal{S}_{12} \cup \mathcal{P}_2}} \sum_{n \in \mathcal{N}(k)} R_{\text{front}}^{k,n} \cdot \left(I_{\text{front}}^{k,n}\right)^2 \\
&+ \sum_{k \in \mathcal{P}_2} \frac{\rho_{\text{TCO}}^k d_{\text{absorber}}^k}{\omega_k} \cdot \left(I_{\text{P2}}^k\right)^2 \\
&+ \sum_{\substack{k \in \mathcal{P}_2 \\ \cup \mathcal{S}_{23} \cup \mathcal{P}_3}} \sum_{n \in \mathcal{N}(k)} R_{\text{back}}^{k,n} \cdot \left(I_{\text{back}}^{k,n}\right)^2
\end{aligned} \tag{6.14}$$

6.2.11 P2 Contact Resistance

Since two conducting materials form a joint interface within the P2 region, a contact resistance can occur. According to Equation (4.35), the area-normalized contact resistivity $r_{\text{P2}}^{\text{cont}}$ can be used to calculate the total power loss. In practice, this contact resistance between the front TCO and the back conductor is typically low and can be neglected. Nevertheless, it is still listed here as a loss path.

$$P_{\text{loss}}^{\text{P2 cont}} = \sum_{k \in \mathcal{P}_2} \frac{r_{\text{P2}}^{\text{cont}}}{\omega_k} \cdot \left(I_{\text{P2}}^k\right)^2 \tag{6.15}$$

6.2.12 P1 and P3 Shunts

At the P1 trench as well as at the P3 trench are possibilities for shunting effects. As shown in Figure 2.9, shunting currents along both red paths can flow in the reversed direction and counteract the photocurrent generation. The total power loss across the P1 trench can be calculated by Ohm's law within all neighboring elements $n \in \mathcal{N}(k)$ of all elements k that are within the the P1 region \mathcal{P}_1 and its adjacent gap region \mathcal{S}_{12} .

$$P_{\text{loss}}^{\text{P1}} = \sum_{k \in \mathcal{P}_1 \cup \mathcal{S}_{12}} \sum_{n \in \mathcal{N}(k)} R_{\text{back}}^{k,n} \cdot \left(I_{\text{back}}^{k,n}\right)^2 \tag{6.16}$$

Within the P1 trench, often the space charge region plays a crucial role in prohibiting shunting paths^[137]. Analogously, the loss across P3 can also be calculated via

$$P_{\text{loss}}^{\text{P3}} = \sum_{k \in \mathcal{S}_{23} \cup \mathcal{P}_3} \sum_{n \in \mathcal{N}(k)} R_{\text{front}}^{k,n} \cdot \left(I_{\text{front}}^{k,n}\right)^2. \tag{6.17}$$

However, shunting effects across the P3 trench can be neglected in practice very often since the isolating material is air, which has a comparably good dielectric strength. Nevertheless, parasitic splinters in fact can short P3 gaps.

6.2.13 External Contact Resistance

Finally, a contact resistance is possible at finite elements that have an external cell contact and therefore belong to $\mathcal{E}_{\text{front}}$ or $\mathcal{E}_{\text{back}}$. This might be due to the contact ribbon for modules in the field or due to the measuring tips for solar cells in the laboratory. Following Equations (4.29a) and (4.29b) the total power loss due to contact resistances is given by the sum of both front- and backside effects.

$$P_{\text{loss}}^{\text{cont}} = \sum_{k \in \mathcal{E}_{\text{front}}} \frac{(\Phi_{\text{front}}^k - V_{\text{op}})^2}{R_{\text{front},k}^{\text{cont}}} + \sum_{k \in \mathcal{E}_{\text{back}}} \frac{(\Phi_{\text{back}}^k)^2}{R_{\text{back},k}^{\text{cont}}} \quad (6.18)$$

6.3 Applied Loss Analysis on Solar Cells

This section introduces a first applied loss analysis of thin-film solar cells. The same cells as in Section 5.3 are used. If larger cells were used, electrical losses would be much more prominent. All electrical and optical losses will be calculated and plotted as a function of different quantities [290]. However, in order to first gain the reader's trust, the reflectance loss and overall achieved PCE is validated experimentally in the beginning.

6.3.1 Verification by Reflection Measurements

To verify the simulated data, experimental reflection measurements have been performed. Samples with the entire multi-layer cell stacks are measured for their wavelength-dependent reflectance $R(\lambda)$. The orange dashed line in Figure 6.2 shows the reflectance of a cell with a TCO thickness of 111 nm. Typical distinct thin-film interferences can be observed.

The upper blue line in Figure 6.2 shows the AM1.5G spectrum up to 1200 nm. To calculate the totally reflected power, the input AM1.5G spectrum is weighted with the spectrally resolved reflection $\text{AM1.5G}(\lambda) \cdot R(\lambda)$. The result can be seen as the lower blue line in Figure 6.2. The quantity of interest will be the weighted and integrated reflection up to the absorber band gap of 1.13 eV, which is equal to 1100 nm. This weighted reflectance R_w is visually represented as the light blue area under the lower blue curve and can be calculated via

$$R_w(d_{\text{AZO}}) = \frac{\int_0^{\lambda_{\text{gap}}} \text{AM1.5G}(\lambda) \cdot R(\lambda)}{\int_0^{\lambda_{\text{gap}}} \text{AM1.5G}(\lambda)}. \quad (6.19)$$

This procedure has been performed for multiple thicknesses of the top layer TCO and the resulting weighted reflectance $R_w(d_{\text{AZO}})$ plotted as a function of TCO thickness in Figure 6.3 as orange crosses. The same reflectance calculations have been performed on the digital TMM model of the entire layer stack. The blue line in Figure 6.3 represents the simulated weighted reflectance, which is calculated the same way as the experimental reflectance in Equation (6.19). Thin-film

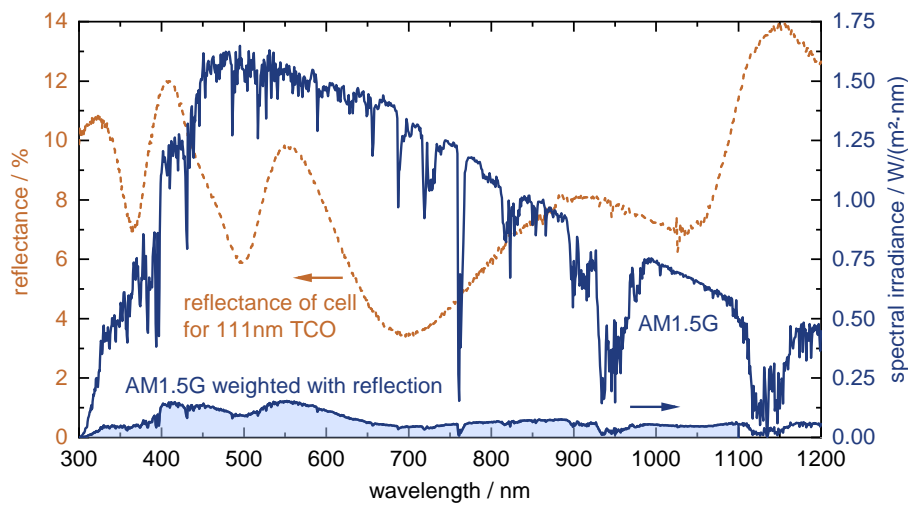


Figure 6.2: Measured wavelength-dependent reflection of a CIGS cell. The upper blue spectrum is the AM1.5G spectrum, while the lower one is the multiplication of the AM1.5G spectrum with the orange reflection. The integrated light blue area represents the spectrum-weighted reflection for the loss analysis.

interferences can be seen for different thicknesses. Finally, the agreement of both experimental and simulated data shows the reliability of the optical simulation model. Especially, the close match to the simulated reflection at the interference patterns at 100 nm and 250 nm reveals the accurate optical model.

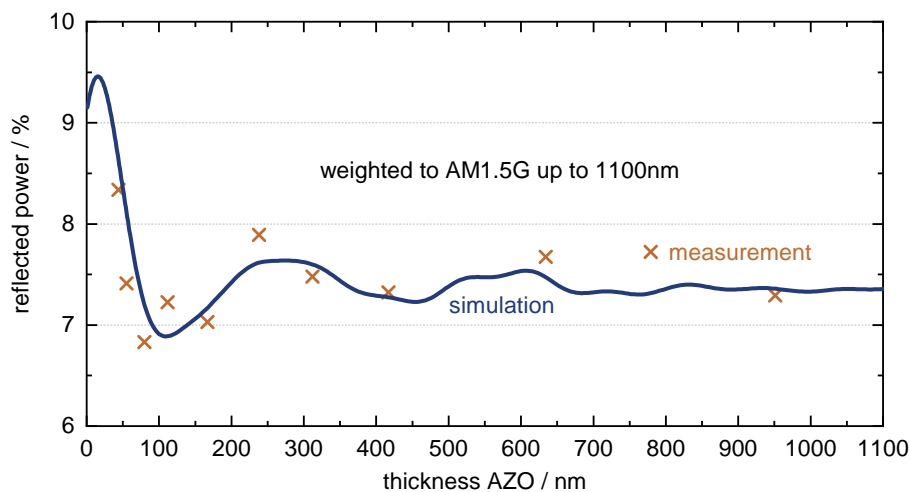


Figure 6.3: Comparison of simulated and measured AM1.5G-weighted reflections. All orange measurement points are determined as shown in Figure 6.2 and described in the main text. The blue curve represents the simulated reflected power from a TMM simulation.

6.3.2 Comparing Measured Data to Simulated Loss Analysis

Finally, an entire loss analysis can be performed with the absorber material as input I–V curve, as shown in Figure 6.4. The latter was calculated via the REF procedure. All optical losses are calculated with the TMM approach. Parasitic absorption in each of the buffer and window layers all together are a large fraction of power loss. As it can be seen in Figure 5.6, most of the parasitic light

absorption happens in the ultraviolet (UV) range of the spectrum due to the high band gap of the buffer materials. The largest individual loss is the above described reflection. Both experimentally measured and simulated loss values are shown in the graph and match well to each other.

The largest electrical loss mechanism is the resistive loss within the AZO layer since the back conducting layer is a metallic molybdenum (Mo) contact. Ohmic losses in the contact layers always result in spatially distributed voltage gradients, which straightforwardly result in local MPP mismatches. Losses due to the local MPP mismatch are the second largest electrical loss mechanism. Finally, I-V measurements have been performed on multiple cells and the resulting PCE plotted as black dots in Figure 6.4. Despite the large standard deviation of the experimental measurements, the median PCE agrees very well with the digitally forecast PCE of 18 %.

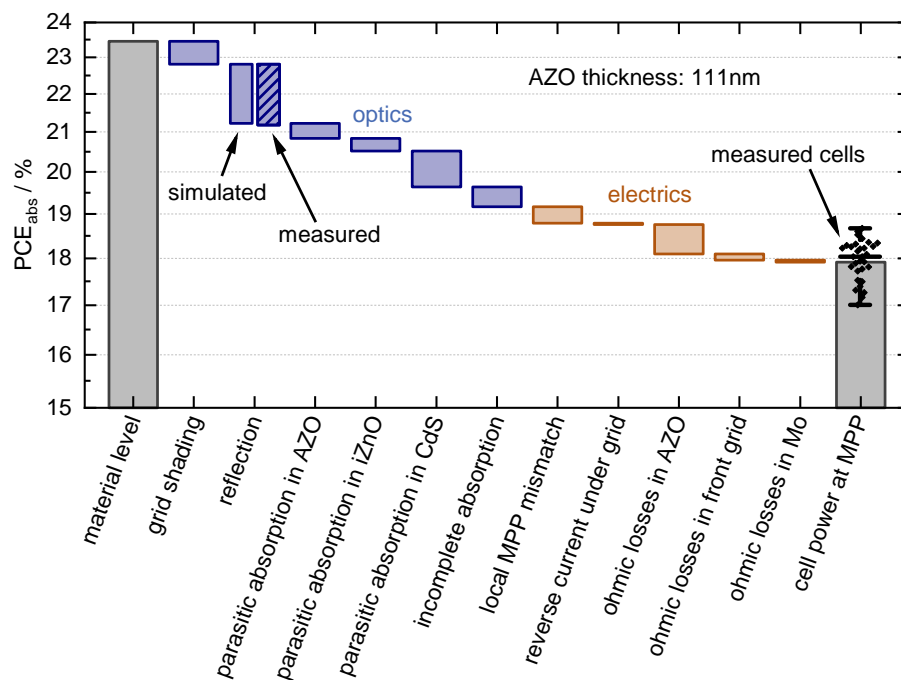


Figure 6.4: Loss analysis of a CIGS cell with a 111 nm thick AZO layer as front contact. All losses are simulated and shown in the graph. Moreover, the reflection losses are measured as described above and plotted as well. Furthermore, the finally measured PCE of all measured cells are shown in the graph.

6.3.3 Finding the Ideal TCO Thickness

Without any optical and electrical losses, the REF-fitted semiconductor material curve has a PCE of 23.46 %, which can be achieved at $V_{oc} = 619$ mV. Depending on the thickness of the front TCO layer, the coupled simulation predicts cell efficiencies between 14 % and 18 %. An exact shape of the TCO thickness-dependent PCE behavior can be seen in Figure 6.5. For the examined cell setup with its given layer stack and geometry, a maximum efficiency of around 18 % is possible for a TCO thickness of around 150 nm. As mentioned previously, this simulation can quickly answer the often discussed question in literature of the ideal thickness of the front TCO layer. The exact calculation of the optimum PCE is a significant improvement with respect to the conventional empirical determination. In fact, the simulation assigns and quantifies all power losses between the material level and the cell level instead of only calculating the optimum TCO thickness.

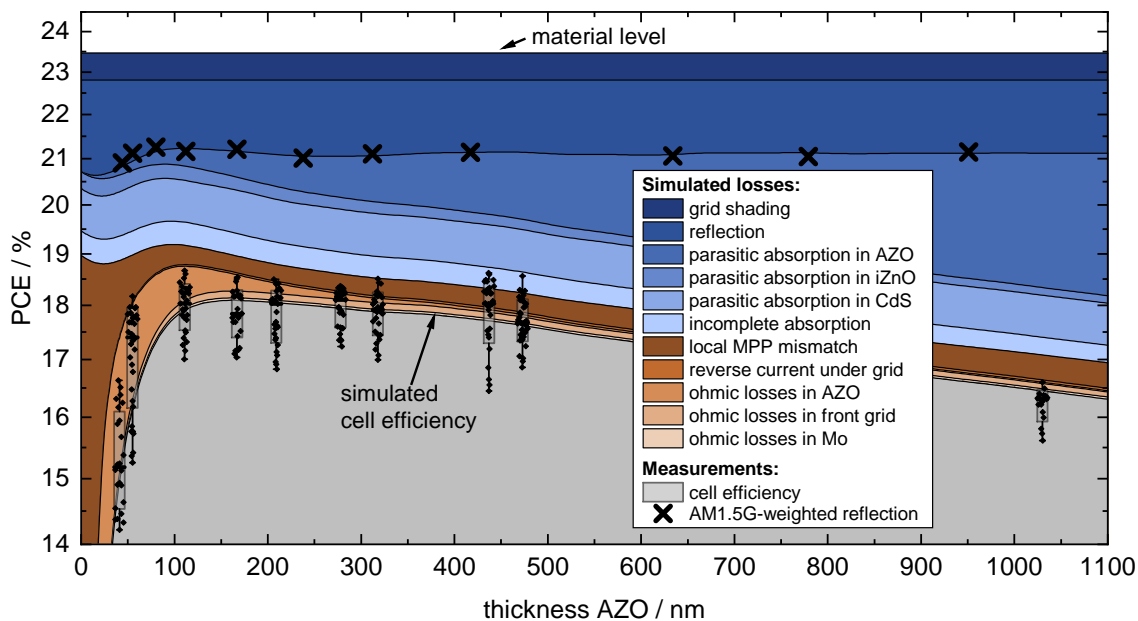


Figure 6.5: Loss analysis plotted as a function of the contact layer thickness. All electrical (orange) and optical (blue) losses are determined with the described methodology. Two experimental verification measurements are shown. The reflectance from Figure 6.3 is marked with black crosses and the finally measured PCE of the cells are plotted as black box plots.

As in the analysis before, the losses are allocated to their mechanisms and split up into optical (blue) and electrical (orange) losses. The calculated analysis can be used to identify the main loss mechanisms, which helps to improve the PCE of thin-film solar cells. For cells with a thicker TCO layer, optical losses, especially parasitic absorption in the TCO layer, are the dominant loss mechanisms. Yet, cells with a comparably thin TCO layer suffer from ohmic losses in the front TCO layer. As explained in the section above, the high sheet resistances due to the thin TCO layer cause a large gradient in the electrical voltage distribution, which lead to large local voltage drops close to V_{oc} for many locations of the cell. This inhibits the current generation and therefore is called local MPP mismatch. The corresponding loss is plotted in dark orange in Figure 6.5. Due to the sufficiently high shunt resistance, the reverse current underneath the grid does not have a large impact on the PCE for any TCO thickness. Finally, incomplete absorption is the power, which is transmitted through the absorber layer. Due to the typically high absorptance of the absorber layer, this optical power is mainly in the infrared (IR) part of the spectrum at energies lower than the absorber band gap. The power loss due to incomplete absorption is mainly constant as a function of the TCO layer thickness. However, some light power is absorbed within the front TCO in the corresponding spectral range. This reduces the power loss due to incomplete absorption from $0.5\%_{rel}$ for an infinitesimally thin TCO layer down to $0.3\%_{rel}$ for 1100 nm TCO.

The reflection measurements from Figure 6.3 are shown in Figure 6.5 as black crosses again for reference. The black box plots in Figure 6.5 represent experimentally measured cell data as shown in Figure 6.4 for a single TCO thickness. The height of the boxes is calculated from the standard deviation of around 30 cells each. Their behavior as a function of the TCO layer thickness matches well with the simulated PCE. Again, this validates the interplay of the optical and electrical model.

As an advantage of the simulation, hypothetical technological improvements can be assumed and their expected impact on the cell performance can be investigated. Exemplarily, an improved conductivity of the front TCO layer of 30 % results in a differently shaped PCE behavior than the one plotted in Figure 6.5. Its efficiencies reach 0.72 %_{rel} higher for a TCO layer thickness of 140 nm. An improvement of the optical extinction coefficient (imaginary part k of the complex refractive index) by 30 % would increase the PCE by only 0.66 %_{rel} for an optimum thickness of 170 nm. Combining both improvements could boost the PCE by 1.27 %_{rel} up to 18.32 %.

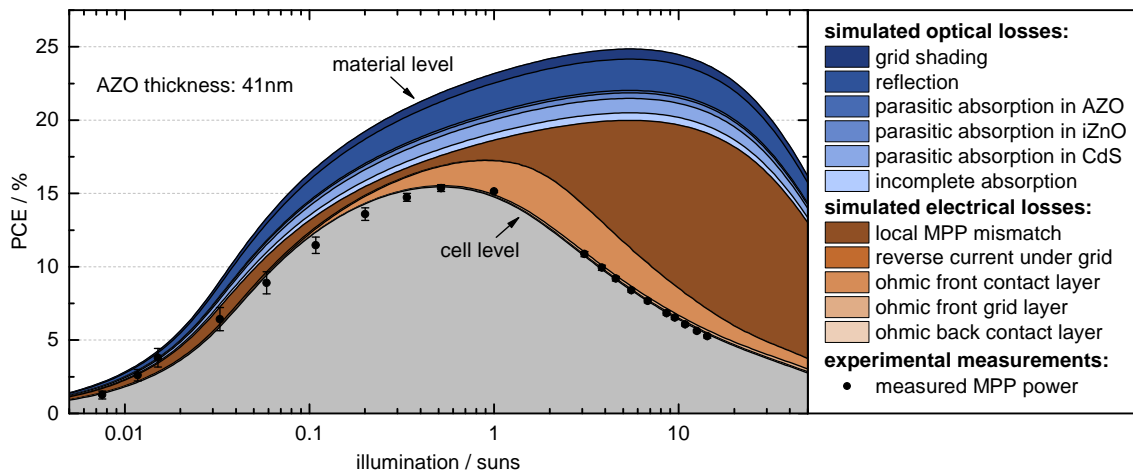
6.3.4 Different TCO Thicknesses Suitable for Different Irradiation Intensities

Since high efficiencies can be achieved by a concentrator technology in the wafer technology^[291] as well as in thin-film technology^[292], it is worth taking a look at the loss analysis for concentrated light conditions. Moreover, modules in the field often receive less than the standardized 1000 W/m² at STC. Therefore, the low-light behavior also needs to be part of comprehensive loss investigations.

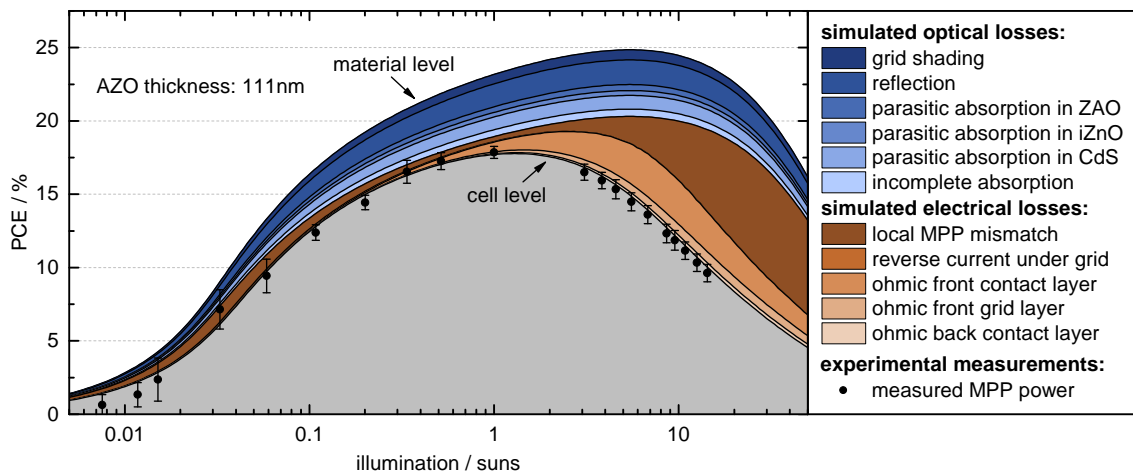
For three different thicknesses of the TCO layer, different illumination intensities with the same spectral distribution have been investigated. The resulting PCE in Figure 6.6 shows that the optical and electrical behaviors change dramatically as a function of irradiation intensity. As in the previous loss plots, the top line represents the efficiency of the absorber material, all electrical losses are plotted in orange, all optical losses in blue and the final simulated cell efficiency is shown in gray. Moreover, four cells for each thickness are measured and their resulting PCE at the different illumination intensities are shown as black data points with their standard deviation as error bar. Experimentally the low intensities are realized with neutral density filters. Since the high intensities are achieved with a focusing lens, the high power densities need to be thermally stabilized. This was realized by a cooling system with a nitrogen gas stream. For the simulation, the different intensities are achieved by a multiplication of the AM1.5G spectrum by the corresponding amount of suns.

The simulation data lies well within the error bars of the corresponding four measured cells. This confirms once more the accuracy of the optical and electrical approach as well as the interplay of both models. Especially the local MPP mismatch is simulated precisely, which primarily can be seen for the thin samples. The two drops towards high and low irradiation intensities are due to the series and shunt resistance. From the correct modeling of these two features, it can be seen that the established model is appropriate and generated with correct simulation parameters.

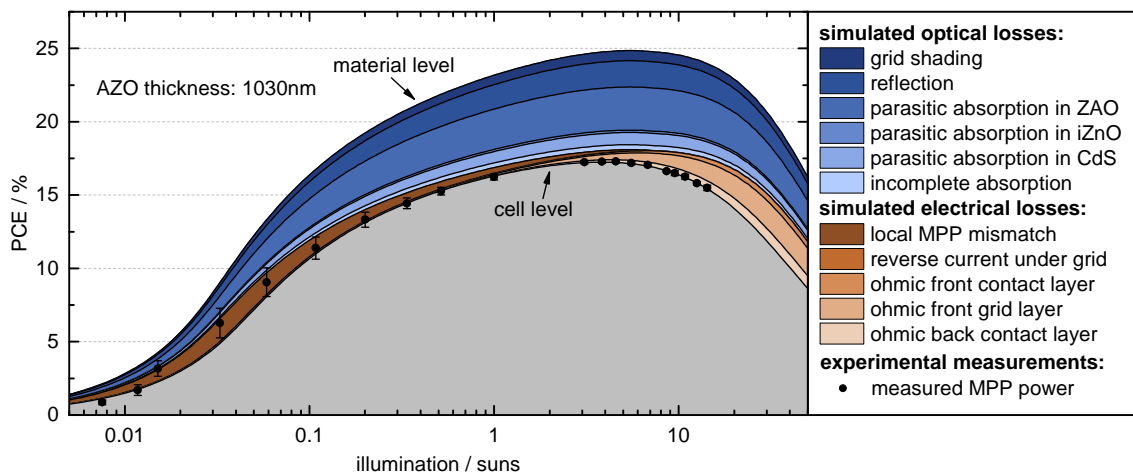
Different irradiation intensities favour different TCO layer thicknesses in order to optimize the device efficiency. Exemplarily, at 4 suns an AZO layer thickness of 1030 nm is the most efficient one. These thick TCO layers offer such a good conductivity that even for high irradiation intensities and therefore high internal currents, no substantial electric losses occur. However, their thick window layer causes larger optical losses, which leads to an irradiance-independent damping of the incident light power. This effect prohibits these cells from being efficient record cells, but enables them to have a broad maximum as a function of the incident light power. Thinner cells however, achieve a higher maximum PCE, as it can be seen for cells with a 111 nm thick TCO layer in Figure 6.6b. This difference in their absolute height is due to the differently pronounced optical absorption for the three layer thicknesses.



(a) Illumination-dependent loss analysis for a CIGS cell with a 41 nm thick front TCO layer.



(b) Illumination-dependent loss analysis for a CIGS cell with a 111 nm thick front TCO layer.



(c) Illumination-dependent loss analysis for a CIGS cell with a 1030 nm thick front TCO layer.

Figure 6.6: Illumination-dependent loss analysis for different thickness of the front contact layer. Thin layers show large electrical losses, while thick TCO layers mainly result in optical losses. For each configuration, a different optimum illumination is observed, which is larger for thicker contact layers.

6.4 Applied Loss Analysis on Solar Modules

To address the industry-oriented aspect of this work, this section also examines modules instead of just cells. Therefore, the module N-G1000E105 from NICE Solar Energy GmbH was analyzed. This module has a spatial dimension of 1200 mm × 600 mm and an edge area of 19 mm and 9 mm on the top and bottom sides, respectively. The edge and contact area on both long sides is given by 14.4 mm. The remaining active area of 6695 cm² is split into 144 monolithically interconnected cells. The interconnect width between the single cells is 265 μm. Hence, each individual cell has a height of 1172 mm and a width of around 4 mm. The total inactive edge and contact area can be calculated from the dimensions given above to be 505 cm², which accounts for around 7% of the total module area. The investigated module has the following layer stack: 400 nm Mo / 2100 nm CIGS / 50 nm CdS / 50 nm i-ZnO / 800 nm AZO / 750 μm encapsulant film / 3.2 mm top side anti-reflective coating (ARC)-coated low-iron solar float glass. More details can be found in [228].

To gain a holistic model of the monolithically integrated module, the methodology of this work is combined with a drift-diffusion model. Therefore, consequences on the semiconductor material level can be investigated as well.

6.4.1 Evolving the Digital Model and its Parameters under Standard Testing Conditions

As for modeling cells, all measurable quantities of the module are implemented into the digital model. These are mainly the geometrical data as mentioned above, the optical data in the form of complex refractive indices of all thin-film layers and the encapsulant layer as well as electric data in the form of specific resistivities of all conducting layers. Afterwards, for the drift-diffusion model, data from literature was implemented [92, 293, 294, 295, 296, 297]. All quantities can be found in Table 6.2 as the non-bold numbers. Both density of states (DOS) are given at 300 K. Since within drift-diffusion models, also the non-lateral out-of-plane direction is considered, gradients in the GGI profile need to be taken into account. The behavior within this absorber has a linear grading from 0.2 to 0.4. Since the band gap strongly depends on the GGI, the conversion formula

$$E_{\text{gap}}(\text{GGI}) = (1 - \text{GGI}) \cdot E_{\text{gap,CIS}} + \text{GGI} \cdot E_{\text{gap,CGS}} + b \cdot \text{GGI} \cdot (1 - \text{GGI}) \quad (6.20)$$

is used, where the band gaps $E_{\text{gap,CIS}} = 1.04 \text{ eV}$ and $E_{\text{gap,CGS}} = 1.68 \text{ eV}$ and the bowing factor 0.2 are used within this work [298, 299]. The fitted donor density within the CdS and the acceptor density within the CIGS layer is on a comparable level with values found in literature [293, 294, 92, 295, 296]. However, evidence for a noticeably higher electron mobility of $\mu_e = 200 \frac{\text{cm}}{\text{V}\cdot\text{s}}$ instead of the commonly used value of $100 \frac{\text{cm}}{\text{V}\cdot\text{s}}$ [92, 294, 295, 296, 297] has been found, which results in a higher electron diffusion length.

After implementing all geometrical, optical, and electrical quantities, a REF procedure is executed in order to get parameters for the drift-diffusion model. Therefore, experimental I-V data is needed, which can be found as black points in Figure 6.7. The module I-V characteristic is broken down to a single monolithically integrated cell with a V_{oc} of around 0.7 V. First of all, it is noticeable that the shunting effect is of the same size at every point, regardless of the voltage. Hence, there are no large jumps within the I-V curve. This indicates that each individual cell has an equally large, homogeneous shunting effect and justifies the assumption of a sufficiently homogeneous p-n junction for all finite elements without pronounced hot-spot shunt regions in individual cells.

Table 6.2: Material parameters for the drift-diffusion model. All REF-fitted quantities are printed in bold numbers. All other values are adapted from literature. Both effective DOS are at 300 K.

		CIGS	CdS	i:ZnO	AZO
thickness	d / nm	2100	50	50	800
band gap	$E_{\text{gap}} / \text{eV}$	1.13 - 1.25	2.4	3.3	3.3
chemical potential	χ / eV	4.5	4.2	4.45	4.45
relative permittivity	ϵ_r	12.9	10	9	9
eff. conduction band DOS	$N_c / \frac{1}{\text{cm}^3}$	$2.2 \cdot 10^{18}$	$2.2 \cdot 10^{18}$	$2.2 \cdot 10^{18}$	$2.2 \cdot 10^{18}$
eff. valence band DOS	$N_v / \frac{1}{\text{cm}^3}$	$1.8 \cdot 10^{19}$	$1.8 \cdot 10^{19}$	$1.8 \cdot 10^{19}$	$1.8 \cdot 10^{19}$
donor density	$N_D / \frac{1}{\text{cm}^3}$	-	$1 \cdot 10^{17}$	-	$1 \cdot 10^{19}$
acceptor density	$N_A / \frac{1}{\text{cm}^3}$	$3 \cdot 10^{15}$	-	-	-
electron mobility	$\mu_e / \frac{\text{cm}}{\text{Vs}}$	200	100	100	100
hole mobility	$\mu_h / \frac{\text{cm}}{\text{Vs}}$	25	25	25	25

This data is used for a three-level REF procedure down to the drift-diffusion model. In contrast to the previously used methodology, a third numerical simulation is included and therefore the inputs for the horizontal drift-diffusion model are fitted instead of diode parameters. This way, the experimentally difficult to access donor and acceptor densities and the charge carrier mobilities within the CIGS and CdS layer can be fitted. The resulting numbers of the three-level REF procedure can be found as bold numbers in Table 6.2.

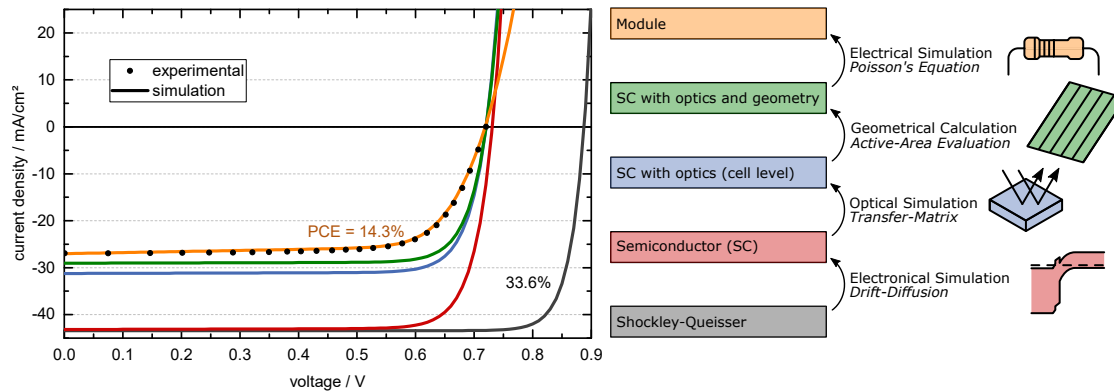


Figure 6.7: Different I–V curves for the module N-G1000E105 from NICE Solar Energy GmbH under STC. While the black line represents the Shockley-Queisser limit, all colored curves include one loss mechanism category more. The black points show measured I–V data in the field under STC. All intermediate PCEs are given in Figure 6.8.

All in all, in this section, a drift-diffusion model was attached to the existing two-level digital model, which together forms an entirely holistic model of a solar module ^[159]. This approach enables to calculate from the Shockley-Queisser limit down to the module level and identifies all relevant loss mechanisms. A more detailed description of the linking of the different simulation levels can be found in ^[228]. In Figure 6.7, a successive addition of losses can be considered. The black line represents the Shockley-Queisser limit for the corresponding band gap of 1.13 eV. The described drift-diffusion simulation allows to account for all recombination losses, which lead to a V_{oc} drop, as it can be seen in the red I–V curve after the material level simulation. Optical effects

are not yet included, which is why j_{sc} did not change. The blue curve however was calculated from the drift-diffusion I–V characteristic and additionally considered all optical losses as reflection or parasitic absorption. A drastic decrease in j_{sc} can be observed. The resulting I–V characteristic is often referred to as cell level, since losses on the material level and inevitable optical effects are accounted for, but electrical and geometrical effects are not considered. Afterwards, all geometrical effects, such as edge area or dead area within the module interconnect are taken into account. The resulting reduction in effective cell area also affects j_{sc} , while V_{oc} is hardly changed. Finally, current collection and transport effects are considered by the quasi-three-dimensional Poisson’s equation solver. The increased series resistance within the conducting layers and an additional shunting effect on the module level reduce the fill factor. Moreover, the shunt in combination with a local MPP mismatch lead to a further reduction in j_{sc} . The final output I–V curve of the three-staged model under STC is shown in orange in Figure 6.7. Its high coefficient of determination with respect to the experimentally measured I-V data (black dots) of 99.7% reveals the high precision of the assembled model.

6.4.2 Holistic Loss Analysis from Shockley-Queisser Limit to Module Level

After presenting the development of an improved simulation model with three instead of two stages in the last section, this section reveals a loss analysis for solar modules that are actually used within the field. Still the same module N-G1000E105 is used as an example. Figure 6.8 shows the entire loss analysis on a logarithmic scale with all relevant losses. The gray bars correspond to the PCE of the I–V characteristics from Figure 6.7. All losses on the material level are allocated to a lumped loss mechanism, which is called recombination. In principle, they could be split into different recombination mechanisms, such as Shockley-Read-Hall recombination^[300, 301], Auger recombination^[302, 303], radiative recombination^[148], and recombination at surfaces and interfaces^[304]. However, their detailed analysis and the origin of those mechanisms are beyond the scope of this work.

The Shockley-Queisser level minus all lumped recombination losses reveal the material level with an absolute PCE of 25%. This is a comparably similar number as the REF procedure on the single cells in Figure 6.4. Smaller deviations arise from a different layer stack and from differently grown individual layers. Starting from the material level, a similar picture as for the cells emerges for modules as well. The most critical layer is the front contact (here AZO) with its optical and electrical losses. The largest individual loss is the optical parasitic absorption of the AZO layer, which is due to its comparably high absorption coefficient, especially in the IR range (compare Figure 5.4). The resistive losses of the AZO result in ohmic losses but also in a spatial voltage distribution, which causes local MPP mismatches. These two losses are the two major ones in the electrical part of the loss analysis. In contrast to laboratory cells, modules in the field also have large geometrical losses due to the reduction in effective area. Both the edge area at the module rim as well as the monolithic interconnect are major area loss mechanisms and contribute more than 3%_{abs} of absolute power loss. Their improvement offers a large potential for boosting the overall module PCE, which could for example be realized by smaller edge areas, shorter module interconnect trenches, or a more precise positioning of the trenches which allows smaller gaps between the individual P1, P2, and P3 trenches.

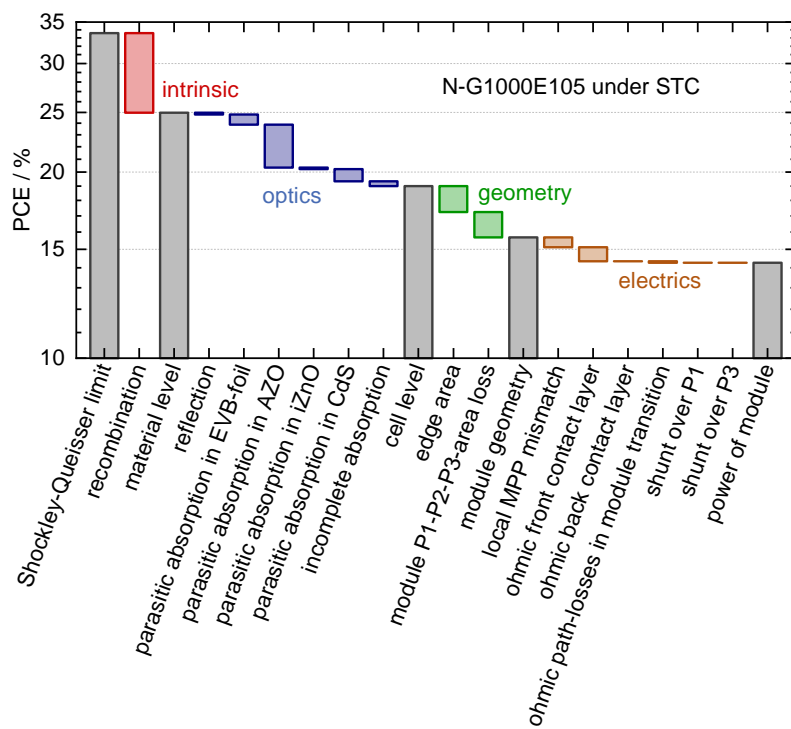


Figure 6.8: Detailed loss analysis for the module N-G1000E105 from NICE Solar Energy GmbH under STC. The losses are grouped in the different categories and correspond to the different I–V curves in Figure 6.7.



Answering this Chapter's Guiding Scientific Question

How can all relevant losses on the device level be allocated and quantified and which loss is the bottleneck for thin-film solar devices?

Optical losses can be quantified via the parasitic loss paths within the TMM approach, while electric losses due to shunting and series effects can be calculated via Ohm's law within the FEM of the diode network model. A further electrical loss arises from the high non-linearity of solar cells. It results from the spatial voltage distribution, which prohibits the solar cell from working at the MPP at all regions and is therefore called local MPP mismatch. To finalize the holistic loss analysis, geometrical losses are determined via the comparison of the additional areas besides from the effective cell area. Using this methodology, holistic loss analyses can be executed for any thin-film device. Aside from the intrinsic recombination losses, the largest power losses of devices with ARC layers arise from the front TCO layer, both electrically due to non-sufficient conductivity and optically due to parasitic absorption. Therefore, this tradeoff is a central challenge for producing high-efficiency solar devices, which can be calculated in advance with the methodology of this work. For entire modules instead of individual cells, the geometrical losses due to edge and interconnect area are also a crucial loss path.

7

Predicting Power in the Field – Time-resolved Yield Forecast for Modules Exposed to Natural Environmental Conditions

***S**ince energy yield is the most important factor for renewable power generation [305, 306, 307], this chapter describes a methodology to analyze the energy yield of thin-film solar modules as opposed to efficiency at STC. In order to gain a holistic model from the physical efficiency limit down to the actual module power, the developed methodologies of TMM and electrical FEM need to be combined with an external drift-diffusion model to account for the semiconducting p-n junction. The resulting holistic model allows multiple novel possibilities, e.g. the ab-initio yield forecast for modules in the field with variable irradiation and temperature, loss analyses at non-STC, as well as sensitivity analyses and bidirectional calculations including the fitting of material parameters via this work's REF procedure.¹*

This Chapter's Guiding Scientific Question

How can the daily yield and time-dependent losses of a thin-film solar module be forecast under real-world conditions?

¹ This chapter is based on a journal article by the author of this work to be published under M. Zinßer et al., Accepted from Communications Physics (2022) [228].

7.1 Variation of Illumination Intensities

To investigate the simulation’s precision for different illumination intensities, the same module as in Section 5.2.2 has been used. This time, it is simulated and measured not only at 1000 W/m^2 but also under non-STC. The plotted data in Figure 7.1 is the same as shown previously in Section 6.3.4. The simulated PCE is summarized here in a single plot for all TCO thicknesses. On the left side of the plot, the simulation model is checked for correct low-light conditions. From the high agreement for all TCO thicknesses, it can be concluded that the model is appropriate and the shunting resistance is implemented correctly. For large irradiation intensities, a lot of photocurrent is generated. Hence, the spatial voltage distribution is rather hilly leading to prominent losses due to local MPP mismatches. This effect decreases the PCE for too high irradiances depending on the thickness of the TCO layer. All relevant electrical losses for high photocurrents can be modeled well, which can be seen by the good agreement of the drop towards higher intensities. All in all, this batch shows the capability of the model to handle at least four orders in magnitude of different illumination intensities. This range is far more than needed for a real-world simulation.

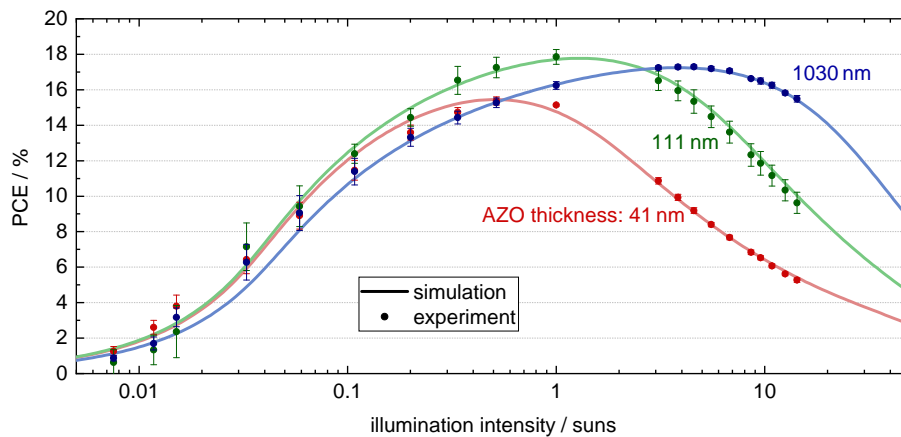


Figure 7.1: PCE of a CIGS as a function of illumination intensity. For a small irradiance, the PCE goes down due to the relatively increasing shunting resistance. For a large irradiance, the large generated current causes a large ohmic loss, forcing the PCE to shrink as well. For every thickness of the TCO, this tradeoff has its maximum for a different irradiance.

7.2 Variation of Temperature

The second big environmental impact for a module simulation with actual meteorologic data is the dependence on changing temperature. A changing module temperature mainly influences the intrinsic semiconductor properties on the material level within the p-n junction. Hence, simulations to examine the temperature-dependence must include a drift-diffusion model in order to appropriately map these effects as described in Section 6.4. However, to correctly get the temperature-dependence of the device, it must be linked with the optical and electrical model.

In Figure 7.2, the dependence of the open-circuit voltage and the fill factor as a function of the temperature can be seen for the internal p-n junction (solid lines) and for the final device (dashed lines). As described in Section 5.1.2 and shown in Figure 5.3, the impact of the temperature on the conductivity of the contact layer can be neglected in a very good approximation. However, strong

effects happen on the material level with a variable temperature. The band gap decreases with temperature^[308], but the main effect of temperature is the enhanced thermal generation of electron-hole pairs^[309]. The latter increases the intrinsic carrier concentration, which is responsible for the decreasing behavior of V_{oc} and FF with rising temperature as seen in Figure 7.2.

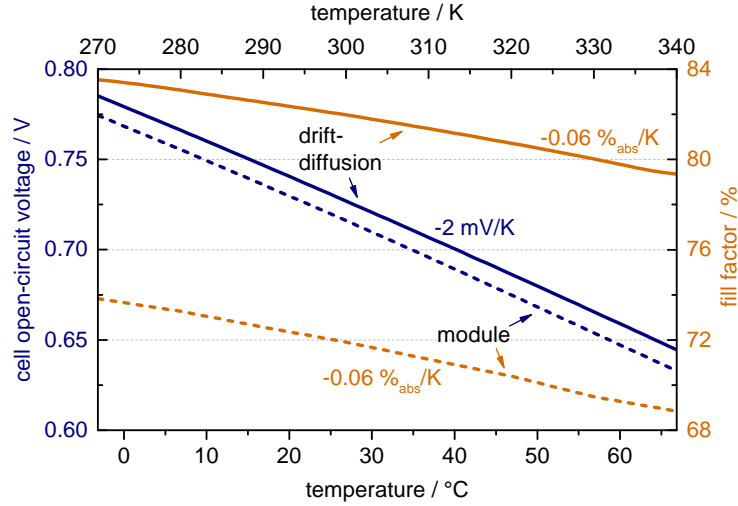


Figure 7.2: Modeled temperature-dependence of the open-circuit voltage and the fill factor. While the solid line shows the results of the drift-diffusion calculation without any optical and electrical losses, the dashed line represents the entire module behavior. With increasing temperature the intrinsic carrier concentration increases, while the band gap decreases. This leads to the observed decreasing behavior of V_{oc} and FF.

Figure 7.3 additionally shows the dependence of j_{sc} and the PCE as a function of temperature. As in Figure 7.2, the solid lines show the values calculated solely by the drift-diffusion model, whereas the dashed lines represent the overall module behavior simulated with the linkage of all three simulation stages. As expected, the photo-generated current is hardly affected by temperature, which results in an almost constant short-circuit current density. Thus, the negative impact of rising temperature on the PCE comes from the V_{oc} - and FF-dependence from Figure 7.2. As all solar-module parameters show a nearly linear temperature-dependence, temperature coefficients can be calculated. For a single cell's open-circuit voltage, a coefficient of -2.0 mV/K is observed both for the p-n junction and for the device. The fill factor also shows for both simulations the same absolute dependence of $-0.06 \text{ \%}/\text{K}$. Both effects result in a temperature-dependence of the PCE of $-0.1 \text{ \%}_{abs}/\text{K}$ for the internal p-n junction and $-0.05 \text{ \%}_{abs}/\text{K}$ for the entire device. These findings agree with practical experience^[310] and a more detailed comparison with experimentally measured temperature-dependencies in literature and theoretical calculations are shown in the next sections.

7.2.1 Comparison with Theoretical Predictions

In order to calculate theoretical predictions for temperature-dependencies of solar-module parameters, theoretical models with an empirical cubic temperature-dependence of the saturation-current density^[311] can be assumed. Using this correlation, the theoretical temperature-dependence of V_{oc} can be determined by^[312]

$$\frac{dV_{oc}}{dT} = -\frac{E_{gap}/q_e - V_{oc} + 3k_B T/q_e}{T}. \quad (7.1)$$

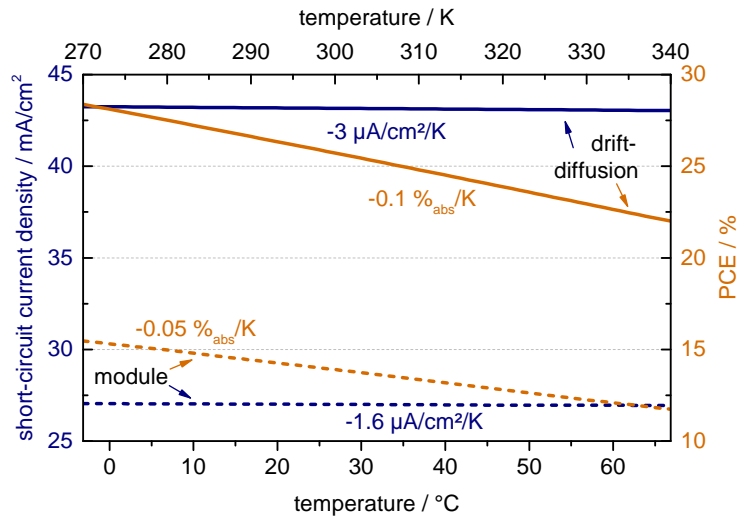


Figure 7.3: Modeled temperature-dependence of the short-circuit current density and the power conversion efficiency. While the solid line shows the results of the drift-diffusion calculation without any optical and electrical losses, the dashed line represents the entire module behavior. As expected j_{sc} is almost invariant as a function of temperature. The PCE decreases due to the temperature-dependence of V_{oc} and FF in Figure 7.2.

With the band gap of 1.13 eV of the considered module and an open-circuit voltage of 0.72 V, the theoretical dependence is given by -1.6 mV/K. This value is reasonably close to the simulated -2.0 mV/K mentioned above.

For an ideal fill factor under the assumption of no parasitic resistances, the expression

$$FF = \frac{q_e V_{oc} / (k_B T) - \log_e (q_e V_{oc} / (k_B T) + 0.72)}{q_e V_{oc} / (k_B T) + 1} \quad (7.2)$$

can be found ^[311]. From this correlation and Equation (7.1), a temperature-dependence of the fill factor can be calculated ^[313].

$$\frac{dFF}{dT} = \frac{dV_{oc}/dT - V_{oc}/T}{V_{oc} + k_B T/q_e} \cdot \left(\frac{q_e V_{oc} / (k_B T) - 0.28}{q_e V_{oc} / (k_B T) + 0.72} - FF \right) \quad (7.3)$$

With the above mentioned numbers, a theoretically predicted value of -0.015 %/K is found. This is slightly lower than the -0.06 %/K revealed by the simulation. However, these deviations can be explained by the effects of shunting and series resistances. As experimentally measured cells include these effects, the next section compares the temperature-coefficients of this work with published data in literature.

7.2.2 Comparison with Literature

In Table 7.1, the simulated temperature-dependencies of the solar-module parameters on the device level of this work are compared with experimentally measured results published in literature. Within the publication Virtuani et al ^[314], only relative values are published. Therefore, suitable solar-module parameters are assumed ($V_{oc} = 0.7$ V, $j_{sc} = 27$ mA/cm², FF = 72 %, PCE = 14 %)

and converted into absolute numbers in order to compare it with this work's simulation. The dependence of the short-circuit current density is hardly noticeable and therefore probably more affected by fluctuations than by physical findings, although in theory an increased temperature minimally boosts the j_{sc} . The simulated temperature-dependence of V_{oc} and FF of this work fits perfectly into the series of actual measurements on real-world devices. To determine the quantity $dPCE/dT$ on the device level, drift-diffusion models are not sufficient any more. The linkage with the two other simulations reveals a value of $-0.05 \text{ \%}_{abs}/K$, which is in perfect agreement with the laboratory measurements, as seen in Table 7.1.

Table 7.1: Comparison of device temperature coefficients with experimentally measured data in literature. In the publication Virtuani et al, only relative values are given, which are therefore converted via standard CIGS parameters ($V_{oc} = 0.7 \text{ V}$, $j_{sc} = 27 \text{ mA/cm}^2$, $FF = 72 \text{ \%}$, $PCE = 14 \text{ \%}$).

	$dV_{oc}/dT /$ mV/K	$dj_{sc}/dT /$ $\mu\text{A/cm}^2/K$	$dFF/dT /$ $\text{\%}_{abs}/K$	$dPCE/dT /$ $\text{\%}_{abs}/K$
Virtuani et al ^[314]	-2.2	+5.4	-0.058	-0.05
Liu et al ^[315]	-2.4	-5.1	/	-0.04
Theelen et al (Au) ^[312]	-2.1	-6.0	-0.090	-0.06
Theelen et al (In) ^[312]	-1.9	-10	-0.080	-0.05
This work's simulation	-2.0	-1.6	-0.063	-0.05

From these theoretical calculations and the comparison with experimental data, it can be concluded that with this work's holistic approach the effects of temperature can be properly modeled.

7.3 Applying Real-world Meteorological Data to the Digital Model

To simulate a real-world solar device, the CIGS module N-G1000E105 from NICE Solar Energy GmbH was mounted facing south with a fixed tilt angle of 40° without any tracking at the Zentrum für Sonnenenergie- und Wasserstoff-Forschung Baden-Württemberg (ZSW) test field Widderstall located at 09.713° N , 48.536° E and 750 m above sea level. During the exposition, I-V curve scans of the module are conducted and recorded continuously at 1 min intervals by an individual electronic load. Between the scans, the module was operated at its MPP.

As shown in the two previous sections, the effects of varying temperature and irradiance are correctly simulated by the digital model and therefore real-world data can be applied to it. This includes variations in temperature and irradiance at the same time. The incident irradiance and the module temperature on September 9, 2020 can be seen as a function of daytime in Figure 7.4. The plane of array irradiance measurement was performed with a secondary standard pyranometer. The module temperature was measured with a PT1000 resistive sensor at the rear glass surface of the module. The day September 9, 2020 was chosen as a sample day, since it was a clear day without clouds. Locally present trees cover the sun at low altitudes in the morning, which causes the kink at the left side of the irradiance graph (black line) before half past 7. Besides that, the

irradiance follows a trigonometric behavior as it is expected for the course of the sun within a day. The module temperature (blue-red line) roughly shows the same behavior as the irradiance. However, the inert thermal system causes it to lag behind the incident sunlight.

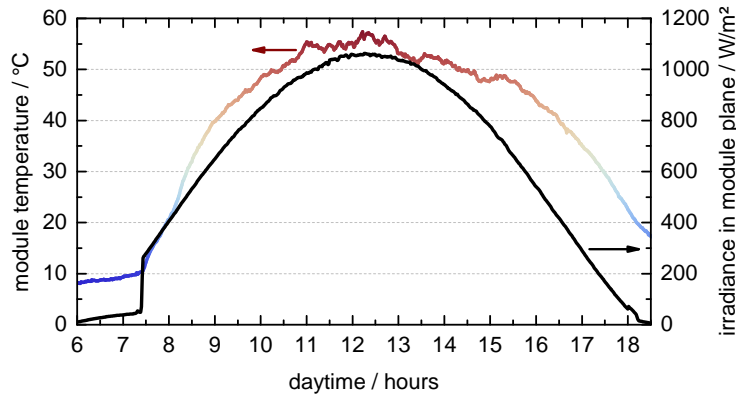


Figure 7.4: External meteorologic conditions on the solar module during daytime of September 9, 2020. The illumination intensity (black line) is measured within the module plane follows a trigonometrical dependence on the time of day. The prominent kink before 7:30 am is due to trees that block the sunlight. The temperature is measured on the back of the module (blue-red line) and shows the same behavior as the irradiance but lags behind it.

The thermal course over the day was implemented into the drift-diffusion model, whereas the corresponding irradiance conditions are fed into the TMM calculation. Finally, the generated data of both simulations is used as input for the subsequent Poisson's equation solver. The resulting simulated solar-module parameters, can be seen as orange lines in Figure 7.5 as a function of daytime. The experimentally measured data in the field is plotted as black dotted points. As there is a very high agreement of the predicted simulation data with the measured data, the interplay of all three simulation stages is proven to work accurately.

Multiple features within the experimental data can now be understood by the simulated three-stage model. The main feature of the open-circuit voltage is its fixed value of roughly 95 V most of the day. However, in the early morning and late evening hours, V_{oc} drops due to low irradiation intensities. The latter cause lower photocurrents, which have a logarithmic influence on V_{oc} . Moreover, a distinctive feature within the open-circuit voltage is its increase in the morning hours. This effect is due to the low module temperatures in the morning, as the thermal behavior lags behind the irradiance behavior. At half past 7, the nearby trees do not hide the sun any more causing a sudden increase in irradiance. Due to the inertia of the thermal system, the module is briefly exposed to high irradiance at comparably low temperatures. This combination explains the temporarily increased open-circuit voltage, which relaxes and plateaus while a thermal equilibrium is reached over time.

Since the short-circuit current is linearly dependent on the irradiance, it follows this basic behavior of the irradiance curve from Figure 7.4. This effect can be seen in the experimental as well as in the simulated data. The kink in the morning before half past 7 is due to the shadowing of the locally present trees.

Within the graph of the fill factor, there are many features that can be outlined and explained. The most prominent feature is the huge drop in the morning and evening. This can be explained with the low irradiation intensities at these times. They cause a comparably low photocurrent in contrast to the constantly present shunting currents, which decreases the fill factor due to the manipulated ratio

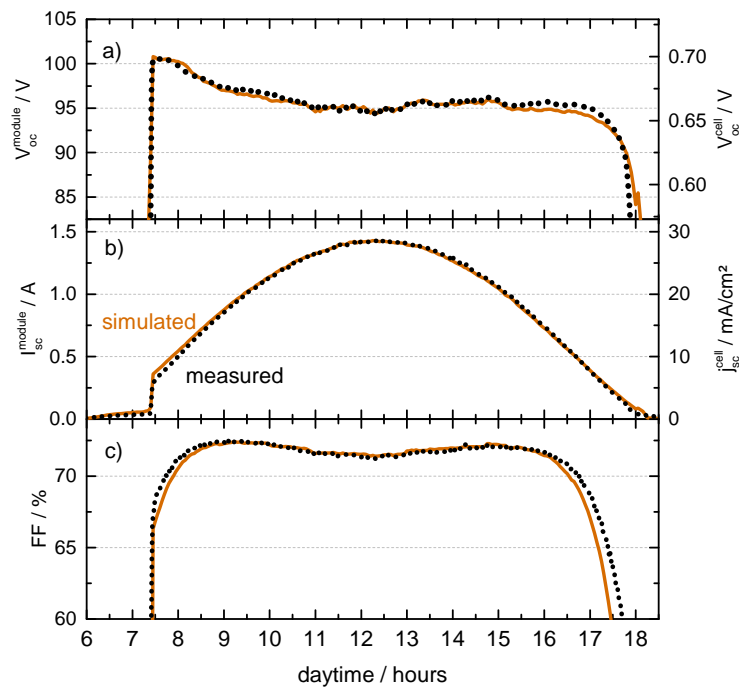


Figure 7.5: Simulated and measured solar-module parameters during daytime of September 9, 2020. The open-circuit voltage stays rather constant except for the early morning and late evening hours. The short-circuit current, on the other hand, nearly linearly follows the irradiance curve from Figure 7.4. The decrease in the fill factor in the morning and evening is due to a low photocurrent. Moreover, the saddle at noontime in the FF is due to a high temperature and a huge lateral current density.

of both. Another feature is the extensive drop around noontime. This is the result of two different effects. The first is given by the high temperatures, which decrease the fill factor within this time frame according to Figure 7.2. Secondly, the high irradiance at noon causes large generated current densities, which result in large amount of lateral currents. They cause a large gradient within the spatial voltage distribution, which is always associated with large local MPP losses and resistive losses and therefore a lower fill factor.

Figure 7.6 shows the same dependence for the temperature and irradiance on a more cloudy day (September 6, 2020). As a result of the clouds, a much more spiky temperature and illumination behavior throughout the day can be observed. As an effect of the shading by clouds, the module temperature does not go as high as for the sunny day studied above. Solar-module parameters are predicted the same way as for the sunny day and shown in graphs b), c), and d). Despite the huge fluctuations a similar good agreement between measured and simulated data can be seen. Starting at 5pm, the experimental behavior of the open-circuit voltage and the fill factor shows some deviations from the predicted values. This is due to the very low irradiation at this time. The resulting simulated I-V data is much harder to fit which causes smaller deviations, especially for the fill factor. Another source of error might be introduced by the measurement of the module temperature at the back side, which probably not exactly matches the temperature at the simulated p-n junction. Fortunately, the low irradiation intensities at these times result in low generated powers. Therefore, the absolute impact on the yield is comparably small, as it can be seen in graph e). As a result, the simulated and measured time-dependent behavior of the power match well.

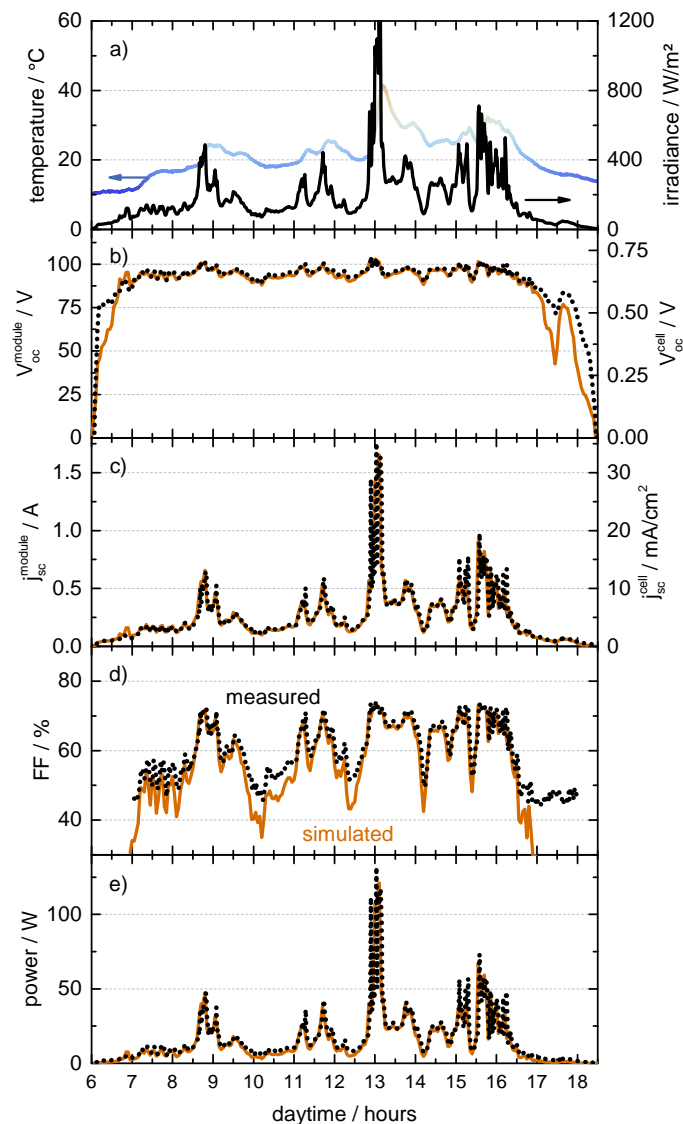


Figure 7.6: External meteorologic conditions, solar-module parameters, and produced power during daytime of September 9, 2020. The partially cloudy day shown here has more complex weather conditions than the sunny day shown in Figure 7.4. The presence of clouds introduces a jagged behavior within the time-dependent irradiance. Moreover, the module temperatures stay lower than on a sunny day.

7.4 From Shockley-Queisser to Module Power – Time-resolved Holistic Loss Analysis for Solar Modules

In Figure 7.7, a time-resolved holistic loss analysis for the module on September 9, 2020 is shown. All occurring loss mechanisms are introduced in Chapter 6. The top black curve on the edge of the red area is the determined via the Shockley-Queisser model ^[148]. It is expressed in absolute power units, is normalized to the module’s overall size and depends on the current illumination and temperature conditions from Figure 7.4. This curve represents the theoretical maximum power that could be converted under the given meteorological conditions. Within each time step, a three-stage

simulation is executed. All losses are quantified and allocated to their loss mechanism, which are marked with different colors. The material limit is given as the Shockley-Queisser power minus the intrinsic recombination losses. In theory, an optically and electrically ideal module could achieve this power. A more realistic limit is given by the infinitesimally small cell level. This takes into account all optical losses but does not suffer from any geometrical module area losses or electrical transport effects. This limit is between the blue and green areas. Finally, the imaginary infinitesimal small cell is laterally extended into a real-world module. This introduces geometrical (green areas) and electrical (orange) losses. After considering its two-dimensional expansion and the corresponding losses, the module is expected to generate the power marked by the gray area. The integration over the entire day results in a total yield of 698.9 Wh. Integrating over the experimental power data (plotted in black dots) give a total yield 698.7 Wh for the entire day, which is in remarkable agreement with the predicted simulated value. As the module has a nominal power of 103 W_p under STC, this equals a yield-to-nominal-power ratio of 6.8 kWh/kW_p for the considered day. Because the considered day was a perfect sunny day, this value will be much lower for an entire year. It can be concluded that with the described three-level simulation approach, it is possible to precisely model real-world thin-film solar modules under non-STC, predict its yield, and even allocate all relevant losses to their origins.

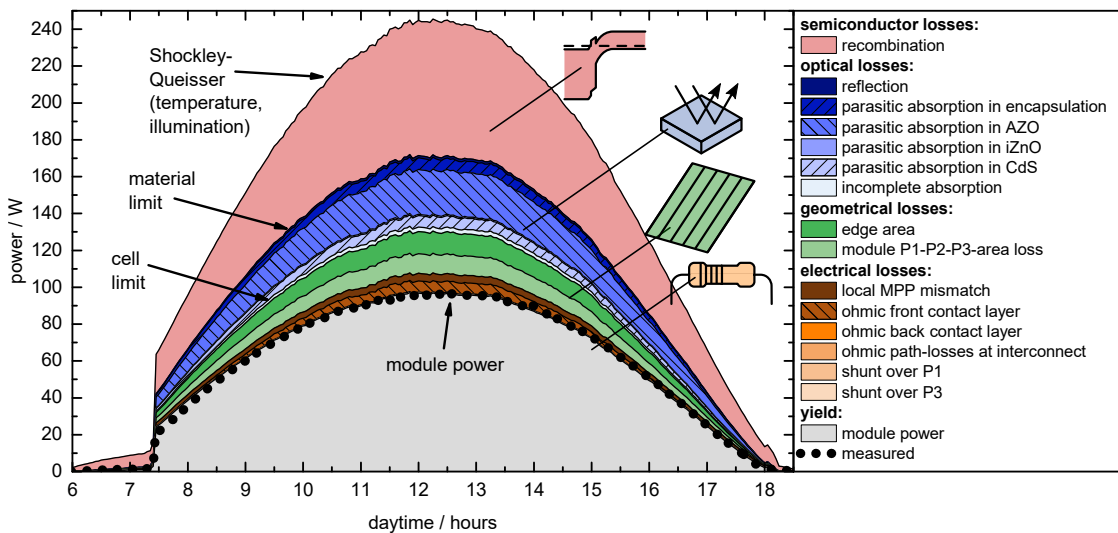


Figure 7.7: Time-dependent loss analysis and generated module yield during daytime of September 9, 2020. The upper edge of the red colored area is given as the temperature- and irradiance-dependent Shockley-Queisser limit for the module's band gap of 1.13 eV . It is scaled for the module size. All colored areas represent different loss mechanisms, while the module is predicted to produce the power indicated as gray area. For comparison, actual measurements in the field are marked as black dots.

In order to put these results in perspective, the resulting module PCE is compared with the PCE calculated from the Shockley-Queisser model. In graph a) in Figure 7.8, a colormap of the Shockley-Queisser limit for a single-junction solar cell with a band gap of 1.13 eV for a given temperature and irradiance is shown. As it can be seen, the Shockley-Queisser approach is a variable model depending on the two shown input parameters (and the band gap) rather than a single, fixed efficiency limit. In fact, the PCE limit varies from 29% up to 34% , even within these realistic non-STC conditions. The entire day, the simulated module is within the shown boundaries of graph a). The exact trajectory of operating conditions of the device on September 9, 2020 is shown by the black line with the blue points. Its projection on the daytime is shown in graph b). All relative losses are shown in this graph as well with the same color code as in Figure 7.7. The

experimentally measured points from Figure 7.7 are shown again as black points. Their overall agreement with the simulation is rather high, except for the early morning hours. The main reason for this deviation is that the PCE is a relative quantity and therefore the absolute errors from Figure 7.7 appear to be relatively large even though these errors for low intensities are actually extremely small. Another physical error source can be the absence of a thermal model [316], which could predict the exact temperature at the p-n junction and not only at the sensor at the rear side of the module. The actual temperature might heat up by around 2 to 3 K. In the early morning and late evening hours the effect of low-light conditions reduce the actual module PCE disproportionately more than the Shockley-Queisser limit. This effect is due to the module’s low shunting resistance, which causes a relatively large shunting effect for low irradiation as it can be seen in Figure 7.1. Furthermore, the high module temperatures around noontime affect the module’s PCE more than than the Shockley-Queisser PCE. This can be attributed to the high temperature coefficients as shown in Section 7.2, respectively.

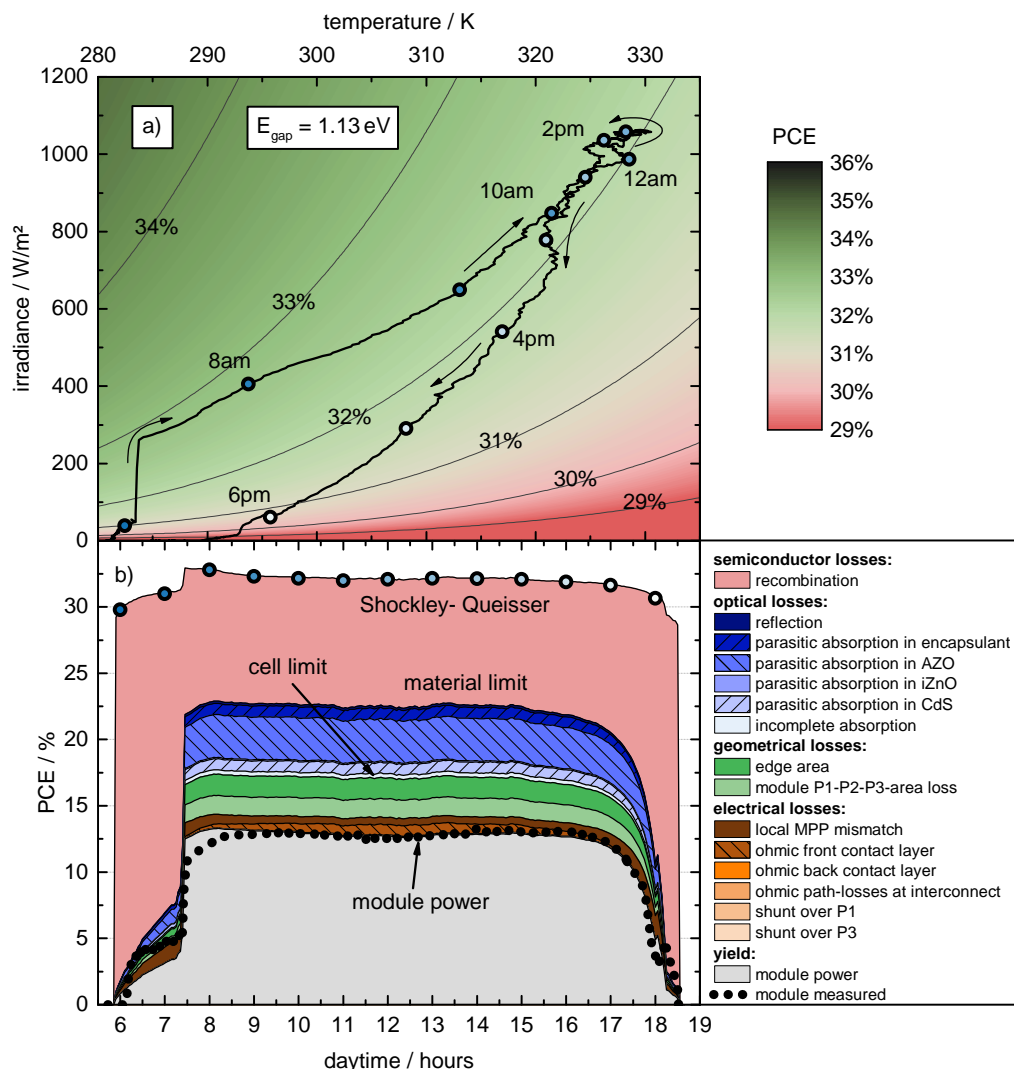


Figure 7.8: Trajectory of the operating module conditions compared with the Shockley-Queisser model during daytime of September 9, 2020. In graph a), the Shockley-Queisser limit is plotted as a colormap for the module’s band gap of 1.13 eV as a function of temperature and irradiance. The black line shows the course of the module conditions during that day. The same curve is shown in graph b) as a function of daytime in combination with all losses from Figure 7.7. All loss mechanisms and the actual module power have the same color coding as in Figure 7.7.

7.5 Possible Improvements on Module Level

As the largest single loss mechanism is the loss due to recombination, it is reasonable to direct research efforts towards the improvements of the absorber material. This has been often suggested and even realized in literature ^[153, 276, 278, 317, 318, 319, 320, 321]. However, this section focuses on the improvements on the device level without touching the actual light-absorbing material. It serves as a sensitivity analysis to get a feeling for which parameters have a significant effect on the PCE and hence guide future research and development efforts. As calculated in Section 6.4, the actual PCE of the reference module at STC is 14.27 %. In this section, individual measures to get a PCE gain of 0.65 % and therefore an overall PCE of 14.92 % are investigated.

The five following points are the main consideration of this section: Reducing sheet resistance in the TCO layer, reducing optical absorption in the TCO layer, reducing optical absorption in the encapsulant, reducing edge areas, and reducing interconnect areas. In order to achieve the mentioned PCE gain via a reduction in the electrical losses in the front TCO layer, the Poisson solver can be used to calculate the necessary improvement. A required sheet resistance of 7.75Ω instead of the actual 25Ω would be needed for the same grid resistivity. To get the same PCE effect via reducing the optical losses in the TCO layer, its absorption needs to be reduced by around 26 % within the relevant wavelength range. Reducing the parasitic absorption of the encapsulant entirely would result in the same PCE gain. Alternatively, the geometrical losses can be addressed. Reducing the edge area from around 505 cm^2 (7 % of total module) to around 190 cm^2 (2.6 % of total module) results in the same 0.65 % gain of PCE. Finally, the interconnect width needs to be reduced from $265 \mu\text{m}$ to $100 \mu\text{m}$ in order to gain the same PCE improvement. To do so, the cell width needs to be reduced to 3.5 mm to minimize ohmic losses, as it can be seen in Table 7.2.

In first order, one could assume that implementing all of the five improvement suggestions mentioned above would improve the efficiency by a factor of five times the individually improved 0.65 %, which equals to 3.25 % and therefore an overall module efficiency of 17.52 %. However, with all five improvement suggestions at the same time, the PCE is increased by 3.63 % to a total efficiency of 17.90 %. This overlap in improvement without modifying the CIGS deposition process is due to the interactions of the efficiency-increasing effects. Exemplarily, the more conductive TCO layer allows a larger cell width of 4.2 mm despite the smaller interconnect area.

Table 7.2: Comparison of geometric dimensions and characteristic electrical data for differently improved modules. The first line shows the standard reference module, while in the second line the interconnect area was reduced and in the last line all improvements from the main text are implemented (TCO sheet resistance, TCO transmittance, encapsulant transmittance, interconnect and edge area).

(a) Module geometries.

implemented improvements	module height / mm	module width / mm	interconnect width / μm	ideal cell width / mm	# cells
none	1200	600	265	4.0	144
interconnect area	1200	600	100	3.5	163
all described	1200	600	100	4.2	136

(b) Characteristic electrical data.

implemented improvements	$V_{oc}^{\text{module}} / \text{V}$	$V_{oc}^{\text{cell}} / \text{V}$	I_{sc} / A	$j_{sc} / \text{mA/cm}^2$	FF / %	PCE / %
none	103.7	0.720	1.35	27.0	73.4	14.27
interconnect area	117.3	0.719	1.24	28.1	73.8	14.92
all described	98.2	0.722	1.34	30.9	80.3	17.90



Answering this Chapter's Guiding Scientific Question

How can the daily yield and time-dependent losses of a thin-film solar module be forecast under real-world conditions?

A holistic digital model of a real-world solar module can be achieved by the connection of the three different simulation levels of electronical drift-diffusion simulation, optical TMM, and electrical Poisson's equation solver. This simulation model can handle fluctuations in temperature by the drift-diffusion method and irradiance by the TMM and their interplay by the Poisson solver. A holistic top-down loss analysis from the Shockley-Queisser model down to the actual module power can be calculated as introduced in Chapter 6 for each simulated time step. The overall daily yield is determined by integrating over the entire day. It was verified with an experimentally measured module and proven to have a precision of less than one per mill accuracy.

8

Pushing the Performance – Optimizing Power Conversion Efficiency and Annual Yield

The previous chapters described how solar cells and modules can be simulated, their losses modeled, and the final PCE forecast. The consistent next logical step is therefore the targeted optimization of solar devices. Since there are many suggestions and realizations of how to improve the light-absorbing material [276, 278, 317, 319, 277], this chapter only deals with improvements on the device level. This includes conventional parameter optimizations with typically few optimization parameters as well as computationally expensive design optimization with typically several tens of thousands of optimization parameters.¹

This Chapter's Guiding Scientific Question

How can individual solar device parameters be optimized and what is the perfect metallization grid pattern?

¹ This chapter is based on a journal article by the author of this work published under M. Zinßer et al., MRS Advances 7, 706–712 (2022) [322].

8.1 Optimization of Device Parameters

If the basic geometry of a solar device is predefined and only a few parameters can be optimized, a conventional parameter optimization is used. Examples for such parameters are the width of a monotonically interconnected cell, the distance between two grid fingers or the thickness of the front TCO layer. All those examples are a tradeoff between two beneficial effects. Exemplarily, a thicker TCO layer improves the electrical conductivity, while a thinner layer promotes a better optical transparency. Figure 8.1 shows this example for a $5 \times 2.6 \text{ mm}^2$ monolithically integrated cell with the same layer stack as in Section 5.2.2. Graph b) reveals the tradeoff between conductivity and transparency in terms of fill factor versus short-circuit current density. Their linear influence on the PCE reveals a maximum of 14% in graph a) at around 700 nm thickness. Since only one parameter was optimized, an entire batch could be executed and every reasonable TCO layer thickness can be tested.

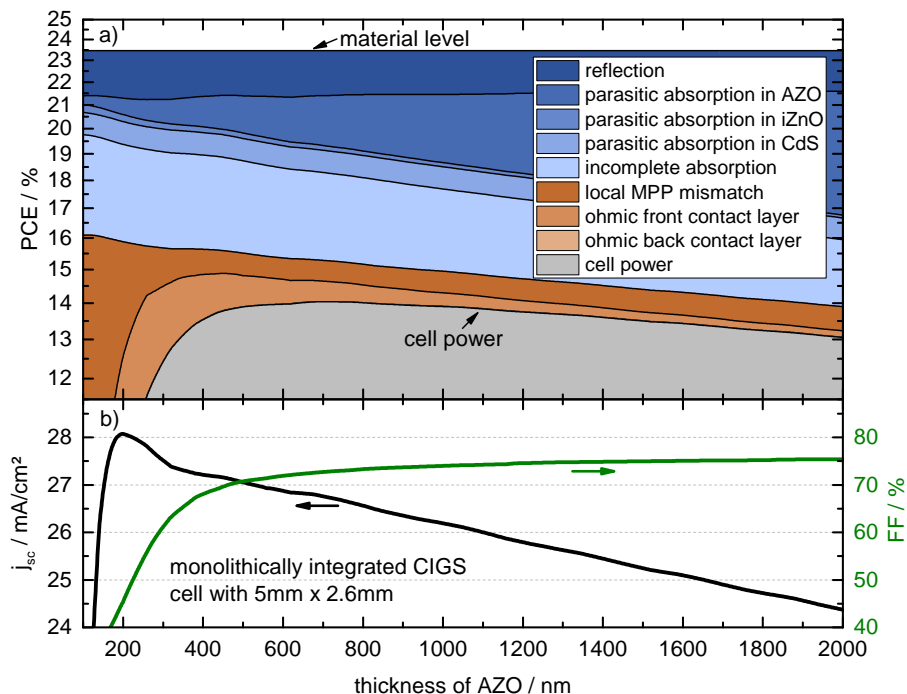


Figure 8.1: Optimization of the TCO layer thickness for a monolithically integrated CIGS cell with the dimensions of $5 \times 2.6 \text{ mm}^2$. The bottom plot shows the tradeoff between a high short-circuit current density for thin TCO layers and a high FF for thick TCO layers. V_{oc} is nearly unaffected by the TCO thickness.

However, for optimizations with multiple optimization parameters, such broadband batches would scale up the runtime to excessively long time periods. Therefore, a targeted optimization algorithm is needed, which optimizes all parameters without knowing the entire landscape of the problem. Due to the typically flat landscape within the parameters space, straightforward conventional optimization algorithms can be used to find the maximum. Nevertheless, a gradient with respect to all optimization parameters is not straightforward available and would take as many further simulations as present optimization parameters when calculating the derivative with a forward difference quotient. Since such numerically expensive calculations should be avoided, only gradient-free

optimization algorithms are considered to solve such problems. This work uses a downhill-simplex algorithm ^[233] due to its fast convergence and simple handling. This procedure will later be used in Chapter 9 to optimize a module for its maximum PCE for three variable parameters.

8.2 The Ideal Metallization Grid – Topology Optimization of Metallization Patterns

The content of this section has been developed and implemented in collaboration with Benedikt Braun.

Another common field of optimization for solar devices is the design of the top metallization grid. A similar tradeoff as for the TCO layer thickness is present for the grid pattern: Due to their induced shading effect, grid structures are a tradeoff between an improved electrical conductivity and optical shading. Hence, the determination of an appropriate grid pattern has always deserved special attention ^[163]. Early approaches assumed a pre-defined grid structure with a few tuning parameters and developed analytical models to calculate the PCE ^[161, 162, 164, 165, 166]. Their optimization works the same way as the parameter optimization procedure described above.

However, approaches for developing a grid pattern can be made without any restrictions in the design thanks to powerful modern computers. The only limitation is the numerical quantization for the FEM model. The most common approach for such problems is the method of topology optimization (TO) ^[323], which has been applied for problems in heat transfer ^[324, 324], mechanical statics ^[325, 326], fluid mechanics ^[327], and to solve Poisson's equation ^[184]. Even multi-objective optimizations have been executed ^[328, 329]. One group already applied the methodology of TO to the grid designing problem of solar devices ^[186]. A novelty of this work is the application not only to solar cells ^[187] or solar pin-up modules ^[188, 189] but also to monolithically integrated cells. The following sections only describe the new developments of this work. For any deeper investigations, the reader is referred to further literature ^[188].

8.2.1 Mathematical Basics – The Problem Formulation

From the FEM procedure, a huge variety of grid designs could be constructed. Each element k can either consist of a metallization layer on top or not. This binary information will be stored in the grid density x_k . The vector of all listed grid densities of each element will be referred to as $\underline{x} \in \{0, 1\}^N$. Each of the 2^N possible combinations represents a well defined grid pattern. Furthermore, the function

$$f : \{0, 1\}^N \rightarrow \mathbb{R}, \underline{x} \mapsto \text{PCE} \quad (8.1)$$

maps each of these possibilities \underline{x} on a well defined PCE using the developed FEM. According to Equation (4.45), the produced power depends on each finite element and its grid density x_k . Finally, the optimization problem is defined as finding the density vector that leads to the maximum

$$\max_{\underline{x} \in \{0, 1\}^N} \text{PCE}(\underline{x}) \quad (8.2)$$

of the extremely high-dimensional function f . Physically, this optimum represents a preferably flat voltage distribution for as little metallization grid as possible. This arrangement reveals the best tradeoff between less shading and the voltage of all finite elements being close to their MPP.

8.2.2 Topology Optimization as Improvement Idea

Since an application-oriented TO procedure needs a fine quantization, a large number of finite elements is used within the FEM simulation. Therefore the number of possible grid arrangements 2^N exceeds pretty fast the number of FEM calculations that could be executed within a finite amount of time. Even if only grid arrangements with cohesive structures are used, the runtime cannot be reduced to a reasonable time scale. Fortunately, similar to neural networks, the multi-dimensional parameter landscape has many local maxima and it is not necessary to find a global optimum. A very good local optimum is by far sufficient within a typical parameter landscape with many local extrema that are only infinitesimally worse than the global optimum. This enables to use algorithms such as the method of moving asymptotes ^[185] or the gradient adjoint method ^[330].

Within each parameter dimension x_k , only two values (0 and 1) are defined for real-world solar devices, which in principle could be handled by mathematical approaches for discrete optimizations ^[331]. However, a continuous optimization receives more information about the environment of the parameter landscape. To develop a continuous problem, also intermediate values between 0 and 1 are allowed and afterwards a binarization is applied to get rid of those values. The behavior of finite elements with intermediate grid densities lies between those of binarized elements. However, this interpolation is not linear. Otherwise, intermediate values could be favoured by the algorithm and a subsequent binarization destroys the built structures. In fact, the interpolation needs to promote a very good conductivity for $x_k = 1$ and a very good transparency for $x_k = 0$. Intermediate values are disadvantaged in both quantities by introducing an exponential interpolation function with a certain degree of bowing in between. Using this approach, an aspiration towards an intrinsic binarized grid structure is made. This work uses solid isotropic material with penalization (SIMP) functions with exponential interpolation functions ^[329, 332, 333, 334]. Those SIMP functions are defined as a function of grid density x_k by

$$f_{\text{SIMP}}^{\text{gen}}(x_k) = \frac{1}{\beta_{\text{SIMP}}^{\text{gen}}} \cdot (\beta_{\text{SIMP}}^{\text{gen}} + 1)^{1-x_k} - \frac{1}{\beta_{\text{SIMP}}^{\text{gen}}} \quad (8.3)$$

and

$$f_{\text{SIMP}}^{\text{con}}(x_k) = \frac{1}{\beta_{\text{SIMP}}^{\text{con}}} \cdot (\beta_{\text{SIMP}}^{\text{con}} + 1)^{x_k} - \frac{1}{\beta_{\text{SIMP}}^{\text{con}}} \quad (8.4)$$

with the bowing factors $\beta_{\text{SIMP}}^{\text{gen}}$ and $\beta_{\text{SIMP}}^{\text{con}}$ of typically 10 to 100. The derivatives with respect to x_k are given by

$$\frac{d}{dx_k} f_{\text{SIMP}}^{\text{gen}}(x_k) = -\frac{\log(\beta_{\text{SIMP}}^{\text{gen}} + 1)}{\beta_{\text{SIMP}}^{\text{gen}}} \cdot (\beta_{\text{SIMP}}^{\text{gen}} + 1)^{1-x_k} \quad (8.5)$$

and

$$\frac{d}{dx_k} f_{\text{SIMP}}^{\text{con}}(x_k) = \frac{\log(\beta_{\text{SIMP}}^{\text{con}} + 1)}{\beta_{\text{SIMP}}^{\text{con}}} \cdot (\beta_{\text{SIMP}}^{\text{con}} + 1)^{x_k} \quad (8.6)$$

Both SIMP functions and their derivatives are shown in Figure 8.2. A prominent feature is that for $x_k = 0$ the generation SIMP function reaches 1, while the conductivity SIMP function vanishes. For $x_k = 1$ the opposite values are reached. The interpolation in between is exponential, as defined in Equations (8.3) and (8.4). This gives finite elements with a grid density of $x_k = 0.5$ a conductivity that is worse than 50% and an optical transparency that is also worse than 50%. Hence, the desired intrinsic trend towards either $x_k = 0$ or $x_k = 1$ is implemented.

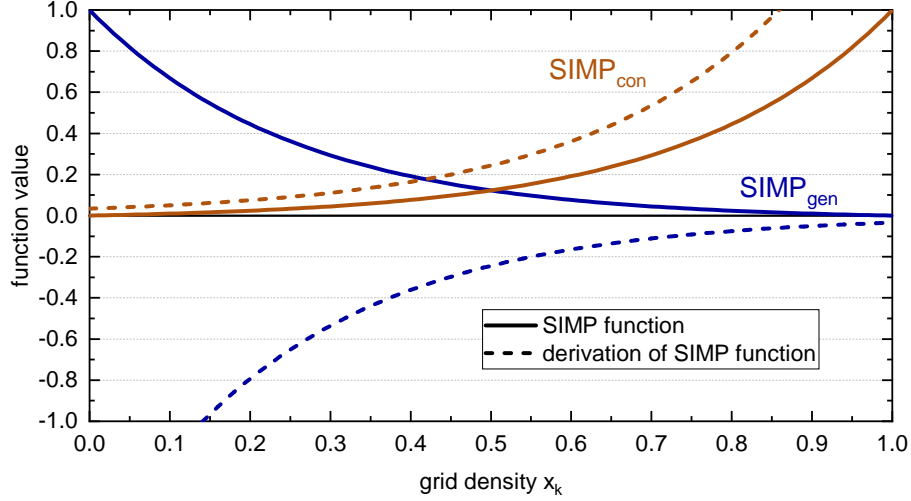


Figure 8.2: Behavior of the SIMP functions and their derivatives with bowing factors $\beta_{\text{SIMP}}^{\text{gen}} = \beta_{\text{SIMP}}^{\text{con}} = 50$.

The two SIMP functions find their way into the simulation as prefactors for the generated photocurrent within the optical TMM and the used grid resistor within the electrical simulation. The grid resistor within the FEM simulation from Equation (4.24) is modified to

$$R_{\text{grid}}^{k,n} = \rho_{\text{grid}} \cdot \frac{\|x_k - x_n\|}{2A_{\text{grid}}} \cdot \frac{1}{f_{\text{SIMP}}^{\text{con}}(x_k)}. \quad (8.7)$$

Since the resistor is the reciprocal value of the conductivity, it is inversely dependent on the SIMP function $f_{\text{SIMP}}^{\text{con}}(x_k)$. The generated photocurrent density from Equation (4.18) is changed to

$$\begin{aligned} I_{\text{net}}^k = & -f_{\text{optics}} \cdot f_{\text{SIMP}}^{\text{gen}}(x_k) \cdot I_{\text{ph}} \\ & + I_0 \cdot \left(\exp \left(\frac{q_e \cdot (\Phi_{\text{front}}^k - \Phi_{\text{back}}^k - I_{\text{net}}^k R_s)}{n_d^{\text{mat}} k_B T} \right) - 1 \right) \\ & + \frac{\Phi_{\text{front}}^k - \Phi_{\text{back}}^k - I_{\text{net}}^k R_s}{R_{\text{sh}}}. \end{aligned} \quad (8.8)$$

Hereby, the exponential dependency of both SIMP functions are introduced to the FEM simulation. Table 8.1 shows the summarized conductivities and light transparency for the extreme values $x_k = 0$ and $x_k = 1$.

Combining Equations (4.47) and (4.45) reveals the final output power

$$P_{\text{out}} = V_{\text{op}} \cdot \sum_{k \in \mathcal{K}} I_{\text{net}}^k = V_{\text{op}} \cdot \sum_{k \in \mathcal{K}} I_{\text{net}}^k(x_k, \Phi_k(x_k)), \quad (8.9)$$

Table 8.1: Behavior of finite elements with and without grid.

	with grid	without grid
grid density x_k	1	0
incident light	reflection	absorption
photocurrent $f_{\text{SIMP}}^{\text{gen}}(x_k) \cdot I_{\text{ph}}$	0	I_{ph}
conductivity	good	bad
grid resistor in FEM $\frac{1}{f_{\text{SIMP}}^{\text{con}}(x_k)} \cdot R_{\text{grid}}^{k,n}$	$R_{\text{grid}}^{k,n}$	∞

which now depends on x_k . The direct dependency of $I_{\text{net}}^k(x_k)$ arises from the modified photocurrent density, while the indirect dependency $I_{\text{net}}^k(\Phi_k(x_k))$ arises from the modified spatial voltage distribution. According to Equation 4.48, the PCE linearly depends on the generated power P_{out} , which is why the optimization problem from Equation 8.2 is still valid.

Figure 8.3 visually summarizes the basic idea of TO for a solar device. White colored finite elements stand for elements with grid on top, while black colored elements do not have a front grid. Elements with colors in between have properties that are interpolated by the SIMP functions. In Graph 8.3a, an initial guess with spatially randomized grid densities is assumed. Graph 8.3b visualizes a sensitivity analysis for each element's grid density x_k . In simple words, this shows the necessity for a higher grid density, where green means need for more grid and red means need for less grid. In practice, this quantity is mathematically represented by the N -dimensional gradient $\frac{d}{dx_k} P_{\text{out}}$ with respect to the grid density of each element k . Its calculation will be part of the next section. The updated grid density is shown in graph 8.3c, which typically demonstrates a better PCE via Equation (8.9). The steps in graphs 8.3b and 8.3c are repeated for several times until a certain convergence criteria is reached. Typically a maximum number of iterations of 50 to 100 iterations are allowed. In graph 8.3d, the binarization is performed. Each element is either set to $x_k = 0$ or to $x_k = 1$ based on a certain threshold. As mentioned before, this step is necessary since real-world solar devices can only have a full metallization grid on top, but not a fraction of it. Typical structures only consist of cohesive grid patterns. Actual calculation results will be shown in Section 8.2.4.

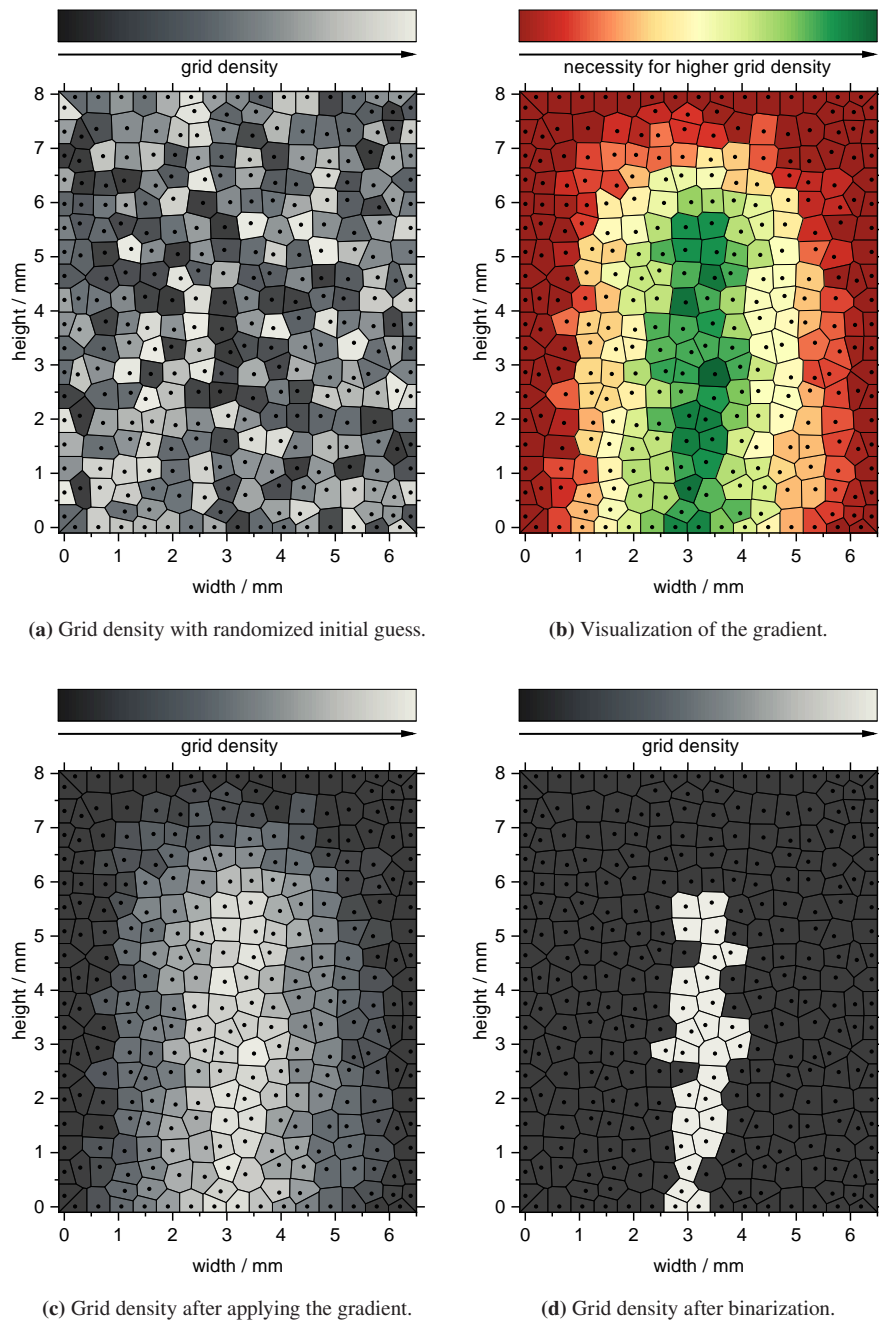


Figure 8.3: Visualization of the idea of topology optimization for a $6.4 \times 7.95 \text{ mm}^2$ large cell. A randomized grid density is used as a starting point in plot (a). Afterwards, the sensitivity of each finite element for more or less grid is checked in plot (c) and used for an updated better grid distribution in plot (c). This procedure is executed several times until a certain criteria is reached. Finally, the grid density is binarized element-wise as seen in plot (d).

8.2.3 Improved Optimization – Calculation of the Gradient

The gradient $\frac{d}{dx_k} P_{\text{out}}$ reveals valuable information about the nearest local extremum. Therefore, its calculation on top of the current loss function in Equation 8.9 can be rather useful if it does not consume too much runtime to calculate. The gradient could be calculated by changing the grid density of one element by a small number and compare the changed PCE according to Equation

8.9 with the initially calculated PCE. This could be done for each parameter x_k and basically represents a difference quotient. However, such a procedure requires $N + 1$ simulations for N elements. Since for TO simulations, typically tens of thousands of finite elements are involved, this does not result in any practicable runtime. Therefore, one can make use of the knowledge of the influence of the SIMP function within the simulation. By the chain rule and the total derivative, the gradient can be rewritten to

$$\frac{d}{dx_k} P_{\text{out}} = \frac{\partial P_{\text{out}}}{\partial I_{\text{net}}^k} \cdot \frac{dI_{\text{net}}^k}{dx_k} \quad (8.10)$$

$$= \frac{\partial P_{\text{out}}}{\partial I_{\text{net}}^k} \cdot \left(\frac{\partial I_{\text{net}}^k}{\partial x_k} + \frac{\partial I_{\text{net}}^k}{\partial \Phi_k} \cdot \frac{d\Phi_k(x_k)}{dx_k} \right). \quad (8.11)$$

Here the direct grid-density dependence of I_{net}^k and the indirect dependence via the electrical voltage drop Φ_k of the k -th element is taken into account. This leaves four differentials to be calculated. The first one can be trivially calculated via Equation (8.9), which results in

$$\frac{\partial P_{\text{out}}}{\partial I_{\text{net}}^k} = V_{\text{op}}. \quad (8.12)$$

The second and third differential $\frac{\partial I_{\text{net}}^k}{\partial x_k}$ and $\frac{\partial I_{\text{net}}^k}{\partial \Phi_k}$ are also easily solvable via Equation (8.8). However, the fourth differential

$$\frac{d\Phi_k(x_k)}{dx_k} \quad (8.13)$$

relies on the mentioned knowledge of the equation system $-\underline{I}_{\text{net}} = \mathbf{G} \cdot \underline{\Phi}$ from (4.30) with the voltage-drop vector $\underline{\Phi}$ of all local voltage drops Φ_k from Equation (4.31) and the stiffness matrix \mathbf{G} from (4.34). On both sides, the derivative with respect to x_k is calculated and on the right side, the product rule is applied.

$$\begin{aligned} -\frac{d\underline{I}_{\text{net}}(x_k)}{dx_k} &= \frac{d\mathbf{G}(x_k)}{dx_k} \cdot \underline{\Phi} + \mathbf{G} \cdot \frac{d\underline{\Phi}(x_k)}{dx_k} \\ \Leftrightarrow \frac{d\underline{\Phi}(x_k)}{dx_k} &= -\mathbf{G}^{-1} \cdot \left(\frac{d\mathbf{G}(x_k)}{dx_k} \cdot \underline{\Phi} + \frac{d\underline{I}_{\text{net}}(x_k)}{dx_k} \right) \end{aligned} \quad (8.14)$$

While this gives an expression for Equation (8.13), it yields two new differentials. The first one $\frac{d\mathbf{G}(x_k)}{dx_k}$ can be trivially calculated via the definition in (4.34) and the therein derived components in Equation (8.7). The second one $\frac{d\underline{I}_{\text{net}}(x_k)}{dx_k}$ however, is calculated via an approximation. Only the dependencies in first order are considered, which changes the full derivative $\frac{d}{dx_k}$ into a partial derivative $\frac{\partial}{\partial x_k}$ [335]. This dependency can be calculated from Equation (8.8). Finally, Equation (8.14) is typically not solved by calculating the inverse of the matrix \mathbf{G} but by solving a system of linear equations. Due to efficient solving methods like biconjugate gradient methods [231] with an incomplete LU decomposition [232] as preconditioning procedure, this method is much faster than calculating an inverse of a large matrix, even though it is only sparsely populated. Finally, from $\frac{d\underline{\Phi}(x_k)}{dx_k}$ the single components $\frac{d\Phi_k(x_k)}{dx_k}$ can be obtained component-wise, which are needed in Equation (8.14). Thus, the gradient is determined completely.

The advantage in runtime is shown in Figure 8.4 for a restricted amount of finite elements. Due to its increase in runtime of more than three orders of magnitude, the calculation of the gradient is roughly on the same time scale as calculating the actual function value according to Equation 8.9. Therefore, gradient-based optimization algorithms can be used, which consist of a supremely small amount of function evaluations and therefore speed up the entire runtime for a TO calculation. A comparison of several optimizers are shown in the next section.

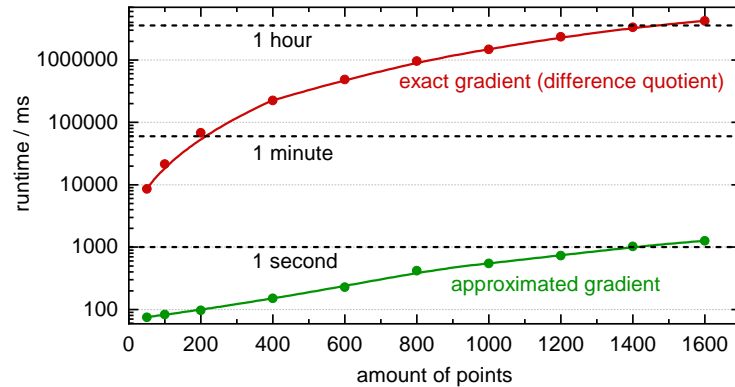


Figure 8.4: Comparison of the calculation of the gradient for the topology optimization. The approximated calculation of the gradient is more than three orders of magnitude faster than the exact calculation via a difference quotient.

8.2.4 Different Optimizing Algorithms

Having access to an approximated yet quickly calculated gradient

$$\text{grad}_{\underline{x}}(\text{PCE}(\underline{x})) \quad (8.15)$$

allows to use gradient-based optimization algorithms. This section compares different algorithms that can deal with a large number of optimization parameters. Within this high-dimensional parameter space, the landscape is rather hilly and therefore highly non-convex with a lot of local maxima. A straightforward gradient descent method is compared with a Broyden–Fletcher–Goldfarb–Shanno (BFGS) ^[336, 337, 338, 339] optimizer and an adaptive moment estimation (ADAM) ^[340] optimization algorithm. The resulting grid patterns in real space can be seen in Figure 8.5 for around 40000 finite elements. Moreover, Figure 8.6 reveals insightful information about the iteration-dependent PCE of each optimization algorithm. Despite their rather different looking grid pattern in Figure 8.5, all tested optimizers roughly converge to the same final PCE. This proves the hypothesis of many local maxima within the parameter landscape and makes finding a global maximum extremely difficult but also irrelevant. However, the ADAM optimizer frequently reaches the intended level of optimization with the fewest iterations. Therefore, only this algorithm will be used in this work. For all symmetrical modules or cells, a symmetry axis in the middle was introduced, as shown in Figure 8.5. This cuts the amount of finite elements in half and therefore drastically reduces the optimization problem resulting in a much shorter runtime.

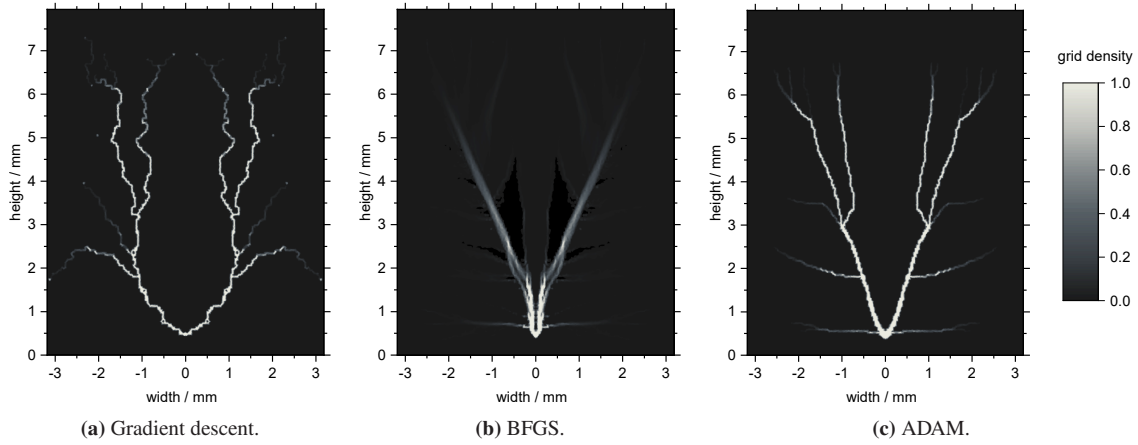


Figure 8.5: Resulting grid pattern for different numerical optimizers after 50 iterations.

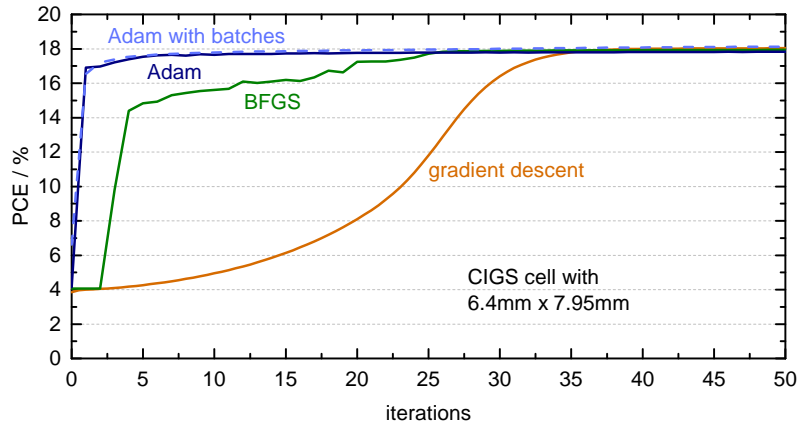


Figure 8.6: Development of the PCE for different optimizers as a function of the number of iterations.

8.2.5 Further Refinements for the Optimization Strategy

Some smaller improvements are implemented into this work's optimization algorithms that are only briefly explained here. A more detailed explanation can be found in [335].

8.2.5.1 Density Filter

In order to make sure that the grid pattern does not form any checker-board patterns or a too thin grid finger, a density filter is used [341, 342]. This filter modifies the grid densities from x_k to \tilde{x}_k by the following modification rule.

$$\tilde{x}_k = \frac{1}{\sum_{i \in \mathcal{K}} w_{k,i}} \cdot \sum_{i \in \mathcal{K}} w_{k,i} \cdot x_i \quad (8.16)$$

Here, $w_{k,i}$ are weight functions that use the Euclidean distance between the k -th and i -th element. Within this work, the weights are chosen to obey the Gaussian distribution function [343]

$$w_{k,i} = \exp\left(-\frac{\|x_k - x_i\|^2}{2\sigma^2}\right) \quad (8.17)$$

with the variance σ^2 . This kind of filtering correlates the grid densities of neighboring elements, which supports the formation of cohesive grid structures and inhibits the formation of individual grid islands.

8.2.5.2 Gaussian Blur

In order to avoid getting stuck in a certain grid configuration, a Gaussian blur filter is used. This methodology averages the grid densities of a given element k with their neighbors' density. It is calculated via

$$\tilde{x}_k = \frac{1}{\xi} \sum_{i \in \mathcal{K}} \exp\left(-\frac{\|x_k - x_i\|^2}{2\zeta^2}\right) \cdot x_i, \quad (8.18)$$

where ζ corresponds to a filter radius in real space and ξ is chosen in a way, that no \tilde{x}_k exceeds the value of 1. This effect broadens and blurs all built grid branches. This gives the optimization algorithm the chance to re-choose the exact position of already formed grid fingers.

8.2.5.3 Batch Optimization

Finally, the rate of convergence and the final result can be improved by using a non-linear localization strategy ^[344]. Thereby, all finite elements are randomly divided into several subgroups, so called batches. The associated finite elements are optimized one batch after another. This procedure ensures an isolated optimization of all elements within a batch, allowing finer adjustments to the grid. A result of an optimized grid pattern using a batch optimization within an ADAM algorithm can be seen in Figure 8.7. Moreover, the behavior of the light blue line in Figure 8.6 shows an even better convergence than the conventionally used ADAM optimizer and in fact, a slightly higher final PCE. Therefore, in the following only the ADAM method in the batch variation is used.

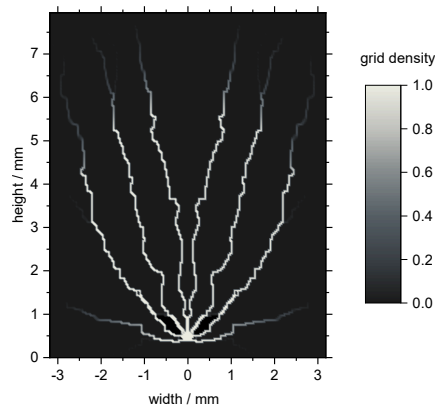


Figure 8.7: Resulting grid pattern for the ADAM optimizer with the usage of batches after 50 iterations.

8.3 Real-world Applications – From PCE Optimization to Yield Optimization

This section deals with the application of TO on real-world solar modules. In Figure 8.8, the averaged irradiance in Stuttgart (Germany) between the years 2005 and 2020 was gathered from the TMY PVGIS-ERA5 data set ^[251] in hourly time steps. Although the chosen location in Stuttgart is with a latitude of 48.738° N very close to the normalized solar zenith angle of 48.19° N referenced by the AM1.5G spectrum, the local irradiance rarely reaches or even exceeds the standardized 1000 W/m^2 . This effect is mainly due to local clouds, incident solar angle during the daytime, and a low sun due to seasons. Weighting the irradiance with the temporal distribution of this irradiance reveals a value of only 598 W/m^2 for the Stuttgart location. Therefore, the question arises whether an optimization of photovoltaic devices for STC with its irradiance of 1000 W/m^2 is reasonable. Lower irradiances result in lower locally generated currents, which requires less conductance, i.e. enables thinner TCO layers and less metallization grid. Therefore, an optimization for lower irradiances and hence for an annual yield seems to be very reasonable. This would result in a reduction of the PCE at STC, but would increase the annual yield as well as reduce the production costs due to a lower material consumption. In principle, an optimization with the annual yield as the optimization function could be attempted. However, calculating a PCE can be achieved in a few seconds while a yield calculation takes around 300 times longer and therefore up to several minutes. A topology optimization that uses the yield as the optimization function, would also be expanded by the factor 300. Since TO algorithms use a large amount of finite elements, the runtime on a standard PC would increase to several weeks, which is far longer than practically usable. Thus, instead of the annual yield, simply a lower PCE is used as loss function and the final yield calculation is only used for validation and further analysis.

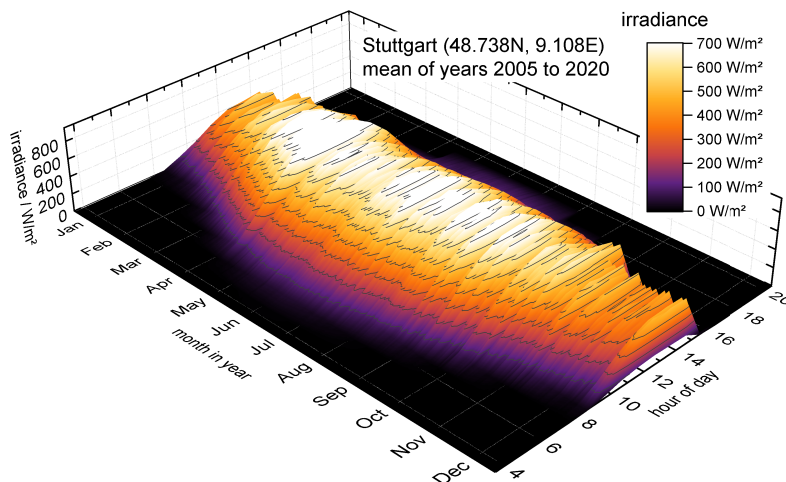


Figure 8.8: Visualization of the time-dependent sun's illumination power in Stuttgart averaged over the years from 2005 to 2020.

8.3.1 New Grid Designs for Yield Optimization

As in the beginning of this chapter in Section 8.1, a $5 \times 2.6 \text{ mm}^2$ monolithically integrated cell is optimized. This time, not only the TCO layer thickness is adjusted, but also simultaneously the grid structure is optimized via a TO. The introduction of a grid increases the overall PCE from roughly 14 % to around 18 %. In Figure 8.9, the smallest periodic structure of two different cell designs are shown. Each of them is optimized for a different irradiance intensity [322]. The left orange design is optimized for the standardized 1000 W/m^2 distributed over the AM1.5G spectrum as defined in STC. It consists of a grid coverage of 2.89 % and a 180 nm thick front TCO layer. Its grid pattern looks like a radio-antenna, which gives this design its name. The right blue design is optimized for only 500 W/m^2 with the same spectral distribution as the AM1.5G spectrum. It has a grid coverage of only 1.35 % and a TCO layer thickness of 90 nm. Due to its shape, this cell design is referred to as champagne-glass design in the following. The factor of 2 in the TCO layer thickness as well as in the grid coverage perfectly matches the difference in irradiance, for which the two designs are optimized. Such a reduction in TCO and grid material significantly lowers the material consumption and therefore production costs of thin-film solar modules. Both topological grid designs in Figure 8.9 are a manually adapted combination of multiple TO attempts. Therefore, both designs are a merged design of several individual optimizations. Moreover, both designs are generated with a symmetry axis in the middle of the horizontal direction. As mentioned above, this reduces the amount of finite elements, which drastically speeds up the runtime of the TO.

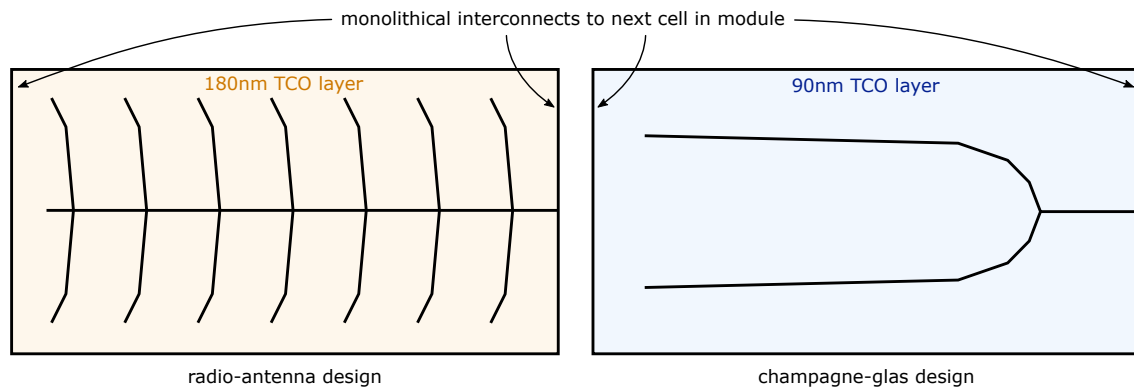


Figure 8.9: Two different grid designs optimized for different irradiance intensities. The radio-antenna design was optimized for an irradiance of 1000 W/m^2 , whereas the champagne-glass design as optimized for 500 W/m^2 . The designs differ in their grid pattern and the thickness of their top TCO layer.

Figure 8.10 compares the I–V curves of both cell designs for 1000 W/m^2 and 500 W/m^2 incident irradiance. Since the radio-antenna design was optimized for 1000 W/m^2 , it has the higher MPP than the champagne-glass design for the higher illumination. The same argument holds for the champagne-glass design for 500 W/m^2 . For reference, the I–V characteristic at the material level is shown for both irradiation intensities as well.

Such I–V curves can be obtained for many irradiation intensities. Their resulting solar-module parameters are plotted in Figure 8.11b). While the radio-antenna design consists of a higher FF for all irradiances due to its grid pattern and its thicker TCO layer, the champagne-glass design has a higher short-circuit current density due to its lower grid coverage and its thinner TCO layer. Graph a) shows the interplay in terms of the PCE. For low irradiances the demand for a good conductivity is comparably low since only little current is generated that needs to be extracted. This tradeoff towards a less shading and lower conductivity is realized in the champagne-glass design,

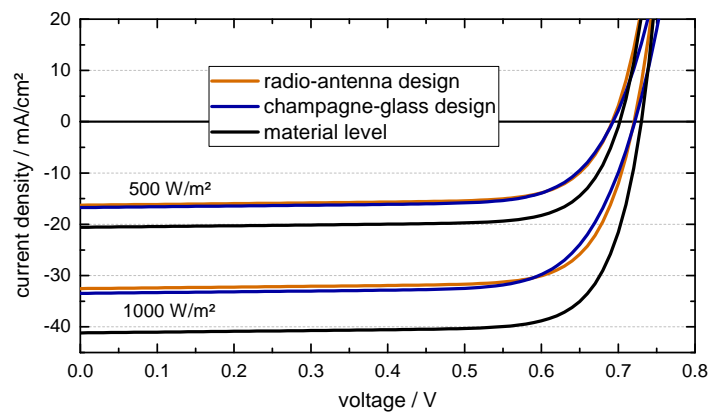


Figure 8.10: I–V curves for different illumination intensities for two different cell designs. The black lines represent the material level without any electrical and optical losses.

making it the supreme design for low irradiances. For illuminations above 870 W/m^2 significantly more current is generated, which entails the need for high electrical conductivity. This is given within the radio-antenna design. Therefore, its higher FF for high irradiances outperforms its lower short-circuit current density. To summarize, this analysis shows that the champagne-glass design is more favorable for small irradiances despite having a worse PCE at STC. For the same irradiances, both designs have almost the same open-circuit voltage.

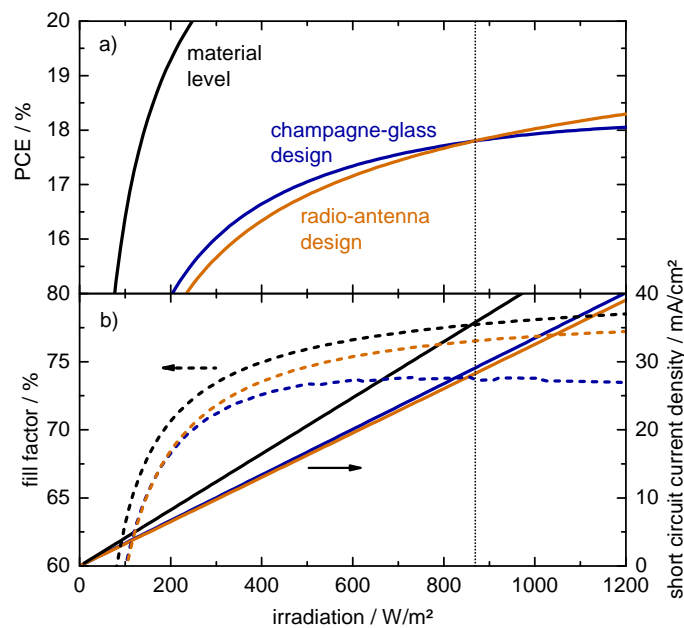


Figure 8.11: Illumination-dependent solar cell parameters for two different cell designs. For low irradiances, the higher j_{sc} of the champagne-glass designs compensates its slightly lower FF. At the vertical dotted line, this effect vanished and is reversed for higher intensities. The black lines mark the material level without any electrical and optical losses.

In order to test both designs for monolithically integrated cells on realistic data, irradiance data as in Figure 8.8 has been gathered for multiple locations with different latitudes reaching from 64° N to 30° N . The irradiance data has been processed into multiple irradiance bins as seen as the gray histogram in Figure 8.12. Multiplication of the histograms with the irradiance on the

x-axis reveals the red curves. In practice, they show at which irradiance levels the annual yield is predominantly generated from. As introduced in Section 4.6.3, for such a data set, the annual power can be efficiently calculated. Calculating the weighted mean of the red curve indicates the virtual irradiance value, where most of the annual power is generated at. This value as well as the maximum peak of the red curves increases for a decreasing latitude.

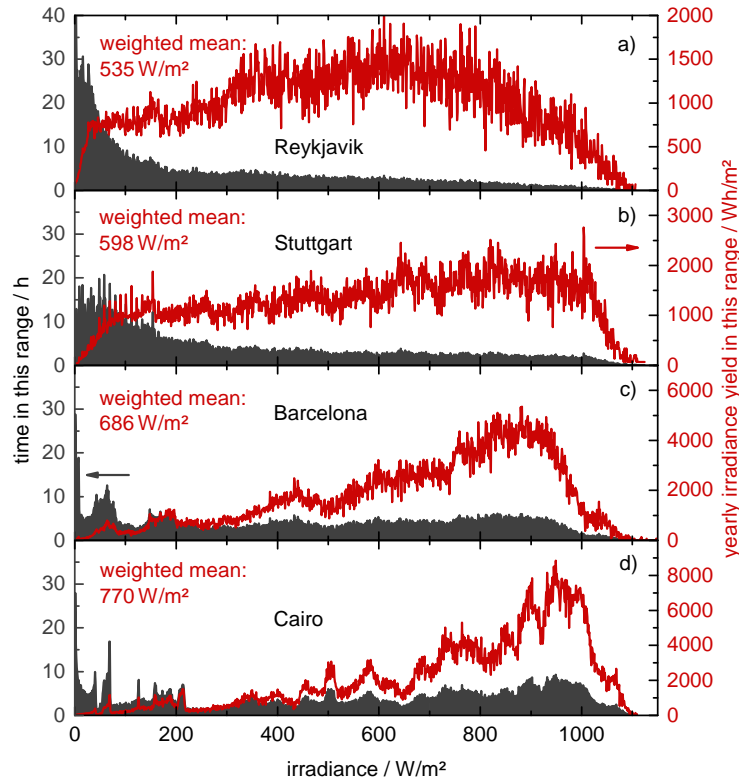


Figure 8.12: Irradiance intensities for different locations on the northern hemisphere.

The modules in all locations are pointed directly towards south and have an optimized angle of attack, which is 48° N for Reykjavik, 42° N for Stuttgart, 39° N for Barcelona, and 30° N for Cairo. From each monolithically integrated cell, digital models are created and simulated at each of the four locations. The results in PCE and yield can be found in Table 8.2. As already determined, the PCE of the radio-antenna design exceeds the one of the champagne-glass design by $0.51\%_{\text{rel}}$. However, the annual yield of the champagne-glass design outperforms the radio-antenna design in every location. The advantage reaches from $0.36\%_{\text{rel}}$ in Cairo up to $1.28\%_{\text{rel}}$ in Reykjavik. This superior behavior in yield generation is due to the given irradiance conditions, since the vast majority of them happens to be in low-light conditions far below 1000 W/m^2 . As this effect is even more presents for lower annual mean irradiances, it has more prominent impacts for locations far away from the equator. Even for locations with extremely high irradiances, such as the Lago Salar de Arizaro in the north-west of Argentina, the radio-antenna design does not exceed the champagne-glass design in yield. Here, both designs produce the same annual yield of 439.0 kWh/m^2 . Even at this location most of the power is generated below 1000 W/m^2 of irradiance because of non-peak conditions due to low sun and clouds. Hence, independent of the geographical location, for every yield optimization an irradiance of less than 1000 W/m^2 should be considered.

Table 8.2: Comparison of the performance in PCE and yield of two cell designs. In the last column, the drawbacks and advantages of the champagne-glass design with respect to the radio-antenna are outlined.

	radio-antenna	champagne-glass	champagne-glass vs. radio-antenna
optimized for	1000 W/m ²	500 W/m ²	
grid coverage	2.89 %	1.35 %	
TCO thickness	180 nm	90 nm	
PCE at STC	18.02 %	17.93 %	-0.51% _{rel}
Annual yield in Reykjavik (64.15° N)	177.3 kWh/m ²	179.6 kWh/m ²	+1.28 % _{rel}
Annual yield in Stuttgart (48.78° N)	243.1 kWh/m ²	245.8 kWh/m ²	+1.08 % _{rel}
Annual yield in Barcelona (41.39° N)	339.6 kWh/m ²	342.0 kWh/m ²	+0.71 % _{rel}
Annual yield in Cairo (30.04° N)	421.3 kWh/m ²	422.8 kWh/m ²	+0.36 % _{rel}

Resulting yields of cross-combined cell designs with one grid design and the TCO thickness of the other design and vice versa lie in between the yields of the two standard combinations. For example, for Stuttgart, the radio-antenna grid design with a non-optimized TCO layer thickness of 90 nm has an annual yield of 245.6 kWh/m², whereas the champagne-glass grid design with non-optimized 180 nm of TCO reveals a yield of 245.4 kWh/m².

Therefore, both the individual optimizations of topological grid and thickness of the TCO layer provide a yield improvement on the original PCE-optimized radio-antenna design. Nevertheless, the optimal solution for annual yield is the combination of both optimizations, which is listed in Table 8.2 as champagne-glass design.

8.3.2 Superior Low-light Behavior Explained by Loss Analysis

Using the holistic loss analysis introduced in Chapter 6, an explanation can be given, why the radio-antenna design has a higher PCE at the standardized 1000 W/m² and the champagne-glass design a higher PCE at 500 W/m². For this purpose, loss analyses for both designs with both irradiation intensities are executed and shown in Figure 8.13. To be able to compare the loss mechanisms, all losses have been normalized to the maximum potential of the corresponding material level. Therefore, optical losses appear at the same height in this visualization.

The larger grid coverage and thicker TCO layer of the radio-antenna design make losses due to grid shading and parasitic absorption within the TCO layer much more dominant than in the champagne-glass design. However, this setup provides a better conductivity, resulting in reduced resistive losses within the TCO layer and front grid. All ohmic losses consistently reduce by a factor of 2 for half the irradiation intensity. Simultaneously, the relative losses due to local MPP mismatches slightly increase because the MPP shifts away from the MPP on the material level. On top of that, the relative reverse currents under the grid become larger for half the irradiation intensity since the backwards shunt currents stay at the same absolute value, while the photocurrent

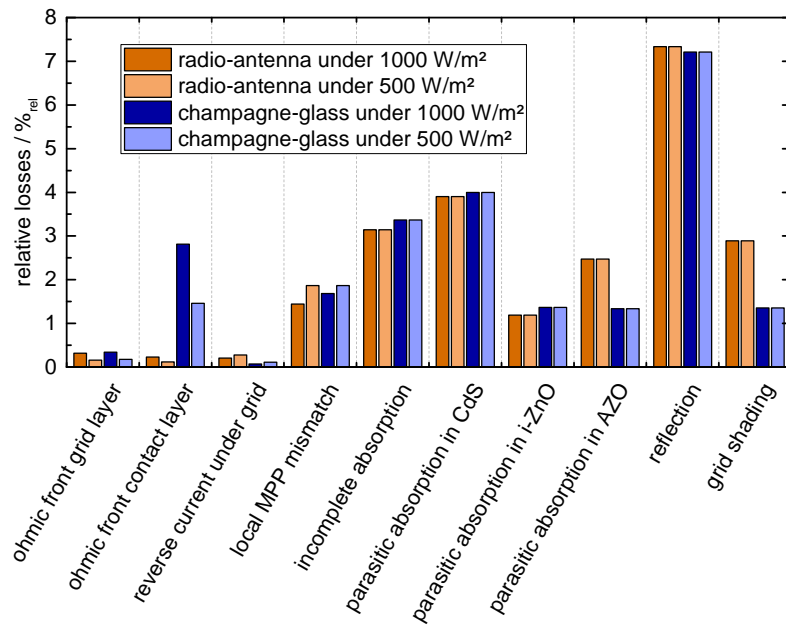


Figure 8.13: Loss analysis for two cell designs. All losses are normalized to the maximum potential at the material level. The radio-antenna design has an advantage in the electrical behavior. However, for low irradiation intensities, the electrical effects are less important and the optical advantages of the champagne-glass design outperform the radio-antenna design.

is reduced by a factor of 2. Effects of an increased module temperature could also be implemented at the material level within a drift-diffusion simulation. However, its impacts would not interfere with the results on the device level.

To conclude this yield analysis, it can be said that the radio-antenna design has a better tradeoff of optical and electrical losses for 1000 W/m² irradiance due to its optimization for STC conditions. Nevertheless, the champagne-glass design deals better with non-STC low-light conditions, due to its optimization for 500 W/m². Such a low-light advantage reveals the benefits of a yield calculation, since real-world solar devices are not exposed to the laboratory-standardized 1000 W/m² most of the time.



Answering this Chapter's Guiding Scientific Question

How can individual solar device parameters be optimized and what is the perfect metallization grid pattern?

Single device parameters like the cell width, the TCO layer thickness, or the grid-finger distance can be optimized using a sweep across a plausible range of the parameter to be optimized. For multiple optimization parameters at the same time, a more sophisticated procedure in the form of a gradient-free optimization algorithm must be used since the number of possible parameter combinations quickly rises with the amount of parameters. A much more complex challenge is the design of an optimized structure of the metallization grid pattern due to its tremendous number of degrees of freedom. Advanced methods such as topology optimization (TO) have to be used, in order to perform optimizations with multiple tens of thousands of free parameters. Furthermore, the ultimate design depends on multiple external circumstances, like the device geometry and even the illumination conditions. It has been shown that for locations at different terrestrial latitudes the prevailing annual mean irradiation conditions favor different grid patterns. This work has developed a methodology to not only improve the PCE but also the annual yield of a device by TO and standard parameter optimization. Gains of over 1% in yield are shown to be achievable despite a worse PCE at STC and at the same time reducing material consumption for the grid and TCO layer up to 50%.

9

Exploring the Limits – Current Technological Efficiency Limit of CIGS Thin-film Solar Modules

*A*fter optimizing modules in the last chapter, this chapter is dedicated to the calculation of an absolute efficiency limit of CIGS thin-film solar modules. Similar considerations have already been carried out on the cell level, where charged extended defects like grain boundaries and Shockley-Read-Hall (SRH) recombination are found to be responsible for the main losses on the cell level^[317]. A comparison of all emerging photovoltaic cell technologies with respect to their absolute physical limit can be found in^[345]. This chapter extends these calculations on the module level and investigates the issue of a maximum possible solar module with CIGS as an absorber layer. However, it is important to define a framework within which the optimization is carried out. Therefore, this chapter sets its clear boundary conditions on the currently available technology considering materials and manufacturing processes.

This Chapter's Guiding Scientific Question

What is the currently maximum achievable PCE for a thin-film CIGS module and how will the PCE develop in the future?

9.1 Boundary Conditions for Best Possible Module

As stated in the introduction of this chapter, it is of crucial importance for the module optimization to set its clear framework. Therefore, only materials and technologies that are currently available are considered. In particular, the following restrictions are used.

- As absorber material (and therefore as internal semiconductor I–V curve), the best published cell material in terms of V_{oc} compared to its band gap is used. The consideration and detailed calculation of this curve is shown in Section 9.2. A mathematical challenge will be to calculate out all the electrical transport and optical absorption losses and therefore receive an I–V curve with only intrinsic material losses, which result in V_{oc} losses.
- An encapsulated module stack with air / ARC / glass / hydrogenated indium oxide (IOH) / 50 nm magnesium-doped zinc oxide $Zn_xMg_{1-x}O$ (ZMO) / 50 nm zinc oxysulfide ZnO_xS_{1-x} (ZnOS) / 2200 nm CIGS / 1000 nm Mo / glass was used. This layer stack has simultaneously a better optical and electrical behavior than an AZO / i-ZnO / CdS version. Especially the usage of IOH instead of AZO and ZnOS instead of CdS offers the possibility for high efficiency cells ^[346, 347] with a larger j_{sc} due to their lower parasitic absorption. However, the usage of IOH is still very limited for the mass production of CIGS thin-film modules. The first reason for this is that the band alignment is much better with AZO and does not form a barrier. To eliminate this problem, combinations of AZO/IOH layers have been studied ^[346]. Moreover, for an IOH layer with cutting-edge properties, IOH needs to be annealed at temperatures that harm the lower layers within a CIGS cell stack. Even temperatures at 150 ° lead to a degradations in the CdS or ZnOS buffer layers, which results in a decreasing V_{oc} ^[348]. However, this work does use the assumption of a well conducting IOH layer since it only looks for the feasibility of the most efficient CIGS module and not the profitability of up-scaling this technique. Moreover, ZnOS has a much better optical behavior than CdS ^[349], especially having a larger band gap and correspondingly reduced parasitic absorption.
- The module has no removed edge area. Therefore, the benchmark area is only the active area itself.
- All specific resistivities and therefore all sheet resistances are measured from real materials.
- All optical refractive data was measured on real materials via ellipsometry measurements as described in Section 5.1.3.
- It is assumed that at the ARC layer at the air / glass interface suppresses all reflections which occur at this interface. Such effects can be achieved for example by microstructures ^[350, 351]. However, typical internal reflections for thin-film are still present and are listed under the loss mechanism reflection.
- A grid on top of the TCO layer is assumed since efficiencies with a grid are far better than without one. Also for that reason, it is the current state-of-the-art product. The grid design is considered to be a straight line along the entire cell, as seen in Figure 9.1. As the module geometry is very symmetric, a line-grid is the best compromise between a good conductivity and a feasible large-scale fabrication. In principle, the grid fingers do not need to extend till the left end of the cell. However, the deposition of the grid is often technically realized by screenprinting lines across multiple cells and afterwards cutting the shunting parts directly with the P3 trench. Therefore, extending lines till the end of the cells are assumed. Additionally, within the P2 area, a cross connection with a grid bus bar is present.

- Grid fingers cannot be arbitrarily thin. To match technological constraints of mass production, they are set to a minimum width of $40\ \mu\text{m}$. Moreover, there is no scientific drawback with arbitrarily high grid fingers. However, it takes more time to deposit a thicker grid. Therefore, a reasonable height of $2.5\ \mu\text{m}$ is assumed.
- Further attention must be drawn on the module connection. A monolithic interconnect between the cells is assumed. From a theoretical electrical point of view, the three trenches P1, P2, and P3 could be as short as the front TCO is thin. However, this extremely precise structuring cannot be achieved by today's technical standard production methods. Therefore, P1 is set to a width of $10\ \mu\text{m}$ to prevent the module from shunting. P2 is assumed to be $20\ \mu\text{m}$ wide to provide a sufficiently large contact area to overcome the contact resistivity. Finally, P3 is set to $10\ \mu\text{m}$ due to the brittleness of the TCO layer during the formation of the P3 trench.
- Between the trenches, there are no gaps assumed, which is technically challenging but still possible. Without these wasted areas, the entire module interconnect shrinks down to only the sum of the trench widths.

These requirements leave three undetermined quantities: the thickness of the top TCO layer, the cell width, and the distance between two grid fingers within the symmetrical grid structure. They will be optimized in Section 9.3.1.

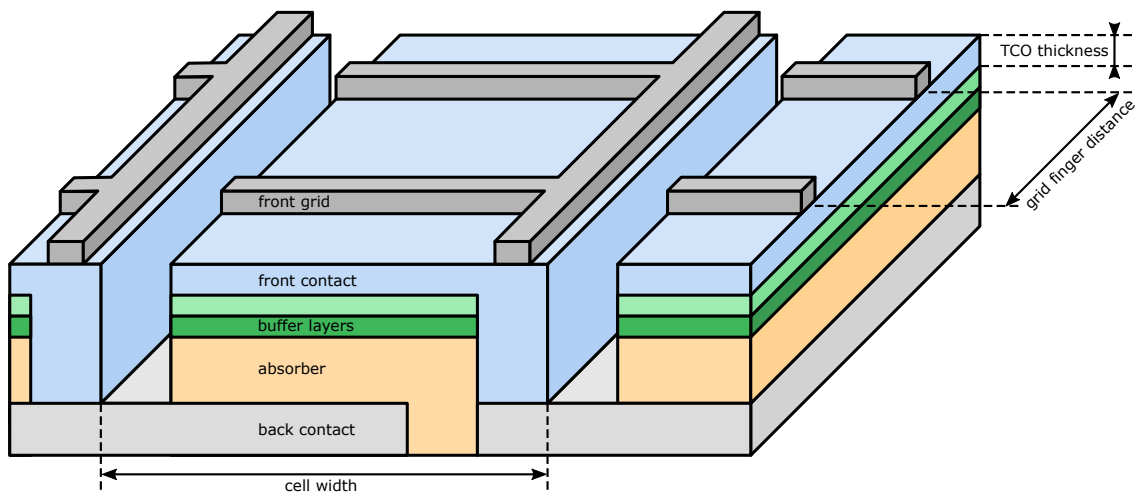


Figure 9.1: Geometry of record module. Its variable sizes are the thickness of the TCO, the distance between the grid fingers, and the width of a single cell.

9.2 Calculating the I–V Curve of the Best CIGS Material in Literature

To get a limit for the solar module efficiency, an absolute material limit needs to be known. Therefore, the best single-junction cell with a CIGS absorber with respect to its V_{oc} was considered ^[1]. However, its I–V curve still contains all kinds of losses like electrical transport losses, optical losses, and recombination. While the latter is part of the material limit, the first ones need to

be calculated out in order to replace them with better-performing options. Afterwards, the loss-adapted I–V curve can be used as an input for the module simulation and optimization. In order to get rid of these losses, a detailed analysis of the measured V_{oc} needs to be done. All the following calculations and simulations are done at STC and therefore at $T = 298$ K.

The measured V_{oc} of the best single-junction CIGS cell in literature is 740.0 mV [1, 352] and will be named V_{oc}^{real} in the following. It has a band gap of 1.12 eV [352, 353], which corresponds to a V_{oc} of 878.5 mV and j_0 of $6.122 \cdot 10^{-14}$ mA/cm² within the Shockley-Queisser model [148], which will be called V_{oc}^{SQ} and j_0^{SQ} in the following. The goal of this section will be to determine a matching j_0^{real} , which includes all recombination losses and therefore reduces only V_{oc} from the Shockley-Queisser model. All other diode parameters will be gathered from the Shockley-Queisser model. Since n_d , r_s , and r_{sh} are trivial within the Shockley-Queisser model, this will only be the photocurrent density j_{ph} . In order to get the material's I–V curve without any optical and electrical losses, the external luminescence quantum efficiency Q_e^{lum} is introduced [354].

$$Q_e^{lum} := \frac{j_0^{SQ}}{j_0^{real}} \quad (9.1)$$

Due to the vanishing shunting and series resistance effects and the trivial diode ideality factor within the Shockley-Queisser model, the diode equation in Equation (2.21) simplifies to

$$j(V) = -j_{ph} + j_0 \left(e^{\frac{q_e V}{k_B T}} - 1 \right). \quad (9.2)$$

At the point of interest at V_{oc} , the current density $j(V) = 0$ vanishes, which results in

$$V_{oc} = \frac{k_B T}{q_e} \ln \left(\frac{j_{ph}}{j_0} + 1 \right). \quad (9.3)$$

Since $j_{ph} \gg j_0$ holds for any reasonable solar cell, the summand +1 can be ignored. Subsequently, the open-circuit voltage of the real cell V_{oc}^{real} is considered and expressed via j_0^{real} , which can be replaced by Equation (9.1). After identifying the term for V_{oc}^{SQ} , the equation can be solved for Q_e^{lum} .

$$\begin{aligned} V_{oc}^{real} &= \frac{k_B T}{q_e} \ln \left(\frac{j_{ph}}{j_0^{real}} \right) \\ &= \frac{k_B T}{q_e} \ln \left(\frac{j_{ph}}{j_0^{SQ}} Q_e^{lum} \right) \\ &= \underbrace{\frac{k_B T}{q_e} \ln \left(\frac{j_{ph}}{j_0^{SQ}} \right)}_{V_{oc}^{SQ}} + \frac{k_B T}{q_e} \ln \left(Q_e^{lum} \right) \\ \Leftrightarrow Q_e^{lum} &= \exp \left(\frac{q_e}{k_B T} \left(V_{oc}^{real} - V_{oc}^{SQ} \right) \right) \end{aligned} \quad (9.4)$$

Putting in all the numbers from above, Q_e^{lum} can be calculated as 0.004823. According to Equation (9.1), j_0^{real} can now be determined as

$$j_0^{\text{real}} = \frac{j_0^{\text{SQ}}}{Q_e^{\text{lum}}} = 1.269 \cdot 10^{-11} \text{ mA/cm}^2. \quad (9.5)$$

After this calculation, all diode parameters for the best raw CIGS material are determined and listed in Table 9.1. V_{oc} of the best material is listed with 741.5 mV, which apparently is 1.5 mV higher than the V_{oc} of the measured cell. This is a plausible effect, since V_{oc} logarithmically depends on the photocurrent, which was raised due to the extraction of the optical losses. Therefore, the I–V curve of the best materials consists of the j_0 from the experimentally measured cell, but the j_{ph} from the Shockley-Queisser model. Both I–V characteristics can be seen in Figure 9.3 as black and red curves. They both have the same j_{sc} , but a drop in V_{oc} can be observed for the red material curve. The two ideal resistances in series and parallel can be justified by a negligible absorber resistance in comparison with the lateral transport resistances and a shunt-free material in an ideal case.

Table 9.1: Comparison of diode parameters and solar cell parameters for the Shockley-Queisser model and the calculated best CIGS material in literature.

	Shockley-Queisser model	reverse calculated best semiconductor material ^[1]
j_{ph}	43.83 mA/cm ²	43.83 mA/cm ²
j_0	$6.122 \cdot 10^{-14}$ mA/cm ²	$1.269 \cdot 10^{-11}$ mA/cm ²
n_{d}	1	1
r_{s}	$0 \Omega \text{ m}^2$	$0 \Omega \text{ m}^2$
r_{sh}	$\infty \Omega \text{ m}^2$	$\infty \Omega \text{ m}^2$
V_{oc}	878.5 mV	741.5 mV
j_{sc}	43.83 mA/cm ²	43.83 mA/cm ²
FF	87.06 %	85.30 %
PCE	33.52 %	27.72 %

In summary, a realistic material-level I–V characteristic for the currently best CIGS cell published in literature is found. The original curve contained recombination losses, optical losses, and lateral electrical transport losses. Since the last two of those are present within this work’s simulation, they need to be calculated out. The result is an I–V curve with only recombination losses and therefore the absolute maximum I–V curve that is currently possible to fabricate. This I–V characteristic will now be used in the following section to calculate the maximum possible module efficiency with this material. Therefore, optical and electrical losses will be again included, but on a module level instead of a cell level and under the condition of optimized parameters.

9.3 Simulate Currently Best Possible Module

The final aim for this section is to find the optimum module parameters and use the above calculated material I–V curve as input for the semiconductor material. Afterwards a loss analysis for the optimum module is performed.

9.3.1 Optimizing Module Geometry Parameters

This paragraph deals with finding the best module configuration for the given semiconductor material. For the resistivity of the front IOH layer, $3 \mu\Omega\text{m}$ was used, which is the lowest found resistivity in literature at layer thicknesses of 155 nm^[355], 180 nm^[356], and 185 nm^[38]. The grid resistivity of the grid structure was measured as $27 \cdot 10^{-9} \Omega\text{m}$. This results in a sheet resistance of around $0.01 \Omega_{\square}$ for the 2500 nm thick grid layer, which is in accordance with literature data^[357].

Finally, all input parameters are known and an optimization for the module geometry can be performed. As shown in Figure 9.1, three quantities are still variable: the thickness of the front TCO layer, the cell width, and the distance between two grid fingers within the periodic grid pattern. A large parameter space for all combinations has been sampled. The cell width was varied from 1 mm to 20 mm, the grid-finger distance from 0.1 mm to 5 mm, and the TCO layer thickness from 2 nm to 1000 nm. Multiple initial parameter sets are used for the optimization, which is performed by a downhill simplex method^[233].

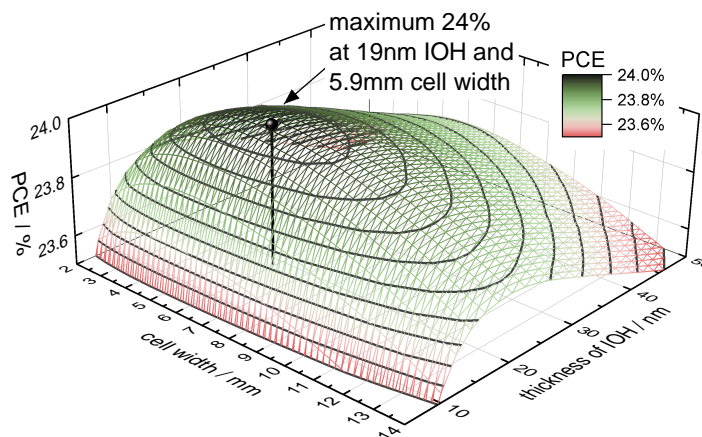


Figure 9.2: PCE of the optimum module as a function of the cell width and the thickness of the top IOH layer. While the cell width has a comparably small influence due to the high conductivity of the grid and the short distance of the module-interconnect area, the thickness of the IOH layer has a larger impact. The optimum configuration turns out to be at a cell width of 5.9 mm and a TCO layer thickness of 19 nm with a resulting PCE of 24 %.

In Figure 9.2, the efficiency is plotted as a function of two of the three variables for a narrow parameter space. As seen in Figure 9.2, the impact of the cell width on the total PCE is comparably weak. This is due to the used line-grid structure, which gives the potential distribution within the cell a nearly one-dimensional shape. The impact on the PCE would have been even weaker for a thicker grid. The TCO layer thickness however needs to have a certain thickness in order to provide the necessary electrical conductivity. After reaching this point at around 20 nm, the conductivity is sufficiently high. Further increases in the TCO thickness add to the parasitic optical absorption

and thus slowly decreases the overall efficiency. The global optimum of the three-dimensional function is determined to be at a cell width of 5.9 mm, a grid-finger distance of 1.55 mm, and a TCO layer thickness of 19 nm, which is shown in Figure 9.2.

Table 9.2: Input parameters for an analytical approximation to calculate the optimum cell width within a module.

quantity	symbol	used value
voltage of the best material at MPP	V_{MPP}	0.65 V
current density of the best material at MPP	j_{MPP}	42.36 mA/cm ²
length of the total interconnect area	w_{gap}	40 μm
sheet resistance of the grid	R_{\square}^{grid}	0.0108 Ω _□
width of the grid fingers	w_{grid}^{finger}	40 μm
distance between two grid fingers	d_{grid}^{finger}	1.55 mm

To prove the reliability of the simulations, an available analytical approximation for the optimum cell width w_{cell}^{opt} is used for comparison [182].

$$w_{cell}^{opt} = \sqrt[3]{\frac{1.5 \cdot V_{MPP} \cdot w_{gap} \cdot w_{grid}^{finger}}{j_{MPP} \cdot R_{\square}^{grid} \cdot d_{grid}^{finger}}} \tag{9.6}$$

With the parameters in Table 9.2, an optimum cell width of 6.04 mm is determined. This value differs only by a few percent from the precisely calculated value from the simulation. This analytical calculation proves the trustworthiness of the performed simulations.

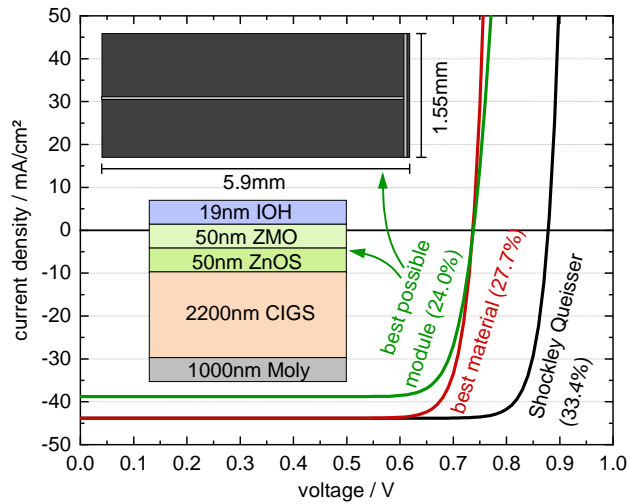


Figure 9.3: I-V curves of optimized record module. The black curve represents the Shockley-Queisser model with a band gap of 1.12 eV, the red curve the material limit with a modified j_0 , and the green curve the resulting best possible I-V curve of a module with the parameters from Figure 9.2

Knowing the best parameter configuration from Figure 9.2, the resulting I-V curve is simulated and plotted with the reference curves in figure 9.3. A significant drop in V_{oc} can be seen from the Shockley-Queisser model to the material curve, whereas the module I-V characteristic only differs in j_{sc} from the material I-V curve.

9.3.2 Loss Analysis for Currently Best Possible Module

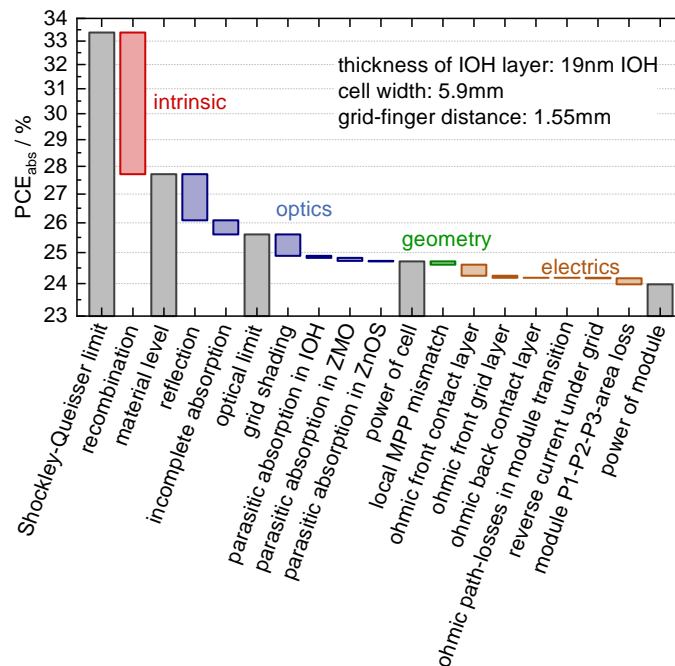


Figure 9.4: Loss analysis of the optimum module for the present day feasible scenario. Starting from the Shockley-Queisser limit with a band gap of 1.12 eV, this plot shows all losses down to the module efficiency. The module-geometry configuration are taken from the optimum of Figure 9.2.

Finally, the module with the optimum parameters is analyzed in detail. All losses are calculated and shown in Figure 9.4. Starting from the Shockley-Queisser limit, the intrinsic material losses are shown in red, which show up as V_{oc} losses due to the calculation in Section 9.2. As the internal reflections and the incomplete absorption are unavoidable with the given materials, this level will be called the optical limit. Afterwards, the efficiency is further reduced by the grid shading and all parasitic absorption losses to get the power of a hypothetical one-dimensional cell without any lateral effects. This cell level is at 24.71 %, which is above the current record efficiency of 23.35 %^[52]. This difference of around 1.36 % mainly arises for two reasons. First, they did not use IOH, but boron-doped zinc oxide (BZO) as a front contact layer, which has slightly worse optical and electrical properties than IOH^[358]. Furthermore, the cell level defined in this work is only valid for infinitesimal small cells without any electric effects. However, the current record cell has an active area of 1 cm², which does result in electrical losses, even at the cell level. Finally the module power is reached after subtracting all the electrical losses and the geometrical loss due to the module interconnect area. In this plot, the efficiency gap between the cell level and the module level (which is called the cell-to-module gap) is rather small. However, the typically large cell-to-module gap in the CIGS technology is mainly attributed to non-optimal TCO materials^[57]. However, since this work assumes IOH instead of AZO as a conducting layer and includes an optimized grid, the electrical losses almost vanish, which drastically shrinks the simulated cell-to-module gap. Moreover, the assumed trench widths are in total only 40 μm wide, which is feasible for single record modules but not for commercial mass-production modules. Finally, this chapter assumes a perfect up-scaling of the absorber material from a small laboratory cell towards a large-scale module without any inhomogeneities, which is not yet possible with cutting-edge technology in mass production.

9.4 Outlook in the Future of CIGS Module Limits

This section will deal with the possibility that the internal CIGS absorber probably will improve in the future. Since it cannot be exactly known how well it will develop, two further scenarios are presented here in addition to the currently possible scenario of the last chapter.

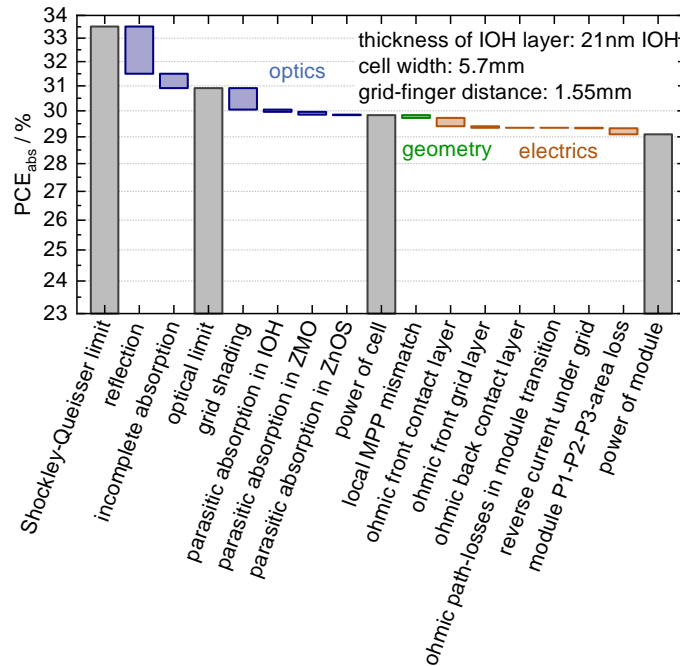


Figure 9.5: Loss analysis of the optimum module for the ideal scenario. As in Figure 9.4, this plot shows all losses down to the module efficiency. The internal I–V curve is chosen to be the physical limit for this scenario.

The first of these scenarios assumes a perfect CIGS absorber according to the Shockley-Queisser model. Therefore, the entire physical potential of an absorber with a band gap of 1.12 eV will be used as the input I–V curve for the absorber material. By doing so, only the radiative recombination is assumed to be present. Any further recombination mechanisms like SRH or Auger recombination are assumed to vanish. The same module optimizations in TCO layer thickness, cell width, and grid-finger distance are performed. Afterwards, a loss analysis including optical and electrical losses is performed for this hypothetical Shockley-Queisser CIGS absorber. The resulting losses and efficiencies can be seen in Figure 9.5. After subtracting all losses from the TMM, from the electrical model, and from the geometrical calculation, a final maximum PCE of around 29% remains. This efficiency is later referred to as the ideal scenario, since the best possible CIGS absorber is assumed.

Since the assumption of a perfect absorber without any parasitic recombination mechanisms is not really realistic, a third scenario with a realistic but optimistic view into the future needs to be established. GaAs is an absorber material that is well developed and reaches cell efficiencies up to 29.1% [28]. Moreover, GaAs is a direct semiconductor, which also holds for CIGS. Therefore, an optimistic scenario for best possible future CIGS absorber can be based on the currently best GaAs absorber. In detail, the external luminescence quantum efficiency Q_e^{lum} of CIGS is assumed to be as good as for the best published GaAs absorber. With a measured open-circuit voltage of 1130 mV with respect to their theoretically possible open-circuit voltage of 1157 mV [359], GaAs shows the potential of absorber optimization and surpasses the silicon technology [354].

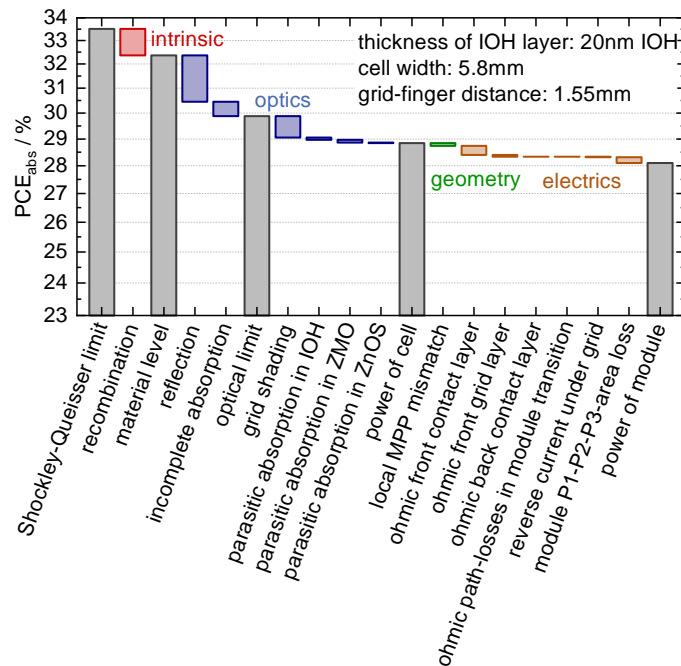


Figure 9.6: Loss analysis of the optimum module for an optimistic scenario. As in the two previous Figures, this plot shows all losses down to the module efficiency. The internal I–V curve for this CIGS module is as close to the physical limit as has been achieved by the current GaAs technology.

By using Equation (9.4), a Q_e^{lum} of 0.3519 can be calculated. Assuming that a CIGS absorber with a band gap of 1.12 eV will someday be as good as a GaAs absorber, Equation (9.1) reveals a j_0 of $1.740 \cdot 10^{-13} \text{ mA/cm}^2$. In Figure 9.6, this value has been used to establish a new hypothetical internal I–V curve and p–n junction, which only consists of minimal intrinsic losses due to recombination. Once more, an optimization in the quantities of TCO layer thickness, cell width, and grid-finger distance is performed and the resulting optimum parameters together with an entire loss analysis can be found in Figure 9.6. The roughly 1 % additional recombination reduces the overall efficiency to around 28 %. This will later be called the optimistic scenario since for a sufficiently long period of development, such a well evolved CIGS absorber is conceivable.

Finally, the calculated values are put in relation to the best published thin-film modules with a CIGS absorber. Due to the required relevance, only large-scale modules with an area larger than 800 cm^2 are considered. Figure 9.7 shows the evolution of their world record efficiencies from 1990 up to date. The currently best published module with the given restrictions mentioned above is from Solar Frontier and has a PCE of 19.2 % [55]. All three elaborated cases (ideal, optimistic, present day feasible) are schematically drawn towards the future. Their point of achievement on the time axis is plotted arbitrarily. While for the present day feasible scenario, less than 5 % in PCE gain can be achieved, the optimistic case is pretty close to the ideal scenario. By optimizing the electrics and optics it is already possible to gain nearly 5 % module efficiency. Further improvements in the CIGS material can potentially deliver another 4 %.

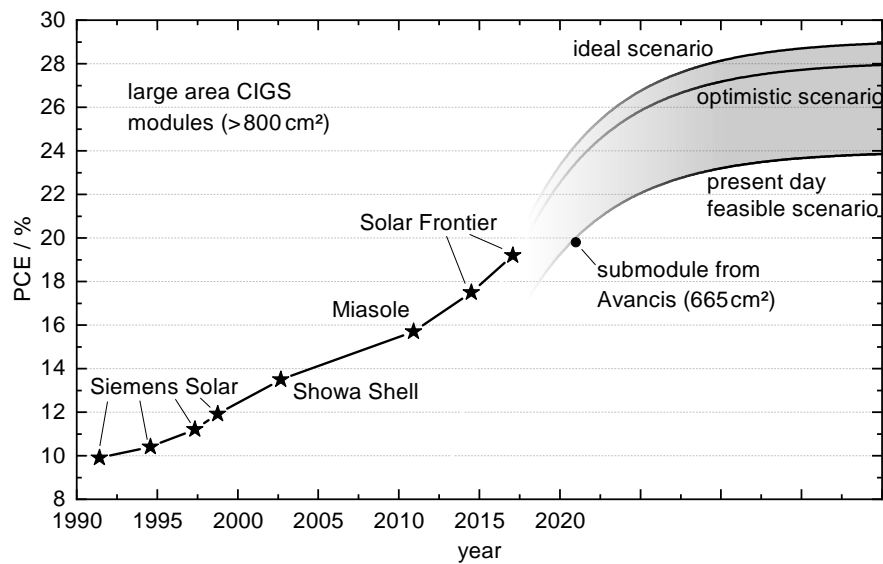


Figure 9.7: Classification of the three efficiency scenarios in the development of CIGS solar modules to date. All stars are world record efficiencies for large-scale modules with an area larger than 800 cm^2 . The present day feasible scenario assumes that the CIGS absorber stays on the current efficiency. Within the optimistic case scenario it is assumed that it improves in external luminescence quantum efficiency up to the efficiency of GaAs. Finally, within the ideal scenario, the CIGS absorber will be perfect in terms of intrinsic losses. All future predictions are plotted on an arbitrary time scale.



Answering this Chapter's Guiding Scientific Question

What is the currently maximum achievable PCE for a thin-film CIGS module and how will the PCE develop in the future?

Within the boundary conditions of currently available materials, technologies, and production tolerances, an upper limit of 24% for the module PCE has been calculated. For this calculation, the currently best CIGS absorber material published in literature was considered. The assumption of an improvement of the CIGS absorber comparable with a GaAs absorber leads to a new upper limit of 28%. For a perfect CIGS absorber without any intrinsic recombination losses, a PCE of 29% would be possible.

10

Summary and Outlook

In a nutshell, the work introduced in this thesis enables researchers to holistically model current-voltage characteristics (I-V characteristics), power conversion efficiencies (PCEs), and yield forecasts of thin-film solar cells and modules on the device level by means of numerical simulations fed by measured data. Using this methodology, all relevant real-world losses can be attributed to their corresponding loss mechanisms temporally resolved. Moreover, device parameters and metallization grid patterns can be optimized for different irradiance conditions and a maximum PCE on the module level for the copper indium gallium diselenide $\text{CuIn}_{1-x}\text{Ga}_x\text{Se}_2$ (CIGS) thin-film technology was determined within this work.

On the device level, two physical models need to be linked in order to model all relevant intra-device processes. All reflection and absorption effects need to be considered by an optical model, while an electrical model is necessary to take into account all resistive effects. These properties are linked by the specific materials in the device. The thin layers within a thin-film solar device cause complex wavelength-dependent interference patterns that obey the Fresnel equations of coherent wave propagation. Roughness effects at the interface and thicker encapsulant layers introduce an incoherent influence. The combination of both effects can be described by a modified transfer-matrix method (TMM) approach, which takes into account coherent interferences as well as incoherent attenuation. Locally generated current within the solar device is guided within electrical conductive layers towards a central contact point. Due to the finite conductivity of the used materials, this results in ohmic effects, especially on the front side, where a transparent conducting oxide (TCO) instead of a metal is used since light needs to penetrate this layer. This results not only in ohmic losses, but also in a spatial gradient in the voltage distribution, which has non-linear effects on the local current generation. This entire electrical behavior is modeled by a Poisson's equation solver within a finite element method (FEM) in this thesis. In order to include the process of local current generation as well, the methodology of this work makes it possible to either link a drift-diffusion model as a third simulation technique or to include the information by means of measured data. The holistic linkage of these three models is one big novelty of this work that bridges the existing gap in literature of a holistic and bidirectional

calculation between simulations of solar cells at material level and calculations of applied system designing at industry level. Due to the all-in-one modeling of this work, the influence of a given parameter on the performance cannot only be determined in the forward direction, but a parameter can also be calculated in the backward direction from a device's current–voltage curve (I–V curve) via a specially designed reverse engineering fitting (REF) process. The benefit of this work's methodology is the development of a tool that calculates the potential of technological innovations not only on the PCE, but also on the annual energy yield of thin-film modules. Such sensitivity analyses give information in advance about which technological improvement efforts are worthwhile in the end, which is valuable information for solar power plant operators. While the investing costs in €/kW_p can be calculated relatively easily, this work can answer the more difficult question of financial return in kWh/a, which depends, for instance, on the irradiance and climate conditions of the specific system location.

The evolved simulation methods are independent of the absorber material and the used thin-film technology. The methodology is verified with measured data under laboratory conditions as well as in outdoor applications. Under standard test conditions, meaning 1000 W/m² irradiance, 25°C module temperature, and AM1.5G spectral distribution (STC), experimentally measured reflection and external quantum efficiency (EQE) data of thin-film solar cells have been proven to accurately match simulated predictions. The correct interaction of electrical and optical models are shown by accurately predicted device I–V curves that include optical as well as electrical effects due to modified short-circuit current density and fill factor (FF), respectively. Their coefficients of determination of simulated I–V curves with respect to experimental verification data reach values of around 95 % for modified cell sizes and more than 99 % for different contact layer thicknesses. Therefore, solar-module parameters can be forecast with a very high accuracy. The interplay with an external drift-diffusion model is shown to accurately predict generated powers even under non-STC, especially with respect to temperature changes, by a yield calculation model for an entire day of a real-world solar module.

Holistic loss analyses can be performed for thin-film solar cells under laboratory conditions as well as for modules in the field. While all optical losses are calculated via parasitic loss paths within the TMM approach, electric losses due to shunting and series effects are determined via Ohm's law within the spatially resolved FEM. Non-linear losses due to spatial voltage distribution as well as geometrical losses due to inactive areas are equally considered within the methodology of this work. In combination with the drift-diffusion method, this three-stage simulation ansatz can manage temperature fluctuations, while irradiance fluctuations are considered by the TMM, and their optoelectronic interplay within the Poisson solver. The simulated module power including all power losses match the actually measured outdoor module power. This proves both the completeness of all losses and the correctness of the simulation methods and the loss analysis.

Furthermore, this work enables fast and effective optimizations on the device level, including single or multiple parameters or even topologically complex structures, such as metallization grids with multiple tens of thousands of optimization variables. Individual device parameters like the TCO layer thickness, the cell width, or the grid-finger distance can be optimized using a sweep across a plausible range. For multiple simultaneous parameters in one optimization, a more sophisticated gradient-free optimization algorithm must be used since the number of possible parameter combinations quickly rises with the amount of parameters. For such complex multi-parameter optimizations, a FEM model is necessary since analytical approximations often encounter only a single optimization variable. Furthermore, such calculations often give no reason for the resulting optimized variables. In combination with the loss analysis, a simulation methodology such as the one in this work can also provide a physical understanding that give valuable information

for the utilization of the results. Moreover, such a FEM model allows for sensitivity analyses that show the influence of input parameters for the overall performance. Even more optimization variable parameters appear in the optimization of topologically complex questions as the design of the metallization grid pattern. In order to give the algorithm as much freedom in design as possible, multiple tens of thousands of free parameters are needed. For such complex problems, the method of topology optimization (TO) is introduced. This methodology has been used to show that the appropriate grid design depends on the prevailing irradiation conditions. This work demonstrates a possible performance gain of over 1 % and material consumption savings for the grid and TCO layer up to 50 %, if grid designs are optimized for annual yield instead of the standardized PCE under STC.

Finally, the developed simulation methodology can be used as a test room to implement future technological improvements to a digital model. Within this work, it is used to calculate an upper efficiency limit for thin-film CIGS modules with respect to currently available materials, technologies, and production tolerances. For the currently best CIGS absorber material, a limit of 24 % is determined, which exceeds the currently best module with 19.2 % efficiency. For an assumed improvement of the CIGS absorber that is comparable to the one of gallium arsenide (GaAs), an advanced limit of around 28 % is calculated. The assumption of a perfect CIGS absorber without any intrinsic recombination losses leads to a maximum upper PCE limit of 29 %.

All in all, the developed simulation methodologies and forecasts of this work add one small but necessary piece in the puzzle to the big picture of understanding, developing, and improving thin-film solar modules and promotes the spread of renewable energies.



Demonstration of the Developed Simulation Platform

*W*ithin this chapter, the implementation of the developed simulation platform^[159] is briefly introduced. In the first part, the procedure of simulating a solar device is shown. The rest of the chapter is spent on a short introduction in the graphical user interface (GUI) of the platform. Due to the possibility of introducing arbitrary material parameters and geometries, the simulation platform acts as a user-friendly test room for new technologies as seen in Chapter 9.

This Chapter's Guiding Scientific Question

How are the theoretical simulation methods for solar devices implemented in the simulation platform?

A.1 Overview of the Program

This section briefly introduces the basic procedure of simulating a solar cell or module on the device level. The around 45 000 lines of object-oriented code were programmed in collaboration with Tim Helder and are stored on the version control service GitHub ^[159]. The basic structure of a device simulation is shown in the following block of C# code.

```
1 // Create object
2 ModelDevice model = new ModelDevice("myDevice", temperature);
3
4 // Create mesh
5 model.SetMesh(geometryFilePath, desiredNumberOfPoints);
6
7 // Set properties
8 model.SetOptics(opticMode, spectrumAM15G, illuminationIntensity);
9 model.SetElectrics(potentialSelector);
10 model.SetPreferencesForModuleInterconnect(geometryFilePath);
11
12 // Set initial guess and start simulation
13 model.SetInitialGuess();
14 model.Solve(voltageMode);
15
16 // Output simulation results
17 model.OutputPotential(outputPath + "solutionPotential.dat");
18 model.OutputCharacteristics(outputPath + "solutionCharacteristics.dat");
19 model.WriteResultsToGUI();
20 model.PlotResultsToGUI();
```

The first line creates the object `model` from the class `ModelDevice` with a name and its temperature as input values. Afterwards, a mesh with the desired number of finite elements is created by using a geometry file as input. This input file has the file ending `2dg` (two-dimensional geometry) and contains all geometrical data like the definition of points and areas, the external contact points, and the layer stack for each area. The next three lines of code call methods that set preferences to all generated finite elements. These preferences are obtained from a database that contains all electrical and optical material data. Further necessary optical inputs are the optical model (Lambert-Beer method or TMM as described in the Sections 4.2.1 and 4.2.2), the input spectrum (usually AM1.5G), and the illumination intensity in kW/m^2 . The function `SetElectrics()` mainly sets all neighbor resistors as described in Section 4.3.2.2. Finally, the method to set module preferences creates the defined interconnect areas in order to connect monolithically interconnected cells. Subsequently, an initial guess is set for all front and back potentials within all finite elements. The method `Solve()` solves the equation system from Equations (4.27a) and (4.27b) with the boundary conditions (4.29a) and (4.29b) for a single or multiple voltages. Finally, all results are printed and written into files and to the GUI.

Using this procedure, a digital model can be created and different experiments can be executed. For example, the voltage can be swept, geometrical parameters such as thicknesses of individual layers can be adapted and optimized, or a yield calculation can be done by varying the variable `illuminationIntensity`. This way, a model does not need to be created completely new from

scratch, but can be modified by calling the preference methods. This is a huge advantage of simulations in comparison with laboratory experiments. Therefore, this simulation platform acts as a test room for developing new ideas and technologies.

A.2 Graphical User Interface of the Simulation Platform

This section briefly shows the GUI of the simulation platform that was developed within this work. Figure A.1 shows the home-screen of the platform. Basically, four different software modules are accessible. On the left, materials can be defined, edited, and deleted. The front end shows all material parameters in the GUI, while on the back end, this module reads and writes to a database. In the optics section, an optical-only simulation can be executed that gives useful information about the spectrally resolved reflection and absorption in the different layers. The third module represents the drift-diffusion section of the platform, which was mainly created by Tim Helder within the framework of his dissertation. Here, simulation models of semiconductors and p-n junctions can be created and simulated. The last program section is for creating and simulating models of macroscopic solar cells and modules. These devices are created by clicking on the left designer button and simulated under the right button. This program part will be subject of the next section.

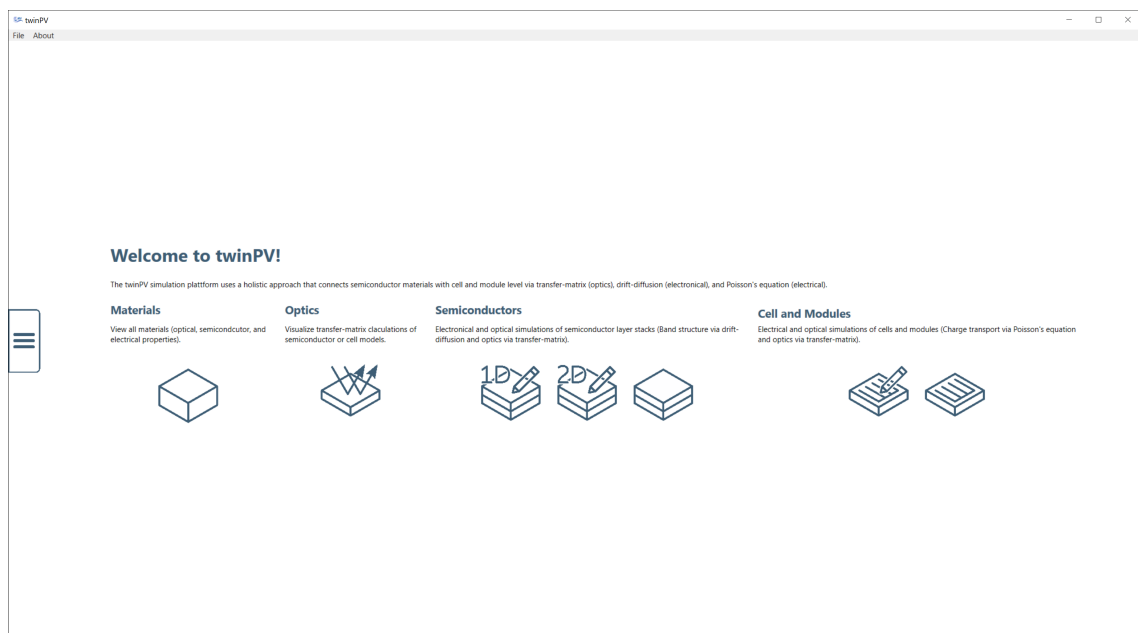


Figure A.1: Screenshot of the home-screen of the simulation platform. There are four separate program modules that can be accessed.

A.2.1 Device Simulations within the Simulation Platform

Figure A.2 shows a screenshot of the tool within the simulation platform that is capable of designing arbitrary solar cells and modules. The main graph in the middle shows the topview of the device with all grid fingers in light gray and the rest of the device in dark gray. New regions and points can be added by the buttons on the left. Regions are added by successively adding new points, which are connected by segments and enclose a certain area. On the right side, all points, segments, and areas are listed. Here, external device contacts can be set by check boxes and a contact resistance is optional to insert in the text box next to it. The contact can be a point, a segment, or an area and also a multiple of those geometries combined. At least one external contact is required on the front and on the back, respectively. On the bottom, a measurement unit can be chosen. Saving a geometry leads to the generation of a `2dg`-file that is saved to the database. This file can be used later to simulate this geometry.

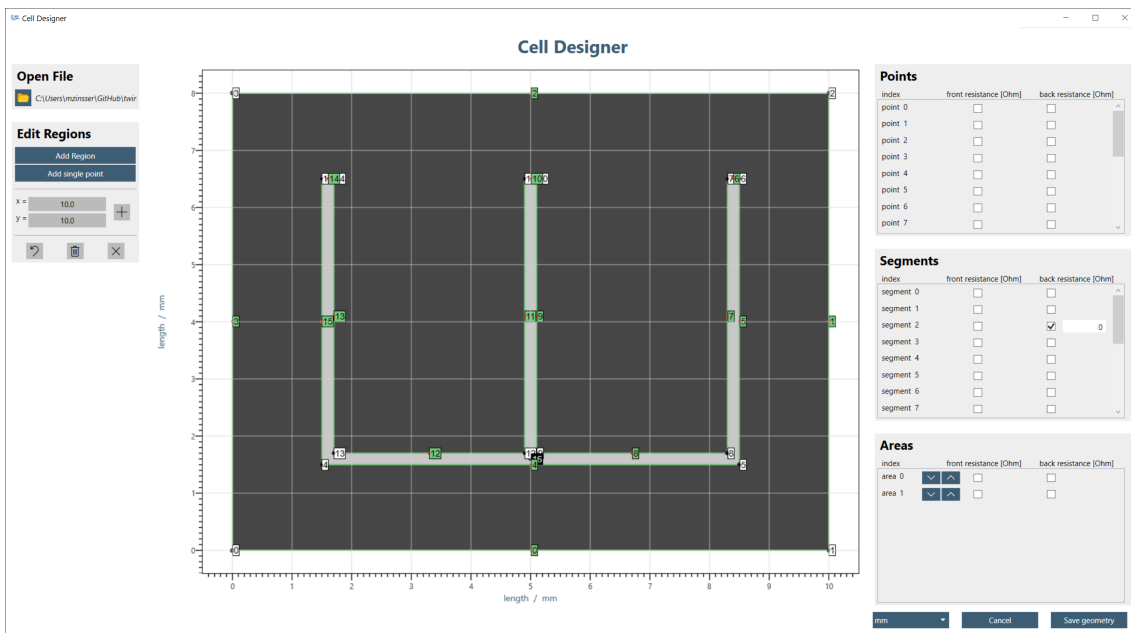


Figure A.2: Screenshot of the design screen of the simulation platform. In this digital model, solar cells and modules can be designed and edited.

Double clicking an area in the designer window opens a new window that specifies the layer stack of this area, as shown in Figure A.3. For each region, it is necessary to define a central p-n junction that can be either simulated in a drift-diffusion model or engineered by a REF procedure. Furthermore, two contact layers on each side of the absorber material can be defined. One of them is usually used as TCO material and the other one for an optional grid layer. It is also necessary to define the materials that are on top and below the active layer stack. Most often for thin-film devices, these materials will be air and glass. Additionally, optional optical layers can be defined that only contribute to the optical model and not to the electrical model. It is possible to introduce optically coherent layers at each point within the layer stack and optically incoherent layers on top of the layer stack. The latter is often used for encapsulant materials. Furthermore, the thicknesses of all layers need to be defined. On the bottom, it can be selected whether this region is a module interconnect area or a regular cell region. Moreover, an optical shading factor can be introduced that stands for the amount of shading within this region. For unshaded regions, this factor will be

0, but can go up to 1 for entirely shaded regions. Finally, a check box can be set that determines whether this region counts to the definition of the aperture area of the device and thus is considered for the calculation of the PCE.

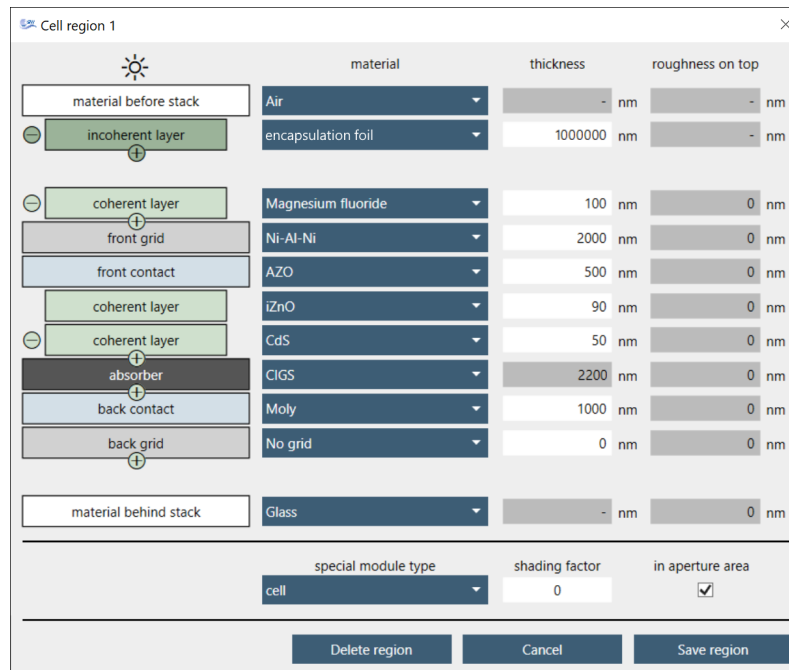


Figure A.3: Screenshot of the layer stack manager of the simulation platform. The content of this screen is belongs to an individual region and defines the layer stack within this region.

The simulation window in Figure A.4 is divided into three columns. On the left, all inputs can be chosen, while the two right ones show the simulation results. The top left text box determines how many finite elements should be used to simulate the solar device from the geometry file that is defined in the file chooser dialog below. In the preferences section, several options can be set. The first drop down box defines which potentials should be modeled within a simulation. Most often, both front and back potentials will be simulated, but it is also possible to simulate only one potential while keeping the other one a perfect conductor without any transport resistance. Moreover, the optical model can be chosen as either a TMM approach or a Lambert-Beer calculation. Finally, the illumination intensity in kW/m^2 can be entered. For a regular illumination with the AM1.5G spectrum, this will be 1. In the next section, the voltage mode is set via radio buttons. The device can be simulated either at a predefined fixed voltage, at the maximum power point (MPP) voltage, an entire I–V curve with predetermined voltage steps, or an I–V curve with a subsequent precise search for the MPP. The buttons within the last group start simulations. The most basic simulation is a single shot with the selected input parameters and the defined voltage mode. However, the simulation platform also enables to vary an arbitrary parameter, which could be for example the thickness of any layer, the cell width of a module, the illumination intensity, or the distance between grid fingers. The results will be shown afterwards as a function of the one or multiple batch parameters. Finally, yield calculations can be executed for a given input file with hourly meteorological data that can be downloaded from ^[251].

In the middle column, there is a three-dimensional model of the cell with the front and back potential plotted on top and on the bottom, as it was introduced in Section 4.4.1 of this work. Below this plot, I–V curves (black) and power-voltage curves (red) are shown. Dark lines are

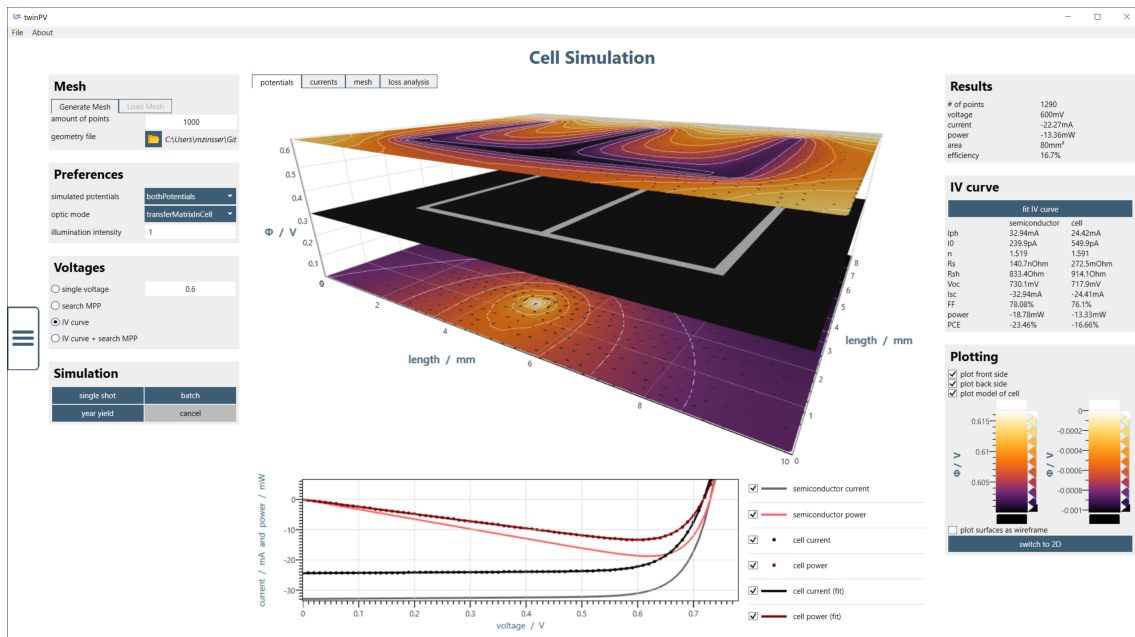


Figure A.4: Screenshot of the simulation screen of the simulation platform. This is the main simulation window and shows a plot of the electrical potential distribution, the simulated I–V curve, and fitted simulation parameters on the right.

characteristic curves of the simulated device, while the light ones are the material-level curves that work as input for the simulation. The right side of the window shows numerical results like current and voltage at the MPP, the diode parameters and solar-cell parameters.

In another tab, the loss analysis of the simulated device at the defined voltage is shown, as shown in Figure A.5. As used in the main part of this work, starting from the material limit on the left side, electrical, optical, and geometrical losses are plotted in red, while the generated power of the simulated device is shown in gray on the right side. With the help of this plot, the most pronounced losses can be quickly identified.

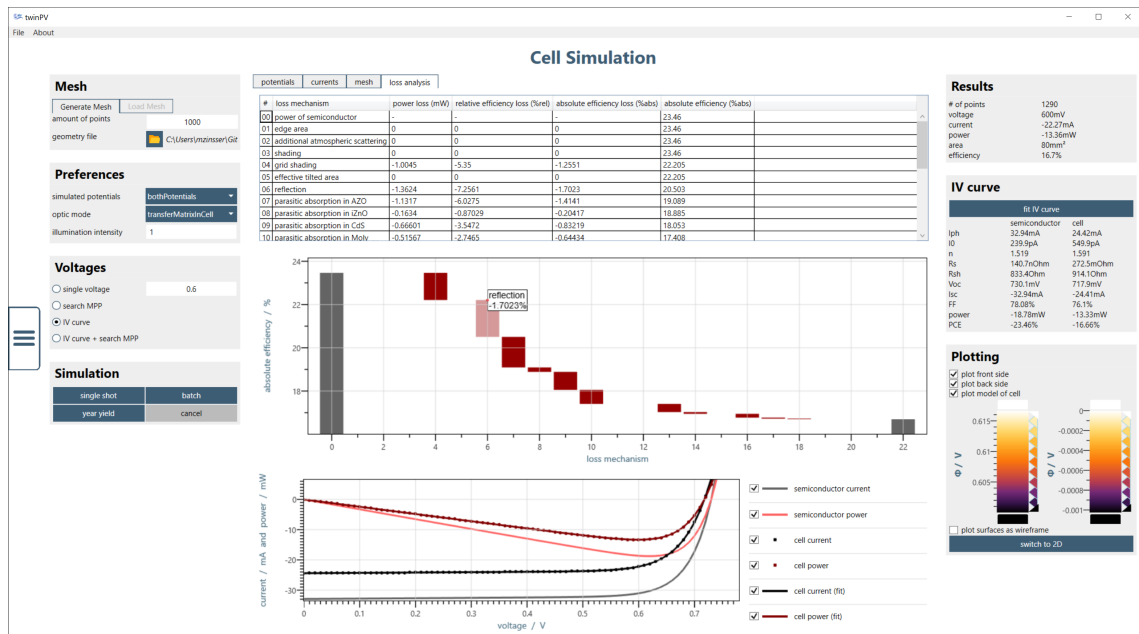


Figure A.5: Screenshot of the loss analysis screen of the simulation platform. In this screen, all losses from the material level to the generated power of the solar devices are listed and plotted.



Answering this Chapter's Guiding Scientific Question

How are the theoretical simulation methods for solar devices implemented in the simulation platform?

The simulation platform consists of an object-oriented standard procedure for simulating solar devices that contains individual functions for setting electrical, optical, and module-specific properties. This allows to vary the input parameters without creating an entirely new simulation model. Thus, several different simulations are possible. Single shots at fixed or variable voltages can be executed as well as variations of input parameters in a batch mode and yield calculations, which primarily sweep the illumination intensity. Finally, there is a user-friendly graphical user interface (GUI) that allows a visual and intuitive input and control of the platform without the usage of a command window or having sophisticated programming skills.

B

Calculation of FEM Resistances

The goal of this chapter is to prove that the resistance between two finite elements is physically correct and independent of the chosen FEM mesh. Both properties are necessary for accurate simulation results. The proof for the physical correctness will be accomplished by an empirical proof that includes a simulated four terminal sensing. Since this is an analytically solved problem, the result of the simulation can be compared with the numerical simulation result. The proof for the mesh independence will be accomplished by assuming the resistance between two elements be calculated in the same way as the one of a single wire. Using this method, the total resistance between two elements in a 3-element-mesh is calculated and compared with the resistance, when a fourth element with arbitrary coordinates was added to the mesh. If both calculations yield the same resistance, the assumed method does not depend on the chosen mesh. Moreover, the proof can be generalized from a three-element mesh to an multi-element mesh by replacing the star-triangle transform with a star-mesh transform.

This Chapter's Guiding Scientific Question

How can the correct calculation and the mesh independence of this work's FEM resistors be proven?

B.1 Empirical Proof for Correct Calculation of FEM Resistances

This section will demonstrate introduced way of calculating the transport resistances in Section 4.3.2.2 is the proper way and represents the correct physical behavior. In order to do so, a quadratic meshing domain with the side length w has been meshed with the Delaunay and Voronoi algorithms developed in this work. An example for this arrangement is shown in Figure B.1 for $w = 10$ mm. All transport resistances of each finite element are calculated in the above described way with a specific resistance ρ_{input} . Now the idea is to emulate a four-terminal resistance sensing measurement within the simulated meshing domain and compare the simulated result to the input resistivity. For this reason four contact points with the distance s to each other are placed in a row. Between the outer ones, a current is induced and the potential distribution is calculated by using the Newton-Raphson method [113, 229]. Using the measured voltage drop V between the inner contacts the emulated specific resistance

$$\rho_{\text{emul}} = d_{\text{layer}} \cdot R_{\square} = \frac{\pi}{\log 2} \cdot d_{\text{layer}} \cdot \frac{U}{I} \quad (\text{B.1})$$

is determined, where R_{\square} is the sheet resistance and the prefactor $\pi/\log 2$ is calculated via a topological geometry ansatz [252].

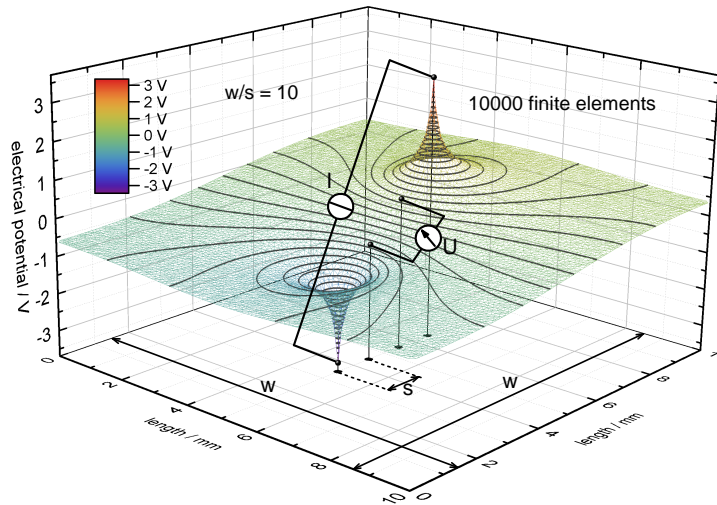


Figure B.1: Potential in a four-terminal sensing setup. The entire meshing domain has a quadratic base area with the side length w . Four contacts are placed in the center with a spacing of s between each contact point. Between the outer two a current is induced and across the two middle contacts the voltage drop is measured.

However, Equation (B.1) is only valid for an infinitely large area and consequently for $w \gg s$. Therefore, before comparing the emulated resistivity with ρ_{input} , a finite w needs to be considered. For this purpose, theoretically calculated correction factors τ_{corr} for different ratios of $\frac{w}{s}$ exist [252]. Using them, a corrected specific resistivity can be computed via

$$\rho_{\text{corr}} = \tau_{\text{corr}} \cdot \rho_{\text{emul}}. \quad (\text{B.2})$$

In Figure B.2 the input resistivity ρ_{input} with respect to the corrected emulated resistivity ρ_{corr} is

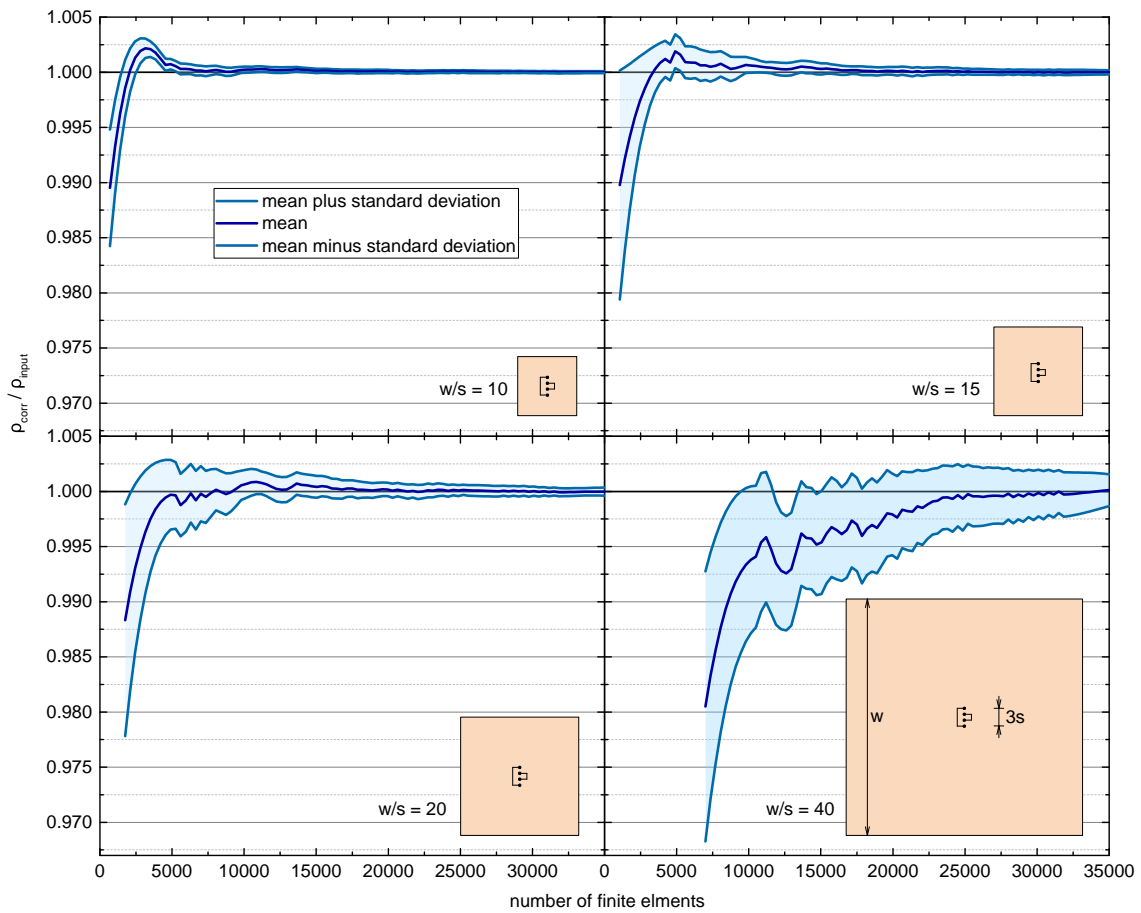


Figure B.2: Emulated resistivities within a four-terminal sensing setup for different ratios of w/s . For each configuration a sufficient number of finite elements results in the correct specific resistivity.

shown for different ratios of w to s . Different densities of finite elements determine the accuracy of meshing. For each data point, sixty randomly created meshes with the same number of elements have been created and the mean value and standard deviation has been plotted as a function of the number of elements. For smoothing the function, a Savitzky–Golay filter^[241] with the order 3 and the framelength 19 has been used. For each graph, a match between both specific resistivities can be observed. For bigger ratios of w/s , more elements are needed to achieve this accordance due to the larger meshing domain. If there are not enough elements, the spatial potential distribution is not correctly resolved resulting in a too small emulated resistivity due to large potential steps.

The above paragraph proved the correctness of calculating the transport resistance via Equation (4.24) by means of numerical emulation. Another important feature of calculating transport resistances is the scale invariance and hence the mesh independence. An analytical proof of this characteristic is given in the next section. The fact that the calculated resistance still changes with the number of finite elements despite the mesh independence (compare Figure B.2) is not due to the incorrect calculation of the transport resistances, but due to the insufficient meshing resolution of the sample.

B.2 Mesh Independence of FEM Resistances

B.2.1 Resistance of Single Wire

When a current I flows uniformly distributed through a single piece of material, a voltage drop $\Delta\Phi$ is created. The ratio of both quantities is the resistance $R = \frac{\Delta\Phi}{I}$. The resistance can be calculated

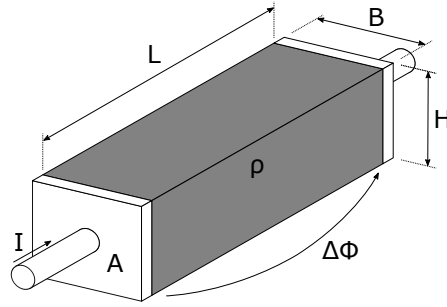


Figure B.3: The resistance of a wire is calculated via the specific resistivity ρ and the geometric lengths B and H perpendicular to the current direction and L along the current direction.

by geometric parameters (see Figure B.3) and the specific resistance ρ of the used material.

$$R = \rho \frac{L}{A} = \rho \frac{L}{HB} \quad (\text{B.3})$$

In the following, the height H and the specific resistance ρ are identical for each resistance and for the sake of simplicity set to 1. This leads to a new definition of a reduced resistance

$$\tilde{R} = \underbrace{\frac{\rho}{H}}_{:=1} \cdot \frac{L}{B} = \frac{L}{B}. \quad (\text{B.4})$$

B.2.2 Resistance between Two Finite Elements

We define a mesh with four finite elements. Two of them can be set to discrete coordinates without loss of generality due to the free choice of the coordinate system.

$$P_1 = (0, 0) \quad (\text{B.5a})$$

$$P_2 = (0, 1) \quad (\text{B.5b})$$

$$P_3 = (x_3, y_3) \quad (\text{B.5c})$$

$$P_4 = (x_4, y_4) \quad (\text{B.5d})$$

In order to calculate the resistance between two finite elements a and b , the distance between both center points and the length of the commonly shared edge are required. The distance is given via the Euclidean 2-norm of position vectors $\|\overrightarrow{P_a P_b}\|$ and the shared edge length is the distance of the two common Voronoi corners. The Cartesian coordinates of the Voronoi corner C_{abc} is determined

via the center of the circumscribed circle of the triangle with both elements P_a and P_b and a third neighboring element P_c .

$$C_{abc} = \left(\frac{(x_a^2 + y_a^2)(y_b - y_c) + (x_b^2 + y_b^2)(y_c - y_a) + (x_c^2 + y_c^2)(y_a - y_b)}{2x_a(y_b - y_c) + 2x_b(y_c - y_a) + 2x_c(y_a - y_b)}, \right. \\ \left. \frac{(x_a^2 + y_a^2)(x_c - x_b) + (x_b^2 + y_b^2)(x_a - x_c) + (x_c^2 + y_c^2)(x_b - x_a)}{2x_a(y_b - y_c) + 2x_b(y_c - y_a) + 2x_c(y_a - y_b)} \right). \quad (\text{B.6})$$

Applying (B.6) to the elements (B.5a) to (B.5d) results in the following Voronoi corners.

$$C_{123} = \left(\frac{x_3^2 + y_3^2 - y_3}{2x_3}, \frac{1}{2} \right) \quad (\text{B.7a})$$

$$C_{124} = \left(\frac{x_4^2 + y_4^2 - y_4}{2x_4}, \frac{1}{2} \right) \quad (\text{B.7b})$$

$$C_{134} = \left(\frac{y_4(x_3^2 + y_3^2) - y_3(x_4^2 + y_4^2)}{2x_3y_4 - 2x_4y_3}, \frac{x_3(x_4^2 + y_4^2) - x_4(x_3^2 + y_3^2)}{2x_3y_4 - 2x_4y_3} \right) \quad (\text{B.7c})$$

$$C_{234} = \left(\frac{(1 - y_4)(x_3^2 + y_3^2) + (y_3 - 1)(x_4^2 + y_4^2) - y_3 + y_4}{2x_4(y_3 - 1) + 2x_3(1 - y_4)}, \right. \\ \left. \frac{-x_3(x_4^2 + y_4^2) + x_4(x_3^2 + y_3^2) + x_3 - x_4}{2x_4(y_3 - 1) + 2x_3(1 - y_4)} \right) \quad (\text{B.7d})$$

All finite elements and corners are visualized in Figure B.4a for three elements and in B.4b for four elements. The goal is to calculate the resistances between the elements P_1 , P_2 , and P_3 for the given 3-element-mesh. We then insert a fourth element P_4 and calculate the resistances between the first three elements again. Both variants should reveal the same resistances to prove the mesh-independence of the method, how the resistances are calculated in the first place. The equivalent resistor circuit diagrams are shown in Figures B.4c and B.4d. The resistors R_{12}^{out} , R_{13}^{out} , and R_{23}^{out} can be neglected for the comparison since they are present in both meshes.

With the short forms

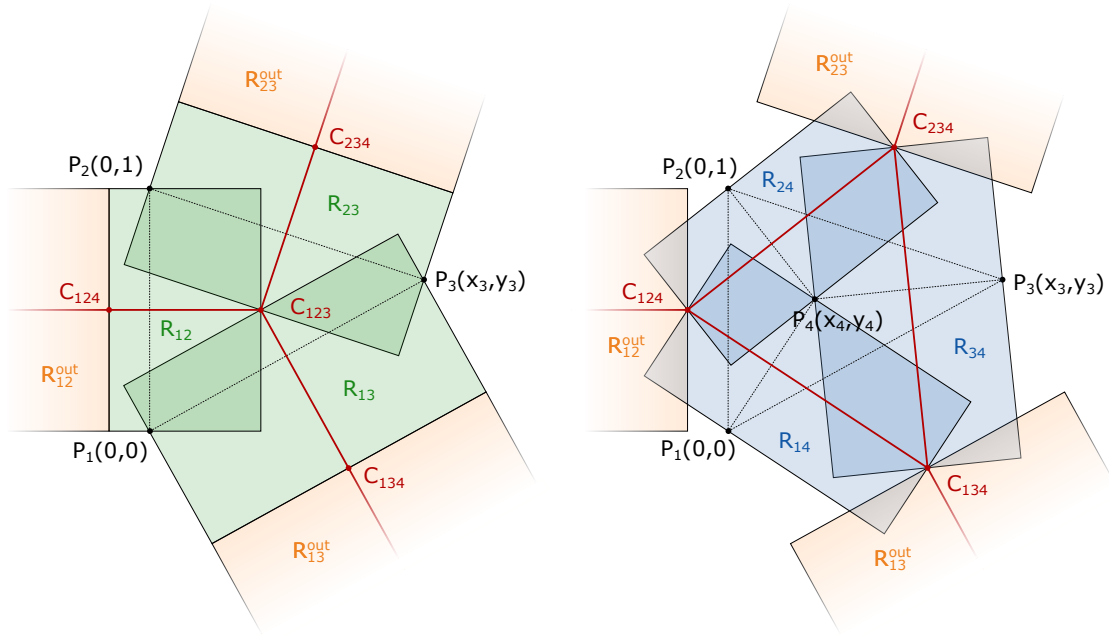
$$f := \frac{1}{2} (x_3^2 x_4 - x_4^2 x_3 - (y_4 - 1)x_3 y_4 + (y_3 - 1)y_3 x_4) \quad (\text{B.8a})$$

$$g := x_3 - x_3 y_4 - x_4 + y_3 x_4 \quad (\text{B.8b})$$

$$h := x_3 y_4 - y_3 x_4 \quad (\text{B.8c})$$

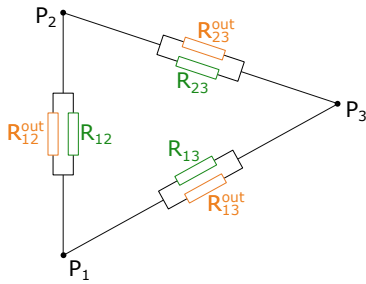
and the resulting identity

$$g + h = x_3 - x_4 \quad (\text{B.9})$$

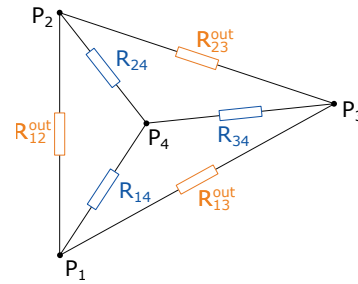


(a) Geometric representation of mesh with 3 finite elements.

(b) Geometric representation of mesh with 4 finite elements.



(c) Equivalent resistor circuit diagram with 3 finite elements.



(d) Equivalent resistor circuit diagram with 4 finite elements.

Figure B.4: Sketches of two meshes with 3 and 4 finite elements P_1 to P_4 . The dotted lines indicate the Delaunay mesh and the red lines the border of the Voronoi cells. The resistances in (c) and (d) are calculated via the indicated areas in (a) and (b).

we can calculate the reduced resistances according to (B.4) for both meshes.

$$\tilde{R}_{12} = \frac{\|\overrightarrow{P_1 P_2}\|}{\|\overrightarrow{C_{123} C_{124}}\|} = \frac{x_3 x_4}{f} \quad (\text{B.10a})$$

$$\tilde{R}_{13} = \frac{\|\overrightarrow{P_1 P_3}\|}{\|\overrightarrow{C_{123} C_{134}}\|} = \frac{x_3 h}{f} \quad (\text{B.10b})$$

$$\tilde{R}_{23} = \frac{\|\overrightarrow{P_2 P_3}\|}{\|\overrightarrow{C_{123} C_{234}}\|} = \frac{x_3 g}{f} \quad (\text{B.10c})$$

$$\tilde{R}_{14} = \frac{\|\overrightarrow{P_1 P_4}\|}{\|\overrightarrow{C_{124} C_{134}}\|} = \frac{x_4 h}{f} \quad (\text{B.10d})$$

$$\tilde{R}_{24} = \frac{\|\overrightarrow{P_2 P_4}\|}{\|\overrightarrow{C_{124} C_{234}}\|} = \frac{x_4 g}{f} \quad (\text{B.10e})$$

$$\tilde{R}_{34} = \frac{\|\overrightarrow{P_3 P_4}\|}{\|\overrightarrow{C_{134} C_{234}}\|} = \frac{gh}{f} \quad (\text{B.10f})$$

To compare the resistances \tilde{R}_{12} , \tilde{R}_{13} , and \tilde{R}_{23} with the resistances \tilde{R}_{14} , \tilde{R}_{24} , and \tilde{R}_{34} we need to transform the equivalent resistor circuits to the same diagram for both meshes. This is accomplished by a star-triangle transform ^[360] of the 4-element-mesh. We use Equations (B.10d), (B.10e), and (B.10f) to compute the transformed virtual resistances \tilde{R}_{12}^Δ , \tilde{R}_{13}^Δ , and \tilde{R}_{23}^Δ .

$$\tilde{R}_{12}^\Delta = \frac{\tilde{R}_{14}\tilde{R}_{24} + \tilde{R}_{24}\tilde{R}_{34} + \tilde{R}_{34}\tilde{R}_{14}}{\tilde{R}_{34}} = \frac{x_4gh(x_4 + g + h)}{fgh} = \frac{x_3x_4}{f} = \tilde{R}_{12} \quad (\text{B.11a})$$

$$\tilde{R}_{13}^\Delta = \frac{\tilde{R}_{14}\tilde{R}_{24} + \tilde{R}_{24}\tilde{R}_{34} + \tilde{R}_{34}\tilde{R}_{14}}{\tilde{R}_{24}} = \frac{x_4gh(x_4 + g + h)}{fx_4g} = \frac{x_3h}{f} = \tilde{R}_{13} \quad (\text{B.11b})$$

$$\tilde{R}_{23}^\Delta = \frac{\tilde{R}_{14}\tilde{R}_{24} + \tilde{R}_{24}\tilde{R}_{34} + \tilde{R}_{34}\tilde{R}_{14}}{\tilde{R}_{14}} = \frac{x_4gh(x_4 + g + h)}{fx_4h} = \frac{x_3g}{f} = \tilde{R}_{23} \quad (\text{B.11c})$$

The comparison of the resistors of the 4-element-mesh \tilde{R}_{12}^Δ , \tilde{R}_{13}^Δ , and \tilde{R}_{23}^Δ are mathematically identical to the ones of the 3-element-mesh \tilde{R}_{12} , \tilde{R}_{13} , and \tilde{R}_{23} . This indicates that the overall resistance between two elements is independent from inserting a new fourth element into the mesh. Further, the proof is generalized from a 3-element-mesh to a multi-element-mesh by replacing the star-triangle transform with a star-mesh transform ^[361]. Finally, this proves the resistances to be completely independent of the used mesh.

q.e.d.



Answering this Chapter's Guiding Scientific Question

How can the correct calculation and the mesh independence of this work's FEM resistors be proven?

The physical correctness of the determination of the FEM resistances has been shown by a comparison for a four terminal sensing arrangement. Since the numerical simulation results match well with the known analytical solution, an empirical proof has been given for the electrical validity. The mesh independence has been shown via a geometrical ansatz and a star-triangle transformation. It was proven that for adding an additional mesh point into a three-point mesh, the total resistance conditions do not change. This can be generalized by a star-mesh transformation in order to prove the given statement.

List of Figures

2.1	Energetic levels within a semiconductor	7
2.2	Band structure of a p-n junction	8
2.3	I–V characteristic of a dark and illuminated solar cell	11
2.4	Generic schematic of a solar cell	13
2.5	Spatially resolved potential distribution of a solar cell	15
2.6	single-diode equivalent-circuit model	16
2.7	Influence of loss mechanisms, diode parameters, and solar cell parameters	17
2.8	Multi-diode network model	18
2.9	Monolithic module interconnect	20
2.10	AM1.5G and Shockley-Queisser limit	21
4.1	Setup of a generic thin-film solar cell	30
4.2	Modified Bowyer-Watson algorithm	33
4.3	Definitions within the contour meshing procedure	34
4.4	Contour meshing procedure	34
4.5	Meshing of Lake Superior	35
4.6	Optics with Lambert-Beer approach	36
4.7	Ray paths in TMM	38
4.8	Optics with TMM	40
4.9	Electrical Finite Elements	43
4.10	Circuit of Resistors in Finite Elements	46
4.11	Determination of Resistances	47
4.12	Model for monolithic module interconnect	49
4.13	Back and front potentials within a solar cell	53
4.14	Histogram of voltage distribution	54
4.15	Cell current distribution	54
4.16	Back and front potentials within a periodic element of a solar module	55
4.17	Simulated I–V curve	57
4.18	Example I–V curves for fitting	58
4.19	Quality of a fit to the single-diode equivalent-circuit model	59
4.20	Sun path diagram of Munich	61
5.1	SEM cross section of a CIGS thin-film cell	64
5.2	Specific resistance as a function of the layer thickness	65
5.3	Temperature-dependent specific resistivity of a thin AZO film	66
5.4	Wavelength-dependent complex refractive index of AZO	67

5.5	Optical behavior of a layer stack for a standard CIGS cell	67
5.6	Comparison between measured EQE data and simulated absorption in CIGS layer . . .	68
5.7	Illustration of the internal semiconductor I–V curve vs. the externally measured I–V curve	69
5.8	I–V characteristics of a REF-fitted CIGS cell	72
5.9	Diode parameters during the REF process	72
5.10	I–V characteristics of simulated and measured CIGS cells	74
5.11	Extracted solar cell parameters	74
5.12	Comparison of a FEM model and a single-diode equivalent-circuit model	76
6.1	Visualization of all loss mechanisms that are calculated within this work	82
6.2	Measured wavelength-dependent reflection of a CIGS cell	88
6.3	Comparison of simulated and measured AM1.5G-weighted reflections	88
6.4	Loss analysis of a CIGS cell with a 111 nm thick AZO layer as front contact	89
6.5	Loss analysis plotted as a function of the contact layer thickness	90
6.6	Illumination-dependent loss analysis for different thickness of the front contact layer .	92
6.7	Different I–V curves for the module N-G1000E105 from NICE Solar Energy GmbH under STC	94
6.8	Detailed loss analysis for the module N-G1000E105 from NICE Solar Energy GmbH under STC	96
7.1	PCE of a CIGS as a function of illumination intensity	100
7.2	Modeled temperature-dependence of the open-circuit voltage and the fill factor	101
7.3	Modeled temperature-dependence of the short-circuit current density and the power conversion efficiency	102
7.4	External meteorologic conditions on the solar module during daytime of September 9, 2020	104
7.5	Simulated and measured solar-module parameters during daytime of September 9, 2020	105
7.6	External meteorologic conditions, solar-module parameters, and produced power during daytime of September 9, 2020	106
7.7	Time-dependent loss analysis and generated module yield during daytime of September 9, 2020	107
7.8	Trajectory of the operating module conditions compared with the Shockley-Queisser model during daytime of September 9, 2020	108
8.1	Optimization of the TCO layer thickness for a monolithically integrated CIGS cell with the dimensions of $5 \times 2.6 \text{ mm}^2$	114
8.2	Behavior of the SIMP functions and their derivatives	117
8.3	Visualization of the idea of topology optimization	119
8.4	Comparison of the calculation of the gradient for the topology optimization	121
8.5	Resulting grid pattern for different numerical optimizers after 50 iterations	122
8.6	Development of the PCE for different optimizers as a function of the number of iterations	122
8.7	Resulting grid pattern for the ADAM optimizer with the usage of batches after 50 iterations	123

8.8	Visualization of the time-dependent sun's illumination power in Stuttgart averaged over the years from 2005 to 2020	124
8.9	Two different grid designs optimized for different irradiance intensities	125
8.10	I–V curves for different illumination intensities for two different cell designs	126
8.11	Illumination-dependent solar cell parameters for two different cell designs	126
8.12	Irradiance intensities for different locations on the northern hemisphere	127
8.13	Loss analysis for two cell designs	129
9.1	Geometry of optimized record module	133
9.2	PCE of the optimum module as a function of the cell width and the thickness of the top IOH layer	136
9.3	I–V curves of optimized record module	137
9.4	Loss analysis of the optimum module for the present day feasible scenario	138
9.5	Loss analysis of the optimum module for the ideal scenario	139
9.6	Loss analysis of the optimum module for a optimistic scenario	140
9.7	Classification of the three efficiency scenarios in the development of CIGS solar modules to date	141
A.1	Screenshot of the home-screen of the simulation platform	149
A.2	Screenshot of the design screen of the simulation platform	150
A.3	Screenshot of the layer stack manager of the simulation platform	151
A.4	Screenshot of the simulation screen of the simulation platform	152
A.5	Screenshot of the loss analysis screen of the simulation platform	153
B.1	Potential in a Four-terminal Sensing Setup	156
B.2	Emulated Resistivities within a Four-terminal Sensing Setup	157
B.3	Resistance of single wire	158
B.4	Equivalent circuit diagrams of two meshes	160

List of Tables

5.1	Comparison of the internal and the external I–V curves and their typical field of application.	69
5.2	Coefficients of determination R^2 for the I–V curves in Figure 5.12b comparing single-diode equivalent-circuit model (SDM) and the FEM.	77
6.1	List of all loss mechanisms that are calculated within this work.	83
6.2	Material parameters for the drift-diffusion model	94
7.1	Comparison of device temperature coefficients with experimentally measured data in literature	103
7.2	Comparison of geometric dimensions and characteristic electrical data for differently improved modules	110
8.1	Behavior of finite elements with and without grid.	118
8.2	Comparison of the performance in PCE and yield of two cell designs	128
9.1	Comparison of diode parameters and solar cell parameters for the Shockley-Queisser model and the calculated best CIGS material in literature.	135
9.2	Input parameters for an analytical approximation to calculate the optimum cell width within a module.	137

List of own Publications

Journal Articles

Zinßer, M., Helder, T., Magorian Friedlmeier, T., Bauer, A., Kirchartz, T., Rau, U., Wächter, R. & Powalla, M. Holistic Yield Modeling, Top-Down Loss Analysis, and Efficiency Potential Study of Thin-Film Solar Modules. *Accepted from Communications Physics* (2022).

Helder, T., Kanvce, A., **Zinßer, M.**, Gutzler, R., Paetel, S., Hempel, W., Magorian Friedlmeier, T. & Powalla, M. How small changes make a difference: Influence of low silver contents on the effect of RbF-PDT in CIGS solar cells. *Progress in Photovoltaics: Research and Applications* (2022).

Zinßer, M., Braun, B., Helder, T., Magorian Friedlmeier, T., Pieters, B., Heinlein, A., Denk, M., Göddeke, D. & Powalla, M. Irradiation-dependent Topology Optimization of Metallization Grid Patterns used for latitude-based Yield Gain of Thin-film Solar Modules. *MRS Advances* **7**, 706–712 (2022).

Zinßer, M. Numerically Robust Methodology for Fitting Current-Voltage Characteristics of Solar Devices with the Single-Diode Equivalent-Circuit Model. *arXiv:2206.13087 [physics.comp-ph]* (2022).

Zinßer, M., Helder, T., Bauer, A., Magorian Friedlmeier, T., Zillner, J., Becker, J.-P. & Powalla, M. Optical and Electrical Loss Analysis of Thin-film Solar Cells combining the Methods of Transfer-Matrix and Finite Elements. *IEEE Journal of Photovoltaics* **12**, 1154–1161 (2022).

Helder, T., Kanevce, A., Bauer, A., **Zinßer, M.**, Paetel, S., Magorian Friedlmeier, T. & Powalla, M. DLTS investigations on CIGS solar cells from an inline co-evaporation system with RbF post-deposition treatment. *EPJ Photovoltaics* **17**, 7 (2022).

Zinßer, M., Loy, M., Helder, T., Bauer, A., Magorian Friedlmeier, T. & Powalla, M. Finite Element Simulation of Electrical Intradvice Physics of Thin-Film Solar Cells and Its Implications on the Efficiency. *IEEE Journal of Photovoltaics* **12**, 483–492 (2022).

Denk, M., Rother, K., **Zinßer, M.**, Petroll, C. & Paetzold, K. Nodal cosine sine material interpolation in multi objective topology optimization with the global criteria method for linear elastic heat transfer potential flow and binary cross entropy sharpening. *Proceedings of the Design Society*, 2247–2256 (2021).

Conference Contributions

Helder, T., Kanevce, A., **ZinBer, M.**, Gutzler, R., Paetel, S., Hempel, W., Magorian Friedlmeier, T. & Powalla, M. Systematic Investigation on the Impact of RbF-PDT in ACIGS. *8th World Conference on Photovoltaic Energy Conversion (WCPEC-8)* (2022).

ZinBer, M., Helder, T., Bauer, A., Magorian Friedlmeier, T., Zillner, J., Becker, J.-P. & Powalla, M. Optical and Electrical Loss Analysis of Thin-film Solar Cells combining the Methods of Transfer-Matrix and Finite Elements. *MRS Spring Meeting & Exhibit* (2022).

Helder, T., Kanevce, A., Bauer, A., **ZinBer, M.**, Magorian Friedlmeier, T. & Powalla, M. DLTS Investigations on CIGS Solar Cells from an Inline Co-Evaporation System with RbF Post-Deposition Treatment. *38th European Photovoltaic Solar Energy Conference and Exhibition (EU PVSEC)*, 3BV.2.2 (2021).

ZinBer, M., Loy, M., Helder, T., Bauer, A., Magorian Friedlmeier, T. & Powalla, M. Electrical FEM Simulations of Physics in Thin-Film Solar Cells. *38th European Photovoltaic Solar Energy Conference and Exhibition (EU PVSEC)*, 1BV.3.6 (2021).

Bibliography

- [1] Kato, T., Wu, J.-L., Hirai, Y., Sugimoto, H. & Bermudez, V. Record efficiency for thin-film polycrystalline solar cells up to 22.9% achieved by Cs-treated Cu(In,Ga)(Se,S)₂. *IEEE Journal of Photovoltaics* **9**, 325–330 (2018).
- [2] Obama, B. The irreversible momentum of clean energy. *Science* **355**, 126–129 (2017).
- [3] Hansjürgens, B. & Antes, R. *Economics and Management of Climate Change* (Springer, 2008).
- [4] Allouhi, A. *et al.* Energy consumption and efficiency in buildings: current status and future trends. *Journal of Cleaner Production* **109**, 118–130 (2015).
- [5] Cao, X., Dai, X. & Liu, J. Building energy-consumption status worldwide and the state-of-the-art technologies for zero-energy buildings during the past decade. *Energy and Buildings* **128**, 198–213 (2016).
- [6] Pérez-Lombard, L., Ortiz, J. & Pout, C. A review on buildings energy consumption information. *Energy and Buildings* **40**, 394–398 (2008).
- [7] Chu, S. & Majumdar, A. Opportunities and challenges for a sustainable energy future. *Nature* **488**, 294–303 (2012).
- [8] BP. Statistical review of world energy 2021. <https://www.bp.com/content/dam/bp/business-sites/en/global/corporate/pdfs/energy-economics/statistical-review/bp-stats-review-2021-full-report.pdf>. Accessed: 2022-08-15.
- [9] Kopp, G. & Lean, J. L. A new, lower value of total solar irradiance: Evidence and climate significance. *Geophysical Research Letters* **38** (2011).
- [10] Kardashev, N. S. Transmission of Information by Extraterrestrial Civilizations. *Soviet Astronomy* **8**, 217 (1964).
- [11] Sagan, C. *Carl Sagan's cosmic connection: An extraterrestrial perspective* (Cambridge University Press, 2000).
- [12] Kyoto protocol to the united nations framework convention on climate change. https://treaties.un.org/Pages/ViewDetails.aspx?src=IND&mtdsg_no=XXVII-7-a&chapter=27&clang=_en. Accessed: 2022-08-15.
- [13] Paris agreement. https://treaties.un.org/Pages/ViewDetails.aspx?src=IND&mtdsg_no=XXVII-7-d&chapter=27&clang=_en. Accessed: 2022-08-15.
- [14] Steffen, W. *et al.* Trajectories of the Earth System in the Anthropocene. *Proceedings of the National Academy of Sciences* **115**, 8252–8259 (2018).

- [15] Goldemberg, J. The promise of clean energy. *Energy Policy* **34**, 2185–2190 (2006).
- [16] Traber, T., Hegner, F. S. & Fell, H.-J. An Economically Viable 100% Renewable Energy System for All Energy Sectors of Germany in 2030. *Energies* **14**, 5230 (2021).
- [17] Calvin, M. The path of carbon in photosynthesis. *Journal of Chemical Education* **26**, 639 (1949).
- [18] Zhu, X.-G., Long, S. P. & Ort, D. R. What is the maximum efficiency with which photosynthesis can convert solar energy into biomass? *Current Opinion in Biotechnology* **19**, 153–159 (2008).
- [19] Calvin, M. Solar energy by photosynthesis. *Science* **184**, 375–381 (1974).
- [20] Melis, A. Photosynthesis-to-fuels: From sunlight to hydrogen, isoprene, and botryococcene production. *Energy & Environmental Science* **5**, 5531–5539 (2012).
- [21] Chapin, D. M., Fuller, C. S. & Pearson, G. L. A new silicon p-n junction photocell for converting solar radiation into electrical power. *Journal of Applied Physics* **25**, 676–677 (1954).
- [22] Breyer, C., Koskinen, O. & Blechinger, P. Profitable climate change mitigation: The case of greenhouse gas emission reduction benefits enabled by solar photovoltaic systems. *Renewable and Sustainable Energy Reviews* **49**, 610–628 (2015).
- [23] Lohani, S. P. & Blakers, A. 100% renewable energy with pumped-hydro-energy storage in Nepal. *Clean Energy* **5**, 243–253 (2021).
- [24] Philipps, S. Photovoltaics report 02/2022. <https://www.ise.fraunhofer.de/de/veroeffentlichungen/studien/photovoltaics-report.html>. Accessed: 2022-08-15.
- [25] Armaroli, N. & Balzani, V. Solar electricity and solar fuels: status and perspectives in the context of the energy transition. *Chemistry – A European Journal* **22**, 32–57 (2016).
- [26] CIGS white paper 2019. https://cigs-pv.net/wortpresse/wp-content/uploads/2019/04/CIGS_White_Paper_2019_online.pdf. Accessed: 2022-08-15.
- [27] Wirth, H. & Schneider, K. Aktuelle fakten zur photovoltaik in deutschland. <https://www.ise.fraunhofer.de/content/dam/ise/de/documents/publications/studies/aktuelle-fakten-zur-photovoltaik-in-deutschland.pdf>. Accessed: 2022-08-15.
- [28] Green, M. *et al.* Solar cell efficiency tables (version 58). *Progress in photovoltaics: research and applications* **29**, 3–15 (2021).
- [29] Jackson, P. *et al.* Properties of Cu(In,Ga)Se₂ solar cells with new record efficiencies up to 21.7%. *physica status solidi (RRL) – Rapid Research Letters* **9**, 28–31 (2015).
- [30] Kayes, B. M. *et al.* 27.6% Conversion efficiency, a new record for single-junction solar cells under 1 sun illumination. In *37th IEEE Photovoltaic Specialists Conference*, 000004–000008 (2011).
- [31] Powalla, M. *et al.* Thin-film solar cells exceeding 22% solar cell efficiency: An overview on CdTe-, Cu(In,Ga)Se₂-, and perovskite-based materials. *Applied Physics Reviews* **5**, 041602 (2018).

- [32] Razykov, T. M. *et al.* Solar photovoltaic electricity: Current status and future prospects. *Solar Energy* **85**, 1580–1608 (2011).
- [33] Hegedus, S. Thin film solar modules: The low cost, high throughput and versatile alternative to Si wafers. *Progress in Photovoltaics: Research and Applications* **14**, 393–411 (2006).
- [34] Shah, A. *et al.* Towards very low-cost mass production of thin-film silicon photovoltaic (PV) solar modules on glass. *Thin Solid Films* **502**, 292–299 (2006).
- [35] Peng, J. *et al.* Centimetre-scale perovskite solar cells with fill factors of more than 86 per cent. *Nature* **601**, 573–578 (2022).
- [36] Kayes, B. M., Zhang, L., Twist, R., Ding, I.-K. & Higashi, G. S. Flexible thin-film tandem solar cells with >30% efficiency. *IEEE Journal of Photovoltaics* **4**, 729–733 (2014).
- [37] Gaillard, N. *et al.* Wide-bandgap Cu(In,Ga)S₂ photocathodes integrated on transparent conductive F:SnO₂ substrates for chalcopyrite-based water splitting tandem devices. *ACS Applied Energy Materials* **2**, 5515–5524 (2019).
- [38] Schultes, M. *et al.* Sputtered Transparent Electrodes (IO:H and IZO) with Low Parasitic Near-Infrared Absorption for Perovskite–Cu(In,Ga)Se₂ Tandem Solar Cells. *ACS Applied Energy Materials* **2**, 7823–7831 (2019).
- [39] Al-Ashouri, A. *et al.* Monolithic perovskite/silicon tandem solar cell with >29% efficiency by enhanced hole extraction. *Science* **370**, 1300–1309 (2020).
- [40] Septina, W. *et al.* In situ Al₂O₃ incorporation enhances the efficiency of CuIn(S,Se)₂ solar cells prepared from molecular-ink solutions. *Journal of Materials Chemistry A* **9**, 10419–10426 (2021).
- [41] Jacobsson, T. J., Fjällström, V., Sahlberg, M., Edoff, M. & Edvinsson, T. A monolithic device for solar water splitting based on series interconnected thin film absorbers reaching over 10% solar-to-hydrogen efficiency. *Energy & Environmental Science* **6**, 3676–3683 (2013).
- [42] Andrei, V. *et al.* Floating perovskite-BiVO₄ devices for scalable solar fuel production. *Nature* **608**, 518–522 (2022).
- [43] Gaillard, N., Prasher, D., Kaneshiro, J., Mallory, S. & Chong, M. Development of chalcogenide thin film materials for photoelectrochemical hydrogen production. *MRS Online Proceedings Library (OPL)* **1558** (2013).
- [44] Lee, C. H., Kim, D. R. & Zheng, X. Transfer printing methods for flexible thin film solar cells: Basic concepts and working principles. *ACS Nano* **8**, 8746–8756 (2014).
- [45] Powalla, M. *et al.* CIGS cells and modules with high efficiency on glass and flexible substrates. *IEEE Journal of Photovoltaics* **4**, 440–446 (2013).
- [46] Moon, S., Kim, K., Kim, Y., Heo, J. & Lee, J. Highly efficient single-junction GaAs thin-film solar cell on flexible substrate. *Scientific Reports* **6**, 1–6 (2016).
- [47] Schubert, M. B. & Werner, J. H. Flexible solar cells for clothing. *Materials Today* **9**, 42–50 (2006).
- [48] Swanson, R. M. A vision for crystalline silicon photovoltaics. *Progress in Photovoltaics: Research and Applications* **14**, 443–453 (2006).

- [49] Grübel, B. *et al.* Progress of plated metallization for industrial bifacial TOPCon silicon solar cells. *Progress in Photovoltaics: Research and Applications* **30**, 615–621 (2022).
- [50] Yoshikawa, K. *et al.* Silicon heterojunction solar cell with interdigitated back contacts for a photoconversion efficiency over 26%. *Nature Energy* **2**, 17032 (2017).
- [51] Min, H. *et al.* Perovskite solar cells with atomically coherent interlayers on SnO₂ electrodes. *Nature* **598**, 444–450 (2021).
- [52] Nakamura, M. *et al.* Cd-free Cu(In,Ga)(Se,S)₂ thin-film solar cell with record efficiency of 23.35%. *IEEE Journal of Photovoltaics* **9**, 1863–1867 (2019).
- [53] Release, F. S. P. First solar achieves yet another cell conversion efficiency world record. <https://investor.firstsolar.com/news/press-release-details/2016/First-Solar-Achieves-Yet-Another-Cell-Conversion-Efficiency-World-Record/default.aspx>. Accessed: 2022-08-15.
- [54] Mattos, L. S. *et al.* New module efficiency record: 23.5% under 1-sun illumination using thin-film single-junction GaAs solar cells. In *38th IEEE Photovoltaic Specialists Conference*, 003187–003190 (IEEE, 2012).
- [55] Sugimoto, H. High efficiency and large volume production of CIS-based modules. In *IEEE 40th Photovoltaic specialist conference (PVSC)*, 2767–2770 (2014).
- [56] Higuchi, H. & Negami, T. Largest highly efficient 203×203 mm² CH₃NH₃PbI₃ perovskite solar modules. *Japanese Journal of Applied Physics* **57**, 08RE11 (2018).
- [57] Bermudez, V. & Perez-Rodriguez, A. Understanding the cell-to-module efficiency gap in Cu(In,Ga)(S,Se)₂ photovoltaics scale-up. *Nature Energy* **3**, 466–475 (2018).
- [58] Richter, A. *et al.* Design rules for high-efficiency both-sides-contacted silicon solar cells with balanced charge carrier transport and recombination losses. *Nature Energy* **6**, 429–438 (2021).
- [59] Burgelman, M., Nollet, P. & Degraeve, S. Modelling polycrystalline semiconductor solar cells. *Thin Solid Films* **361–362**, 527–532 (2000).
- [60] Carron, R. *et al.* Refractive indices of layers and optical simulations of Cu(In,Ga)Se₂ solar cells. *Science and Technology of Advanced Materials* **19**, 396–410 (2018).
- [61] Pieters, B. E. & Rau, U. A new 2D model for the electrical potential in a cell stripe in thin-film solar modules including local defects. *Progress in Photovoltaics: Research and Applications* **23**, 331–339 (2015).
- [62] Fecher, F. W., Romero, A. P., Brabec, C. J. & Buerhop-Lutz, C. Influence of a shunt on the electrical behavior in thin film photovoltaic modules – A 2D finite element simulation study. *Solar Energy* **105**, 494–504 (2014).
- [63] Kikelj, M., Lipovšek, B., Bokalič, M. & Topič, M. Spatially resolved electrical modelling of cracks and other inhomogeneities in crystalline silicon solar cells. *Progress in Photovoltaics: Research and Applications* **29**, 124–133 (2021).
- [64] Malm, U. & Edoff, M. Influence from front contact sheet resistance on extracted diode parameters in CIGS solar cells. *Progress in Photovoltaics: Research and Applications* **16**, 113–121 (2008).

- [65] Eidelloth, S., Haase, F. & Brendel, R. Simulation tool for equivalent circuit modeling of photovoltaic devices. *IEEE Journal of Photovoltaics* **2**, 572–579 (2012).
- [66] Janssen, G. J. M., Slooff, L. H. & Bende, E. E. 2D-Finite element model of a CIGS module. In *2012 38th IEEE Photovoltaic Specialists Conference*, 001481–001485 (2012).
- [67] Galagan, Y. *et al.* Evaluation of ink-jet printed current collecting grids and busbars for ITO-free organic solar cells. *Solar Energy Materials and Solar Cells* **104**, 32–38 (2012).
- [68] van Deelen, J., Klerk, L. & Barink, M. Optimized grid design for thin film solar panels. *Solar Energy* **107**, 135–144 (2014).
- [69] Koishiyev, G. T. & Sites, J. R. Impact of sheet resistance on 2-D modeling of thin-film solar cells. *Solar Energy Materials and Solar Cells* **93**, 350–354 (2009).
- [70] Lee, S.-Y. *et al.* Analysis of a-Si:H/TCO contact resistance for the Si heterojunction back-contact solar cell. *Solar Energy Materials and Solar Cells* **120**, 412–416 (2014).
- [71] Shen, Y., Li, K., Majumdar, N., Campbell, J. C. & Gupta, M. C. Bulk and contact resistance in P3HT:PCBM heterojunction solar cells. *Solar Energy Materials and Solar Cells* **95**, 2314–2317 (2011).
- [72] Wächter, R., Kaune, G., Repmann, T. & Orgassa, K. Loss Analysis and Efficiency Potentials for CIGS PV Modules without and with Metal Grid: Experimental Results Analyzed by Simulation. In *37th European Photovoltaic Solar Energy Conference and Exhibition*, 1–4 (2020).
- [73] Kiermasch, D., Gil-Escrig, L., Bolink, H. J. & Tvingstedt, K. Effects of masking on open-circuit voltage and fill factor in solar cells. *Joule* **3**, 16–26 (2019).
- [74] Pfreundt, A., Shahid, J. & Mittag, M. Cell-to-module Analysis beyond Standard Test Conditions. In *47th IEEE Photovoltaic Specialists Conference (PVSC)*, 0921–0926 (2020).
- [75] Oppenheimer, D. M. Consequences of erudite vernacular utilized irrespective of necessity: Problems with using long words needlessly. *Applied Cognitive Psychology* **20**, 139–156 (2006).
- [76] Slater, J. C. & Koster, G. F. Simplified LCAO method for the periodic potential problem. *Physical Review* **94**, 1498 (1954).
- [77] Hohenberg, P. & Kohn, W. Inhomogeneous electron gas. *Physical Review* **136**, B864 (1964).
- [78] Kohn, W. & Sham, L. J. Self-consistent equations including exchange and correlation effects. *Physical Review* **140**, A1133 (1965).
- [79] Kevan, S. D. Evidence for a new broadening mechanism in angle-resolved photoemission from Cu (111). *Physical Review Letters* **50**, 526 (1983).
- [80] Gray, A. X. *et al.* Bulk electronic structure of the dilute magnetic semiconductor $\text{Ga}_{1-x}\text{Mn}_x\text{As}$ through hard X-ray angle-resolved photoemission. *Nature Materials* **11**, 957–962 (2012).
- [81] Lim, L. Y. *et al.* Angle-resolved photoemission and quasiparticle calculation of ZnO: The need for d band shift in oxide semiconductors. *Physical Review B* **86**, 235113 (2012).
- [82] Würfel, P. & Würfel, U. *Physics of solar cells: From basic principles to advanced concepts* (John Wiley & Sons, 2016).

- [83] Fermi, E. Zur Quantelung des idealen einatomigen Gases. *Zeitschrift für Physik* **36**, 902–912 (1926).
- [84] Boltzmann, L. Studien über das Gleichgewicht der lebendigen Kraft zwischen bewegten materiellen Punkten. *Wissenschaftliche Abhandlungen* **1**, 49–96 (1868).
- [85] Hunklinger, S. *Festkörperphysik* (De Gruyter Oldenbourg, 2017).
- [86] Dirac, P. A. M. On the theory of quantum mechanics. *Proceedings of the Royal Society of London A* **112**, 661–677 (1926).
- [87] Maxwell, J. C. VIII. A dynamical theory of the electromagnetic field. *Philosophical Transactions of the Royal Society of London* **155**, 459–512 (1865).
- [88] Poisson, S. D. Mémoire sur la théorie du magnétisme en mouvement. *Mémoires de l'Académie Royale des Sciences de l'Institut de France* **6**, 441–570 (1823).
- [89] Van Roosbroeck, W. Theory of the flow of electrons and holes in germanium and other semiconductors. *The Bell System Technical Journal* **29**, 560–607 (1950).
- [90] Farrell, P., Koprucki, T. & Fuhrmann, J. Computational and analytical comparison of flux discretizations for the semiconductor device equations beyond Boltzmann statistics. *Journal of Computational Physics* **346**, 497–513 (2017).
- [91] Scharfetter, D. L. & Gummel, H. K. Large-signal analysis of a silicon read diode oscillator. *IEEE Transactions on Electron Devices* **16**, 64–77 (1969).
- [92] Malm, U. & Edoff, M. 2D device modelling and finite element simulations for thin-film solar cells. *Solar Energy Materials and Solar Cells* **93**, 1066–1069 (2009).
- [93] Shockley, W. The Theory of p-n Junctions in Semiconductors and p-n Junction Transistors. *Bell System Technical Journal* **28**, 435–489 (1949).
- [94] Scheer, R. & Schock, H.-W. *Chalcogenide photovoltaics: physics, technologies, and thin film devices* (John Wiley & Sons, 2011).
- [95] Einstein, A. Über einen die Erzeugung und Verwandlung des Lichtes betreffenden heuristischen Gesichtspunkt. *Annalen der Physik* **322** (1905).
- [96] Matthiessen, A. & Vogt, C. Ueber den Einfluss der Temperatur auf die elektrische Leitungsfähigkeit der Legirungen. *Annalen der Physik* **198**, 19–78 (1864).
- [97] Bhosle, V., Tiwari, A. & Narayan, J. Metallic conductivity and metal-semiconductor transition in Ga-doped ZnO. *Applied Physics Letters* **88**, 032106 (2006).
- [98] Langmuir, I. Oscillations in ionized gases. *Proceedings of the National Academy of Sciences of the United States of America* **14**, 627–637 (1928).
- [99] Tonks, L. & Langmuir, I. Oscillations in ionized gases. *Physical Review* **33**, 195–211 (1929).
- [100] Brown, A. R., de Leeuw, D. M., Havinga, E. E. & Pomp, A. A universal relation between conductivity and field-effect mobility in doped amorphous organic semiconductors. *Synthetic Metals* **68**, 65–70 (1994).
- [101] Haacke, G. New figure of merit for transparent conductors. *Journal of Applied Physics* **47**, 4086–4089 (1976).

- [102] Chen, Z. *et al.* Fabrication of highly transparent and conductive indium–tin oxide thin films with a high figure of merit via solution processing. *Langmuir* **29**, 13836–13842 (2013).
- [103] Liu, W.-S., Liu, Y.-H., Chen, W.-K. & Hsueh, K.-P. Transparent conductive Ga-doped MgZnO/Ag/Ga-doped MgZnO sandwich structure with improved conductivity and transmittance. *Journal of Alloys and Compounds* **564**, 105–113 (2013).
- [104] van der Heide, A. S. H., Bultman, J. H., Hoornstra, J. & Schönecker, A. Error diagnosis and optimisation of c-Si solar cell processing using contact resistances determined with the Corescanner. *Solar Energy Materials and Solar Cells* **74**, 43–50 (2002).
- [105] Burgers, A. R. *New metallisation patterns and light trapping for silicon solar cells*. Ph.D. thesis, Energy Research Centre of the Netherlands (2005).
- [106] Brecl, K., Topič, M. & Smole, F. A detailed study of monolithic contacts and electrical losses in a large-area thin-film module. *Progress in Photovoltaics: Research and Applications* **13**, 297–310 (2005).
- [107] Zinßer, M. *et al.* Finite Element Simulation of Electrical Intradevice Physics of Thin-Film Solar Cells and Its Implications on the Efficiency. *IEEE Journal of Photovoltaics* **12**, 483–492 (2022).
- [108] Augusto, A., Herasimenka, S. Y., King, R. R., Bowden, S. G. & Honsberg, C. Analysis of the recombination mechanisms of a silicon solar cell with low bandgap-voltage offset. *Journal of Applied Physics* **121**, 205704 (2017).
- [109] Bayhan, H. & Bayhan, M. A simple approach to determine the solar cell diode ideality factor under illumination. *Solar Energy* **85**, 769–775 (2011).
- [110] Lambert, J. H. Observationes variae in mathesin puram. *Acta Helvetica Physico-Mathematico-Anatomico-Botanico-Medica* **3**, 128–168 (1758).
- [111] Zinßer, M. Numerically Robust Methodology for Fitting Current-Voltage Characteristics of Solar Devices with the Single-Diode Equivalent-Circuit Model. arXiv:2206.13087 [physics.comp-ph] (2022).
- [112] Jain, A. & Kapoor, A. Exact analytical solutions of the parameters of real solar cells using Lambert W-function. *Solar Energy Materials and Solar Cells* **81**, 269–277 (2004).
- [113] Raphson, J. *Analysis Aequationum Universalis* (Thomas Bradyll, London, 1697).
- [114] Lineykin, S., Averbukh, M. & Kuperman, A. An improved approach to extract the single-diode equivalent circuit parameters of a photovoltaic cell/panel. *Renewable and Sustainable Energy Reviews* **30**, 282–289 (2014).
- [115] Seeland, M. & Hoppe, H. Comparison of distributed vs. lumped series resistance modeling of thin-film solar cells and modules: Influence on the geometry-dependent efficiency. *physica status solidi (a)* **212**, 1991–2000 (2015).
- [116] Pieters, B. E. Spatial modeling of thin-film solar modules using the network simulation method and SPICE. *IEEE Journal of Photovoltaics* **1**, 93–98 (2011).
- [117] Fecher, F. W. *Simulation of thin-film photovoltaic modules: 2D and 3D spatially resolved electrical and electrothermal finite element calculations*. Ph.D. thesis, Friedrich-Alexander-Universität Erlangen-Nürnberg (FAU) (2018).

- [118] Grabitz, P. O., Rau, U. & Werner, J. H. Modeling of spatially inhomogeneous solar cells by a multi-diode approach. *physica status solidi (a)* **202**, 2920–2927 (2005).
- [119] Grabitz, P. O., Rau, U. & Werner, J. H. A multi-diode model for spatially inhomogeneous solar cells. *Thin Solid Films* **487**, 14–18 (2005).
- [120] Nagel, L. W. & Pederson, D. SPICE (Simulation Program with Integrated Circuit Emphasis). Tech. Rep. UCB/ERL M382, EECS Department, University of California, Berkeley (1973). URL <http://www2.eecs.berkeley.edu/Pubs/TechRpts/1973/22871.html>. Accessed: 2022-03-01.
- [121] Zekry, A. & Al-Mazroo, A. Y. A distributed SPICE-model of a solar cell. *IEEE Transactions on Electron Devices* **43**, 691–700 (1996).
- [122] Glass, M. C. Improved solar array power point model with SPICE realization. In *IECEC 96. Proceedings of the 31st Intersociety Energy Conversion Engineering Conference*, 286–291 (1996).
- [123] Greulich, J., Glatthaar, M. & Rein, S. Fill factor analysis of solar cells' current–voltage curves. *Progress in Photovoltaics: Research and Applications* **18**, 511–515 (2010).
- [124] Biryukov, S., Faiman, D. & Goldfeld, A. An optical system for the quantitative study of particulate contamination on solar collector surfaces. *Solar Energy* **66**, 371–378 (1999).
- [125] Daliento, S., Di Napoli, F., Guerriero, P. & d'Alessandro, V. A modified bypass circuit for improved hot spot reliability of solar panels subject to partial shading. *Solar Energy* **134**, 211–218 (2016).
- [126] Hemza, A., Abdeslam, H., Rachid, C. & Aoun, N. Simplified methods for evaluating the degradation of photovoltaic module and modeling considering partial shading. *Measurement* **138**, 217–224 (2019).
- [127] Solheim, H. J., Fjær, H. G., Sørheim, E. A. & Foss, S. E. Measurement and simulation of hot spots in solar cells. *Energy Procedia* **38**, 183–189 (2013).
- [128] Li, K. *et al.* Influence of hot spot heating on stability of large size perovskite solar module with a power conversion efficiency of 14%. *ACS Applied Energy Materials* **1**, 3565–3570 (2018).
- [129] Hasyim, E. S., Wenham, S. R. & Green, M. A. Shadow tolerance of modules incorporating integral bypass diode solar cells. *Solar Cells* **19**, 109–122 (1986).
- [130] Pannebakker, B. B., de Waal, A. C. & van Sark, W. G. J. H. M. Photovoltaics in the shade: one bypass diode per solar cell revisited. *Progress in Photovoltaics: Research and Applications* **25**, 836–849 (2017).
- [131] Green, M. A. Crystalline and thin-film silicon solar cells: State of the art and future potential. *Solar Energy* **74**, 181–192 (2003).
- [132] Kumar, S., Meena, R. & Gupta, R. Finger and interconnect degradations in crystalline silicon photovoltaic modules: A review. *Solar Energy Materials and Solar Cells* **230**, 111296 (2021).

- [133] Zarmai, M. T., Ekere, N. N., Oduoza, C. F. & Amalu, E. H. A review of interconnection technologies for improved crystalline silicon solar cell photovoltaic module assembly. *Applied Energy* **154**, 173–182 (2015).
- [134] Gečys, P. *et al.* CIGS thin-film solar module processing: case of high-speed laser scribing. *Scientific Reports* **7**, 40502 (2017).
- [135] Burn, A. *et al.* All fiber laser scribing of Cu(In,Ga)Se₂ thin-film solar modules. *Physics Procedia* **41**, 713–722 (2013).
- [136] Schubbert, C. *et al.* Performance ratio study based on a device simulation of a 2D monolithic interconnected Cu(In,Ga)(Se,S)₂ solar cell. *Solar Energy Materials and Solar Cells* **157**, 146–153 (2016).
- [137] Vidal Lorbada, R., Walter, T., Fuertes Marrón, D., Lavrenko, T. & Muecke, D. A Deep Insight into the Electronic Properties of CIGS Modules with Monolithic Interconnects Based on 2D Simulations with TCAD. *Coatings* **9**, 128 (2019).
- [138] Gueymard, C. A., Myers, D. & Emery, K. Proposed reference irradiance spectra for solar energy systems testing. *Solar Energy* **73**, 443–467 (2002).
- [139] Solanki, C. S. & Beaucarne, G. Advanced solar cell concepts. *Energy for Sustainable Development* **11**, 17–23 (2007).
- [140] Rühle, S. Tabulated values of the Shockley–Queisser limit for single junction solar cells. *Solar Energy* **130**, 139–147 (2016).
- [141] Godovsky, D. Modeling the ultimate efficiency of polymer solar cell using Marcus theory of electron transfer. *Organic Electronics* **12**, 190–194 (2011).
- [142] Haverkort, J. E. M., Garnett, E. C. & Bakkers, E. P. A. M. Fundamentals of the nanowire solar cell: Optimization of the open circuit voltage. *Applied Physics Reviews* **5**, 031106 (2018).
- [143] De Vos, A. Detailed balance limit of the efficiency of tandem solar cells. *Journal of Physics D: Applied Physics* **13**, 839 (1980).
- [144] Planck, M. Ueber das Gesetz der Energieverteilung im Normalspectrum. *Annalen der Physik* **309**, 553–563 (1901).
- [145] Kirchartz, T. & Rau, U. Detailed balance and reciprocity in solar cells. *physica status solidi (a)* **205**, 2737–2751 (2008).
- [146] Kirchartz, T., Mattheis, J. & Rau, U. Detailed balance theory of excitonic and bulk heterojunction solar cells. *Physical Review B* **78**, 235320 (2008).
- [147] Kirchartz, T., Taretto, K. & Rau, U. Efficiency limits of organic bulk heterojunction solar cells. *The Journal of Physical Chemistry C* **113**, 17958–17966 (2009).
- [148] Shockley, W. & Queisser, H. J. Detailed balance limit of efficiency of p-n junction solar cells. *Journal of Applied Physics* **32**, 510–519 (1961).
- [149] Carnot, S. Réflexions sur la puissance motrice du feu et sur les machines propres à développer cette puissance. *Annales Scientifiques de l'École Normale Supérieure* **1**, 393–457 (1872).

- [150] Moore, G. E. Cramming more components onto integrated circuits. McGraw-Hill New York (1965).
- [151] Gaury, B., Sun, Y., Bermel, P. & Haney, P. M. Sesame: A 2-dimensional solar cell modeling tool. *Solar Energy Materials and Solar Cells* **198**, 53–62 (2019).
- [152] Basore, P. A. Numerical modeling of textured silicon solar cells using PC-1D. *IEEE Transactions on Electron Devices* **37**, 337–343 (1990).
- [153] Topič, M., Smole, F. & Furlan, J. Band-gap engineering in CdS/Cu(In,Ga)Se₂ solar cells. *Journal of Applied Physics* **79**, 8537–8540 (1996).
- [154] Basore, P. A. & Cabanas-Holmen, K. PC2D: A circular-reference spreadsheet solar cell device simulator. *IEEE Journal of Photovoltaics* **1**, 72–77 (2011).
- [155] Altermatt, P. P. Models for numerical device simulations of crystalline silicon solar cells - a review. *Journal of Computational Electronics* **10**, 314–330 (2011).
- [156] Zhu, H., Kalkan, A. K., Hou, J. & Fonash, S. J. Applications of AMPS-1D for solar cell simulation. In *AIP Conference Proceedings*, vol. 462, 309–314 (American Institute of Physics, 1999).
- [157] Gray, J. L. Adept: a general purpose numerical device simulator for modeling solar cells in one-, two-, and three-dimensions. In *The Conference Record of the Twenty-Second IEEE Photovoltaic Specialists Conference - 1991*, 436–438 (IEEE, 1991).
- [158] Liu, Y., Sun, Y. & Rockett, A. A new simulation software of solar cells-wxAMPS. *Solar Energy Materials and Solar Cells* **98**, 124–128 (2012).
- [159] Bauer, A., Helder, T. & Zinßer, M. Simulation platform twinPV. Internally developed at ZSW (2022).
- [160] Bartesaghi, D. & Koster, L. J. A. The effect of large compositional inhomogeneities on the performance of organic solar cells: A numerical study. *Advanced Functional Materials* **25**, 2013–2023 (2015).
- [161] Handy, R. J. Theoretical analysis of the series resistance of a solar cell. *Solid-State Electronics* **10**, 765–775 (1967).
- [162] Saha, H., Mukhopadhyay, K. & Biswas, D. Grid design and series resistance of Cu₂S/CdS solar cell. *International Journal of Electronics* **49**, 313–317 (1980).
- [163] Deb, S. & Ghosh, B. Series resistance and optimum grid design for a thin film solar cell of rectangular shape. *Solar Cells* **13**, 145–162 (1984).
- [164] Heizer, K. W. & Chu, T. L. Solar cell conducting grid structure. *Solid-State Electronics* **19**, 471–472 (1976).
- [165] Wyeth, N. C. Sheet resistance component of series resistance in a solar cell as a function of grid geometry. *Solid-State Electronics* **20**, 629–634 (1977).
- [166] Scharlack, R. S. The optimal design of solar cell grid lines. *Solar Energy* **23**, 199–201 (1979).

- [167] Galiana, B., Algora, C., Rey-Stolle, I. & Vara, I. G. A 3-D model for concentrator solar cells based on distributed circuit units. *IEEE Transactions on Electron Devices* **52**, 2552–2558 (2005).
- [168] Brecl, K. & Topič, M. Simulation of losses in thin-film silicon modules for different configurations and front contacts. *Progress in Photovoltaics: Research and Applications* **16**, 479–488 (2008).
- [169] Losio, P. A., Feurer, T., Buecheler, S. & Ruhstaller, B. Evolutionary optimization of TCO/mesh electrical contacts in CIGS solar cells. In *32nd European Photovoltaic Solar Energy Conference and Exhibition (EU PVSEC)*, 1237–1240 (2016).
- [170] Malm, U. & Edoff, M. Simulating material inhomogeneities and defects in CIGS thin-film solar cells. *Progress in Photovoltaics: Research and Applications* **17**, 306–314 (2009).
- [171] Koishiyev, G. T. *Analysis of impact of non-uniformities on thin-film solar cells and modules with two-dimensional simulations*. Ph.D. thesis, Colorado State University (2010).
- [172] Nardone, M., Dahal, S. & Waddle, J. M. Shading-induced failure in thin-film photovoltaic modules: Electrothermal simulation with nonuniformities. *Solar Energy* **139**, 381–388 (2016).
- [173] Wu, X. *et al.* Accelerated spatially resolved electrical simulation of photovoltaic devices using photovoltaic-oriented nodal analysis. *IEEE Transactions on Electron Devices* **62**, 1390–1398 (2015).
- [174] Haschke, J. *et al.* Lateral transport in silicon solar cells. *Journal of Applied Physics* **127**, 114501 (2020).
- [175] Zandi, S., Saxena, P., Razaghi, M. & Gorji, N. E. Simulation of CZTSSe thin-film solar cells in COMSOL: Three-dimensional optical, electrical, and thermal models. *IEEE Journal of Photovoltaics* **10**, 1503–1507 (2020).
- [176] Kosyachenko, L. A., Mathew, X., Paulson, P. D., Lytvynenko, V. Y. & Maslyanchuk, O. L. Optical and recombination losses in thin-film Cu(In,Ga)Se₂ solar cells. *Solar Energy Materials and Solar Cells* **130**, 291–302 (2014).
- [177] Mohamed, H. A. Dependence of efficiency of thin-film CdS/CdTe solar cell on optical and recombination losses. *Journal of Applied Physics* **113**, 093105 (2013).
- [178] Aberle, A. G., Zhang, W. & Hoex, B. Advanced loss analysis method for silicon wafer solar cells. *Energy Procedia* **8**, 244–249 (2011).
- [179] De Rose, R., Magnone, P., Zanuccoli, M., Sangiorgi, E. & Fiegna, C. Loss analysis of silicon solar cells by means of numerical device simulation. In *14th International Conference on Ultimate Integration on Silicon (ULIS)*, 205–208 (2013).
- [180] Dhankhar, M., Singh, O. P. & Singh, V. N. Physical principles of losses in thin film solar cells and efficiency enhancement methods. *Renewable and Sustainable Energy Reviews* **40**, 214–223 (2014).
- [181] Pieters, B. E. A free and open source finite-difference simulation tool for solar modules. In *IEEE 40th Photovoltaic Specialist Conference (PVSC)*, 1370–1375 (2014).
- [182] Gupta, Y. *et al.* Optimization of a-Si solar cell current collection. In *16th Photovoltaic Specialists Conference*, 1092–1101 (1982).

- [183] Li, K., Yang, Z. & Zhang, X. Size optimization of the front electrode and solar cell using a combined finite-element-genetic algorithm method. *Journal of Photonics for Energy* **11**, 034502 (2021).
- [184] Alberto, E. & Sigmund, O. Topology optimization of multiple physics problems modelled by Poisson's equation. *Latin American Journal of Solids and Structures* **1**, 169–184 (2004).
- [185] Svanberg, K. The method of moving asymptotes - a new method for structural optimization. *International Journal for Numerical Methods in Engineering* **24**, 359–373 (1987).
- [186] Gupta, D. K., van der Veen, G. J., Aragon, A. M., Langelaar, M. & van Keulen, F. Bounds for decoupled design and analysis discretizations in topology optimization. *International Journal for Numerical Methods in Engineering* **111**, 88–100 (2017).
- [187] Gupta, D. K., van Keulen, F. & Langelaar, M. Design and analysis adaptivity in multiresolution topology optimization. *International Journal for Numerical Methods in Engineering* **121**, 450–476 (2020).
- [188] Gupta, D. K., Langelaar, M., Barink, M. & van Keulen, F. Topology optimization of front metallization patterns for solar cells. *Structural and Multidisciplinary Optimization* **51**, 941–955 (2015).
- [189] Gupta, D. K., Langelaar, M., Barink, M. & van Keulen, F. Optimizing front metallization patterns: Efficiency with aesthetics in free-form solar cells. *Renewable Energy* **86**, 1332–1339 (2016).
- [190] Lambert, J. H. *Photometria Sive De Mensura Et Gradibus Luminis, Colorum Et Umbrae* (Verlag von Wilhelm Engelmann, Leipzig, 1760).
- [191] Beer, A. Bestimmung der Absorption des rothen Lichts in farbigen Flüssigkeiten. *Annalen der Physik* **162**, 78–88 (1852).
- [192] Byrnes, S. J. Multilayer optical calculations. arXiv:1603.02720 [physics.comp-ph] (2016).
- [193] Wahid, S., Islam, M., Rahman, M. S. S. & Alam, M. K. Transfer matrix formalism-based analytical modeling and performance evaluation of perovskite solar cells. *IEEE Transactions on Electron Devices* **64**, 5034–5041 (2017).
- [194] Katsidis, C. C. & Siapkis, D. I. General transfer-matrix method for optical multilayer systems with coherent, partially coherent, and incoherent interference. *Applied Optics* **41**, 3978–3987 (2002).
- [195] Pettersson, L. A. A., Roman, L. S. & Inganäs, O. Modeling photocurrent action spectra of photovoltaic devices based on organic thin films. *Journal of Applied Physics* **86**, 487–496 (1999).
- [196] Finkel, R. A. & Bentley, J. L. Quad trees a data structure for retrieval on composite keys. *Acta informatica* **4**, 1–9 (1974).
- [197] Delaunay, B. Sur la sphère vide. A la mémoire de Georges Voronoï. *Bulletin de l'Académie des Sciences de l'URSS* **6**, 793–800 (1934).
- [198] Dirichlet, G. L. Über die Reduction der positiven quadratischen Formen mit drei unbestimmten ganzen Zahlen. *Journal für die reine und angewandte Mathematik* **40**, 209–227 (1850).

- [199] Voronoï, G. Nouvelles applications des paramètres continus à la théorie des formes quadratiques. *Journal für die reine und angewandte Mathematik* **134**, 198–287 (1908).
- [200] Bowyer, A. Computing Dirichlet tessellations. *The Computer Journal* **24**, 162–166 (1981).
- [201] Watson, D. F. Computing the n-dimensional Delaunay tessellation with application to Voronoi polytopes. *The Computer Journal* **24**, 167–172 (1981).
- [202] Tsai, V. J. D. Delaunay triangulations in TIN creation: An overview and a linear-time algorithm. *International Journal of Geographical Information Systems* **7**, 501–524 (1993).
- [203] Möbius, A. F. *Der barycentrische Calcul* (Verlag von Johann Ambrosius Barth, Leipzig, 1827).
- [204] Fortune, S. A sweepline algorithm for Voronoi diagrams. *Algorithmica* **2**, 153–174 (1987).
- [205] Rong, G. & Tan, T.-S. Jump flooding in GPU with applications to Voronoi diagram and distance transform. In *Proceedings of the 2006 symposium on Interactive 3D graphics and games*, 109–116 (2006).
- [206] Shewchuk, J. R. Delaunay refinement algorithms for triangular mesh generation. *Computational geometry* **22**, 21–74 (2002).
- [207] Mohammed, Z. H. The Fresnel Coefficient of Thin Film Multilayer Using Transfer Matrix Method TMM. In *IOP Conference Series: Materials Science and Engineering*, vol. 518, 032026 (IOP Publishing, 2019).
- [208] Ball, J. M. *et al.* Optical properties and limiting photocurrent of thin-film perovskite solar cells. *Energy & Environmental Science* **8**, 602–609 (2015).
- [209] Yin, G., Merschjann, C. & Schmid, M. The effect of surface roughness on the determination of optical constants of CuInSe₂ and CuGaSe₂ thin films. *Journal of Applied Physics* **113**, 213510 (2013).
- [210] Filiński, I. The effects of sample imperfections on optical spectra. *physica status solidi (b)* **49**, 577–588 (1972).
- [211] Chen, G. & Tien, C. L. Thermally Induced Optical Nonlinearity During Transient Heating of Thin Films. *Journal of Heat Transfer* **116**, 311–316 (1994).
- [212] Zinßer, M., Schlegel, K., Dressel, M. & Scheffler, M. Role of non-linear effects and standing waves in microwave spectroscopy: Corbino measurements on superconductors and VO₂. *Review of Scientific Instruments* **90**, 034704 (2019).
- [213] Appel, A. Some techniques for shading machine renderings of solids. In *Proceedings of the April 30 – May 2, 1968, Spring Joint Computer Conference*, 37–45 (1968).
- [214] Fresnel, A.-J. Mémoire sur la double réfraction. *Mémoires de l'Académie Royale des Sciences de l'Institut de France* **7**, 45–176 (1827).
- [215] Prentice, J. Coherent, partially coherent and incoherent light absorption in thin-film multilayer structures. *Journal of Physics D: Applied Physics* **33**, 3139 (2000).
- [216] Centurioni, E. Generalized matrix method for calculation of internal light energy flux in mixed coherent and incoherent multilayers. *Applied Optics* **44**, 7532–7539 (2005).

- [217] Szczyrbowski, J. Determination of optical constants of real thin films. *Journal of Physics D: Applied Physics* **11**, 583 (1978).
- [218] Prentice, J. Optical generation rate of electron-hole pairs in multilayer thin-film photovoltaic cells. *Journal of Physics D: Applied Physics* **32**, 2146 (1999).
- [219] Poynting, J. H. XV. On the transfer of energy in the electromagnetic field. *Philosophical Transactions of the Royal Society of London* **175**, 343–361 (1884).
- [220] Kolodinski, S., Werner, J. H., Wittchen, T. & Queisser, H. J. Quantum efficiencies exceeding unity due to impact ionization in silicon solar cells. *Applied Physics Letters* **63**, 2405–2407 (1993).
- [221] Brewster, D. On the laws which regulate the polarisation of light by reflexion from transparent bodies. *Philosophical Transactions of the Royal Society of London* **105**, 125–159 (1815).
- [222] Fecher, F. W., Adams, J., Vetter, A., Buerhop-Lutz, C. & Brabec, C. J. Loss analysis on CIGS-modules by using contactless, imaging illuminated lock-in thermography and 2D electrical simulations. In *IEEE 40th Photovoltaic Specialist Conference (PVSC)*, 3331–3334 (2014).
- [223] Schwarz, M. Communication. *Archives des Sciences Physiques et Naturelles* **48**, 38–44 (1873).
- [224] Ghani, F., Duke, M. & Carson, J. Numerical calculation of series and shunt resistances and diode quality factor of a photovoltaic cell using the Lambert W-function. *Solar Energy* **91**, 422–431 (2013).
- [225] Alefeld, G. On the convergence of Halley’s Method. *The American Mathematical Monthly* **88**, 530–536 (1981).
- [226] IEEE SA - The IEEE Standards Association. Standard for Floating-Point Arithmetic (IEEE 754) (2019).
- [227] Kirchhoff, S. Ueber den Durchgang eines elektrischen Stromes durch eine Ebene, insbesondere durch eine kreisförmige. *Annalen der Physik* **140**, 497–514 (1845).
- [228] Zinßer, M. *et al.* Holistic yield modeling, top-down loss analysis, and efficiency potential study of thin-film solar modules. *Accepted from Communications Physics* (2022).
- [229] Caswell, J. & Wallis, J. *A Treatise of Algebra, both Historical and Practical* (John Playford, London, 1685).
- [230] Taylor, B. *Methodus incrementorum directa et inversa* (Innys, London, 1715).
- [231] van der Vorst, H. A. Bi-CGSTAB: A fast and smoothly converging variant of Bi-CG for the solution of nonsymmetric linear systems. *SIAM Journal on scientific and statistical Computing* **13**, 631–644 (1992).
- [232] Meijerink, J. A. & van der Vorst, H. A. An iterative solution method for linear systems of which the coefficient matrix is a symmetric M-matrix. *Mathematics of Computation* **31**, 148–162 (1977).
- [233] Nelder, J. A. & Mead, R. A simplex method for function minimization. *The Computer Journal* **7**, 308–313 (1965).

- [234] Rhouma, M. B. H., Gastli, A., Brahim, L. B., Touati, F. & Benammar, M. A simple method for extracting the parameters of the PV cell single-diode model. *Renewable Energy* **113**, 885–894 (2017).
- [235] Chan, D. S. H., Phillips, J. R. & Phang, J. C. H. A comparative study of extraction methods for solar cell model parameters. *Solid-State Electronics* **29**, 329–337 (1986).
- [236] Toledo, F. & Blanes, J. M. Geometric properties of the single-diode photovoltaic model and a new very simple method for parameters extraction. *Renewable Energy* **72**, 125–133 (2014).
- [237] Almonacid, F., Rus, C., Hontoria, L., Fuentes, M. & Nofuentes, G. Characterisation of Si-crystalline PV modules by artificial neural networks. *Renewable Energy* **34**, 941–949 (2009).
- [238] Gastli, A., Ben-Brahim, L. & Rhouma, M. B. H. ANN-based extraction approach of PV cell equivalent circuit parameters. In *17th European Conference on Power Electronics and Applications (EPE'15 ECCE-Europe)*, 1–10 (IEEE, 2015).
- [239] Jervase, J. A., Bourdouce, H. & Al-Lawati, A. Solar cell parameter extraction using genetic algorithms. *Measurement science and technology* **12**, 1922–1925 (2001).
- [240] Ye, M., Wang, X. & Xu, Y. Parameter extraction of solar cells using particle swarm optimization. *Journal of Applied Physics* **105**, 094502 (2009).
- [241] Savitzky, A. & Golay, M. J. E. Smoothing and differentiation of data by simplified least squares procedures. *Analytical Chemistry* **36**, 1627–1639 (1964).
- [242] Levenberg, K. A method for the solution of certain non-linear problems in least squares. *Quarterly of Applied Mathematics* **2**, 164–168 (1944).
- [243] Marquardt, D. W. An algorithm for least-squares estimation of nonlinear parameters. *Journal of the Society for Industrial and Applied Mathematics* **11**, 431–441 (1963).
- [244] Vant-Hull, L. L. & Hildebrandt, A. F. Solar thermal power system based on optical transmission. *Solar Energy* **18**, 31–39 (1976).
- [245] Blanco-Muriel, M., Alarcón-Padilla, D. C., López-Moratalla, T. & Lara-Coira, M. Computing the solar vector. *Solar Energy* **70**, 431–441 (2001).
- [246] Reda, I. & Andreas, A. Solar position algorithm for solar radiation applications. *Solar Energy* **76**, 577–589 (2004).
- [247] Grena, R. An algorithm for the computation of the solar position. *Solar Energy* **82**, 462–470 (2008).
- [248] Walraven, R. Calculating the position of the sun. *Solar Energy* **20**, 393–397 (1978).
- [249] Zhang, T., Stackhouse Jr, P. W., Macpherson, B. & Mikovitz, J. C. A solar azimuth formula that renders circumstantial treatment unnecessary without compromising mathematical rigor: Mathematical setup, application and extension of a formula based on the subsolar point and atan2 function. *Renewable Energy* **172**, 1333–1340 (2021).
- [250] Michalsky, J. J. The astronomical almanac's algorithm for approximate solar position (1950–2050). *Solar Energy* **40**, 227–235 (1988).

- [251] European Commission. Photovoltaic geographical information system. https://re.jrc.ec.europa.eu/pvg_tools/en/tools.html on 2022-03-31 (2019).
- [252] Topsøe, H. Geometric factors in four point resistivity measurement. *Bulletin* **472**, 63 (1968).
- [253] Chung, Y.-Y., Li, C.-F., Lin, C.-T., Ho, Y.-T. & Chien, C.-H. Experimentally Determining the Top and Edge Contact Resistivities of Two-Step Sulfurization Nb-Doped MoS₂ Films Using the Transmission Line Measurement. *IEEE Electron Device Letters* **40**, 1662–1665 (2019).
- [254] Malikov, I. V. & Mikhailov, G. M. Electrical resistivity of epitaxial molybdenum films grown by laser ablation deposition. *Journal of Applied Physics* **82**, 5555–5559 (1997).
- [255] Liu, H.-D., Zhao, Y.-P., Ramanath, G., Murarka, S. P. & Wang, G.-C. Thickness dependent electrical resistivity of ultrathin (< 40 nm) Cu films. *Thin Solid Films* **384**, 151–156 (2001).
- [256] Dutta, S. *et al.* Thickness dependence of the resistivity of platinum-group metal thin films. *Journal of Applied Physics* **122**, 025107 (2017).
- [257] Schmiedl, E., Wissmann, P. & Finzel, H.-U. The electrical resistivity of ultra-thin copper films. *Zeitschrift für Naturforschung A* **63**, 739–744 (2008).
- [258] Lacy, F. Developing a theoretical relationship between electrical resistivity, temperature, and film thickness for conductors. *Nanoscale Research Letters* **6**, 1–14 (2011).
- [259] Edwards, P. P., Porch, A., Jones, M. O., Morgan, D. V. & Perks, R. M. Basic materials physics of transparent conducting oxides. *Dalton transactions* 2995–3002 (2004).
- [260] Marom, H. & Eizenberg, M. The temperature dependence of resistivity in thin metal films. *Journal of Applied Physics* **96**, 3319–3323 (2004).
- [261] Frobose, K. & Jackle, J. On the temperature dependence of the electrical resistivity of amorphous metals. *Journal of Physics F: Metal Physics* **7**, 2331 (1977).
- [262] Nagel, S. R. Temperature dependence of the resistivity in metallic glasses. *Physical Review B* **16**, 1694 (1977).
- [263] Minoura, S. *et al.* Optical constants of Cu(In,Ga)Se₂ for arbitrary Cu and Ga compositions. *Journal of Applied Physics* **117**, 195703 (2015).
- [264] Liu, Z. T., Kwok, H. S. & Djurišić, A. B. The optical functions of metal phthalocyanines. *Journal of Physics D: Applied Physics* **37**, 678 (2004).
- [265] Singh, P. & Ravindra, N. M. Optical properties of metal phthalocyanines. *Journal of Materials Science* **45**, 4013–4020 (2010).
- [266] von Blanckenhagen, B., Tonova, D. & Ullmann, J. Application of the Tauc-Lorentz formulation to the interband absorption of optical coating materials. *Applied Optics* **41**, 3137–3141 (2002).
- [267] Ochoa-Martínez, E. *et al.* Refractive indexes and extinction coefficients of n- and p-type doped GaInP, AlInP and AlGaInP for multijunction solar cells. *Solar Energy Materials and Solar Cells* **174**, 388–396 (2018).
- [268] Park, J.-S. *et al.* Electronic structure and optical properties of α -CH₃NH₃PbBr₃ perovskite single crystal. *The Journal of Physical Chemistry Letters* **6**, 4304–4308 (2015).

- [269] Li, W. *et al.* Effects of deposition methods and processing techniques on band gap, interband electronic transitions, and optical absorption in perovskite $\text{CH}_3\text{NH}_3\text{PbI}_3$ films. *Applied Physics Letters* **111**, 011906 (2017).
- [270] Yamada, T., Makino, H., Yamamoto, N. & Yamamoto, T. Ingrain and grain boundary scattering effects on electron mobility of transparent conducting polycrystalline Ga-doped ZnO films. *Journal of Applied Physics* **107**, 123534 (2010).
- [271] Shan, C. *et al.* Optical and Electrical Properties of Sol–Gel Derived $\text{Ba}_{1-x}\text{La}_x\text{SnO}_3$ Transparent Conducting Films for Potential Optoelectronic Applications. *The Journal of Physical Chemistry C* **118**, 6994–7001 (2014).
- [272] Ibdah, A.-R. A. *et al.* Optical simulation of external quantum efficiency spectra of $\text{CuIn}_{1-x}\text{Ga}_x\text{Se}_2$ solar cells from spectroscopic ellipsometry inputs. *Journal of Energy Chemistry* **27**, 1151–1169 (2018).
- [273] Abou-Ras, D. *et al.* Formation and characterisation of MoSe_2 for $\text{Cu}(\text{In,Ga})\text{Se}_2$ based solar cells. *Thin Solid Films* **480**, 433–438 (2005).
- [274] Zhu, X. *et al.* Determining factor of MoSe_2 formation in $\text{Cu}(\text{In,Ga})\text{Se}_2$ solar cells. *Solar Energy Materials and Solar Cells* **101**, 57–61 (2012).
- [275] Sun, H.-y., Li, P.-h., Xue, Y.-m., Qiao, Z.-x. & Sai, L. Effect of MoSe_2 on the performance of CIGS solar cells. *Optoelectronics Letters* **15**, 428–434 (2019).
- [276] Helder, T. *et al.* DLTS investigations on CIGS solar cells from an inline co-evaporation system with RbF post-deposition treatment. *EPJ Photovoltaics* **13**, 7 (2022).
- [277] Helder, T. *et al.* How small changes make a difference: Influence of low silver contents on the effect of RbF-PDT in CIGS solar cells. *Progress in Photovoltaics: Research and Applications* (2022).
- [278] Kanevce, A., Paetel, S., Hariskos, D. & Magorian Friedlmeier, T. Impact of RbF-PDT on $\text{Cu}(\text{In,Ga})\text{Se}_2$ solar cells with CdS and Zn(O,S) buffer layers. *EPJ Photovoltaics* **11**, 8 (2020).
- [279] Kijima, S. & Nakada, T. High-temperature degradation mechanism of $\text{Cu}(\text{In,Ga})\text{Se}_2$ -based thin film solar cells. *Applied physics express* **1**, 075002 (2008).
- [280] Wi, J.-H. *et al.* Photovoltaic Performance and Interface Behaviors of $\text{Cu}(\text{In,Ga})\text{Se}_2$ Solar Cells with a Sputtered-Zn(O,S) Buffer Layer by High-Temperature Annealing. *ACS Applied Materials & Interfaces* **7**, 17425–17432 (2015).
- [281] Schmid, D., Ruckh, M., Grunwald, F. & Schock, H. W. Chalcopyrite/defect chalcopyrite heterojunctions on the basis of CuInSe_2 . *Journal of Applied Physics* **73**, 2902–2909 (1993).
- [282] Yetkin, H. A. *et al.* Decay mechanisms in CdS-buffered $\text{Cu}(\text{In,Ga})\text{Se}_2$ thin-film solar cells after exposure to thermal stress: Understanding the role of Na. *Progress in Photovoltaics: Research and Applications* **29**, 1034–1053 (2021).
- [283] Yetkin, H. A. *et al.* Elucidating the Effect of the Different Buffer Layers on the Thermal Stability of CIGSe Solar Cells. *IEEE Journal of Photovoltaics* **11**, 648–657 (2021).
- [284] Küffner, J. *et al.* Nanoparticle Wetting Agent for Gas Stream-Assisted Blade-Coated Inverted Perovskite Solar Cells and Modules. *ACS Applied Materials & Interfaces* **12**, 52678–52690 (2020).

- [285] Wahl, T., Hanisch, J., Meier, S., Schultes, M. & Ahlswede, E. Sputtered indium zinc oxide rear electrodes for inverted semitransparent perovskite solar cells without using a protective buffer layer. *Organic Electronics* **54**, 48–53 (2018).
- [286] Rakocevic, L. *et al.* Perovskite modules with 99% geometrical fill factor using point contact interconnections design. *Progress in Photovoltaics: Research and Applications* **28**, 1120–1127 (2020).
- [287] Ritzer, D. B. *et al.* Upscaling of perovskite solar modules: The synergy of fully evaporated layer fabrication and all-laser-scribed interconnections. *Progress in Photovoltaics: Research and Applications* (2021).
- [288] Burgelman, M. & Niemegeers, A. Calculation of CIS and CdTe module efficiencies. *Solar Energy Materials and Solar Cells* **51**, 129–143 (1998).
- [289] Burgelman, M. & Niemegeers, A. Influence of illumination conditions on the design of thin-film modules. *Solar Energy Materials and Solar Cells* **57**, 85–95 (1999).
- [290] Zinßer, M. *et al.* Optical and Electrical Loss Analysis of Thin-film Solar Cells combining the Methods of Transfer-Matrix and Finite Elements. *IEEE Journal of Photovoltaics* **12**, 1154–1161 (2022).
- [291] Slade, A. & Garboushian, V. 27.6% efficient silicon concentrator solar cells for mass production. In *Technical Digest, 15th International Photovoltaic Science and Engineering Conference, Beijing* (2005).
- [292] Ward, J. S. *et al.* A 21.5% efficient Cu(In,Ga)Se₂ thin-film concentrator solar cell. *Progress in Photovoltaics: Research and Applications* **10**, 41–46 (2002).
- [293] Boukortt, N. E. I., Patanè, S., Adouane, M. & AlHammadi, R. Numerical optimization of ultrathin CIGS solar cells with rear surface passivation. *Solar Energy* **220**, 590–597 (2021).
- [294] Díaz-Loera, A., Ramos-Serrano, J. R. & Calixto, M. E. Semiconducting CuIn (SX, Se1- X) 2 thin-film solar cells modeling using SCAPS-1D. *MRS Advances* **7**, 28–32 (2022).
- [295] Sun, X., Silverman, T., Garris, R., Deline, C. & Alam, M. A. An illumination-and temperature-dependent analytical model for copper indium gallium diselenide (CIGS) solar cells. *IEEE Journal of Photovoltaics* **6**, 1298–1307 (2016).
- [296] Sozzi, G. *et al.* Influence of conduction band offsets at window/buffer and buffer/absorber interfaces on the roll-over of JV curves of CIGS solar cells. In *IEEE 44th Photovoltaic Specialist Conference (PVSC)*, 2205–2208 (2017).
- [297] Mostefaoui, M., Mazari, H., Khelifi, S., Bouraiou, A. & Dabou, R. Simulation of high efficiency CIGS solar cells with SCAPS-1D software. *Energy Procedia* **74**, 736–744 (2015).
- [298] Witte, W. *et al.* Gallium gradients in Cu(In,Ga)Se₂ thin-film solar cells. *Progress in Photovoltaics: Research and Applications* **23**, 717–733 (2015).
- [299] Richter, M., Hammer, M., Sonnet, T. & Parisi, J. Bandgap extraction from quantum efficiency spectra of Cu(In,Ga)Se₂ solar cells with varied grading profile and diffusion length. *Thin Solid Films* **633**, 213–217 (2017).
- [300] Shockley, W. T. R. W. & Read Jr, W. T. Statistics of the recombinations of holes and electrons. *Physical Review* **87**, 835 (1952).

-
- [301] Hall, R. N. Electron-hole recombination in germanium. *Physical Review* **87**, 387 (1952).
- [302] Meitner, L. Über die Entstehung der β -Strahl-Spektren radioaktiver Substanzen. *Zeitschrift für Physik* **9**, 131–144 (1922).
- [303] Auger, P. Sur les rayons β secondaires produits dans un gaz par des rayons x. *Comptes Rendus hebdomadaires des Séances de l'Académie des Sciences* **177**, 169–171 (1923).
- [304] Eades, W. D. & Swanson, R. M. Calculation of surface generation and recombination velocities at the Si-SiO₂ interface. *Journal of Applied Physics* **58**, 4267–4276 (1985).
- [305] Schmager, R. *et al.* Methodology of energy yield modelling of perovskite-based multi-junction photovoltaics. *Optics Express* **27**, A507–A523 (2019).
- [306] Langenhorst, M. *et al.* Energy yield of all thin-film perovskite/CIGS tandem solar modules. *Progress in Photovoltaics: Research and Applications* **27**, 290–298 (2019).
- [307] De Bastiani, M. *et al.* Efficient bifacial monolithic perovskite/silicon tandem solar cells via bandgap engineering. *Nature Energy* **6**, 167–175 (2021).
- [308] Hegedus, S. S. & Shafarman, W. N. Thin-film solar cells: device measurements and analysis. *Progress in Photovoltaics: Research and Applications* **12**, 155–176 (2004).
- [309] Wenham, S. R., Green, M. A., Watt, M. E., Corkish, R. & Sproul, A. *Applied Photovoltaics* (Routledge, 2013).
- [310] Meneses-Rodríguez, D., Horley, P. P., Gonzalez-Hernandez, J., Vorobiev, Y. V. & Gorley, P. N. Photovoltaic solar cells performance at elevated temperatures. *Solar Energy* **78**, 243–250 (2005).
- [311] Green, M. A. *Solar cells: operating principles, technology, and system applications* (Englewood Cliffs, 1982).
- [312] Theelen, M. *et al.* Determination of the temperature dependency of the electrical parameters of CIGS solar cells. *Journal of Renewable and Sustainable Energy* **9**, 021205 (2017).
- [313] Singh, P. & Ravindra, N. M. Temperature dependence of solar cell performance - an analysis. *Solar Energy Materials and Solar Cells* **101**, 36–45 (2012).
- [314] Virtuani, A., Pavanello, D. & Friesen, G. Overview of temperature coefficients of different thin film photovoltaic technologies. In *25th European Photovoltaic Solar Energy Conference and Exhibition / 5th World Conference on Photovoltaic Energy Conversion*, vol. 4, 4248–4252 (2010).
- [315] Liu, S. H. *et al.* Evaluation of thin-film solar cell temperature coefficients for space applications. *Progress in Photovoltaics: Research and Applications* **13**, 149–156 (2005).
- [316] Mittag, M., Vogt, L., Herzog, C. & Neuhaus, H. Thermal modelling of photovoltaic modules in operation and production. In *36th European Photovoltaic Solar Energy Conference and Exhibition (EUPVSEC)* (2019).
- [317] Siebentritt, S. What limits the efficiency of chalcopyrite solar cells? *Solar Energy Materials and Solar Cells* **95**, 1471–1476 (2011).

- [318] Lundberg, O., Edoff, M. & Stolt, L. The effect of Ga-grading in CIGS thin film solar cells. *Thin Solid Films* **480**, 520–525 (2005).
- [319] Jackson, P. *et al.* Effects of heavy alkali elements in Cu(In,Ga)Se₂ solar cells with efficiencies up to 22.6%. *Physica Status Solidi (RRL) - Rapid Research Letters* **10**, 583–586 (2016).
- [320] Carron, R. *et al.* Advanced alkali treatments for high-efficiency Cu(In,Ga)Se₂ solar cells on flexible substrates. *Advanced Energy Materials* **9**, 1900408 (2019).
- [321] Lindahl, J. *et al.* Inline Cu(In,Ga)Se₂ Co-evaporation for high-efficiency solar cells and modules. *IEEE Journal of Photovoltaics* **3**, 1100–1105 (2013).
- [322] Zinßer, M. *et al.* Irradiation-dependent Topology Optimization of Metallization Grid Patterns used for latitude-based Yield Gain of Thin-film Solar Modules. *MRS Advances* **7**, 706–712 (2022).
- [323] Bendsøe, M. P. & Kikuchi, N. Generating optimal topologies in structural design using a homogenization method. *Computer Methods in Applied Mechanics and Engineering* **71**, 197–224 (1988).
- [324] Gersborg-Hansen, A., Bendsøe, M. P. & Sigmund, O. Topology optimization of heat conduction problems using the finite volume method. *Structural and Multidisciplinary Optimization* **31**, 251–259 (2006).
- [325] Proos, K. A., Steven, G. P., Querin, O. M. & Xie, Y. M. Multicriterion evolutionary structural optimization using the weighting and the global criterion methods. *AIAA Journal* **39**, 2006–2012 (2001).
- [326] Zolfagharian, A., Denk, M., Bodaghi, M., Kouzani, A. Z. & Kaynak, A. Topology-optimized 4D printing of a soft actuator. *Acta Mechanica Solida Sinica* **33**, 418–430 (2020).
- [327] Dede, E. M. Multiphysics topology optimization of heat transfer and fluid flow systems. In *Proceedings of the COMSOL Users Conference*, vol. 715 (2009).
- [328] Kim, W.-Y., Grandhi, R. V. & Haney, M. Multiobjective evolutionary structural optimization using combined static/dynamic control parameters. *AIAA Journal* **44**, 794–802 (2006).
- [329] Denk, M., Rother, K., Zinßer, M., Petroll, C. & Paetzold, K. Nodal cosine sine material interpolation in multi objective topology optimization with the global criteria method for linear elasto static heat transfer potential flow and binary cross entropy sharpening. In *Proceedings of the Design Society*, 2247–2256 (2021).
- [330] Van Keulen, F., Haftka, R. T. & Kim, N.-H. Review of options for structural design sensitivity analysis. Part 1: Linear systems. *Computer Methods in Applied Mechanics and Engineering* **194**, 3213–3243 (2005).
- [331] Beckers, M. Topology optimization using a dual method with discrete variables. *Structural Optimization* **17**, 14–24 (1999).
- [332] Bendsøe, M. P. Optimal shape design as a material distribution problem. *Structural Optimization* **1**, 193–202 (1989).
- [333] Zhou, M. & Rozvany, G. I. N. The COC algorithm, Part II: Topological, geometrical and generalized shape optimization. *Computer Methods in Applied Mechanics and Engineering* **89**, 309–336 (1991).

- [334] Mlejnek, H. Some aspects of the genesis of structures. *Structural Optimization* **5**, 64–69 (1992).
- [335] Braun, B. Topology Optimization of Metalization Grid Patterns to Improve the Power Conversion Efficiency of Thin-Film Solar Cells. *University of Stuttgart* (2021).
- [336] Broyden, C. G. The convergence of a class of double-rank minimization algorithms 1. general considerations. *IMA Journal of Applied Mathematics* **6**, 76–90 (1970).
- [337] Fletcher, R. A new approach to variable metric algorithms. *The Computer Journal* **13**, 317–322 (1970).
- [338] Goldfarb, D. A family of variable-metric methods derived by variational means. *Mathematics of Computation* **24**, 23–26 (1970).
- [339] Shanno, D. F. Conditioning of quasi-Newton methods for function minimization. *Mathematics of Computation* **24**, 647–656 (1970).
- [340] Kingma, D. P. & Ba, J. Adam: A method for stochastic optimization. *arXiv:1412.6980 [cs.LG]* (2014).
- [341] Bruns, T. E. & Tortorelli, D. A. Topology optimization of non-linear elastic structures and compliant mechanisms. *Computer Methods in Applied Mechanics and Engineering* **190**, 3443–3459 (2001).
- [342] Sigmund, O. Morphology-based black and white filters for topology optimization. *Structural and Multidisciplinary Optimization* **33**, 401–424 (2007).
- [343] Bruns, T. E. & Tortorelli, D. A. An element removal and reintroduction strategy for the topology optimization of structures and compliant mechanisms. *International Journal for Numerical Methods in Engineering* **57**, 1413–1430 (2003).
- [344] Cresta, P., Allix, O., Rey, C. & Guinard, S. Nonlinear localization strategies for domain decomposition methods: Application to post-buckling analyses. *Computer Methods in Applied Mechanics and Engineering* **196**, 1436–1446 (2007).
- [345] Almora, O. *et al.* Device Performance of Emerging Photovoltaic Materials (Version 2). *Advanced Energy Materials* **11**, 2102526 (2021).
- [346] Jäger, T. *et al.* Hydrogenated indium oxide window layers for high-efficiency Cu(In,Ga)Se₂ solar cells. *Journal of Applied Physics* **117**, 205301 (2015).
- [347] Witte, W. *et al.* IZO or IOH window layers combined with Zn(O,S) and CdS buffers for Cu(In,Ga)Se₂ solar cells. *physica status solidi (a)* **214**, 1700688 (2017).
- [348] Koprek, A. *et al.* Cd and impurity redistribution at the CdS/CIGS interface after annealing of CIGS-based solar cells resolved by atom probe tomography. *IEEE Journal of Photovoltaics* **7**, 313–321 (2016).
- [349] Tai, K. F., Kamada, R., Yagioka, T., Kato, T. & Sugimoto, H. From 20.9 to 22.3% Cu(In,Ga)(S,Se)₂ solar cell: Reduced recombination rate at the heterojunction and the depletion region due to K-treatment. *Japanese Journal of Applied Physics* **56**, 08MC03 (2017).
- [350] Hünig, R. *et al.* Flower power: exploiting plants' epidermal structures for enhanced light harvesting in thin-film solar cells. *Advanced Optical Materials* **4**, 1487–1493 (2016).

- [351] Hobbs, D. S. Laser damage threshold measurements of anti-reflection microstructures operating in the near UV and mid-infrared. In *Laser-Induced Damage in Optical Materials: 2010*, vol. 7842, 509–521 (SPIE, 2010).
- [352] Levi, D. H. *et al.* Solar cell efficiency tables (version 51). *Progress in Photovoltaics* **26**, 3–12 (2017).
- [353] Nayak, P. K., Mahesh, S., Snaith, H. J. & Cahen, D. Photovoltaic solar cell technologies: analysing the state of the art. *Nature Reviews Materials* **4**, 269–285 (2019).
- [354] Guillemoles, J.-F., Kirchartz, T., Cahen, D. & Rau, U. Guide for the perplexed to the Shockley–Queisser model for solar cells. *Nature Photonics* **13**, 501–505 (2019).
- [355] Scherg-Kurmes, H. *et al.* Optimization of the post-deposition annealing process of high-mobility In_2O_3 : H for photovoltaic applications. *Thin Solid Films* **599**, 78–83 (2016).
- [356] Addonizio, M. L., Spadoni, A., Antonaia, A., Usatii, I. & Bobeico, E. Hydrogen-doped In_2O_3 for silicon heterojunction solar cells: Identification of a critical threshold for water content and rf sputtering power. *Solar Energy Materials and Solar Cells* **220**, 110844 (2021).
- [357] Li, Y., Yang, S., Zhang, X. & Xiao, X. Optimal design of a CIGS module grid. *MRS Online Proceedings Library (OPL)* **1315** (2011).
- [358] Tahar, R. B. H. & Tahar, N. B. H. Boron-doped zinc oxide thin films prepared by sol-gel technique. *Journal of Materials Science* **40**, 5285–5289 (2005).
- [359] Green, M. A. & Ho-Baillie, A. W. Y. Pushing to the limit: Radiative efficiencies of recent mainstream and emerging solar cells. *ACS Energy Letters* **4**, 1639–1644 (2019).
- [360] Kennelly, A. E. The equivalence of triangles and three-pointed stars in conducting networks. *Electrical World and Engineer* **34**, 413–414 (1899).
- [361] Rosen, A. A new network theorem. *Journal of the Institution of Electrical Engineers* **62**, 916–918 (1924).

Acknowledgements

Three years ago I started my PhD-journey somewhere at the intersection of environmental engineering, scientific programming, solid-state physics, and electrical and optical laboratory work. By looking back on this time retrospectively, it is a pleasure for me to have taken this path. However, the opportunity in doing so should not be treated as granted but rather as a great gift that I am very happy to have received. Having in mind all laboratory misfortunes, all programming bugs, all external rejections, all dead end thoughts, all my own doubts, and endless days and nights in front of tens of thousands of lines of code, I have learned like never before:

MINDSET IS EVERYTHING!

Simply by looking at these things from another perspective shows that all these obstacles are one by one just possibilities to find new experimental ways, opportunities to improve written code, external incentive to my own motivation, open-minded and non-biased thoughts covering the entire cognitive spectrum and eventually leading to new ideas, meaningful consideration of my own work, and finally a perfect training for my own perseverance.

After dedicating three and a half years to finish this sustainability-inspired simulation project, evolving passionate commitment and determination, and finally to submit this thesis, I am very proud to contribute a tiny pixel into the gigantic picture of the interdisciplinary nature of fascinating reality. I am thankful to the nature of scientific research, where the reactions to simulated results typically switch between indifferent banality and refusing contradiction. No matter if discussing solid-state physics in the office, characterizing solar cells in the laboratory or programming FEM simulations at home during the COVID-19 pandemic, I am very grateful to always be driven by an inexhaustible well of splashing vital energy, relentless motivation and curiosity for undiscovered phenomena and dedicated love of life. During two consecutive years of global pandemic we all realized the importance of not only acquiring knowledge and emotions but also sharing them with all kinds of people. Finally I am thankful for having the possibility to take my PhD time as a great opportunity to learn scientific issues and engineering approaches but also to gather experience in interdisciplinary fields and to keep track of the never-ending learning curve in personal development.

This path to finally reach the desired goal would not have been possible without several persons. There are countless people that always believed in me and never gave up on me regardless of how unpromising the current situation looked. The following personally addressed acknowledgements are not my duty but my sublime pleasure.

First of all, I would like to thank my doctoral advisor Prof. Dr.-Ing. Michael Powalla for your guidance towards the final goal and for keeping me on track by always having in mind the big picture. Your willingness to give me the freedom for my research topic allowed me to evolve and implement my own ideas. Your trust and interest in my work and your fruitful vision for simulations in scientific engineering were always a big motivation for me.

Further gratitude goes to Prof. Dr.-Ing. Thomas Kirchartz for kindly accepting to be co-referee for this thesis. With your wide experience and theoretical background information you contributed well to helpful discussions and pointed hints towards new directions of research.

Special thanks goes to my direct supervisor Dr.-Ing. Andreas Bauer. You always had the ambitious and determined vision for the project, from the beginning till the end. Thank you for your broad spectrum of wide-ranging ideas and impulses and - which should definitely not be taken for granted - for being able to discuss on an equal footing even in the deepest specialized issues.

Moreover, I'd like to thank Dr.-Ing. Theresa Magorian Friedlmeier for your user-oriented view on the simulation platform and of course for taking over being my supervisor in the final phase of my PhD time. Thank you for listening to all my crazy ideas and publication concepts and for helping out in all kinds of business challenges and for sure, for the continuous proof-reading of my publications.

This project definitively would not have gone so smoothly without the help of Tim Helder. Discussions with you were always results-oriented, on the point, and clearly focused on a realistic assessment of the feasibility and practicability. Your experienced laboratory work and your willingness in letting me benefit from it accelerated my scientific progress significantly. Moreover, your openness for interdependent worksharing and cooperative collection of ideas and their implementation simplified the work stages of this work.

Furthermore, I thank Dr.-Ing. Moritz Loy for sharing your sheer knowledge in seemingly every imaginable topic, your contribution to the simulation based on your experimental experience, and your love and endowment in exciting story telling. In addition, thanks goes to Dr.-Ing. Erwin Lotter, Dr. Stefan Paetel, Dr. Jan-Philipp Becker, Dr. Ana Kanevce, Dr. Rolf Wächter, Dirk Stellbogen, and Prof. Dr. Uwe Rau for productive and purposeful discussions and sharing your longstanding experience. Also I want to thank to Dr.-Ing. Julia Zillner, Dr.-Ing. Johannes Küffner, and Alexander Eslam for fighting the same battle with the same goal and for the pleasant and enjoyable interaction with each other.

My thanks also goes to my bachelor student Benedikt Braun for contributing a mathematical aspect to my thesis, his eager motivation for a joint development and improvement of the optimization algorithm, and the more than thousand design proposals for a new optimized grid pattern.

Moreover, I love to thank Dr. Nicolas Gaillard and Kai Outlaw from Hawai'i Natural Energy Institute (HNEI) at the University of Hawai'i (UH) for their patience to explain all their laboratory to me, for taking care of all the bureaucracy for my stay abroad at UH, and for the combination of a comfortable working atmosphere and nevertheless a high joint workload.

In particular, I would like to thank Martin Tschöpe for his rational and objective opinions on my simulations from an external and unbiased point of view and for being the seed of one idea or another. Additionally I thank you for looking beyond the horizon reaching all topics from optimization problems to machine learning, from innovative solar applications to energy storage systems, and from turbochargers to orbital rocket launch systems.

Last, but definitely not least, I am proud to thank my parents for their pivotal mental contribution, the continuous and unconditional support, and, most of all, for enabling this nearly three decades of education.

